The Preparation of Topological Modes in a Strongly-Coupled Two-Component Bose-Einstein Condensate

by

James Edgar Williams

B.S., University of Iowa, 1994

A thesis submitted to the
Faculty of the Graduate School of the
University of Colorado in partial fulfillment
of the requirements for the degree of
Doctor of Philosophy
Department of Physics
1999

This thesis entitled:
The Preparation of Topological Modes in a Strongly-Coupled Two-Component Bose-Einstein Condensate
written by James Edgar Williams
has been approved for the Department of Physics

_____
Prof. Murray Holland

_____
Prof. John Cooper

Date _____

The final copy of this thesis has been examined by the signatories, and we find that both the content and the form meet acceptable presentation standards of scholarly work in the above mentioned discipline.

Williams, James Edgar (Ph.D., Physics)

The Preparation of Topological Modes in a Strongly-Coupled Two-Component Bose-Einstein Condensate

Thesis directed by Prof. Murray Holland

In this thesis, we present a detailed theoretical study of a coupled two-component Bose-Einstein condensate in a magnetic trap. We first present a quantum kinetic theory describing the Bose-condensed gas, that applies to general finite-temperature and nonequilibrium situations. We then treat the coupled, two-component condensate at zero-temperature by solving the Gross-Pitaevskii equation, in which the fluctuations are neglected. We show that in the weak-coupling limit, the system behaves like a nonlinear Josephson-junction, analogous to two condensates in a double-well potential that are coupled due to quantum tunneling. In the opposite limit of strong coupling between internal states, we show that the condensate can be prepared in a variety of new topological states. In particular, we predict a scheme for generating a quantized vortex in this two-component system, where one component sits in the center with a uniform phase while the other circulates around it. Subsequent related experimental work at JILA by the group of Eric Cornell and Carl Wieman has demonstrated these predictions in the laboratory —this is the first observation of a vortex in a dilute-gas Bose-Einstein condensate. Finally, we study the kinetic evolution of a single-component gas above the critical temperature by solving the Boltzmann equation and investigate the possibility of achieving a steady-state condensation, which can occur if atoms are injected into the trap during evaporative cooling.

Acknowledgements

This thesis work is really the culmination of many years of learning, and I speak not only of my studies here in graduate school at the University of Colorado, but also of my undergraduate studies at the University of Iowa and my time at Shenandoah High School. Looking back over the years, I recall with heartfelt gratitude the many people who have inspired and encouraged me along my journey that began in a rural town in Iowa. I am very fortunate to have been guided along the way by teachers, family, friends, and colleagues, who have all played a role in helping me to realize my potential. As I close this chapter of my life and turn the page to the next, it is important for me to express my sincere appreciation of their support.

I have been very lucky to have not only one, but two amazing advisors. It has been a great pleasure working with Murray Holland and Jinx Cooper, who have given me the opportunity to work on such an exciting and rewarding project; I deeply appreciate their constant guidance and encouragement throughout my research. Their thoughtful choices of projects have allowed me to learn many different aspects of BEC and to establish a broad knowledge base upon which to build further understanding. Furthermore, they have given me the freedom to explore each problem and to pose new questions myself, so that I could develop the creative problem-solving skills needed to do original research. For this I am forever grateful. From them I have also developed an appreciation for the need to link theory to experiment, and the question "What's the observable?" will forever be imprinted on my psyche. I am also glad to have developed a friendship with both Murray and Jinx during my time at JILA, which has made my experience here all the more memorable. I look forward to new collaborations with them in the future.

I am also grateful for the opportunity to have collaborated with Eric Cornell and Carl Wieman, which has made my research experience at JILA immensely more meaningful. I thank them for inviting me to their weekly experimental meetings, where I gained an appreciation for their craft. It was Eric who provided the impetus for our theoretical investigations of the coupled, two-component condensate and gave us continual feedback, which helped us to stay closely tied to the experiments. I feel very lucky to have been a part of the exciting discoveries leading up to the observation of a vortex in the two-component system and it is an experience I will never forget (for such an opportunity is certainly rare). I have also benefitted from discussions with Carl, who has always taken the time to understand our theoretical work. It was he who planted the seed for our study of steady-state BEC, an idea I believe that will someday be realized in the laboratory.

JILA has been such a stimulating environment to do research, for I have benefitted greatly from my frequent interactions with professors, post-docs, and fellow graduate students, who are all part of a fertile scientific community here. I would especially like to acknowledge the generosity of Reinhold Walser in our theory group, who is one of the

most helpful persons I have ever met. I have thoroughly enjoyed our frequent discussions about physics and life in general. I am indebted to him for his work on quantum kinetic theory, without which Chapter 2 of this thesis could not have been written. I have also enjoyed interacting with Jae Park, whose curiosity and questions (that I can rarely answer) always make me realize that I still have much to learn. I also want to express my deepest gratitude to the BEC experimentalists, especially Mike Matthews, Brian Anderson, Paul Haljan, and David Hall, who have played a major role in the development of our work on the coupled two-component condensate. Their expertise in the lab has been a real source of inspiration and I have enjoyed learning from them. I also thank them for sharing experimental data with me. I have also benefitted from discussions with Chris Greene, Brett Esry, Jim Burke, and John Bohn over the years.

An important part of a graduate student's education is traveling and interacting with fellow colleagues from other institutions. During my time at JILA, I have had the chance to meet many scientists from around the world, who make up part of an international BEC community. I have especially enjoyed my interactions with Allan Griffin and Eugene Zaremba, who were visiting fellows at JILA this year. I was also very fortunate to have been given the opportunity to travel to Europe on two occasions, and I owe Murray my gratitude for sending me. In the summer of 1997 I spent two months at the Institute for Theoretical Physics in Innsbruck with the group of Peter Zoller and Ignacio Cirac. It was a memorable experience for me and I sincerely appreciate Peter's gracious hospitality. In the summer of 1998, I traveled to Italy to attend the Enrico Fermi summer school on BEC, which was an extremely inspiring learning experience. That trip would not have been possible without the help of Eric and Jinx. I especially would like to thank Marilu' Chiofalo for her invitation for me to speak at SNS in Pisa during my visit to Italy. I will not forget the week I spent there and the genuine hospitality of Marilu' and Massimilliano. I have also enjoyed the several visits Marilu' made to JILA, for we had many stimulating discussions on BEC while she was here.

I would also like to thank the staff at JILA for their assistance over the years, especially Pat Mcinerny for providing me with a private office to write my thesis. I don't think I would have ever finished on time otherwise. I also would like to thank Linda Frueh and Susan Thompson in the physics office, who have always been very helpful.

I know for sure that my success in graduate school would not have been possible without the preparation I received at the University of Iowa as an undergraduate. I especially would like to thank Bill Klink, who deeply inspired me to take my studies of physics to a higher level. I still have my lecture notes from quantum mechanics and a lingering affinity for group theory that he instilled in me. I also would like to thank Paul Kleiber for giving me my first taste of atomic physics and Karl Lonngren for letting me do experiments in his lab on ion-acoustic waves in a plasma, which I will always remember.

I also can not forget my two favorite high school teachers, who were the first teachers to really inspire me over a decade ago. I am grateful to my science teacher, Larry Oiler, whose passion for science was contagious. It was in his custom-made course "Science and Society" that I got my first taste of the wonderment of discovery. I especially want to thank my art teacher, Julie Gee, for always believing in me and encouraging me. She has always been a real inspiration to me and a true friend.

I owe my deepest, most solemn thanks to my parents, who have always supported me without question and who brought me into a loving and caring family. All of the education in the world can not teach me what they have mastered, and what I will always struggle to achieve: kindness and generosity toward other people. I also thank my two older brothers,

John and Michael, for always being there for me and for encouraging me to go all the way. I thank my entire family, including my sister-in-law, Heidi, and my little niece Lexi, for putting up with my neglect over the last five years with my head in my books.

Finally, I would like to express my sincere thanks to my best friend, Tanya Ramond, who has been my companion throughout graduate school. She is the most giving and caring person I have ever met. She has always been there for me when I needed encouragement and support to get through the tough times. She has also put up with my increasing self-absorption with my studies and has always listened to me ramble on excitedly about my research. Her courage and perseverance through some of the most challenging times in graduate school are an inspiration to me and I look forward to watching her continue to grow, both as a physicist and a person.

Contents

List of Figures

List of Tables

Chapter 1

Introduction

Experimental observation of Bose-Einstein condensation

The first experimental observation of Bose-Einstein condensation (BEC) in a dilute atomic gas occurred in the summer of 1995 at the University of Colorado by a team of scientists at JILA, led by Professors Carl Wieman and Eric Cornell [1], and soon after by the group of Professor Wolfgang Ketterle [2] at the Massachusetts Institute of Technology (MIT). In a short span of four years, the number of experimental groups that have observed BEC has increased from two in the United States to over twenty worldwide [3]. Because these atomic systems are relatively easy to probe and manipulate in the laboratory, a wealth of experimental data is becoming available for comparison to theory and many new questions are being asked that are pushing the theory of low-temperature, many-particle physics in exciting new directions. This cutting-edge research has opened up a thriving new field of physics, as indicated by the assignment of its own section, entitled *Matter Waves*, in the journal *Physical Review A*. It has caught the interest of some of the most talented scientists from across a broad range of fields, such as atomic and molecular physics, quantum optics, and condensed matter physics.

This experimental breakthrough has had such a tremendous impact on low-temperature physics because these dilute atomic gases offer a long list of new properties that make them very attractive to study in the lab and extremely interesting to consider theoretically. The ability to control and probe these atomic systems with electromagnetic radiation has played a key role throughout this exciting development. The internal structure of the alkali atoms used in these experiments is very well known and a large array of transitions ranging from optical to radio frequency can be accessed with inexpensive lasers and synthesizers. Innovative new technologies, such as laser cooling and trapping, are based on a detailed understanding of atom-light interaction and have provided physicists with the tools needed to cool the atomic gas to the ultra-low temperatures required to reach BEC [4, 5, 6]. Laser light is also used to image the gas sample to obtain either the density or the momentum distribution of the gas, from which many useful properties of the condensate can be ascertained. The condensate can also be probed by varying the magnetic fields of the confining potential in a controlled manner in order to investigate the collective modes of the system, for example.

With so many different ways to probe and excite the condensate, it is not surprising that many new properties are being explored that had never been considered previously in the vast literature on Bose-condensed systems. One such novel system is that of a driven, two-

component condensate, where an external electromagnetic field is applied that coherently couples two internal states of the atoms. Recent experiments at JILA by the group of Eric Cornell and Carl Wieman [7, 8, 9, 10, 11, 12, 13, 14] have explored many interesting properties of this system; this experimental work provides the inspiration for several related projects presented in Chapters 4 through 6 of this thesis. As a result of this productive experiment-theory collaboration at JILA, a surprising new development has occurred that is pushing our understanding of BEC in an exciting new direction: we have discovered a way to coherently transfer atoms in the condensate from the usual mean-field ground state of the trap to a variety of different macroscopic excited states, such as a vortex. This technique exploits a rather non-intuitive effect arising from the subtle interplay between the internal and motional dynamics of the condensate, which we describe in detail in Chapter 6. This collaborative effort has lead to the first experimental observation of a vortex in a dilute Bose-condensed gas [14].

What is Bose-Einstein condensation?

In order to appreciate the remarkable new developments in this growing field, one should first understand the basic properties of BEC in a dilute atomic gas. The most striking feature of BEC is that the wave-like behavior of matter predicted by quantum mechanics is exhibited on a macroscopic scale due to the condensation of, typically, millions of identical atoms into the same quantum state. Just as a classical electromagnetic field is described by an amplitude and a phase, so too is this quantum gas. One of the most visually stunning observations of quantum coherence on a macroscopic scale was made by allowing two initially isolated condensates to overlap; the resulting density pattern displayed interference fringes, analogous to the interference between coherent light waves emanating from a double slit [15]. Another intriguing property of Bose-condensed systems is the unrestricted flow of particles in the sample, such as persistent currents in super-fluid helium that flow without observable viscosity, and electric currents in superconductors that flow without observable resistance. These "super" properties of Bose-condensed systems occur because the macroscopic occupation of a quantized mode, such as a vortex, can provide a stabilizing mechanism that inhibits decay due to thermal relaxation [16]. The recent observation of a vortex in the dilute Bose-condensed gas has opened the door to the study of super-fluidity in these systems [14].

The idea of a macroscopic number of identical particles acting in unison to exhibit wave-like behavior is counter-intuitive to our daily experience of the world, where objects are distinguishable and behave like particles that follow classical trajectories described by Newton's laws of motion. In the BEC experiments, this classical description of the system is initially valid when the atomic sample is loaded into a vacuum cell and laser cooling begins, followed by evaporative cooling in a second stage of the experiment. Imagine this gas of particles in the container at room temperature. Based on our intuition, we can label a particle and track its motion in the gas: it travels the mean free path l of the gas before passing by another particle within some interaction radius a. This results in a momentum-changing collision, and then it continues until the next collision and so on. This evolution of the gas is given by the classical Boltzmann kinetic equation, which predicts that in equilibrium the system is described by the Maxwell-Boltzmann distribution.

Quantum mechanics, however, predicts that as the temperature of the gas approaches some critical value T_c, the wave-like nature of the particles becomes important to consider. As the gas is cooled down, the particles become smeared out and each one can best be

described as a wave-packet, with a characteristic wavelength $\lambda_{\rm dB} = (2\pi\hbar^2/mk_BT)^{1/2}$, called the thermal de Broglie wavelength, where m is the mass of the atom and T is the temperature. As the temperature is lowered close to $T_{\rm c}$, the effect of smearing the position of a single particle becomes so enhanced that the de Broglie wavelength becomes comparable to the mean-free path, $\lambda_{\rm dB} \approx l$ and the wave-packets begin to overlap. At this point it becomes impossible to distinguish one particle from another. Due to this indistinguishability, the particles become correlated in a particular way, depending on whether they are bosons or fermions. For bosons, this correlation causes all of the particles to "condense" into a single wave-packet with the longest wavelength permitted by the size of the box. Since photons are bosons, they too exhibit this phase transition, which takes the form of the ubiquitous laser, which produces a phase-coherent beam of light. One obvious application of BEC, then, would be to produce a phase-coherent beam of atoms—an atom laser [17, 18, 19].

Of course this description is overly simplified. In fact, one has to incorporate both of the particle and wave concepts described above into a proper treatment of BEC. In other words, one must unify the notion of collision-induced fluctuations with the idea of having a single coherent wave packet. If the interactions between particles in the system are very strong, then the strong correlations due to collisions will dominate the system and obscure the coherence properties of the condensate, which typically had been the situation for Bose-condensed systems studied in condensed matter physics, such as super-fluid helium. In sharp contrast, interactions between particles in a dilute atomic gas have a weak effect, so that the wave-like condensate dominates the system and collisions can be treated perturbatively. In this case, the interaction of all of the particles on a single particle can be summed to give an averaged effect, as a first approximation. This approach is called *mean-field theory* and with suitable approximations gives rise to the *Gross-Pitaevskii equation* that describes the time-evolution of the condensate, in which the effect of interactions gives rise to a density dependent effective potential that makes the dynamics of the condensate nonlinear. This simple description does not include the fluctuations due to collisions, but just treats their averaged effect. This approximation is appropriate in the $T = 0$ limit, which we consider in Chapter 3 for a single component BEC. How to properly treat the collisional fluctuations in these dilute systems is an active area of research in this field [20, 21, 22, 23, 24, 25, 26, 27]. In Chapter 2 we will present our own version of the underlying theory for this system that describes the condensate and fluctuations about it and includes the dissipative effect of collisions.

Overview of the thesis

This thesis is divided into three main parts, as illustrated schematically in the flow chart shown in Figure 1.1. In Chapter 2 we present a quantum kinetic theory describing the dilute Bose-condensed gas at finite temperature. The results of this theory extend the standard treatment of the system by including the dissipative effect of collisions. The main result of the chapter is the closed, coupled set of kinetic equations Eq. (2.70) to Eq. (2.72) describing the mean-field, the normal fluctuations, and the anomalous fluctuations, respectively. By dropping the collision terms from the kinetic equations in section 2.4.1, we recover the usual Hartree-Fock-Bogoliubov result, and if we make the further simplification of neglecting the fluctuations altogether, we recover the Gross-Pitaevskii (GP) equation. This will be the starting point for Chapter 3. We also consider the high temperature limit in section 2.4.2 by completely neglecting the mean-field and anomalous fluctuations. There we derive the

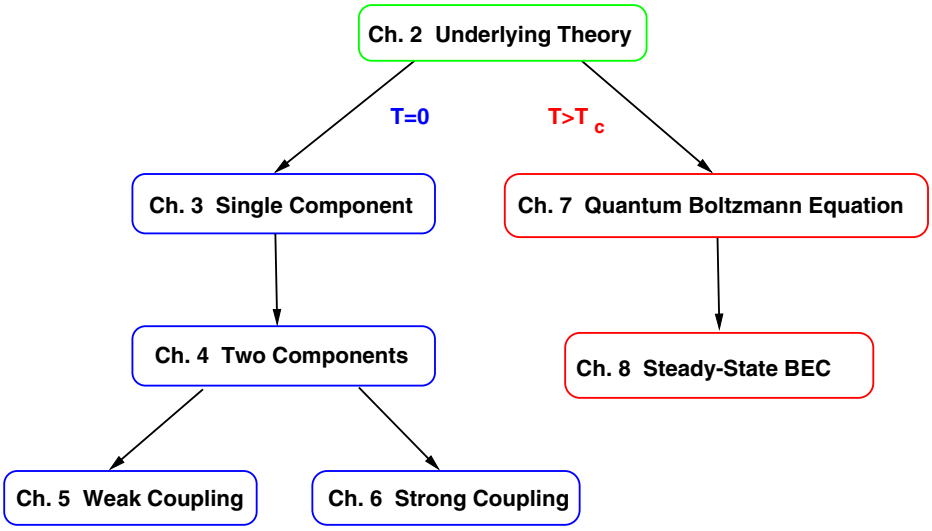

Figure 1.1: Flow chart of the chapters in the thesis. The structure of the thesis consists of three main parts: the underlying theory of BEC, the coupled two-component condensate at $T = 0$, and solutions of the kinetic equation at $T > T_c$.

quantum Boltzmann equation, which is the starting point for Chapter 7.

The first generation of experiments in BEC, and correspondingly most theoretical investigations, dealt with a single-component condensate, where only one atomic species is present. In Chapter 3 we consider this basic system and outline some of the main concepts, such as the condensate ground state, topological modes, and elementary excitations, in order to get an overview of zero temperature mean-field theory for a single-component system. In these systems, condensation occurs into the lowest-energy state of the trap. In the absence of interactions, this would just be the Gaussian-shaped ground state of the harmonic trapping potential. However, the condensate ground state is actually much bigger than this and is shaped like an inverted parabola due to the effect of interactions. In section 3.3 we show results of numerical calculations of the condensate ground state and discuss some of its basic properties.

A great deal of theoretical work has appeared in the literature over the last few years investigating vortices in a single-component dilute-gas BEC. One proposed scheme for preparing the condensate in a vortex mode is to distort the confining potential and mechanically rotate the trap during the cooling process. In this way, the lowest energy mode may be engineered to be circulating about the axis of symmetry. Such an approach is in direct analogy with experiments on vortices in super-fluid helium—the asymmetry of the harmonic trap for the atomic gas plays the role of surface roughness of a rotating vessel. Although conceptually this method appears promising for vortex generation in a trapped gas, so far technical difficulties have precluded its successful implementation. In section 3.4 we outline some of the basic properties of vortices and we also consider other non-ground-state condensates, such as a dipole-mode; we refer to these macroscopic excited states as *topological modes*[1] in order to distinguish them from the concept of an *elementary excitation*

[1]This is somewhat of a misnomer, for we apply "topological" not only to vortex solutions, but also to noncir-

or *linearized collective mode*, which we discuss briefly in section 3.5. In an elementary excitation, a small fraction of atoms are excited out of the condensate on average; the linear response of the condensate to a weak mechanical drive can be expressed in terms of elementary excitations, for example. In contrast, in a topological mode a large fraction of the atoms occupy the same excited state.

One of the most interesting new developments in this field is the creation of multi-component condensates, where different atomic species are Bose-condensed in the same system. The earliest work in this area occurred at JILA in 1996, where two different hyperfine internal states were populated in the condensate [7]. Later work at MIT studied atoms trapped in an optical potential, where three different Zeeman sub-levels were populated in the condensate [28]. These initial experiments on multi-component condensates, along with many more that followed, have spawned a wealth of theoretical studies on these spinor condensates. Early work on these systems was concerned with the ground state properties and elementary excitations of multiple components trapped together [29, 30, 31, 32].

A natural extension of the work on mixtures of different internal states in a condensate is to consider the application of an external electromagnetic field that couples different internal states of the atoms in the condensate. Most of the recent BEC experiments deal with this basic system in some form or another. A useful tool for coupling atoms out of the condensate, which is a basic ingredient of an atom laser, is to apply an external field to the condensate that drives transitions to an untrapped internal level [17, 18, 19]. Alternatively, one can apply an external field to couple internal states that are both trapped. A series of experiments at JILA have explored this situation [8, 9, 10, 11].

In Chapters 4 to 6 we investigate a driven two-component condensate, where two internal hyperfine states are trapped, though each state experiences a slightly different confining potential. In Chapter 4, we derive the coupled two-component Gross-Pitaevskii equation Eq. (4.11), which is a key result for the studies presented in Chapters 4 to 6. Our main focus in Chapter 4 is on the stationary solutions of the two-component system, both with and without coupling. For the case of no coupling, we calculate ground states, and topological modes, the results of which are needed in Chapter 5 and Chapter 6. We also consider the lowest-energy stationary solution of the coupled system, which we call the dressed states.

In Chapter 5 we consider the case of weak coupling between internal states that are in displaced traps, so that the two components are separated along the vertical axis with a finite overlap. This system resembles a different system considered recently in the BEC literature: two condensates in a double well that can tunnel through the central barrier so that the two condensates are weakly coupled, as in the standard Josephson junction in condensed matter physics. Due to the mean-field interaction, the corresponding Josephson-junction equations are nonlinear. We show results of numerical calculations, and give a closed-form approximate solution as well. In Chapter 6 we treat the opposite limit of strong coupling between internal states and show that the condensate can be prepared in a variety of new topological states. In particular, we predict a scheme for generating a quantized vortex in this two-component system, where one component sits in the center with a uniform phase while the other circulates around it. Subsequent related experimental work at JILA by the group of Eric Cornell and Carl Wieman has demonstrated these predictions in the laboratory—this is the first observation of a vortex in a dilute-gas Bose-Einstein condensate [14].

In Chapter 7 we shift our attention to the high temperature limit and study the quantum

culating modes, such as a dipole or quadrupole.

Boltzmann equation, which was derived in section 2.4.2. We first derive the quantum version of the ergodic Boltzmann equation by assuming detailed balance in each degenerate subspace. This results in a distribution function that depends only on energy. We then present a simulation procedure for numerically solving the quantum Boltzmann equation, which is based on the quantum trajectory methods first developed in quantum optics to simulate master equations. We then present explicit calculations of finite number effects on equilibrium, the dynamic build-up of the ground state, and simulations of evaporative cooling.

In Chapter 8 we investigate the possibility of obtaining Bose-Einstein condensation in a steady state by continuously loading atoms into a magnetic trap while keeping the frequency of the RF field fixed. A steady state is obtained when the gain of atoms due to loading is balanced with the three dominant loss mechanisms due to: elastic collisions with hot atoms from the background gas, inelastic 3-body collisions, and evaporation. We describe our model of this system and present results of calculations of the peak phase-space density ρ_0 in order to investigate the conditions under which one can reach the regime $\rho_0 \geq 2.612$ and attain BEC in steady state.

Chapter 2

Underlying Theory

2.1 Introduction

In this thesis we are interested in the particular system of a dilute, finite Bose-Einstein condensed gas of trapped atoms. The theoretical study of this interesting system is motivated by the recent experimental progress in Bose-Einstein condensation [33, 34]. Conceptually, this system resides somewhere between the laser, which can be thought of as a steady-state Bose-condensation of photons into a single cavity mode, and superfluid helium, which is a Bose-condensed liquid. In these two limiting cases, the constituent particles are either uncorrelated in the case of the laser since practically there is no interaction between photons, or highly correlated in the case of superfluid helium due to the strong interactions between particles in such a dense system. The underlying theories of these two limiting cases are well established, yet the approaches taken toward and the questions asked about each system are very different. It is not surprising, then, that a standard theoretical framework for the dilute Bose-Einstein condensed gas, which is somewhat of a conceptual hybrid of these two cases, has not yet been established and is currently a very active area of research in this field [20, 21, 22, 23, 24, 25, 26, 27]. Such a theory must embrace the notions of quantum coherence and irreversible dynamics as envisioned in quantum optics, and the idea of the collective behavior of a system of interacting particles familiar to the condensed matter physicist.

In this chapter we develop a theory for the dilute Bose-condensed gas that describes a coherent mean-field and the fluctuations about it. The main result of our theory is a closed set of coupled equations describing the condensate and the normal and anomalous fluctuations at finite temperature; these equations go beyond the standard Hartree-Fock-Bogoliubov theories [35, 36] by including second-order collisional terms describing incoherent processes that lead to damping in the system. In the collisionless limit, our equations go over to the Hartree-Fock-Bogoliubov equations, while in the large temperature limit, we recover the quantum Boltzmann equation for the populations of a thermal cloud. We formulate our kinetic equations for the condensate and fluctuations in a basis-independent, operator form that allows us to extend the usual treatment of a single component system to the case where the atoms have internal structure, so that multi-component systems with internal coupling can be investigated.

We begin the chapter with an overview of our approach by discussing the main idea of the attenuation of correlations that leads to a reduced description of the system in terms

of a relevant set of observables. This approach is essentially the quantum version of the classical Chapman-Enskog procedure [37, 38, 39, 40] that has been extended to treat a Bose-condensed system (see also Kadanoff and Baym [41]). We then derive the kinetic equations for the mean field and fluctuations in the next section, making a serious effort to clarify the crucial physical assumptions made along the way. After presenting the kinetic equations in section 2.3.7, we then consider the collisionless and high temperature limits of our theory.

2.2 Conceptual ingredients

In general, an isolated macroscopic system of interacting particles will evolve irreversibly to a steady state or equilibrium situation so as to maximize entropy. This is a profound and universal fact of nature that has intrigued scientists and philosophers throughout the twentieth century due to the following paradox: one is faced with the task of deriving irreversible equations of motion for macroscopic observables starting from the reversible microscopic description. One must inevitably address this question in order to construct a theory of Bose-Einstein condensation. We take a rather pragmatic approach to solving this problem by postulating a reduced description of the system, which is essentially a coarse-graining of the quantum Liouville equation [38, 39].

2.2.1 Separation of timescales

In a dilute gas, the interaction radius a given by the scattering length of a two-particle collision is assumed to be much smaller than the mean distance between particles,

$$na^3 \ll 1, \tag{2.1}$$

where n is the average density. Based on this inequality, we can identify four distinct timescales that allow for a simplified description. The shortest timescale is the duration of a collision, $\tau_0 = a/v$, where v is the average velocity. The time between collisions $\tau_c = 1/(na^2v)$ is much longer than τ_0 in a dilute gas, and gives us the second timescale. In general, there will be a third timescale τ_h during which the system relaxes to a state of local equilibrium, which requires multiple collisions per atom. And finally, there is the time $\tau_{\rm eq}$ it takes the system to relax to global equilibrium. We summarize these timescales as

$$\tau_0 \ll \tau_c \ll \tau_h \ll \tau_{\rm eq}. \tag{2.2}$$

In other words, the system passes through three stages of evolution during its approach to equilibrium.

Let us imagine that we have complete knowledge of the initial state of the system, given by the N-particle density operator $\rho(0)$. Suppose we allow the dilute gas of interacting particles to evolve for some time interval Δt. During the first very short stage of evolution $\Delta t \leq \tau_0$, correlations between particles due to collisions have not had time to die out, so if we want to track the evolution of the system on such a fine timescale, we have to include all of the correlations between particles. This means that we must solve for the full N-body density matrix $\rho(t)$, which is certainly an intractable problem.

The situation becomes much easier if we are not interested in tracking the system on the very fine time-scale of the duration of a collision τ_0. Instead, suppose we consider a

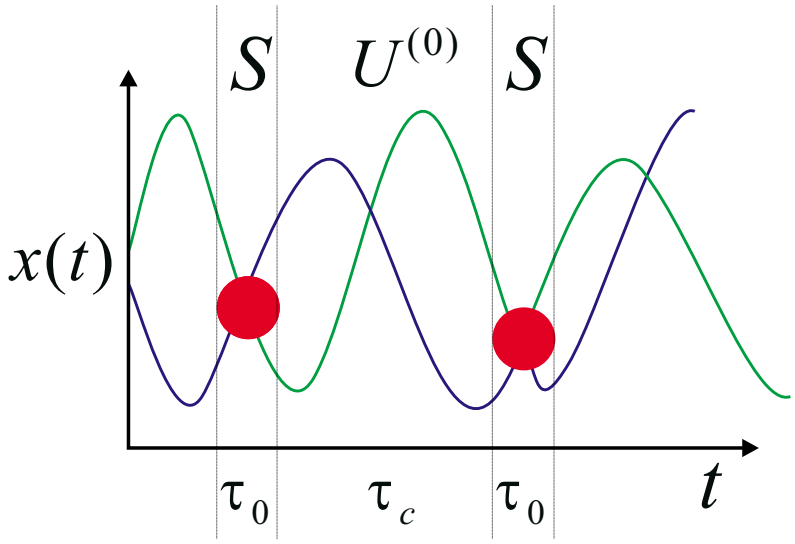

Figure 2.1: One dimensional illustration of the kinetic stage of evolution for a trapped gas. A particle oscillates freely in the harmonic trap between the collision events shown in red.

larger time interval $\tau_0 \ll \Delta t \ll \tau_h$. During this time, any pairs of atoms that were initially undergoing a collision have separated along their asymptotic trajectories, which consist of free oscillations within the external potential, before experiencing a second collision, as illustrated schematically in Figure 2.1. In other words, the initial correlations between atoms have died out and correlations between new pairs of atoms have formed. This timescale of $\Delta t \approx \tau_c$ is called the *kinetic stage* of evolution, and the rapid decay of correlations is often referred to as molecular chaos or the attenuation of correlations.

The third stage of evolution occurs for the time interval $\tau_c \ll \Delta t \ll \tau_{\rm eq}$ and is called the *hydrodynamic stage* of evolution, when the system has reached local equilibrium. For an extremely dilute gas we have $\tau_h \approx \tau_{\rm eq}$, so that the hydrodynamic stage loses its meaning. In the opposite limit of a very dense system, for which the time between collisions is nearly the same as the duration of a collision $\tau_c \approx \tau_0$, the kinetic stage loses its meaning. This is often called the hydrodynamic regime and is typically applied to the study of superfluid helium, for example. We will not consider this case in any detail.

2.2.2 Reduced description

An important consequence of the attenuation of correlations is that higher-order correlations between atoms can be expressed in terms of lower-order correlations, which are described by a physically relevant set of master variables $\{\gamma_q(t)\} \equiv \{\gamma_1(t), \gamma_2(t), \cdots\}$ that are given by the trace over the N-body density operator

$$\gamma_q(t) = \mathrm{Tr}\{\rho(t)\,\hat{\gamma}_q\}. \tag{2.3}$$

Here $\hat{\gamma}_q$ is the corresponding relevant operator. The particular choice of variables depends on the specific properties of the system, such as how dilute it is and whether it is in the quantum degenerate regime. An example of a relevant observable is the single-atom density

matrix $f_{\vec{m}\vec{n}}(t) = \mathrm{Tr}\{\rho(t)\hat{a}^\dagger_{\vec{n}}\hat{a}_{\vec{m}}\}$, where $\hat{a}^\dagger_{\vec{m}}$ and $\hat{a}_{\vec{m}}$ are creation and annihilation operators for the single-particle state labeled by the index $\vec{m}$. In a classical system, the analogous quantity is the single-atom phase-space density $f(\mathbf{x}, \mathbf{p})$.

This reduced description is equivalent to coarse-graining the quantum Liouville equation over a time interval $\tau_0 \ll \Delta t \ll \tau_c$. As we will show in more detail below, this leads to a coarse-grained form $\sigma_{\{\gamma_q(t)\}}$ of the N-body density operator that does not contain explicit time dependence but is a functional of the master variables $\{\gamma_q(t)\}$ i.e.

$$\rho(t) \approx \sigma_{\{\gamma_q(t)\}}. \tag{2.4}$$

Due to the attenuation of correlations, the information required to specify the state of the system has been greatly reduced to the small set of variables $\{\gamma_q(t)\}$.

We can further simplify the problem by observing that the particular form of $\sigma_{\{\gamma_q(t)\}}$ is irrelevant, so long as the trace given by Eq. (2.3) gives the correct values of the observables $\{\gamma_q(t)\}$. In fact, there is an infinite set of N-body density matrices that will satisfy Eq. (2.3) for a particular choice of operators $\hat{\gamma}_q$; we can think of this set as forming an ensemble. Using arguments familiar from the study of equilibrium statistical mechanics, we can construct a representative form of $\sigma_{\{\gamma_q(t)\}}$ that is the most probable in the ensemble if we maximize the *information entropy* $S(t)$, with the constraints given by Eq. (2.3). That is, we seek an extremum of the functional

$$S[\sigma'(t)] = -\mathrm{Tr}\big\{\sigma'(t)\ln[\sigma'(t)]\big\} - \sum_q \Upsilon^q\,\mathrm{Tr}\{\sigma'(t)\hat{\gamma}_q\}, \tag{2.5}$$

where Υ^q are Lagrange multipliers, which are the conjugate thermodynamic coordinates of the operators $\hat{\gamma}_q$. Varying $S[\sigma'(t)]$ with respect to σ' and then setting the first variation to zero, $\delta S = 0$, we obtain the following *reference distribution*

$$\sigma^{(0)}_{\{\gamma\}} \quad = \quad \exp\left(\hat{\gamma}_q\,\Upsilon^q\right). \tag{2.6}$$

Here we have assumed the summation over repeated indices and we have simplified the notation for the index by writing $\{\gamma_q(t)\} = \{\gamma\}$. The exponential form given in Eq. (2.6) will allow us to simplify averages of products of operators using Wick's theorem [42, 43].

It is important to realize the difference between the three density operators ρ, $\sigma_{\{\gamma\}}$, and $\sigma^{(0)}_{\{\gamma\}}$ we have introduced. The exact state of the N-body system is given by ρ. However, due to the attenuation of correlations, it is not necessary to track the evolution of the system with infinitesimally precise time resolution, so that we can obtain a coarse grained solution $\sigma_{\{\gamma\}}$ that is governed by the set of relevant observables $\{\gamma_q(t)\}$. We do not need to know the detailed form of $\sigma_{\{\gamma\}}$; all that is required is for it to be a functional of the observables and satisfy the self-consistency conditions

$$\gamma_q(t) = \mathrm{Tr}\{\rho(t)\,\hat{\gamma}_q\} = \mathrm{Tr}\{\sigma_{\{\gamma\}}\,\hat{\gamma}_q\}. \tag{2.7}$$

Although it is not necessary to take a particular form for $\sigma_{\{\gamma\}}$, we have constructed a reference distribution $\sigma^{(0)}_{\{\gamma\}}$ for convenience that we obtained by maximizing the information entropy. The reference distribution must also satisfy the following self-consistency conditions

$$\gamma_q(t) = \mathrm{Tr}\{\sigma_{\{\gamma\}}\,\hat{\gamma}_q\} = \mathrm{Tr}\{\sigma^{(0)}_{\{\gamma\}}\,\hat{\gamma}_q\}. \tag{2.8}$$

2.2.3 Master variables $\{\gamma_q(t)\}$

We are interested in describing a dilute Bose-condensed gas over the range of temperatures $T = 0$ to $T \geq T_c$, so it is useful to consider the theory for these two limiting cases; our choice of relevant variables must be consistent with standard results in these two limits. At high temperature, we should recover the standard kinetic theory as given by the Boltzmann transport equation describing the irreversible evolution of the single-atom distribution of populations $f_{\vec{m}\vec{m}}(t)$. In equilibrium the populations are distributed according to the Maxwell-Boltzmann distribution. As we lower the temperature close to T_c, our theory should contain the Bose-enhancement factors $[1 + f_{\vec{m}\vec{m}}(t)]$ for the output channels of a collision, which give rise to the Bose-Einstein distribution of populations in equilibrium. Furthermore, as the system cools even further, quantum coherences may play a role, so that in general we must consider off-diagonal elements $f_{\vec{m}\vec{n}}(t)$ of the single-atom density matrix. It is clear, then, that our set of master variables must contain the single-atom density matrix $f_{\vec{m}\vec{n}}(t)$.

In the opposite limit of zero temperature $T = 0$, the most basic description of the system is given by the time-dependent Gross-Pitaevskii (GP) equation for the single-atom wave function $\psi(\mathbf{r}, t)$. In this mean-field description, interactions are treated to first order and give rise to the nonlinear term in the GP equation. The corresponding equilibrium state of the system is one in which all of the atoms occupy the same lowest-energy single-particle state $\phi_0(\mathbf{r})$. This state of equilibrium is drastically different than the Maxwell-Boltzmann distribution at $T > T_c$, which allows only fractional populations ($f_{\vec{m}\vec{m}} << 1$). The most striking feature of the system at $T = 0$ is the spatial coherence, or off-diagonal long range order, represented by the fact that the single atom density matrix $f^{(c)}(\mathbf{r}, \mathbf{r}') = \phi_0(\mathbf{r})\phi_0^*(\mathbf{r}')$ is non-zero for large values of $|\mathbf{r} - \mathbf{r}'|$ ranging over the entire extent of the condensate. Represented in an arbitrary single particle basis, the single-atom density matrix of the condensate is written $f^{(c)}_{\vec{m}\vec{n}}(t) = \psi^*_{\vec{n}}(t)\psi_{\vec{m}}(t)$, where $\psi_{\vec{m}}(t)$ is the mean-value given by $\psi_{\vec{m}}(t) = \mathrm{Tr}\{\rho(t)\,\hat{a}_{\vec{m}}\}$[1]. In order to correctly describe the system in the $T = 0$ limit, our set of master variables must also include the mean-field $\psi_{\vec{m}}(t)$.

Based on theories that include higher-order corrections to the GP equation, anomalous averages may be important and also must be included in our set of master variables. The anomalous averages, also referred to as pair correlations, are given by $m_{\vec{m}\vec{n}}(t) = \mathrm{Tr}\{\rho(t)\,\hat{a}_{\vec{m}}\hat{a}_{\vec{n}}\}$ and $n_{\vec{m}\vec{n}}(t) = \mathrm{Tr}\{\rho(t)\,\hat{a}^\dagger_{\vec{m}}\hat{a}^\dagger_{\vec{n}}\}$. These quantities have a direct analogy to the squeezing terms found in the description of squeezed states of light encountered in quantum optics, which occur when appropriate coherent interactions are applied in a nonlinear medium.

Based on the above considerations, we now specify the set of relevant operators to use in our theory:

- $\hat{a}_{\vec{m}}\ ,\ \hat{a}^\dagger_{\vec{m}}$,
- $\hat{\tilde{f}}_{\vec{m}\vec{n}} = (\hat{a}^\dagger_{\vec{n}} - \psi^*_{\vec{n}})(\hat{a}_{\vec{m}} - \psi_{\vec{m}})$,
- $\hat{\tilde{m}}_{\vec{m}\vec{n}} = (\hat{a}_{\vec{m}} - \psi_{\vec{m}})(\hat{a}_{\vec{n}} - \psi_{\vec{n}})$,
- $\hat{\tilde{n}}_{\vec{m}\vec{n}} = (\hat{a}^\dagger_{\vec{m}} - \psi^*_{\vec{m}})(\hat{a}^\dagger_{\vec{n}} - \psi^*_{\vec{n}})$.

[1] The index $\vec{m}$ refers to a single particle state $|\vec{m}\rangle$. If $|\vec{m}\rangle$ is chosen to be the position vector $|\boldsymbol{r}\rangle$, then we use the notational convention $\psi(\boldsymbol{r}, t) \equiv \psi_{\boldsymbol{r}}(t)$, and correspondingly, $\hat{\Psi}(\boldsymbol{r}) \equiv \hat{a}_{\boldsymbol{r}}$.

The corresponding expectation values of these operators give us the set of master variables $\{\psi_{\vec{m}},\, \psi^*_{\vec{m}}, \tilde{f}_{\vec{m}\vec{n}},\, \widetilde{m}_{\vec{m}\vec{n}},\, \widetilde{n}_{\vec{m}\vec{n}}\}$. The indices $\vec{m}$ and $\vec{n}$ refer to a generic basis of single-particle states, the particular choice of which we discuss below. Not shown but also included in our set is the identity operator $\mathbf{1}$. Here we have defined the normal fluctuations $\tilde{f}_{\vec{m}\vec{n}}$ and the anomalous fluctuations $\widetilde{m}_{\vec{m}\vec{n}}$ and $\widetilde{n}_{\vec{m}\vec{n}}$ by subtracting off the mean values $\psi_{\vec{m}}$ in the averages.

With this set of independent variables, i.e., the mean field and the fluctuations around it, we can parameterize the reference distribution as

$$\sigma^{(0)}_{\{\psi,\psi^*,\tilde{f},\widetilde{m},\widetilde{n}\}} = \exp\left(\hat{1}\,\Omega - \hat{\tilde{f}}_{12}\,\Upsilon^{12} - \hat{\widetilde{m}}_{12}\,\Lambda^{12} - \hat{\widetilde{n}}_{12}\,\Lambda^{12\,*}\right). \tag{2.9}$$

Here, we use the implicit summation convention for repeated indices. The conjugate thermo-dynamic coordinates $\{\Omega, \Upsilon, \Lambda\}$ are implicitly defined by the quantum averages

$$\langle\hat{o}\rangle \quad = \quad \mathrm{Tr}\left\{\hat{o}\,\sigma^{(0)}_{\{\psi,\psi^*,\tilde{f},\widetilde{m},\widetilde{n}\}}\right\}, \tag{2.10}$$

where $\hat{o}$ represents a relevant operator. The average of any other multiple operator product, occurring during the evaluation of the kinetic equations, is greatly simplified by the Gaussian structure of the reference distribution for it allows us to utilize Wick's theorem.

It is worth remarking that the set of relevant observables consists of single operators and pairs of operators, which gives the reference distribution its Gaussian form. This implies that the reference distribution given in Eq. (2.9) will not violate positive definiteness, that is, it will not generate negative probabilities. This subtle, and perhaps pedantic, point is based on the Marcinkiewicz theorem, or M-theorem, which states that the characteristic function of a probability distribution function can not be an exponential of a polynomial of degree larger than two, or it will violate its positive definitness [44]. In other words, if we were to extend our relevant set of operators to include higher-order correlation functions that involve, for example, a product of three or four operators, then the exponential form of the reference distribution would not be satisfactory since it may be associated with negative probabilities for the occupation of single particle states.

2.2.4 Single-particle basis

In the section that follows, we derive the quantum kinetic equations for the mean-field and fluctuations independent of a particular single-particle basis. However, when we want to carry out calculations, we must choose a specific basis in which to represent the equations. Such a basis can include quantum numbers for both internal states of the atoms, such as the hyperfine level[2] $|F, M_F\rangle$, as well as the external spatial quantum numbers determined by the form of the confining potential. When we work in the $T = 0$ limit and ignore fluctuations, for which our kinetic equations reduce to the GP equation describing the condensate wavefunction, we will represent the external part of the system in the position representation.

However, when one considers finite temperature and includes the fluctuations about the mean field, a particular eigenbasis should be chosen wherever possible that minimizes computational effort and clarifies the basic dynamical structure of the solution. Typically for a

[2]The quantum number F represents the total angular momentum of the atom, given according to $\vec{F} = \vec{L} + \vec{S} + \vec{I}$, which is a sum over the orbital angular momentum $\vec{L}$, electronic spin $\vec{S}$, and nuclear spin $\vec{I}$. M_F is the projection of $\vec{F}$ onto a chosen axis.

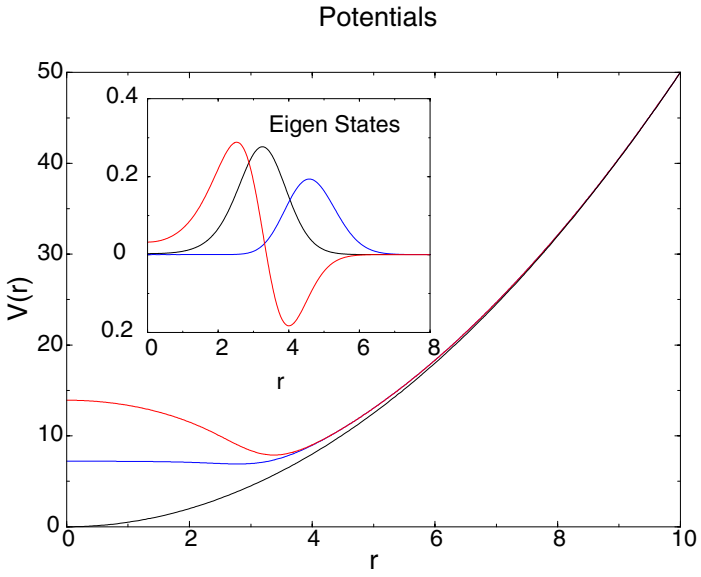

Figure 2.2: Potentials for the isotropic harmonic oscillator. The black curve is the bare harmonic trapping potential, the blue one is the potential seen by the condensate, and the red one is the potential seen by the non-condensate, or fluctuations. Example eigenstates of the non-condensate potential are shown in the inset.

homogeneous system, the most useful representation is the basis of plane wave solutions. This is not the best basis for the system we consider, which is confined in a harmonic potential. The eigenstates of the bare harmonic oscillator are also not very useful, since they do not account for the effect of the mean-field interaction potential. A better choice is the basis of eigenmodes of the potential seen by the fluctuations, as shown in Figure 2.2. The mean-field interaction potential experienced by the fluctuations (red curve) is twice as large as that felt by the condensate (blue curve) due to the bosonic enhancement of fluctuations. Consequently, the eigenmodes of the red potential are not centered at the origin, but sit at the edge of the condensate, as demonstrated by the eigenstates shown in the inset. Another possibility is to expand the equations in the Hartree-Fock-Bogoliubov normal modes that we discuss in section 2.4.

2.3 Derivation of the quantum kinetic equations

We now turn to the task of formulating the quantum kinetic theory for a dilute, Bose condensed gas using the basic ideas presented in the previous section. The approach we use is well established for quantum gases above the critical temperature $T > T_c$ and the details of the formalism can be found in the two well written accounts given by Zubarev et al. [39, 45] and Akhiezer et al. [38], for example. Rather than reproduce all of the mathematical details, which have appeared in a recent publication by our group (see Walser et al. [27]), we instead focus on the most important steps in the derivation in order to understand how the concepts discussed in the previous section are incorporated into the theory. In this way, the

new aspects of the theory that arise from extending it to a Bose-condensed gas will become apparent.

2.3.1 Second quantized description

We are interested in describing the evolution in time of a system of N interacting bosonic atoms confined in a harmonic potential. This system is described within the framework of elementary quantum mechanics by a many-particle wavefunction $\Psi(\boldsymbol{r}_1, \boldsymbol{r}_2, \cdots \boldsymbol{r}_N; t)$ that evolves in time according to the Schrödinger equation

$$i\hbar \frac{d}{dt}\Psi(\boldsymbol{r}_1, \boldsymbol{r}_2, \cdots \boldsymbol{r}_N; t) = H\Psi(\boldsymbol{r}_1, \boldsymbol{r}_2, \cdots \boldsymbol{r}_N; t), \tag{2.11}$$

where the many-body Hamiltonian H for the system is

$$H = \sum_{i=1}^{N} \big[-\frac{\hbar^2}{2m}\nabla_i^2 + U(\boldsymbol{r}_i)\big] + \frac{1}{2}\sum_{i\neq j} V(|\boldsymbol{r}_i - \boldsymbol{r}_j|), \tag{2.12}$$

and m is the mass of the atom. The atoms are confined by the external potential $U(\boldsymbol{r})$, which is typically a harmonic potential for the systems considered throughout this thesis,

$$U(\boldsymbol{r}) = \frac{1}{2}m\big(\omega_x^2 x^2 + \omega_y^2 y^2 + \omega_z^2 z^2\big), \tag{2.13}$$

with trap oscillation frequencies ω_x, ω_y, and ω_z along each axis. We assume it is sufficient to describe interactions between atoms by a two-body potential $V(|\boldsymbol{r}_i - \boldsymbol{r}_j|)$, although in reality interactions between two particles are modified by the presence of a third particle due to their finite extent; such effects lead to three-body recombination, for example. However, in the limit of Eq. (2.1), these effects should be negligible. The basic form of $V(|\boldsymbol{r}_i - \boldsymbol{r}_j|)$ is a short-ranged van der Waals type of interatomic potential, the detailed structure of which depends on the particular type of atom being considered. Because we are only interested in the very low temperatures at which Bose-Einstein condensation occurs, the kinetic energy in a collision is very low, so that we need keep only the s-wave term in a partial-wave expansion. Furthermore, a generic form for the interatomic potential can be used that is independent of the details of the two-body potential, but depends only on the s-wave scattering length a. A pseudo-potential, given by

$$V(|\boldsymbol{r} - \boldsymbol{r}'|) = V_0\, \delta^3(\boldsymbol{r} - \boldsymbol{r}'), \tag{2.14}$$

can be used, which reproduces the correct s-wave scattering length for a collision [46]. The parameter V_0 is given as

$$V_0 = \frac{4\pi\hbar^2 a}{m}. \tag{2.15}$$

So far we have not included the possibility that the atoms have internal structure. Later on in the thesis, we will consider the case where the internal structure of the atoms can be treated as a two-level system. In particular, we will be interested in the situation where a harmonic electromagnetic field is applied to the system that coherently couples the two internal states. For such a system, consisting of both internal and external degrees of freedom, it is more convenient to work directly with the state vector of the system $|\Psi(t)\rangle$,

expanded in a single-particle product basis, for example,

$$|\Psi(t)\rangle = S\Big\{ \sum_{\vec{m}_1,\vec{m}_2,\cdots\vec{m}_N} C(\vec{m}_1,\vec{m}_2,\cdots\vec{m}_N;t)|\vec{m}_1\rangle|\vec{m}_2\rangle\cdots|\vec{m}_N\rangle\Big\}, \tag{2.16}$$

where $C(\vec{m}_1,\vec{m}_2,\cdots\vec{m}_N;t)$ is an expansion coefficient. The vector $\vec{m}_i$ represents the quantum numbers that uniquely specify the single-particle state of the ith atom, determined by some appropriately chosen complete set of commuting observables. For an atom confined in the harmonic potential $U(\boldsymbol{r})$ given by Eq. (2.13), an example of a possible set of quantum numbers is $|\vec{m}\rangle = |n_x, n_y, n_z, F, M_F\rangle$, where n_i are the quanta of excitation in the harmonic trap along each Cartesian coordinate, F designates a particular hyperfine manifold, and M_F is a Zeeman magnetic sublevel. It is useful to keep track of the external and internal degrees of freedom separately by writing $|\vec{m}\rangle = |i,\alpha\rangle$, where i denotes all of the quantum numbers that specify the external degree of freedom, and α signifies the internal state of the atom.

Due to the indistinguishability of identical particles, quantum spin statistics requires that the state vector $|\Psi(t)\rangle$ be symmetric under particle exchange for a system of bosons. We therefore explicitly symmetrize the state vector in Eq. (2.16), as indicated by the operation $S\{\ \}$. Carrying out this operation can be a tedious procedure, making the single-particle product basis rather cumbersome to use in the formulation of a many-particle theory. We will instead use the second quantization formalism, also known as the occupation number representation, because the quantum statistics are built in to the theory in a very compact way via the commutation relations between the creation and annihilation operators.

For a system of bosons, the operators $\hat{a}^\dagger_{i,\alpha}$ and $\hat{a}_{i,\alpha}$ create or destroy an atom in the single particle state $|i,\alpha\rangle$, and satisfy the commutation relations, given by

$$[\hat{a}_{i,\alpha}, \hat{a}^\dagger_{j,\beta}] = \delta_{ij}\delta_{\alpha\beta}, \qquad [\hat{a}_{i,\alpha}, \hat{a}_{j,\beta}] = [\hat{a}^\dagger_{i,\alpha}, \hat{a}^\dagger_{j,\beta}] = 0. \tag{2.17}$$

In this new basis, we denote a general state by

$$|n_1\, n_2\, \cdots\, n_\infty\rangle, \tag{2.18}$$

where n_1 is the number of atoms in the single-particle basis state $|1\rangle$. These states are orthonormal, eg

$$\langle n_1'\, n_2'\, \cdots\, n_\infty'|n_1\, n_2\, \cdots\, n_\infty\rangle = \delta_{n_1' n_1}\, \delta_{n_2' n_2} \cdots \delta_{n_\infty' n_\infty}. \tag{2.19}$$

The operators $\hat{a}_{i,\alpha}$ and $\hat{a}^\dagger_{i,\alpha}$ have the following creation and annihilation properties when acting on a state

$$\begin{aligned}
\hat{a}^\dagger_{i,\alpha}\hat{a}_{i,\alpha}\,|n_1\, n_2\, \cdots\, n_{i,\alpha}\cdots\, n_\infty\rangle &= n_{i,\alpha}\,|n_1\, n_2\, \cdots\, n_{i,\alpha}\cdots\, n_\infty\rangle, \\
\hat{a}_{i,\alpha}\,|n_1\, n_2\, \cdots\, n_{i,\alpha}\cdots\, n_\infty\rangle &= \sqrt{n_{i,\alpha}}\ |n_1\, n_2\, \cdots\, (n_{i,\alpha}-1)\cdots\, n_\infty\rangle, \\
\hat{a}^\dagger_{i,\alpha}\,|n_1\, n_2\, \cdots\, n_{i,\alpha}\cdots\, n_\infty\rangle &= \sqrt{n_{i,\alpha}+1}\ |n_1\, n_2\, \cdots\, (n_{i,\alpha}+1)\cdots\, n_\infty\rangle.
\end{aligned} \tag{2.20}$$

In this representation, the many-body Hamiltonian Eq. (2.12) describing our system takes the form

$$\hat{H} = \langle i,\alpha|\hat{H}_0|j,\beta\rangle\, \hat{a}^\dagger_{i,\alpha}\hat{a}_{j,\beta} + \frac{1}{2}\langle i,\alpha\,;\,j,\beta|\hat{V}|k,\alpha';\,l,\beta'\rangle\, \hat{a}^\dagger_{i,\alpha}\hat{a}^\dagger_{j,\beta}\hat{a}_{k,\alpha'}\hat{a}_{l,\beta'}, \tag{2.21}$$

where summation over repeated indices is implied. The first term describes the free evolution in the harmonic trap, and possibly an additional external field that couples the two internal states. The matrix element can be written as

$$\langle i,\alpha|\hat{H}_0(t)|j,\beta\rangle = \int d^3r\phi_i^*(\boldsymbol{r})\Big[\Big(-\frac{\hbar^2}{2m}\nabla^2 + U_\alpha(\boldsymbol{r}) + \delta_{ij}\epsilon_\alpha\Big)\delta_{\alpha\beta} + \delta_{ij}H^{\rm d}_{\alpha\beta}(t)\Big]\phi_j(\boldsymbol{r}), \tag{2.22}$$

where $\phi_i(\boldsymbol{r}) \equiv \langle \boldsymbol{r}|i\rangle$ form a basis. The quantity ϵ_α is the internal energy of the state $|\alpha\rangle$. Here we include the possibility that the external trapping potential for each state can be different U_α. We have also included a time-dependent drive that couples the internal states $H^{\rm d}_{\alpha\beta}(t)$.

The second term in Eq. (2.21) describes binary interactions between atoms with the matrix element given by

$$\langle i,\alpha\,;j,\beta|V|k,\alpha';l,\beta'\rangle = \int d^3r\, d^3r' \phi_i^*(\boldsymbol{r})\phi_j^*(\boldsymbol{r}')V_{\alpha,\beta;\alpha'\beta'}(|\boldsymbol{r}-\boldsymbol{r}'|)\phi_k(\boldsymbol{r}')\phi_l(\boldsymbol{r}). \tag{2.23}$$

This is of a general form that includes the possibility of internal-state changing collisions. However, we will restrict ourselves to elastic collisions that do not allow the internal state of an atom to change due to collisions. We generalize the pseudo-potential to allow for different scattering lengths depending on the internal states of the colliding partners, so that Eq. (2.23) can be written

$$\langle i,\alpha\,;j,\beta|V|k,\alpha';l,\beta'\rangle = V_{\alpha\beta}\,\delta_{\alpha\alpha'}\delta_{\beta\beta'}\int d^3r\phi_i^*(\boldsymbol{r})\phi_j^*(\boldsymbol{r})\phi_k(\boldsymbol{r})\phi_l(\boldsymbol{r}), \tag{2.24}$$

where $V_{\alpha\beta} = 4\pi\hbar^2 a_{\alpha\beta}/m$ and the scattering length $a_{\alpha\beta}$ depends on the internal states of the atoms. For example, for a two-level atom with internal states $|1\rangle$ and $|2\rangle$, there are three different collision processes: $|1\rangle|1\rangle \to |1\rangle|1\rangle$ described by a_{11}, $|2\rangle|2\rangle \to |2\rangle|2\rangle$ described by a_{22}, and $|1\rangle|2\rangle \to |1\rangle|2\rangle$ described by a_{12}. The external part of the matrix element Eq. (2.24) is simply the overlap of the wavefunctions for the "in" and "out" channels.

The state vector describing this many-particle system then evolves in time according to

$$i\hbar\frac{d}{dt}|\Psi(t)\rangle = \hat{H}|\Psi(t)\rangle, \tag{2.25}$$

with $\hat{H}$ given by Eq.(2.21). In the occupation number representation for a given single-particle basis, the general form of $|\Psi(t)\rangle$ is

$$|\Psi(t)\rangle = \sum_{n_1 n_2\cdots n_\infty} c(n_1,n_2,\cdots,n_\infty;t)\,|n_1\,n_2\,\cdots\,n_\infty\rangle, \tag{2.26}$$

where $c(n_1,n_2,\cdots,n_\infty;t)$ is an expansion coefficient. This is just Eq. (2.16) rewritten in the occupation number representation. Since we are considering a fixed number of atoms, the occupation numbers must add up to the total number of atoms $\sum_i n_i = N$.

2.3.2 Statistical description

Ultimately we are interested in observable quantities, that might be measurable in the laboratory. Such observables $\mathcal{O}(t)$ are found by taking the average of the corresponding operator $\hat{\mathcal{O}}$ for the system in state $|\Psi(t)\rangle$

$$\mathcal{O}(t) = \langle\Psi(t)|\hat{\mathcal{O}}|\Psi(t)\rangle. \tag{2.27}$$

Expanding $|\Psi(t)\rangle$ as in Eq. (2.26), we get

$$\mathcal{O}(t) = \sum_{\{n\}\{n'\}} c^*\big(\{n\};t\big)c\big(\{n'\};t\big)\langle n_1\, n_2\, \cdots\, n_\infty|\hat{\mathcal{O}}|n'_1\, n'_2\, \cdots\, n'_\infty\rangle, \tag{2.28}$$

where $\{n\}$ stands for the set of occupation numbers $\{n_1, n_2, \cdots, n_\infty\}$. For a system with a large number of interacting particles, we can never measure the precise quantum state $|\Psi(t)\rangle$. In a general situation, we can only give a statistical description of the state of the system, in terms of classical probabilities $w(\{n\};t)$

$$\mathcal{O}(t) = \sum_{\{n\}} w\big(\{n\};t\big)\langle n_1\, n_2\, \cdots\, n_\infty|\hat{\mathcal{O}}|n_1\, n_2\, \cdots\, n_\infty\rangle. \tag{2.29}$$

The most general description of the state of the system is given by the density operator $\hat{\rho}(t)$, which can describe both mixed and pure quantum states. The observable $\mathcal{O}(t)$ is found by taking the trace of $\hat{\rho}(t)$ times the operator $\hat{\mathcal{O}}$

$$\mathcal{O}(t) = \mathrm{Tr}\big\{\hat{\rho}(t)\hat{\mathcal{O}}\big\} \tag{2.30}$$

If the system is in the pure state $|\Psi(t)\rangle$, the density operator simply takes the form $\hat{\rho}(t) = |\Psi(t)\rangle\langle\Psi(t)|$. The dynamical evolution of the density operator is given according to

$$\frac{\partial\hat{\rho}(t)}{\partial t} = \frac{1}{i\hbar}[\hat{H},\, \hat{\rho}(t)], \tag{2.31}$$

which is true for both mixed and pure states. This is usually referred to as the quantum Liouville equation, since it resembles the Liouville equation found in classical mechanics describing the classical phase space density.

2.3.3 Coarse-grained density operator

The quantum Liouville equation can be solved formally as

$$\hat{\rho}(t) = e^{-i(t-t_0)\hat{\mathcal{L}}}\,\hat{\rho}(t_0), \tag{2.32}$$

where $\hat{\mathcal{L}}$ is a super-operator, which is defined as $\hat{\mathcal{L}}\hat{\mathcal{O}} = [\widehat{H}, \hat{\mathcal{O}}]/\hbar$. Starting from some initial state $\hat{\rho}(t_0)$ for the many-particle system, the system evolves reversibly in time according to Eq. (2.32). However, due to the attenuation of correlations discussed in section 2.2.2, the system "forgets" the precise details of the initial state after some time $\Delta t > \tau_0$, and the behavior of the system depends only on some reduced set of relevant observables $\{\gamma_q(t)\}$. We can therefore describe the system by the reference distribution[3] $\hat{\sigma}^{(0)}(t_0)$ at the initial time t_0

$$\hat{\rho}(t) = e^{-i(t-t_0)\hat{\mathcal{L}}}\hat{\sigma}^{(0)}(t_0), \tag{2.33}$$

keeping in mind that we have chosen the particular form $\hat{\sigma}^{(0)}$ given in Eq. (2.6) so that it satisfies the self-consistency conditions

$$\gamma_q(t) = \mathrm{Tr}\{\rho(t)\,\hat{\gamma}_q\} = \mathrm{Tr}\{\hat{\sigma}^{(0)}\,\hat{\gamma}_q\}. \tag{2.34}$$

[3] We now drop the subscript on $\sigma_{\{\gamma\}}$ and $\sigma^{(0)}_{\{\gamma\}}$, which was used to emphasize that these operators are functionals of the master variables $\{\gamma_q(t)\}$.

Within the assumption of the attenuation of correlations, the macroscopic observables $\{\gamma_q(t)\}$ evolve on a much slower time-scale than the rapid decay and build-up of particle correlations described by $\hat{\rho}(t)$. Therefore, we can coarse-grain over a time $t-t_0$ that is long compared to the duration of a collision, but short enough that we do not also coarse-grain over the evolution of the macroscopic quantities $\{\gamma_q(t)\}$,

$$\hat{\sigma}(t) = \frac{1}{t-t_0}\int_{t_0}^{t} e^{-i(t-t')\hat{\mathcal{L}}}\hat{\sigma}^{(0)}(t')\,dt'. \tag{2.35}$$

Here we are making a distinction between the true solution $\hat{\rho}(t)$ and the coarse-grained solution $\hat{\sigma}(t)$. After some algebra, Eq. (2.35) can be brought to the equivalent form

$$\frac{\partial\hat{\sigma}(t)}{\partial t} - \frac{1}{i\hbar}[\widehat{H},\,\hat{\sigma}(t)] = -\frac{\hat{\sigma}(t)-\hat{\sigma}^{(0)}(t)}{t-t_0}, \tag{2.36}$$

which is the quantum Liouville equation with a source term that provides for the boundary condition given in Eq. (2.35). A crucial point is that by course-graining in time to wash out the rapid fluctuation of correlations in the system, we have introduced irreversibility into the evolution of the system.

If we take the limiting case where the initial time is in the distant past $t_0 \to -\infty$, Eq. (2.36) can be brought to the more useful form

$$\frac{\partial\hat{\sigma}(t)}{\partial t} - \frac{1}{i\hbar}[\widehat{H},\,\hat{\sigma}(t)] = -\varepsilon\{\hat{\sigma}(t)-\hat{\sigma}^{(0)}(t)\}, \tag{2.37}$$

where $\varepsilon \to 0$ in the limit of $t_0 \to -\infty$. Here we have made use of Abel's theorem, given by [39]

$$\lim_{T\to\infty}\frac{1}{T}\int_{-T}^{0} f(t)dt = \lim_{\varepsilon\to+0}\int_{-\infty}^{0} f(t)e^{\varepsilon t}dt. \tag{2.38}$$

Physically, the idea that the system "forgets" the details of the initial state after a long enough time is embodied in Eq. (2.37), for in the limit $\varepsilon \to 0$, the source term goes away and we simply recover the quantum Liouville equation. There are, however, some subtle issues regarding taking this limit, which we defer to a discussion later in the chapter.

The integral equation form of Eq. (2.37) can be obtained and is given by

$$\hat{\sigma}(t) = \hat{\sigma}^{(0)}(t) - \int_{-\infty}^{t} dt' e^{-\varepsilon(t-t')}\widehat{U}(t,t')\Big\{\frac{1}{i\hbar}[\hat{\sigma}^{(0)}(t'),\widehat{H}(t')] + \frac{\partial\hat{\sigma}^{(0)}(t')}{\partial t'}\Big\}\widehat{U}^{\dagger}(t,t'). \tag{2.39}$$

The propagator $\widehat{U}(t,t')$ gives the full evolution from t' to t and is given by

$$\widehat{U}(t,t') = \widehat{T}\exp\Big\{-\frac{i}{\hbar}\int_{t'}^{t}\widehat{H}(\tau)d\tau\Big\}, \tag{2.40}$$

where $\widehat{T}$ signifies the time-ordering of the exponential. Here we are allowing for a time dependent Hamiltonian $\widehat{H}(t)$, which might arise if we are driving the system with an external harmonic force, for example. It is clear from Eq. (2.39) that $\hat{\sigma}(t)$ is a functional of the set of master variables $\{\gamma_q(t)\}$ through its dependence on $\hat{\sigma}^{(0)}(t)$, though in general a very complicated one; for after a short time, $\hat{\sigma}(t)$ evolves away from the particular form of the initial state $\hat{\sigma}^{(0)}(t)$ we have chosen.

2.3.4 Mean-field shifted energies

The total Hamiltonian operator $\widehat{H}(t)$ that governs the evolution of a weakly-interacting, dilute gas permits a partitioning of the energy into a free part $\widehat{H}^{(0)}(t)$, that could include a driving field, and a presumably "weak" interaction $\widehat{H}^{(1)}$

$$\widehat{H} \quad = \quad \widehat{H}^{(0)}(t) + \widehat{H}^{(1)}. \tag{2.41}$$

One could use the bare, single-particle energy that determines the free kinetic evolution of the gas as a starting point of a series expansion of the coarse-grained density operator in terms of the interaction strength. However, it is well known that the mean-field interaction will significantly affect the single-particle energies. Anticipating this, we will shift the expansion point $\widehat{H}^{(0)}(t)$ by an as yet undetermined single-particle energy $\widehat{Q}^{(1)}_{\gamma}$ to a dressed energy prior to carrying out a perturbation expansion

$$\widehat{H}^{(0)}_{\gamma}(t) \quad = \quad \widehat{H}^{(0)}(t) + \widehat{Q}^{(1)}_{\gamma}. \tag{2.42}$$

To conserve energy, we have to reduce the interaction energy by an equal amount

$$\widehat{H}^{(1)}_{\gamma} \quad = \quad \widehat{H}^{(1)} - \widehat{Q}^{(1)}_{\gamma}. \tag{2.43}$$

This partitioning of the Hamiltonian is reminiscent of the Bogoliubov transformation that leads to a description of the system as consisting of fictitious, noninteracting quasi-particles, in the first order approximation, with higher order corrections accounting for the fluctuations due to the weak interactions between quasi-particles. The explicit form of the single-particle renormalization energy $\widehat{Q}^{(1)}_{\gamma}$ will be determined in the course of this calculation. The subscripts γ signify a dependence on the master variables $\{\gamma_q(t)\}$.

2.3.5 Interaction representation of the integral equation

Based on this partitioning of the Hamiltonian into a free part $\widehat{H}^{(0)}_{\gamma}(t)$ and a weak interaction $\widehat{H}^{(1)}_{\gamma}$, we reorganize the terms in Eq. (2.37) as

$$\Big(\frac{\partial}{\partial t} + \varepsilon\Big)\hat{\sigma}(t) - \frac{1}{i\hbar}[\widehat{H}^{(0)}_{\gamma},\, \hat{\sigma}(t)] = \varepsilon\hat{\sigma}^{(0)}(t) + \frac{1}{i\hbar}[\widehat{H}^{(1)}_{\gamma},\, \hat{\sigma}(t)] \tag{2.44}$$

It is straightforward to show that this can be rewritten as an equivalent integral equation of the form

$$\begin{aligned}\hat{\sigma}(t) = \hat{\sigma}^{(0)}(t) - \int_{-\infty}^{t} dt'\, e^{-\varepsilon(t-t')} \\ \times \widehat{U}^{(0)}_{\gamma}(t,t')\Big\{\frac{\partial\hat{\sigma}^{(0)}(t')}{\partial t'} + \frac{1}{i\hbar}[\hat{\sigma}^{(0)}(t'), \widehat{H}^{(0)}_{\gamma}(t')] + \frac{1}{i\hbar}[\hat{\sigma}(t'), \widehat{H}^{(1)}_{\gamma}]\Big\}\ \widehat{U}^{(0)^{\dagger}}_{\gamma}(t,t').\end{aligned} \tag{2.45}$$

There are two crucial differences compared to the equivalent integral equation in Eq. (2.39). The propagator $\widehat{U}^{(0)}_{\gamma}(t,t')$ appearing in Eq. (2.45) evolves the system according to the free Hamiltonian $\widehat{H}^{(0)}_{\gamma}(t)$, which is given by

$$\widehat{U}^{(0)}_{\gamma}(t,t') = \widehat{T}\exp\Big\{-\frac{i}{\hbar}\int_{t'}^{t}\widehat{H}^{(0)}_{\gamma}(\tau)d\tau\Big\}. \tag{2.46}$$

This is in contrast to Eq. (2.39), in which the full propagator is used. Also, the full coarse-grained solution $\hat{\sigma}(t)$ appears in the third term in the integral in Eq. (2.45); that is, $\hat{\sigma}(t')$ appears on both sides of Eq. (2.45), in contrast to Eq. (2.39), where only $\hat{\sigma}^{(0)}(t)$ appears on the right-hand side.

This integral equation can be further simplified by finding the explicit form of $\partial\hat{\sigma}^{(0)}(t)/\partial t$. Due to its exponential functional form, it can be shown that $\hat{\sigma}^{(0)}(t)$ satisfies a master equation of the form [39]

$$\frac{\partial\hat{\sigma}^{(0)}(t)}{\partial t} + \frac{1}{i\hbar}[\hat{\sigma}^{(0)}(t), \widehat{H}_{\gamma}^{(0)}(t)] = \frac{\partial\hat{\sigma}^{(0)}(t)}{\partial\gamma_q(t)} L_q(t), \tag{2.47}$$

where

$$L_q(t) = \frac{1}{i\hbar}\mathrm{Tr}\big\{[\hat{\gamma}_q, \widehat{H}_{\gamma}^{(1)}]\hat{\sigma}(t)\big\}. \tag{2.48}$$

In obtaining Eq. (2.47), use has been made of the Lie algebra of the relevant operators $\hat{\gamma}$ with the free Hamiltonian $\widehat{H}_{\gamma}^{(0)}$

$$[\widehat{H}_{\gamma}^{(0)}, \hat{\gamma}_q] = \mathcal{A}_q^p(\gamma)\hat{\gamma}_p. \tag{2.49}$$

The structure constants $\mathcal{A}_q^p(\gamma)$ are well-defined for our particular set of operators $\hat{\gamma}_q$. Inserting Eq. (2.47) into Eq. (2.45) gives us

$$\begin{aligned}\hat{\sigma}(t) \;=\; & \hat{\sigma}^{(0)}(t) \\ & -\int_{-\infty}^{t} dt' e^{-\varepsilon(t-t')}\widehat{U}_{\gamma}^{(0)}(t,t')\Big\{\frac{\partial\hat{\sigma}^{(0)}(t')}{\partial\gamma_q(t')}L_q(t') + \frac{1}{i\hbar}[\hat{\sigma}(t'), \widehat{H}_{\gamma}^{(1)}]\Big\}\,\widehat{U}_{\gamma}^{(0)^{\dagger}}(t,t').\end{aligned} \tag{2.50}$$

The commutator $[\hat{\sigma}(t'), \widehat{H}_{\gamma}^{(1)}]$ explicitly contains the interaction Hamiltonian $\widehat{H}_{\gamma}^{(1)}$, which is convenient for using a perturbation expansion in this weak interaction.

2.3.6 Generalized quantum kinetic equations

We now turn to the second stage of the derivation, of obtaining the generalized kinetic equations for the set of master variables $\{\gamma_q(t)\}$. An observable $\gamma_q(t)$ is found by taking the statistical average over the state of the entire system $\hat{\sigma}(t)$, given by

$$\gamma_q(t) = \mathrm{Tr}\big\{\hat{\sigma}(t)\,\hat{\gamma}_q\big\}. \tag{2.51}$$

In the Schrödinger picture, the time dependence is in the density operator, so that to find the time rate of change of the of the observable $\gamma_q(t)$ we have

$$\frac{\partial\gamma_q(t)}{\partial t} = \mathrm{Tr}\Big\{\frac{\partial\hat{\sigma}(t)}{\partial t}\,\hat{\gamma}_q\Big\}. \tag{2.52}$$

Substituting $\partial\hat{\sigma}(t)/\partial t$ given in Eq. (2.37) into this equation gives us

$$\frac{\partial\gamma_q(t)}{\partial t} + \frac{1}{i\hbar}\mathrm{Tr}\Big\{[\widehat{H}_{\gamma}^{(0)}, \hat{\gamma}_q]\hat{\sigma}(t)\Big\} = -\frac{1}{i\hbar}\mathrm{Tr}\Big\{[\widehat{H}_{\gamma}^{(1)}, \hat{\gamma}_q]\hat{\sigma}(t)\Big\} \tag{2.53}$$

The source term appearing in Eq. (2.37) drops out due to the self-consistency condition Eq. (2.8). The second term on the left-hand side of Eq. (2.53) can be reduced using the operator algebra properties Eq. (2.49) and the self-consistency condition Eq. (2.8). Finally, inserting Eq. (2.50) into Eq. (2.53) on the right-hand side, we obtain

$$\begin{aligned}\frac{\partial\gamma_q(t)}{\partial t} &+ \frac{1}{i\hbar}\mathrm{Tr}\Big\{[\widehat{H},\hat{\gamma}_i]\hat{\sigma}^{(0)}(t)\Big\} = \frac{1}{i\hbar}\int_{-\infty}^{t} dt' e^{-\varepsilon(t-t')} \\ &\times \mathrm{Tr}\Big\{[\widehat{H}_\gamma^{(1)}(t,t'),\hat{\gamma}_q(t,t')]\Big(\frac{\partial\hat{\sigma}^{(0)}(t')}{\partial\gamma_p(t')}\widehat{L}_p(t') + \frac{1}{i\hbar}[\hat{\sigma}(t'),\widehat{H}_\gamma^{(1)}]\Big)\Big\},\end{aligned} \tag{2.54}$$

where we have defined

$$\hat{\mathcal{O}}(t,t') = \widehat{U}_\gamma^{(0)^\dagger}(t,t')\,\hat{\mathcal{O}}\,\widehat{U}_\gamma^{(0)}(t,t'). \tag{2.55}$$

We note that the Hamiltonian $\widehat{H}$ appearing on the left-hand side is the total Hamiltonian independent of our partitioning.

The generalized kinetic equation Eq. (2.54) gives the full evolution of the master variables $\gamma_q(t)$; without making any further assumptions, Eq. (2.54) is exact. This may seem surprising, given that we have "built-in" irreversibility from the start by coarse graining the evolution of $\hat{\sigma}(t)$, which gave rise to the regularizing function $\exp[\varepsilon(t-t')]$ appearing in the integral. However, as written, Eq. (2.54) still describes the rapid fluctuations due to the decay and build-up of correlations in the system. In fact, at this stage we could still choose an infinite set of $\{\hat{\gamma}_q\}$ that describe all of the correlations in the system. It is only when we restrict our choice of $\{\hat{\gamma}_q\}$ to single-particle operators—allowing us to use Wick's theorem for the resulting Gaussian averages—and make the Born and Markov assumptions that the full coarse-graining procedure has been implemented. In conjunction with these further assumptions, the limiting procedure $\varepsilon \to 0$ will take on a more definite physical meaning.

Perturbation expansion

In the case of a weakly interacting system, we can seek the solution of the integral equation Eq. (2.54) in the form of a power series expansion of the density operator $\hat{\sigma}(t)$. In the extreme case where interactions can be neglected altogether, we have $\hat{\sigma}(t) = \hat{\sigma}^{(0)}(t)$ and $L_q(t) = 0$. To treat the weak interactions, we therefore make the expansions

$$\begin{aligned}\hat{\sigma}(t) &= \hat{\sigma}^{(0)}(t) + \sum_{n=1}^{\infty}\hat{\sigma}^{(n)}(t), \\ L_q(t) &= \sum_{n=1}^{\infty} L_q^{(n)}(t).\end{aligned} \tag{2.56}$$

Physically, we are assuming that the actual coarse-grained density operator $\hat{\sigma}(t)$ deviates only slightly from the Gaussian form of the reference distribution $\hat{\sigma}^{(0)}(t)$ because the interactions are so weak[4]. Substituting these successive approximations into Eq. (2.54) gives

[4]We will argue later that "weak" can apply to strong interactions which are well separated in time when we make appropriate modification of the Born approximation.

us the generalized kinetic equations expanded in powers of the weak interaction $\widehat{H}_\gamma^{(1)}$. By keeping just the first term in each expansion, eg.

$$\begin{aligned} \hat{\sigma}(t) &\approx \hat{\sigma}^{(0)}(t), \\ L_q(t) &\approx L_q^{(1)}(t) = \frac{1}{i\hbar}\mathrm{Tr}\big\{[\hat{\gamma}_q, \widehat{H}_\gamma^{(1)}]\hat{\sigma}^{(0)}(t)\big\}, \end{aligned} \tag{2.57}$$

the kinetic equations are obtained to second order in the interaction $\widehat{H}_\gamma^{(1)}$. Inserting the approximations Eq. (2.57) into Eq. (2.54) gives us the kinetic equations in the Born approximation

$$\begin{aligned} &\frac{\partial\gamma_q(t)}{\partial t} + \frac{1}{i\hbar}\langle[\widehat{H}, \hat{\gamma}_q]\rangle_{(0)}^t = -\frac{1}{\hbar^2}\int_{-\infty}^t dt' e^{-\varepsilon(t-t')} \\ &\times\left\langle\Big[\widehat{H}_\gamma^{(1)}, [\widehat{H}_\gamma^{(1)}(t,t'), \hat{\gamma}_q(t,t')] + \hat{\gamma}_p\Big(i\hbar\frac{\partial L_q^{(1)}(t,t')}{\partial\gamma_p(t')} + \langle[\frac{\partial\widehat{H}_\gamma^{(1)}(t,t')}{\partial\gamma_p(t')}, \hat{\gamma}_q(t,t')]\rangle_{(0)}^{t'}\Big)\Big]\right\rangle_{(0)}^{t'}, \end{aligned} \tag{2.58}$$

where we have performed a partial differentiation of the first term in the integral from Eq. (2.54). We have introduced the notation

$$\big\langle\hat{\mathcal{O}}\big\rangle_{(0)}^t = \mathrm{Tr}\Big\{\hat{\mathcal{O}}\hat{\sigma}^{(0)}(t)\Big\} \tag{2.59}$$

for the statistical average of an operator $\hat{\mathcal{O}}$ with respect to the reference distribution $\hat{\sigma}^{(0)}(t)$.

Truncating the expansion Eq. (2.56) at first order has simplified the kinetic equations in two ways. The assumption of weak interactions between particles in this dilute system allows us to simultaneously 1) treat the interactions only to second order and 2) to assume that the fluctuations of higher-order correlations are Gaussian, as dictated by the exponential form of the reference distribution $\hat{\sigma}^{(0)}(t)$. This allows us to use Wick's theorem to reduce multiple operator averages into a factorized form. Consequently, we now have a closed set of kinetic equations for the master variables $\{\gamma_q(t)\}$.

Markov approximation

As written, Eq. (2.58) is the most general second-order kinetic equation for a weakly interacting dilute system, which includes memory effects, since the relevant observables depend on t' in the integral. In general, this non-Markovian form of the kinetic equations is difficult to solve. It can readily be simplified by observing that the correlated averages in the collision kernel fluctuate on a rapid timescale compared to the assumed slow evolution of the macroscopic observables $\{\gamma_q(t)\}$. The Markov approximation is made by taking $\gamma_q(t') \to \gamma_q(t)$ in the collision integral, which gives us the Born-Markov form of the kinetic equations

$$\begin{aligned} &\frac{\partial\gamma_q(t)}{\partial t} + \frac{1}{i\hbar}\langle[\widehat{H}, \hat{\gamma}_q]\rangle_{(0)}^t \\ &= -\frac{1}{\hbar^2}\int_{-\infty}^0 d\tau e^{\varepsilon\tau}\left\langle\Big[\widehat{H}_\gamma^{(1)}(\tau), [\widehat{H}_\gamma^{(1)}, \hat{\gamma}_q] + \hat{\gamma}_p\Big(i\hbar\frac{\partial L_q^{(1)}(t)}{\partial\gamma_p(t)} + \langle[\frac{\partial\widehat{H}_\gamma^{(1)}}{\partial\gamma_p(t)}, \hat{\gamma}_q]\rangle_{(0)}^t\Big)\Big]\right\rangle_{(0)}^t, \end{aligned} \tag{2.60}$$

The collision kernel contains multiparticle correlations that can be factorized according to Wick's theorem. As we will show in the next section, these factorized multiparticle correlations include the Bose-enhancement factors for scattering into populated output channels, which are due to the correlations arising from quantum statistics.

The first term in the collision integral resembles the second-order term appearing in the master equations found in quantum optics for a system in contact with a static reservoir. In contrast, for the situation we are studying, the "reservoir" (eg. the N-body reference distribution $\hat{\sigma}^{(0)}(t)$) evolves in time according the the master variables, so that both the "system" (eg. the master variables $\{\gamma_q(t)\}$) and the "reservoir" depend on one another. This makes our problem inherently nonlinear. One implication of this is that the factorized multiparticle correlations appearing in the collision integral contain products of the master variables, i.e. $\gamma_q(t)\gamma_p(t)$. Also, the last two terms appearing in the collision integral do not appear in the master equation from quantum optics because they are due to this nonlinear behavior. The middle term originated from the time-variation of our reference distribution $\partial\hat{\sigma}^{(0)}(t)/\partial t$, while the third term appears because we have shifted the energies by the mean-field interaction $\widehat{Q}_\gamma^{(1)}$, which depends on the variables $\{\gamma_q(t)\}$.

The regularizing function $\exp(\varepsilon\tau)$ appearing in Eq. (2.60) originated from our coarse graining of the system's evolution based on the assumption of the attenuation of correlations. The full meaning of this point can now be understood. If we were to calculate the correlation function in the collision integral of the full kinetic equation Eq. (2.54) (i.e. before we make the Born approximation), we would find that it falls off with some characteristic time, on the order of a collision time $\sim\ \tau_0$. Another way to say this is that during a collision we can go off of the energy shell by an amount $\sim \hbar/\tau_0$. However, between collisions, we have free evolution according to the commutator on the left-hand side of Eq. (2.60), consequently the contribution of the far-off-the-energy-shell terms becomes negligible. This would not be true if the requirement for the attenuation of correlations was not met, that is, if the time between collisions was roughly the same as the duration of a collision so that successive collision events could not be well separated in time. The parameter ε, then, must be chosen consistently with this physical interpretation. Since we have made the Born approximation, taking the limit $\varepsilon \to 0$ would be equivalent to staying on the energy shell so that only energy conserving events are considered—this would give rise to an energy conserving delta-function in Eq. (2.60). However, a careful analysis of the collision kernel [47] in Eq. (2.54), which includes the full evolution during a collision (before the Born and Markov approximations), would show that the appropriate correlation time is the order of τ_0, so that the most appropriate choice is $\epsilon\ \sim\ 1/\tau_0$. With this choice the Born approximation result most closely approximates the full non-Markovian collision kernel. In this manner by choosing $\epsilon\ \sim\ 1/\tau_0$ we allow the Born approximation to more closely correspond to what, under some circumstances, would be the full off-the-energy-hsell T-matrix. It also allows strong interactions that are well-separated in time to be considered as "weak."

It is worth remarking that there is an alternative approach, based on the BBGKY hierarchy and cumulant expansion method, in which the two-particle interactions can more readily be treated to all orders, while still truncating the hierarchy of correlations [39]. This leads to essentially the same kinetic equations, but instead of treating interactions within the Born approximation, the full two-body T-matrix is used. Of course, we could also treat interactions to all orders in our approach, but this would require us to include many more terms in our perturbation series, which is cumbersome. This is because our decorrelation assumption is strongly tied to the notion of weak interactions. Such an assumption is not

necessary, for, as mentioned above, it is possible to have "strong" interactions that are well separated in time, which also allows for a reduced description of correlations.

2.3.7 Kinetic equations for mean fields and fluctuations

The Born-Markov kinetic equations Eq. (2.60) have been derived for a general set of master variables $\{\gamma_q(t)\}$, which must be chosen appropriately for the particular physical situation being described. For a dilute Bose gas above the critical temperature T_c for condensation, there is only one master variable that is relevant, the single-particle density matrix $f_{\vec{m}\vec{n}}(t)$, defined as

$$f_{\vec{m}\vec{n}}(t) = \mathrm{Tr}\{\hat{\sigma}(t)\hat{a}^\dagger_{\vec{n}}\hat{a}_{\vec{m}}\}. \tag{2.61}$$

This choice is consistent with the Born and Markov approximations made in the derivation of Eq. (2.60); there is no need to include the two-particle or higher reduced density matrices describing multi-particle correlations since we have already assumed that these quantities fluctuate rapidly on the timescale in which we are interested, so that their averages can be factorized in terms of the single-particle density matrix $f_{\vec{m}\vec{n}}(t)$. In some sense, then, we were predisposed to choose $f_{\vec{m}\vec{n}}(t)$, based on the physical assumptions made throughout the development of Eq. (2.60), even though we have kept the derivation general for an unspecified set $\{\gamma(t)\}$.

The situation is quite different for a Bose-condensed dilute gas at finite temperature, when the macroscopic order parameter $\psi(\boldsymbol{r},t)$ for the condensate plays a dominant role. As discussed in section 2.2.3, in this case the set of macroscopic relevant observables must be expanded to include the coherent mean field $\psi_{\vec{m}}(t)$, given by

$$\psi_{\vec{m}}(t) = \mathrm{Tr}\{\hat{\sigma}(t)\hat{a}_{\vec{m}}\}, \tag{2.62}$$

as well as the possibility for the generation of squeezing terms, or anomalous averages, $m_{\vec{m}\vec{n}}(t)$ and $n_{\vec{m}\vec{n}}(t)$,

$$\begin{aligned} m_{\vec{m}\vec{n}}(t) &= \mathrm{Tr}\{\hat{\sigma}(t)\hat{a}_{\vec{m}}\hat{a}_{\vec{n}}\}, \\ n_{\vec{m}\vec{n}}(t) &= \mathrm{Tr}\{\hat{\sigma}(t)\hat{a}^\dagger_{\vec{m}}\hat{a}^\dagger_{\vec{n}}\}. \end{aligned} \tag{2.63}$$

This choice of master variables does not conflict with our basic assumption of the factorization of multiparticle correlations. Furthermore, the quadratic form of the set of operators permits the use of Wick's theorem, which is valid for the Gaussian form of the reference distribution Eq. (2.9). The kinetic equations Eq. (2.60) for these variables form a closed, coupled set of equations describing the irreversible evolution of a dilute Bose-condensed gas at finite temperature and they conserve number and energy.

In the derivation of the kinetic equations Eq. (2.60), we partitioned the Hamiltonian into a free part $\widehat{H}^{(0)}_\gamma$ that included a mean-field shift $\widehat{Q}^{(1)}_\gamma$, and a weak interaction part $\widehat{H}^{(1)}_\gamma$ describing the fluctuations about the mean field. To complete this procedure, we now make the corresponding transformation of the relevant observables by considering the mean field $\psi_{\vec{m}}(t)$ and the fluctuations about it. This gives us the normal fluctuations $\tilde{f}_{\vec{m}\vec{n}}(t)$

$$\tilde{f}_{\vec{m}\vec{n}}(t) = \mathrm{Tr}\{\hat{\sigma}(t)\big[\hat{a}^\dagger_{\vec{n}} - \psi^*_{\vec{n}}(t)\big]\big[\hat{a}_{\vec{m}} - \psi_{\vec{m}}(t)\big]\}, \tag{2.64}$$

and the anomalous fluctuations $\tilde{m}_{\vec{m}\vec{n}}(t)$ and $\tilde{n}_{\vec{m}\vec{n}}(t)$

$$\begin{aligned} \tilde{m}_{\vec{m}\vec{n}}(t) &= \mathrm{Tr}\{\hat{\sigma}(t)\big[\hat{a}_{\vec{m}} - \psi_{\vec{m}}(t)\big]\big[\hat{a}_{\vec{n}} - \psi_{\vec{n}}(t)\big]\}, \\ \tilde{n}_{\vec{m}\vec{n}}(t) &= \mathrm{Tr}\{\hat{\sigma}(t)\big[\hat{a}^\dagger_{\vec{m}} - \psi^*_{\vec{m}}(t)\big]\big[\hat{a}^\dagger_{\vec{n}} - \psi^*_{\vec{n}}(t)\big]\}. \end{aligned} \tag{2.65}$$

We can now obtain a concrete set of kinetic equations for these master variables $\{\psi, \tilde{f}, \tilde{m}, \tilde{n}\}$ using the generalized kinetic equation Eq. (2.60) that was obtained for the generic set of observables $\{\gamma_q(t)\}$.

So far we have not specified the renormalization potential $\widehat{Q}_\gamma^{(1)}$, the general form of which must be specified before carrying out Wick's theorem to obtain the kinetic equations for our master variables. We assume it has the form

$$\widehat{Q}_\gamma^{(1)} \quad = \quad \frac{1}{2}\langle \vec{m}\,\vec{n}|V|\vec{l}\,\vec{k}\rangle\, \hat{a}_{\vec{m}}^\dagger\, Q_\gamma^{\vec{n}\vec{l}} \hat{a}_{\vec{k}}. \tag{2.66}$$

It turns out that the matrix elements $Q_\gamma^{\vec{n}\vec{l}}$ need not be specified, for the resulting kinetic equations obtained after carrying out the averages according to Wick's rules are independent of $Q_\gamma^{\vec{n}\vec{l}}$ for the single-particle, number-conserving form of $\widehat{Q}_\gamma^{(1)}$ chosen in Eq. (2.66). One could, of course, choose a different form than that given in Eq. (2.66), which could also include products of operators like $\hat{a}_{\vec{m}}\hat{a}_{\vec{n}}$, in which case the collision terms would get modified.

The kinetic equations for the mean field and fluctuations are obtained by first applying the generalized kinetic equations Eq. (2.60) to the chosen set of master variables $\{\psi, \tilde{f}, \tilde{m}, \tilde{n}\}$, and then making use of Wick's theorem to carry out the averages over the multiple operator products. The details of this procedure are outlined in Appendix (A). The large number of individual algebraic transformations (≈ 10000) that were necessary to obtain the final result prohibited attempts to evaluate the collision terms manually. Therefore, a symbolic algebra package was developed by Reinhold Walser to perform the required calculations. Here we do not provide the detailed analysis, but rather simply state the results.

The presentation of the final results of this calculation is greatly simplified by introducing the following single-particle Hilbert-space vectors (co-, contra-variant)

$$\langle\hat{a}\rangle \equiv |\psi\rangle = \psi_{\vec{m}}\ |\vec{m}\rangle\,, \quad \langle\hat{a}\rangle^\dagger \equiv \langle\psi| = \psi_{\vec{m}}^*\ \langle\vec{m}|\,, \tag{2.67}$$

normal operators [tensor rank (1,1)]

$$\tilde{f} = \tilde{f}_{\vec{m}\,\vec{n}}\ |\vec{m}\rangle\,\langle\vec{n}|\,, \quad f^{(c)} = \psi_{\vec{n}}^*\psi_{\vec{m}}\ |\vec{m}\rangle\,\langle\vec{n}|\,, \tag{2.68}$$

pseudo operators [tensor rank (2,0)]

$$\widetilde{m} = \widetilde{m}_{\vec{m}\,\vec{n}}\ |\vec{m}\rangle\,|\vec{n}\rangle\,, \quad m^{(c)} = \psi_{\vec{n}}\psi_{\vec{m}}\ |\vec{m}\rangle\,|\vec{n}\rangle\,, \tag{2.69}$$

and their Hermitian conjugates $\widetilde{n} = \widetilde{m}^\dagger$, $n^{(c)} = {m^{(c)}}^\dagger$. With these definitions, we present the kinetic equations, written in a compact, basis independent, operator form.

Mean field $|\psi\rangle$

$$\frac{d}{dt}|\psi\rangle + \frac{i}{\hbar}\left(H_0 + 1\,U_{f^{(c)}} + 2\,U_{\tilde{f}}\right)|\psi\rangle + \frac{i}{\hbar}\,V_{\widetilde{m}} \angle\ \langle\psi| = L_\psi^{(2)}[\psi, \tilde{f}, \widetilde{m}] \tag{2.70}$$

Normal fluctuations $\tilde{f}$

$$\frac{d}{dt}\tilde{f} + \frac{i}{\hbar}\left[H_0 + 2\,U_{f^{(c)}} + 2\,U_{\tilde{f}}\,,\ \tilde{f}\right] + \frac{i}{\hbar}\,V_{(m^{(c)}+\widetilde{m})} \angle\,\widetilde{n} - \frac{i}{\hbar}\,\widetilde{m} \angle\, V^\dagger_{(m^{(c)}+\widetilde{m})} = L_{\tilde{f}}^{(2)}[\psi, \tilde{f}, \widetilde{m}] \tag{2.71}$$

Anomalous fluctuations $\tilde{m}$

$$\frac{d}{dt}\widetilde{m} + \frac{i}{\hbar}\left(H_0 + 2\,U_{f^{(c)}} + 2\,U_{\bar{f}}\right) \angle\, \widetilde{m} + \frac{i}{\hbar}\,\widetilde{m} \angle \left(H_0 + 2\,U_{f^{(c)}} + 2\,U_{\bar{f}}\right) + \frac{i}{\hbar}\,V_{(m^{(c)}+\widetilde{m})} \angle\, (1+\tilde{f}) + \frac{i}{\hbar}\,\tilde{f} \angle\, V_{(m^{(c)}+\widetilde{m})} \quad = L^{(2)}_{\tilde{m}}[\psi, \tilde{f}, \widetilde{m}] \tag{2.72}$$

The free Hamiltonian H_0 is defined in Eq. (2.22). The mean-field potential is defined in terms of the two-particle interaction matrix elements and a single-particle density operator f that can be either $f^{(c)}$ or $\tilde{f}$

$$U_f \quad = \quad \langle \vec{m}\,\vec{n}|V|\vec{l}\,\vec{k}\rangle\, f_{\vec{k}\vec{n}}\, |\vec{m}\rangle\, \langle \vec{l}|. \tag{2.73}$$

Due to the Hermiticity of the two-particle interaction energy and the positivity of the single particle density, it is also self-adjoint , i.e., $U_f = U_f^\dagger$. The anomalous coupling strength $V_{\widetilde{m}}$ is given by

$$V_m \quad = \quad \langle \vec{m}\,\vec{n}|V|\vec{l}\,\vec{k}\rangle\, m_{\vec{k}\vec{l}}\, |\vec{m}\rangle\, |\vec{n}\rangle\,. \tag{2.74}$$

In here, the subscript m in V_m stands for any anomalous average, either $m^{(c)}$ or $\widetilde{m}$. From the definition of the anomalous coupling, it can be seen easily that $V_m = V_m^\top$ is symmetric. This non-Hermitian coupling is in general mediated by an anomalous average m, and involves a contraction $\angle$. In general, we obtain the contraction of two tensor fields $A \angle B$, from a basis representation of the two fields and a subsequent contraction of the last index of A with the last index of B. For example, for the case of two tensor rank (2,0) pseudo operators, the explicit contraction is

$$A \angle B^\dagger = \sum_{ijk} A_{ik}\,(B^\dagger)_{jk}\,|i\rangle\,\langle j|. \tag{2.75}$$

The collisional terms $L^{(2)}_{\tilde{\gamma}}[\psi, \tilde{f}, \widetilde{m}]$ on the right-hand side are rather involved and are given explicitly in Appendix (B).

The overall structure of the kinetic equations for each of the master variables is the same. The unitary evolution consists of a free part H_0, determined by the external trapping potential and any other applied electro-magnetic fields, and collision-induced mean-field potentials, denoted by $U_{f^{(c)}}$ and $U_{\bar{f}}$. While the first of these potentials is proportional the mean-field density itself, the second potential $U_{\bar{f}}$ reflects the influence of the normal fluctuation upon the mean field. It is important to note the different weighting factors 1 and 2 multiplying the potentials. They arise from the different quantum statistical fluctuation properties of a c-number mean field and a normal single particle density. Exactly the same weighting factors are also found with the variational Hartree-Fock-Bogoliubov approach [35].

Finally, appearing on the right-hand side of the kinetic equations are the second-order collisional terms. The terms in the $L^{(2)}_{\tilde{\gamma}}[\psi, \tilde{f}, \widetilde{m}]$ always appear in pairs where one term corresponds to an in-process while the sign reversed companion describes a loss out of the field. These terms allow for the exchange of norm between the master variables; that is, atoms in the condensate can scatter into the noncondensate and vice versa. These collisional terms generate damping and can also give rise to collisional energy shifts. Another

important point is that only the normal fluctuations $\tilde{f}$ contain Bose-enhancement factors for the out channels. This is not the case for the mean-field density $f^{(c)}$ and the anomalous densities $m^{(c)}$ and $\widetilde{m}$. This behavior is analogous to atomic transition rates described by the Einstein A- and B-coefficients which can be attributed to stimulated absorption and emission, as well as spontaneous emission processes. The fact that the mean-field is never bosonically enhanced supports the interpretation that the mean-field acts as a classical driving field.

2.4 Comparison to previous work

The master equations for the mean field Eq. (2.70), normal fluctuations Eq. (2.71), and anomalous fluctuations Eq. (2.72) obtained in the previous section form a closed set of equations describing the time evolution of a weakly interacting, Bose-condensed gas. The full solution of these dynamical equations for a general nonequilibrium state of a Bose-condensed gas at finite temperature is a monumental task that must be carried out on the computer using advanced numerical techniques, but is certainly within the reach of current technologies. Such a general description is necessary to describe nonequilibrium phenomena, such as the proposed atom laser, where a dynamical steady-state situation occurs due to a balance of the continuous output-coupling of condensate atoms with the replenishing of thermal atoms from a supplied reservoir. Another example of a possible nonequilibrium situation is a two-component condensate being driven by an external field that coherently couples the two internal states. Another point is that the collisional terms are also needed to obtain decay rates for excitations.

2.4.1 Low temperature limit

One can, of course, learn a great deal about the system by considering various limiting cases. Most of the previous work on dilute Bose gases appearing in the literature is focussed on the static properties of BEC at finite temperature, where the collisional terms can be neglected, or condensate dynamics at zero temperature, where, in addition to dropping the collisional terms, the fluctuations about the mean field are set to zero. More recent studies have begun to treat the coupled dynamics of the condensate and fluctuations [20, 21, 22, 23, 24, 25, 26, 27]. For example, in [24], the authors derive a coupled set of kinetic equations in the semiclassical approximation, where one can neglect the off-diagonal distribution functions. Their resulting hydrodynamic equations include the collisional exchange between the condensate and normal density and are equivalent to Eq. (2.70) and Eq. (2.71) if the anomolous fluctuations in those two equations are neglected.

In order to draw a connection to results of earlier work in this field, it is useful to represent the master equations Eq. (2.70) through Eq. (2.72) in the position representation. Here we will not consider the internal atomic structure, but treat only a single component. The case of a coupled two-component system will be dealt with in detail in Chapters 4 to 6. If we project Eq. (2.70) for the mean field $|\psi\rangle$ onto a position vector $\langle \boldsymbol{r}|$, we obtain the following kinetic equation for the wavefunction $\psi(\boldsymbol{r},t) = \langle \boldsymbol{r}|\psi(t)\rangle$

$$\begin{aligned} i\hbar\frac{d\psi(\boldsymbol{r},t)}{dt} - \left[\frac{-\hbar^2}{2m}\nabla^2 + U(\boldsymbol{r}) + V_0\left(|\psi(\boldsymbol{r},t)|^2 + 2\tilde{f}(\boldsymbol{r},t)\right)\right]\psi(\boldsymbol{r},t) - V_0\tilde{m}(\boldsymbol{r},t)\psi^*(\boldsymbol{r},t) \\ = \langle \boldsymbol{r}|L_\alpha^{(2)}[\psi,\tilde{f},\widetilde{m}]. \end{aligned} \tag{2.76}$$

Here, $\tilde{f}(\boldsymbol{r},t) = \langle \boldsymbol{r}|\tilde{f}|\boldsymbol{r}\rangle$ is the local density of the normal fluctuations and $\tilde{m}(\boldsymbol{r},t) = \langle \boldsymbol{r}|\tilde{m}|\boldsymbol{r}\rangle$ is the local density of the anomalous fluctuations. In the ensuing text, we do not consider the collisional terms $L_{\alpha}^{(2)}[\psi,\tilde{f},\tilde{m}]$, therefore we have not written their explicit form in the position representation. One can obtain similar equations for the position representation of Eq. (2.71) and Eq. (2.72) describing the normal and anomalous fluctuations.

The Gross-Pitaevskii equation

The simplest approximation for the description of the condensate is to completely neglect the fluctuations about the mean field by setting $\tilde{f} = \tilde{m} = 0$, and thus also dropping the collisional terms. Such an approximation is appropriate in the limiting case of $T = 0$. The resulting dynamical equation describing the condensate is called the time-dependent Gross-Pitaevskii (GP) equation, given by

$$i\hbar\frac{d\psi(\boldsymbol{r},t)}{dt} = \big[\frac{-\hbar^2}{2m}\nabla^2 + U(\boldsymbol{r}) + V_0|\psi(\boldsymbol{r},t)|^2\big]\psi(\boldsymbol{r},t). \tag{2.77}$$

This is also referred to as the nonlinear Schrödinger equation, due to the dependence on the local density $|\psi(\boldsymbol{r},t)|^2$ arising from treating interactions in an averaged way in the mean-field approximation. In the absence of an external drive, the condensate will condense into the lowest energy solution $\phi_0(\boldsymbol{r})$ of Eq. (2.77), given by

$$\big[\frac{-\hbar^2}{2m}\nabla^2 + U(\boldsymbol{r}) + V_0|\phi_0(\boldsymbol{r})|^2\big]\phi_0(\boldsymbol{r}) = \mu\,\phi_0(\boldsymbol{r}), \tag{2.78}$$

where μ is the chemical potential of the system. This is termed the time-independent GP equation.

Although the lowest temperatures achieved experimentally are not quite at $T = 0$, the GP equation has proven to give a good description of many static and dynamic properties of the system in many different situations at the coldest temperatures. In Chapter 2 we will investigate the basic properties of the GP equation for a single component gas in more detail.

Hartree-Fock-Bogoliubov treatment

There is a hierarchy of standard approximations appearing in the literature for extending the mean-field theory from the zero temperature result of the GP equation, to finite temperatures [35]. In order to elucidate the connection between our work, embodied in the master equations for the condensate and fluctuations in Eq. (2.70) through Eq. (2.72), it is useful to outline an alternative approach based on the work of Bogoliubov, where the field operator $\hat{\Psi}(\boldsymbol{r},t)$ for a Bose-condensed system is written as

$$\hat{\Psi}(\boldsymbol{r},t) = \psi(\boldsymbol{r},t) + \tilde{\psi}(\boldsymbol{r},t). \tag{2.79}$$

Here, $\psi(\boldsymbol{r},t)$ is the mean field $\psi(\boldsymbol{r},t) = \langle\hat{\Psi}(\boldsymbol{r},t)\rangle$ obtained by tracing over the N-body density operator $\hat{\rho}$, and the operator $\tilde{\psi}(\boldsymbol{r},t)$ describes the fluctuations about the mean field $\tilde{\psi}(\boldsymbol{r},t) = \hat{\Psi}(\boldsymbol{r},t) - \psi(\boldsymbol{r},t)$.

In the Heisenberg picture, the field operator obeys the following equation of motion

$$i\hbar\frac{\partial\hat{\Psi}(\boldsymbol{r},t)}{\partial t} = \Big[\frac{-\hbar^2}{2m}\nabla^2 + U(\boldsymbol{r})\Big]\hat{\Psi}(\boldsymbol{r},t) + V_0\hat{\Psi}^{\dagger}(\boldsymbol{r},t)\hat{\Psi}(\boldsymbol{r},t)\hat{\Psi}(\boldsymbol{r},t), \tag{2.80}$$

where we have again used the pseudo-potential introduced in Eq. (2.14) to describe binary interactions. Taking the trace of this with $\hat{\rho}$ gives us the following equation of motion for the mean field $\psi(\boldsymbol{r},t)$

$$i\hbar\frac{\partial\psi(\boldsymbol{r},t)}{\partial t} = \Big[\frac{-\hbar^2}{2m}\nabla^2 + U(\boldsymbol{r})\Big]\psi(\boldsymbol{r},t) + V_0\big\langle\hat{\Psi}^\dagger(\boldsymbol{r},t)\hat{\Psi}(\boldsymbol{r},t)\hat{\Psi}(\boldsymbol{r},t)\big\rangle. \tag{2.81}$$

This can be simplified by substituting the expression for $\hat{\Psi}(\boldsymbol{r},t)$ from Eq. (2.79) into the last term, to give

$$\begin{aligned} i\hbar\frac{\partial\psi(\boldsymbol{r},t)}{\partial t} &= \left[\frac{-\hbar^2}{2m}\nabla^2 + U(\boldsymbol{r}) + V_0\Big(|\psi(\boldsymbol{r},t)|^2 + 2\tilde{f}(\boldsymbol{r},t)\Big)\right]\psi(\boldsymbol{r},t) + V_0\tilde{m}(\boldsymbol{r},t)\psi^*(\boldsymbol{r},t) \\ &+ V_0\big\langle\tilde{\psi}^\dagger(\boldsymbol{r},t)\tilde{\psi}(\boldsymbol{r},t)\tilde{\psi}(\boldsymbol{r},t)\big\rangle, \end{aligned} \tag{2.82}$$

where we recall that the averages over the fluctuations vanish, $\langle\tilde{\psi}\rangle = 0$. Here we have defined the normal and anomalous densities as $\tilde{f}(\boldsymbol{r},t) = \langle\tilde{\psi}^\dagger(\boldsymbol{r},t)\tilde{\psi}(\boldsymbol{r},t)\rangle$ and $\tilde{m}(\boldsymbol{r},t) = \langle\tilde{\psi}(\boldsymbol{r},t)\tilde{\psi}(\boldsymbol{r},t)\rangle$ respectively.

This equation is nearly identical to the kinetic equation Eq. (2.76) describing the mean field. The last term $\langle\tilde{\psi}^\dagger\tilde{\psi}\tilde{\psi}\rangle$ in Eq. (2.82) describes correlations between atoms due to collisions and must at equivalent levels of approximation ultimately reduce to the collision term $L_\alpha^{(2)}[\psi,\tilde{f},\widetilde{m}]$ in our kinetic equation for the mean field. Within the present Bogoliubov approach, one could get a handle on this term by ascending up the hierarchy of equations analogously to the BBGKY approach. One would then obtain an equation of motion for $\langle\tilde{\psi}^\dagger\tilde{\psi}\tilde{\psi}\rangle$ that would link up to higher-order correlations, and then one could truncate the hierarchy according to the assumption of the attenuation of correlations. The advantage of our kinetic approach is that these collisional terms have been calculated explicitly (see Appendix (B)). In contrast, the standard approach is to make the so called self-consistent mean-field approximation by writing [35, 48]

$$\tilde{\psi}^\dagger(\boldsymbol{r},t)\tilde{\psi}(\boldsymbol{r},t)\tilde{\psi}(\boldsymbol{r},t) \approx 2\big\langle\tilde{\psi}^\dagger(\boldsymbol{r},t)\tilde{\psi}(\boldsymbol{r},t)\big\rangle\tilde{\psi}(\boldsymbol{r},t) + \big\langle\tilde{\psi}(\boldsymbol{r},t)\tilde{\psi}(\boldsymbol{r},t)\big\rangle\tilde{\psi}^\dagger(\boldsymbol{r},t). \tag{2.83}$$

Within this approximation, then, the last term in Eq. (2.82) goes to zero, giving us

$$i\hbar\frac{\partial\psi(\boldsymbol{r},t)}{\partial t} = \left[\frac{-\hbar^2}{2m}\nabla^2 + U(\boldsymbol{r}) + V_0\Big(|\psi(\boldsymbol{r},t)|^2 + 2\tilde{f}(\boldsymbol{r},t)\Big)\right]\psi(\boldsymbol{r},t) + V_0\tilde{m}(\boldsymbol{r},t)\psi^*(\boldsymbol{r},t). \tag{2.84}$$

Similarly, this approximation also leads to the following equation of motion for the fluctuating field operator $\tilde{\psi}(\boldsymbol{r},t)$ [35]

$$i\hbar\frac{\partial\tilde{\psi}(\boldsymbol{r},t)}{\partial t} = \Big[\frac{-\hbar^2}{2m}\nabla^2 + U(\boldsymbol{r}) + 2V_0\,n(\boldsymbol{r},t)\Big]\tilde{\psi}(\boldsymbol{r},t) + V_0\,m(\boldsymbol{r},t)\tilde{\psi}^\dagger(\boldsymbol{r},t), \tag{2.85}$$

where we have defined the total density as $n(\boldsymbol{r},t) = |\psi(\boldsymbol{r},t)|^2 + \tilde{f}(\boldsymbol{r},t)$ and the total anomalous average as $m(\boldsymbol{r},t) = \psi^2(\boldsymbol{r},t) + \tilde{m}(\boldsymbol{r},t)$.

These two equations for the mean field $\psi(\boldsymbol{r},t)$ and the fluctuating field operator $\tilde{\psi}(\boldsymbol{r},t)$ are equivalent to the kinetic equations Eq. (2.70) through Eq. (2.72) if we drop the collisional terms $L_\gamma^{(2)}[\psi,\tilde{f},\widetilde{m}]$ in those equations. This approximation is sometimes referred to as treating the collisionless regime, which is assumed to be an adequate description close

to equilibrium where the collisional terms drop out due to detailed balance (in principle one should also include the collisional energy shifts, since detailed balance will occur only if these are included). This description, then, is useful in treating the system in equilibrium at finite temperature, though recent work has been done that treats the coupled dynamics of the system close to equilibrium [22, 23, 24, 26, 49].

If we are interested in the static properties of the system at finite temperature in this approximation, then we must find the stationary solution of the mean field according to

$$\left[\frac{-\hbar^2}{2m}\nabla^2 + U(\boldsymbol{r}) + V_0\Big(|\psi(\boldsymbol{r})|^2 + 2\tilde{f}(\boldsymbol{r})\Big)\right]\psi(\boldsymbol{r}) + V_0\tilde{m}(\boldsymbol{r})\psi^*(\boldsymbol{r}) = \mu\,\psi(\boldsymbol{r}). \quad (2.86)$$

In order to describe the system in equilibrium, we would like to know the excitation spectrum of the system, described by $\tilde{\psi}(\boldsymbol{r},t)$. To find the excitations about the mean field, we subtract the chemical potential μ from the left-hand side of Eq. (2.85). It can then be shown that a general solution of Eq. (2.85), and its Hermitian conjugate, takes the form [35, 36]

$$\begin{aligned}\tilde{\psi}(\boldsymbol{r},t) &= \sum_j \left[u_j(\boldsymbol{r})\hat{b}_j e^{-iE_j t} - v_j^*(\boldsymbol{r})\hat{b}_j^\dagger e^{iE_j t}\right],\\ \tilde{\psi}^\dagger(\boldsymbol{r},t) &= \sum_j \left[u_j^*(\boldsymbol{r})\hat{b}_j^\dagger e^{iE_j t} - v_j(\boldsymbol{r})\hat{b}_j e^{-iE_j t}\right],\end{aligned} \quad (2.87)$$

where the creation and annihilation operators $\hat{b}_j^\dagger$ and $\hat{b}_j$ for this transformation satisfy the usual Bose commutation relations and effectively describe a Bose gas of noninteracting "quasiparticles" that have an energy spectrum E_j. Substituting these expressions into Eq. (2.85) and its hermitian conjugate, it can be shown that the expansion coefficients $u(\boldsymbol{r})$ and $v(\boldsymbol{r})$, or normal modes, and the corresponding energies E_j must satisfy the equations

$$\begin{aligned}\hat{\mathcal{H}}\,u_j(\boldsymbol{r}) - V_0\,m(\boldsymbol{r})v_j(\boldsymbol{r}) &= E_j\,u_j(\boldsymbol{r}),\\ \hat{\mathcal{H}}\,v_j(\boldsymbol{r}) - V_0\,m^*(\boldsymbol{r})u_j(\boldsymbol{r}) &= -E_j\,v_j(\boldsymbol{r}),\end{aligned} \quad (2.88)$$

where the operator $\hat{\mathcal{H}}$ is defined as

$$\hat{\mathcal{H}} = -\frac{\hbar^2}{2m}\nabla^2 + U(\boldsymbol{r}) + 2V_0 n(\boldsymbol{r}) - \mu. \quad (2.89)$$

The transformation defined by equations Eq. (2.87) through Eq. (2.89) generalizes the standard zero-temperature Bogoliubov treatment of the elementary excitations by including the effect the normal and anomalous fluctuations have on the system. This generalization of the Bogoliubov approximation is referred to as the Hartree-Fock-Bogoliubov (HFB) approximation [35].

The expansion of $\tilde{\psi}(\boldsymbol{r},t)$ into the normal modes Eq. (2.87) does not by itself solve the problem, for we still need to solve for the normal $\tilde{f}(\boldsymbol{r})$ and anomolous $\tilde{m}(\boldsymbol{r})$ fluctuations. The fluctuations $\tilde{f}(\boldsymbol{r})$ and $\tilde{m}(\boldsymbol{r})$ take the following form in this quasiparticle representation

$$\begin{aligned}\tilde{f}(\boldsymbol{r}) &= \sum_j \left\{\left[|u_j(\boldsymbol{r})|^2 + |v_j(\boldsymbol{r})|^2\right]\langle\hat{b}_j^\dagger\hat{b}_j\rangle + |v_j(\boldsymbol{r})|^2\right\}\\ \tilde{m}(\boldsymbol{r}) &= -\sum_j u_j(\boldsymbol{r})v_j^*(\boldsymbol{r})\left[2\langle\hat{b}_j^\dagger\hat{b}_j\rangle + 1\right],\end{aligned} \quad (2.90)$$

where $\langle \hat{b}_j^\dagger \hat{b}_j \rangle$ is the population in the quasiparticle level j. An obvious first ansatz is to assume that these modes are occupied thermally according to the Bose-Einstein distribution

$$\langle \hat{b}_j^\dagger \hat{b}_j \rangle = \frac{1}{e^{\beta E_j} - 1}, \tag{2.91}$$

where $\beta = 1/k_{\rm B}T$. This assumption then closes the coupled set of equations for the system, which must be solved self-consistently since the mean-field solution given by Eq. (2.86) depends on the fluctuations $\tilde{f}(\boldsymbol{r})$ and $\tilde{m}(\boldsymbol{r})$, which in turn depend on the mean field through the density $n(\boldsymbol{r})$ and chemical potential μ appearing in $\hat{\mathcal{H}}$ given in Eq. (2.89). This procedure is outlined by Griffin [35], for example.

We can now enumerate the various approximations made within this Hartree-Fock-Bogoliubov description of the system at finite temperature.

1. *Bogoliubov approximation*. This corresponds to the zero temperature case discussed earlier, where the fluctuations are set to zero $\tilde{f}(\boldsymbol{r}) = \tilde{m}(\boldsymbol{r}) = 0$, so that one simply obtains the GP equation Eq. (2.77) describing the mean field. The excitations about the mean field are obtained from the generalized Bogoliubov transformation by setting the fluctuations to zero in Eq. (2.87) through Eq. (2.89), however in the $T = 0$ limit, these excitations are not thermally occupied.

2. *Popov approximation*. In this approximation, the anomalous fluctuations are neglected $\tilde{m}(\boldsymbol{r}) = 0$, but the normal fluctuations $\tilde{f}(\boldsymbol{r})$ are included. The *static* Popov approximation corresponds to assuming the quasiparticle spectrum is thermally populated according to Eq. (2.91) for a given total number and energy (or chemical potential and temperature). The resulting coupled set of HFB-Popov equations must then be solved self-consistently. On the other hand, one can still work in the collisionless regime, but treat the mean field and the normal fluctuations dynamically if one is interested in the excitations of the system. In this case one expands the mean field and normal fluctuations about the equilibrium situation considered in the static Popov approxmation by treating the linear response of the system to a weak drive. Such an approach is called the *dynamic* Popov approximation and has recently been treated by Bijlsma et al. [49], for example.

3. *Hartree-Fock-Bogoliubov approximation*. In this case, the normal $\tilde{f}(\boldsymbol{r})$ and anomalous $\tilde{m}(\boldsymbol{r})$ fluctuations are both included and the excitation spectrum is assumed to be thermally occupied according to Eq. (2.91). One must then solve the HFB equations self-consistently.

We have outlined here the main approximations for treating the dilute Bose-condensed gas at finite temperature. An important point is that the kinetic equations reduce to these various limits if the collisional terms $L_\gamma^{(2)}[\psi, \tilde{f}, \widetilde{m}]$ in Eq. (2.70) through Eq. (2.72) are neglected. Our approach, then, goes far beyond these three standard approaches, which treat the collisionless regime, and is the most general second-order theory for a dilute weakly interacting Bose gas—it describes the irreversible nonequilibrium evolution of the condensate and fluctuations in a dynamical, self-consistent fashion. Naturally, we can obtain damping rates and collisional energy shifts from the kinetic equations.

Of course, such a full treatment is an extremely difficult computational task and is not trivial to implement. A sensible approach is to look toward these standard approaches for guidance in finding a reasonable starting point for including the collisional effects. One

could, for example, carry out the generalized Bogoliubov transformation Eq. (2.87) through Eq. (2.89) in order to simplify the collisional terms; in this representation, the collisional terms might have a much simpler structure. Another useful approach would be to neglect the anomolous fluctuations in the kinetic equations, as considered recently by Zaremba et al. [24].

2.4.2 High temperature limit

In the high temperature limit $T > T_c$, the mean field and anomalous averages can be neglected. In this limit, the density matrix for the fluctuations $\tilde{f}$ just becomes f, the single atom density matrix. We can then write the kinetic equation Eq. (2.71) as

$$\frac{d}{dt}f + \frac{i}{\hbar}\left[H_0, f\right] = L_f^{(2)}[\psi = 0, f, \tilde{m} = 0]. \tag{2.92}$$

The collisional term $L_f^{(2)}[\psi = 0, f, \tilde{m} = 0]$ specified in Appendix (B) takes the much simpler form in this limit

$$L_f^{(2)} = \Gamma_{ff(1+f)} - \Gamma_{(1+f)(1+f)f} + \text{ h.c.} \tag{2.93}$$

The free Hamiltonian H_0 just describes the motion in the harmonic trap (we are not considering the internal structure of the atoms here). It is convenient to expand the operator equation Eq. (2.92) into the eigenstates of this Hamiltonian, $H_0 \left|i\right\rangle = \epsilon_i \left|i\right\rangle$. This gives us the kinetic equations for the matrix elements f_{ij}

$$\dot{f}_{ij} + \frac{i}{\hbar}\left(\epsilon_i - \epsilon_j\right) f_{ij} = \left\langle i\right| L_f^{(2)} \left|j\right\rangle, \tag{2.94}$$

where the collisional term is

$$\begin{aligned} \left\langle i\right| L_f^{(2)} \left|j\right\rangle &= \frac{2\pi}{\hbar}\frac{1}{\hbar\omega_0}\sum_{rstu}\sum_{mnpq}\delta_{\epsilon_m+\epsilon_n,\epsilon_p+\epsilon_q} C(m,n;p,q)C(r,s;t,u) \\ &\times \delta_{uj}\Big[f_{qs}f_{pr}(\delta_{tm}+f_{tm})(\delta_{in}+f_{in}) - f_{tm}f_{in}(\delta_{pr}+f_{pr})(\delta_{qs}+f_{qs})\Big] \\ &+ \text{ h.c.} \end{aligned} \tag{2.95}$$

Here the transition amplitudes $C(m,n;p,q)$ are given by

$$C(n,m;q,p) = V_0 \int d^3r \phi_n^*(\boldsymbol{r})\phi_m^*(\boldsymbol{r})\phi_q(\boldsymbol{r})\phi_p(\boldsymbol{r}), \tag{2.96}$$

where $\left\langle \boldsymbol{r}\right| i\rangle = \phi_i(\boldsymbol{r})$ are the eigenstates of H_0.

Although we have included here the possibility that the coherences f_{ij} might be important, in the high temperature limit we expect these off-diagonal matrix elements to be negligible. Setting $f_{ij} = f_{ij}\delta_{ij}$ in Eq. (2.94) gives us the Uehling-Uhlenbeck equation [38, 39] for the populations f_i

$$\frac{\partial f_i}{\partial t} = \sum_{jkl} W(i,j;k,l)\big[f_k f_l(1+f_i)(1+f_j) - f_i f_j(1+f_k)(1+f_l)\big], \tag{2.97}$$

where the transition rate $W(i,j;k,l)$ appearing in Eq. (2.97) is essentially just Fermi's Golden Rule

$$W(i,j;k,l) = \frac{2\pi}{\hbar}|C(i,j;k,l)|^2 \frac{\delta_{\epsilon_i+\epsilon_j,\epsilon_k+\epsilon_l}}{\hbar\omega_0}. \tag{2.98}$$

This is the quantum version of the classical Boltzmann kinetic equation; it includes the Bose enhancement factors $(1+f_k)$ for scattering into populated output channels of a collision. It gives a valid description above the critical temperature and may describe the initial onset of condensation. Once the condensate has formed, though, it is no longer an accurate description if the mean-field interaction is substantial. We will return to this equation in Chapter 7 and Chapter 8, where we consider specific applications of nonequilibrium kinetic theory in the high temperature limit.

2.5 Summary

In this chapter we have developed a quantum kinetic theory describing a dilute Bose-condensed gas at finite temperature. We showed that in the simplest approximation for low temperatures—obtained by neglecting the normal and anomalous fluctuations—we recover the GP equation. We also showed that in the collisionless limit, we recover the Hartree-Fock-Bogoliubov description. Finally, in the high temperature limit we set the mean field and anomalous averages to zero to obtain the quantum Boltzmann equation for the single-atom density matrix. In the rest of this thesis, we will only treat either the GP equation, which is an approximation of the system at zero temperature, in Chapters 3 through 6, or the high temperature limit above T_c where the the Boltzmann transport equation for the populations is an appropriate description.

Chapter 3

Mean-Field Theory of a Single Component

3.1 Introduction

In this chapter we consider the basic properties of a trapped, single-component condensate at zero temperature. By "single-component," we simply mean that a single atomic species is present, in contrast to chapters 4 though 6 where we consider a two-component condensate, in which two different hyperfine levels are populated. This chapter serves a pedagogical purpose of outlining the well-known solutions to the Gross-Pitaevskii equation for a single component system. We begin with a discussion of the ground-state solution, and present the full numerical solution along with the Thomas-Fermi approximate solution that is valid in the limit of a large number of atoms. We next consider non-ground-state condensates, or topological modes, such as a vortex. It is useful to introduce the notion of a topological mode for the single component condensate, before considering it for the two-component system in Chapters 4 and 6. In the last section we consider the response of the condensate to a mechanical drive and show that for a weak harmonic drive, the linear response of the condensate is a superposition of the collective modes discussed in the previous chapter.

3.2 The Gross-Pitaevskii equation

In Chapter 2 we derived the Gross-Pitaevskii equation within the framework of quantum kinetic theory by neglecting the normal and anomalous fluctuations in the kinetic equation for the condensate Eq. (2.76), which is an approximation for $T = 0$. This leads to a deceivingly simple looking equation describing the condensate wavefunction $\psi(\boldsymbol{r}, t)$ [50, 51]

$$i\hbar \frac{\partial \psi(\boldsymbol{r}, t)}{\partial t} = \Big[-\frac{\hbar^2}{2m}\nabla^2 + U(\boldsymbol{r}) + V_0 N \left|\psi(\boldsymbol{r}, t)\right|^2 \Big] \psi(\boldsymbol{r}, t), \tag{3.1}$$

where m is the mass of the atom, $U(\boldsymbol{r})$ is a trapping potential, and $V_0 = 4\pi\hbar^2 a/m$ is a measure of the strength of binary interactions, proportional to the s-wave scattering length a. Here we have normalized the condensate wavefunction to unity $\int |\psi(\boldsymbol{r}, t)|^2 d^3r = 1$. The system responds to itself through the density term in Eq. (3.1), which makes the equa-

tion nonlinear. A remarkable aspect of BEC in a dilute atomic gas is that there are no fitting parameters in the theory—the physical parameters m, a, and the spring constants of the trap appearing in $U(\boldsymbol{r})$ are all well-defined microscopic quantities.

Although Eq. (3.1) resembles the usual Schrödinger equation describing a single-particle system, we must not forget that $\psi(\boldsymbol{r},t)$ characterizes a many-particle system. In Chapter 2 we obtained the time-dependent GP equation within the statistical ensemble picture of quantum kinetic theory, where we introduced the reduced description based on the assumption that particle correlations can be factorized into products of single-particle quantities. Within that framework, the wavefunction $\psi(\boldsymbol{r},t)$ is a macroscopic mean-field amplitude $\psi(\boldsymbol{r},t) \equiv \langle \hat{\Psi}(\boldsymbol{r},t) \rangle$, where $\hat{\Psi}(\boldsymbol{r},t)$ is a field operator and the brackets $\langle\,\rangle$ represent a statistical average over the N-body state of the system ρ.

An alternative approach that is useful in understanding the GP equation is to describe the system by a many-particle wavefunction Ψ as in Eq. (2.11), instead of the many-particle density matrix ρ used in the statistical approach presented in Chapter 2. In general, the many-particle wavefunction is very complicated due to particle correlations caused by the interactions between atoms. The problem is made tractable by first neglecting these particle correlations and assuming that all of the atoms in the condensed system occupy the same single-particle wavefunction $\psi(\boldsymbol{r},t)$

$$\Psi(\boldsymbol{r}_1,\boldsymbol{r}_2,\boldsymbol{r}_3,...,\boldsymbol{r}_N,t) = \psi(\boldsymbol{r}_1,t)\psi(\boldsymbol{r}_2,t)\psi(\boldsymbol{r}_3,t)...\psi(\boldsymbol{r}_N,t). \tag{3.2}$$

Physically, then we can interpret the GP equation as describing a system of N particles that all act in unison according to Eq. (3.1)[1]. The factorized form of Eq. (3.2) means that correlations between particles are neglected. The static ground state of the condensate can be found within this framework using the variational procedure, starting with the assumption that all of the atoms occupy the same state $\phi_0(\boldsymbol{r})$

$$\Psi(\boldsymbol{r}_1,\boldsymbol{r}_2,\boldsymbol{r}_3,...,\boldsymbol{r}_N) = \phi_0(\boldsymbol{r}_1)\phi_0(\boldsymbol{r}_2)\phi_0(\boldsymbol{r}_3)...\phi_0(\boldsymbol{r}_N). \tag{3.3}$$

The state $\phi_0(\boldsymbol{r})$ is found by minimizing the total energy of the N-particle system with respect to variations of $\delta\phi_0$, using the N-body Hamiltonian in Eq. (2.12). Carrying out this variational ansatz leads to the time-independent GP equation Eq. (3.4) discussed in the next section. This variational procedure can also be used to find the elementary excitations of the condensate, to varying degrees of sophistication [52].

3.3 Ground state properties

The bosonic enhancement factors $(1+f)$ appearing in the collisional terms of the kinetic equations derived in Chapter 2 cause stimulated scattering into the lowest-energy state of the system during condensation. In the limit of an ideal gas, where interactions can be neglected, the state into which the atoms condense is simply the bare harmonic oscillator ground state. However, for a dilute gas, the first-order effect of interactions is to modify the effective external potential, so that in addition to the trapping potential $U(\boldsymbol{r})$ the atoms also experience a net force due to interactions, which is proportional to the local density. The lowest-energy state $\phi_0(\boldsymbol{r})$ then is determined by the solution to the time-independent Gross-Pitaevskii equation

$$\Big[-\frac{\hbar^2}{2m}\nabla^2 + U(\boldsymbol{r}) + V_0 N\,|\phi_0(\boldsymbol{r})|^2\Big]\,\phi_0(\boldsymbol{r}) = \mu\,\phi_0(\boldsymbol{r}), \tag{3.4}$$

[1] One must replace N by $N-1$ in Eq. (3.1) in the strict case of fixed particle number

where μ is the chemical potential. In general, this nonlinear equation must be solved self-consistently using numerical techniques. It should be noted that throughout this thesis, we will only consider the case of a positive scattering length $a > 0$.

3.3.1 Thomas-Fermi limit

Before giving examples of numerical solutions of Eq. (3.4), it is first useful to consider two limiting cases of either very few or many atoms. In the limit that $N \to 1$, the solution to Eq. (3.4) is trivial—it is just the bare harmonic oscillator ground state. The opposite limit of many atoms $N \to \infty$ is referred to as the Thomas-Fermi limit. In this case, the kinetic energy term in Eq. (3.4) becomes negligible. Upon setting the kinetic energy term to zero and solving for ϕ_0, the ground state solution in the Thomas-Fermi limit then becomes

$$\phi_{\rm TF}(\boldsymbol{r}) = \sqrt{\frac{1}{NV_0}\big[\mu_{\rm TF} - U(\boldsymbol{r})\big]}. \tag{3.5}$$

It is useful to consider the specific case of the condensate in an isotropic harmonic potential $U(\boldsymbol{r}) = m\omega_0^2 r^2/2$. The Thomas-Fermi radius is determined by solving for r in the expression $U(\boldsymbol{r}) = \mu_{\rm TF}$, which gives

$$r_{\rm TF} = \sqrt{\frac{2\,\mu_{\rm TF}}{m\omega_0^2}}. \tag{3.6}$$

The chemical potential must be determined from the normalization condition

$$4\pi \int_0^{r_{\rm TF}} r^2\, dr |\phi_{\rm TF}|^2 = 1. \tag{3.7}$$

After carrying out the integral, we find that the chemical potential in the Thomas-Fermi limit is

$$\mu_{\rm TF} = \frac{\hbar\omega_0}{2}\Big[15\,N(\frac{a}{l_{\rm sho}})\Big]^{2/5}, \tag{3.8}$$

where $l_{\rm sho} = \sqrt{\hbar/m\omega_0}$ is the size of the harmonic oscillator ground state. This result tells us that the chemical potential scales like the power of $2/5$ with the population N and the scattering length a. For typical values of parameters in current experiments, the chemical potential is $10 - 100$ times larger than the bare oscillator ground state energy. Upon substituting Eq. (3.8) into Eq. (3.6), we find that the size of the condensate in the Thomas-Fermi limit is given by

$$r_{\rm TF} = l_{\rm sho}\Big(\frac{15\,N\,a}{l_{\rm sho}}\Big)^{1/5}. \tag{3.9}$$

For typical values of the physical parameters, the condensate size is around a factor of 10 larger than the bare oscillator ground state.

In general the trapping potential is not isotropic, but has the form

$$U(\boldsymbol{r}) = \frac{1}{2}m(\omega_x^2 x^2 + \omega_y^2 y^2 + \omega_z^2 z^2). \tag{3.10}$$

In this case, the Thomas-Fermi chemical potential is given by Eq. (3.8), with the substitutions $\omega_0 \to \bar{\omega}$ and $l_{\rm sho} \to \bar{l}_{\rm sho}$, where $\bar{\omega} = (\omega_x\omega_y\omega_z)^{1/3}$ and $\bar{l}_{\rm sho} = \sqrt{\hbar/m\bar{\omega}}$. The extent of the condensate along each axis is given by $l_{\rm TF} = \sqrt{2\mu_{TF}/m\omega_l^2}$, where $l \in \{x, y, z\}$ [53]. Most experiments have at least cylindrical symmetry, with $\omega_x = \omega_y$, although a few experiments actually have used spherically symmetric traps [13].

3.3.2 Lower-dimensional modeling

In many cases, the system possesses a particular symmetry that allows the problem to be modeled in fewer spatial dimensions. Throughout the remainder of this thesis, we will often exploit such a simplification. It is important to understand what we mean by "lower-dimensional modeling". We do not mean that the actual physical system satisfies some limit of aspect ratios of the confining potential. For example, imagine a trap with such a tight confinement in the xy-plane that the system can be treated as a one-dimensional system, which becomes a better approximation as the ratio ω_z/ω_{xy} gets smaller, where $\omega_x = \omega_y \equiv \omega_{xy}$. This is not what we mean; we will not treat systems that satisfy such a constraint. Instead, we consider systems that possess a particular symmetry, such that the main dynamics of the system occur along the z-axis, or in the xy-plane. This point will become clearer as we consider specific cases throughout this thesis.

For a two-dimensional model, the condensate ground state satisfies the GP equation

$$\Big[-\frac{\hbar^2}{2m}\Big(\frac{\partial^2}{\partial x^2}+\frac{\partial^2}{\partial y^2}\Big) + \frac{1}{2}m\big(\omega_x^2 x^2+\omega_y^2 y^2\big) + \alpha_{2\mathrm{d}} V_0 N\,|\psi(x,y)|^2\Big]\,\psi(x,y) = \mu\,\psi(x,y), \tag{3.11}$$

while in the one dimensional model the time-independent GP equation is

$$\Big[-\frac{\hbar^2}{2m}\frac{\partial^2}{\partial z^2} + \frac{1}{2}m\omega_z^2 z^2 + \alpha_{1\mathrm{d}} V_0 N\,|\psi(z)|^2\Big]\,\psi(z) = \mu\,\psi(z). \tag{3.12}$$

We choose the scaling factors $\alpha_{1\mathrm{d}}$ and $\alpha_{2\mathrm{d}}$ so that the chemical potential, or equivalently, the size, of the condensate is the same in the reduced-dimension model as in the three-dimensional problem. This can be achieved by solving for the chemical potentials in the one and two dimensional models in the Thomas-Fermi limit, equating them to the chemical potential given in Eq. (3.8) for the three dimensional case, and solving for the scaling factors $\alpha_{1\mathrm{d}}$ and $\alpha_{2\mathrm{d}}$. After a bit of algebra, we obtain the results

$$\alpha_{2\mathrm{d}} = \frac{15^{4/5}}{16} N^{-1/5}\Big(\frac{\bar{\omega}}{\bar{\omega}_{2\mathrm{d}}}\Big)^2 (a\,\bar{l}_{\mathrm{sho}}^4)^{-1/5}, \tag{3.13}$$

and

$$\alpha_{1\mathrm{d}} = \frac{1}{2\pi}\Big(\frac{5^3}{9}\Big)^{1/5} N^{-2/5}\Big(\frac{\bar{\omega}}{\bar{\omega}_z}\Big)(a^4\,\bar{l}_{\mathrm{sho}}^{16})^{-1/10}, \tag{3.14}$$

where $\bar{\omega}_{2\mathrm{d}} = \sqrt{\omega_x\omega_y}$. Note that $\alpha_{2\mathrm{d}}$ has units of length^{-1} and $\alpha_{1\mathrm{d}}$ has units of length^{-2}, as they must. These coefficients must compensate for the loss of one or two dimensions from the problem, since the interaction parameter V_0 was obtained by assuming s-wave scattering in a three-dimensional space.

In later chapters, we model the dynamical evolution of the condensate using the time-dependent versions of Eq. (3.11) and Eq. (3.12). This simplified description, in essence, makes a factorization assumption about the different axes of the system. Due to the non-linearity of the time-dependent GP equation, we know that the different axes are coupled. For example, if the system possesses cylindrical symmetry and the condensate is being driven by a force with spatial variation along the z-axis but no radial variation, then a one-dimensional model can be implemented. However, due to the coupling between dimensions, radial structure can develop, which is unaccounted for in the one-dimensional model. It is therefore useful to check the lower-dimensional model against the full solution. We will address this issue later in the thesis.

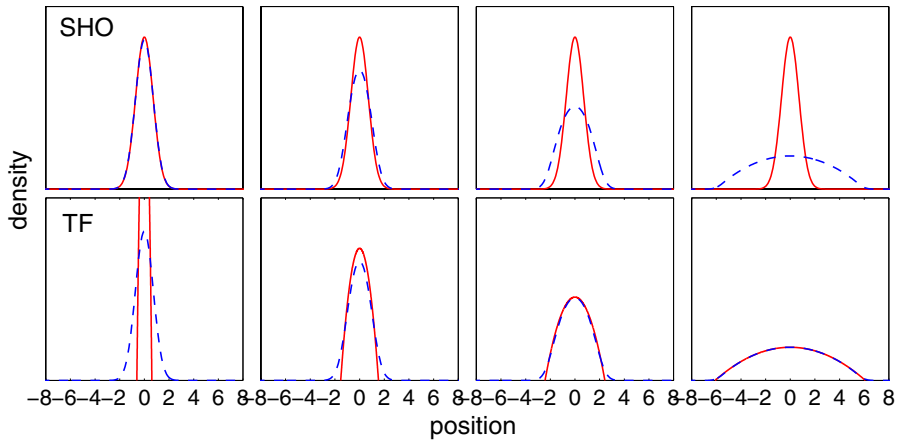

Figure 3.1: The density of the condensate ground state in the one-dimensional model for increasing population. Going from left to right: $N = 10$, 10^3, 10^4, and 10^6. The blue dashed line is the exact numerical solution. The top red solid line is the bare oscillator ground state, while the bottom red solid line is the Thomas-Fermi solution. The position z is in units of l_z. The chemical potentials obtained from the exact solution in each case are $\mu = 0.56$, 1.31, 3.01, and 18.59, while for the Thomas-Fermi solution $\mu_{\rm TF} = 0.19$, 1.17, 2.94, and 18.57. These are given in units of $\hbar\omega_z$. The trap frequencies were taken to be $\nu_z = 65$ Hz and $\nu_{xy} = 24$ Hz, and mass and scattering length were taken for ^{87}Rb.

3.3.3 Numerical solution

We now present results from numerical calculations in order to illustrate the character of the ground state condensate and to demonstrate the two limiting cases of small and large population. We find the ground state solution by propagating the time-dependent GP equation in imaginary time using a finite-difference, Crank-Nicholson method, which we describe in Appendix (C).

One-dimensional case

We first consider the solution of the one-dimensional model given by Eq. (3.12). It is useful to write Eq. (3.12) in dimensionless units, where we take $\hbar\omega_z$ for our unit of energy, $l_z = \sqrt{\hbar/m\omega_z}$ for our unit of position, and $1/\omega_z$ for our unit of time (needed for the time-dependent version of Eq. (3.12)). This rescaling of energy, position, and time can be achieved by setting $\hbar = m = \omega_z = 1$, which yields

$$[-\frac{1}{2}\frac{\partial^2}{\partial z^2} + \frac{1}{2}z^2 + \lambda_{1\rm d}\,|\psi(z)|^2]\,\psi(z) = \mu\,\psi(z), \tag{3.15}$$

where $\lambda_{1\rm d} = 4\pi N\tilde{\alpha}_{1\rm d}(a/l_z)$, and $\tilde{\alpha}_{1\rm d} = \alpha_{1\rm d}l_z^2$.

In Figure 3.1 we show results of a series of calculations of the condensate ground state in which the number of atoms N is varied from $N = 1$ to $N = 10^6$. For each case we plot the density of the bare oscillator ground state, the Thomas-Fermi solution, and the exact numerical solution. We also indicate the chemical potentials for the Thomas-Fermi and exact solutions in the caption. For $N < 10^3$ the Thomas Fermi solution is a poor

approximation, while for $N > 10^4$ the agreement is very good, giving an error of only 2% in the chemical potential for $N = 10^4$ and 0.1% for $N = 10^6$.

The Thomas-Fermi solution is a very good representation of the wave function in the center of the trap, but is a poor description at the very edge of the condensate, where the density is so low that the kinetic energy term in the GP equation can not be neglected [54]. This region at the boundary of the condensate where the density rolls off to zero is called the surface thickness d_s. The surface thickness can be found by setting the potential energy at the surface equal to the kinetic energy associated with the bending of the wavefunction at the surface (i.e. we approximate the Laplacian of ψ as $1/d_s^2$ at the surface). For a spherical trap, these energies take the form $m\omega_0^2 r_{\rm TF}^2$ and $\hbar^2/(2md_s^2)$, respectively. Setting them equal and solving for d_s gives the ratio

$$\frac{d_s}{r_{\rm TF}} = 2^{-1/3}\Big(\frac{l_{\rm sho}}{r_{\rm TF}}\Big)^{4/3}. \tag{3.16}$$

This ratio is small when the Thomas-Fermi approximation is valid.

Two-dimensional case

In a later chapter we consider a two-dimensional model system in which $\omega_x = \omega_y \equiv \omega_{xy}$. As in the above one-dimensional model, it is useful to rewrite Eq. (3.11) in dimensionless units by setting $\hbar = m = \omega_{xy} = 1$, which gives

$$\Big[-\frac{1}{2}\Big(\frac{\partial^2}{\partial x^2} + \frac{\partial^2}{\partial y^2}\Big) + \frac{1}{2}(x^2+y^2) + \lambda_{\rm 2d}|\psi(x,y)|^2\Big]\,\psi(x,y) = \mu\,\psi(x,y), \tag{3.17}$$

where $\lambda_{\rm 2d} = 4\pi N\tilde{\alpha}_{\rm 2d}(a/l_z)$, and $\tilde{\alpha}_{\rm 2d} = \alpha_{\rm 1d} l_z$.

Three-dimensional case

Finally, we consider a three-dimensional solution of Eq. (3.4), where we assume axial symmetry $\omega_x = \omega_y \equiv \omega_{xy}$. The dimensionless form of Eq. (3.4), obtained by setting $\hbar = m = \omega_z = 1$ becomes

$$\Big[-\frac{1}{2}\nabla^2 + \frac{1}{2}\big(\gamma^2\rho^2 + z^2\big) + \lambda|\psi(\boldsymbol{r})|^2\Big]\,\psi(\boldsymbol{r}) = \mu\,\psi(\boldsymbol{r}), \tag{3.18}$$

where $\gamma = \omega_{xy}/\omega_z$ and $\lambda = 4\pi N(a/l_z)$. In Figure 3.2 we show the density of the condensate ground state for this axially symmetric trap, where the population was $N = 10^6$.

In an experiment, it is the column integrated density profile that is measured, so it is useful to represent the solution in this way for more direct comparison to experimental data. In both cases of absorptive or dispersive imaging, the density along the line-of-sight gets spatially averaged in the measurement process. We can take this into account by performing an integration along the y-axis of the solution of Eq. (3.18), for example

$$\tilde{n}(x,z) = \int_{-\infty}^{\infty} dy\,|\psi(x,y,z)|^2. \tag{3.19}$$

We will often represent the solution of either the time-dependent or time-independent GP equation in this column-integrated form in order to compare with experiment. We show an example in Figure 3.3, where we have integrated through the solution shown in Figure 3.2.

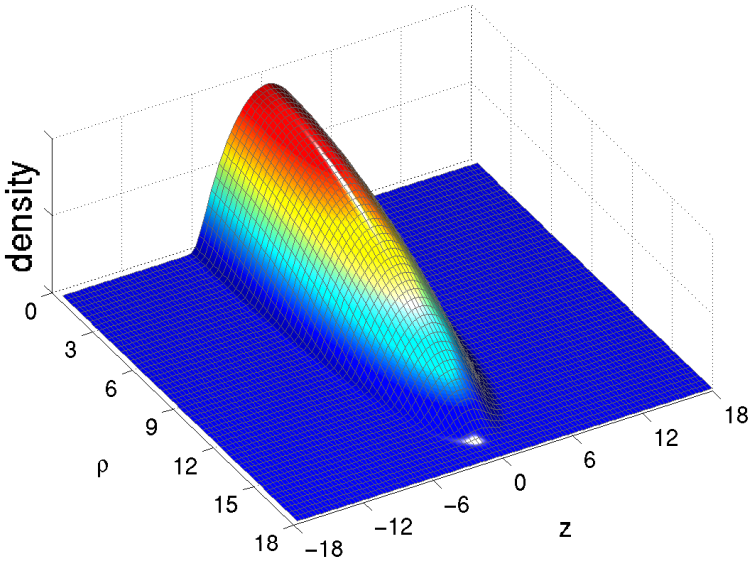

Figure 3.2: The density of the condensate assuming an axially symmetric trap with $\nu_z = 65$ Hz and $\nu_{xy} = 24$ Hz and the population was $N = 10^6$ atoms. Position is given in units of l_z. The solution reflects the tight confinement along the z-axis, compared to the xy plane.

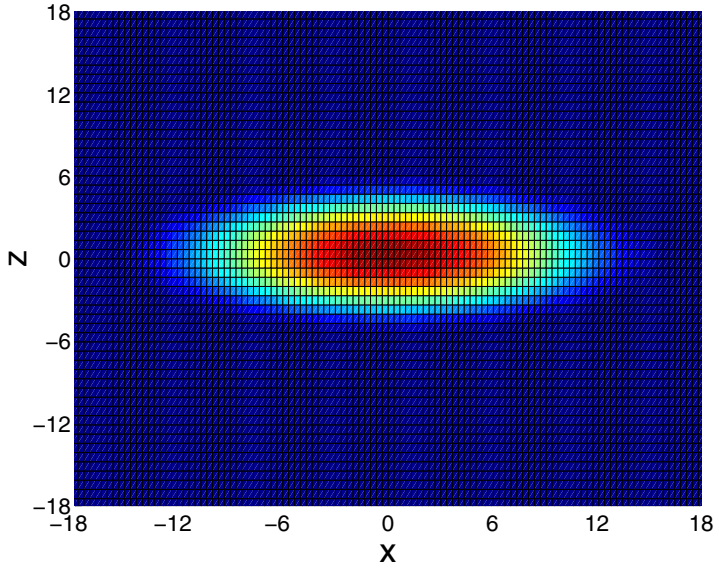

Figure 3.3: The column-integrated density profile for the solution of the condensate ground state shown in Figure 3.2. This mimics how the density would appear on a CCD array in an experiment. With the tighter confinement along the z-axis, the condensate appears as a "pancake".

3.4 Non-ground-state condensates

The time-independent GP equation has many stationary solutions in addition to the nodeless ground state, each of which corresponds to having all of the atoms in a state with an alternative symmetry than that of the ground state. We refer to these states of the condensate as topological modes. One example that is a popular topic of research in the recent literature is a vortex solution, which has quantized angular momentum. Another possible solution is a non-rotating state with odd parity phase behavior along the an axis of symmetry; such a dipole[2] mode has been termed a dark soliton solution. The intriguing aspect of these macroscopically occupied excited modes is that they do not necessarily decay via usual thermal relaxation processes, so that they can be very long-lived. For example, in superfluid helium persistent currents flow unimpeded for as long as one cares to conduct the experiment, while currents in normal liquid helium dissipate on a very short timescale in comparison [16]. In this section we consider some of the basic properties of non-ground-state condensates.

3.4.1 Vortex solution

Let us assume an alternative solution to the GP equation that has the form

$$\psi(\boldsymbol{r}) = \phi_\kappa(\rho, z)e^{i\kappa\phi}, \tag{3.20}$$

where ϕ is the azimuthal coordinate around the z-axis, κ is an integer, and $\phi_\kappa(\rho, z)$ is a real-valued amplitude. This ansatz describes a condensate that has a phase wrap of $2\pi\kappa$ around the z-axis, and thus has angular momentum per particle of $\kappa\hbar$. Substituting this ansatz into the time-independent GP equation Eq. (3.18) yields the following nonlinear Schrödinger equation for $\phi_\kappa(\rho, z)$

$$\Big[-\frac{1}{2}\nabla^2 + \frac{1}{2}\frac{\kappa^2}{\rho^2} + \frac{1}{2}\big(\gamma^2\rho^2 + z^2\big) + \lambda|\psi(\boldsymbol{r})|^2\Big]\,\phi_\kappa(\rho, z) = \mu\,\phi_\kappa(\rho, z). \tag{3.21}$$

The additional centrifugal term $(1/2)(\kappa^2/\rho^2)$ requires the solution to vanish at the origin for $\kappa \neq 0$.

There are two different possible methods for calculating the vortex solution. One way is to solve the ground state of Eq. (3.21), which has the ansatz Eq. (3.20) built in. This gives the amplitude of the solution $\phi_\kappa(\rho, z)$, so that the full solution is $\psi(\boldsymbol{r}) = \phi_\kappa(\rho, z)e^{i\kappa\phi}$. An alternative method is to carry out imaginary time propagation on Eq. (3.17) while forcing the solution to have the correct phase wrap as given by the ansatz Eq. (3.20). This technique is the one we have used and is described in Appendix (C).

We show an example of a vortex solution for the case of one unit of circulation, where we have used the two-dimensional model of the GP equation. In Figure 3.4 we plot the density $|\phi_\kappa(\rho, z)|^2$ and in Figure 3.5 we show the phase. The core of the vortex sits at the origin where the solution vanishes. The size of the vortex core is determined by the healing length ξ (i.e. the scale length for significant density variation), which is set by the balance of the kinetic energy $\hbar^2/(2m\xi^2)$ and the mean-field interaction energy $4\pi\hbar^2 an/m$, where n is the density. Upon setting these two terms equal and solving for ξ, one obtains for the healing length

$$\xi = (8\pi na)^{-1/2}. \tag{3.22}$$

[2]Note that we are using the term *dipole* somewhat loosely here; we are not referring to any specific dipole moment (eg. electric or magnetic), but rather use the term to signify the antisymmetric form of the wavefunction.

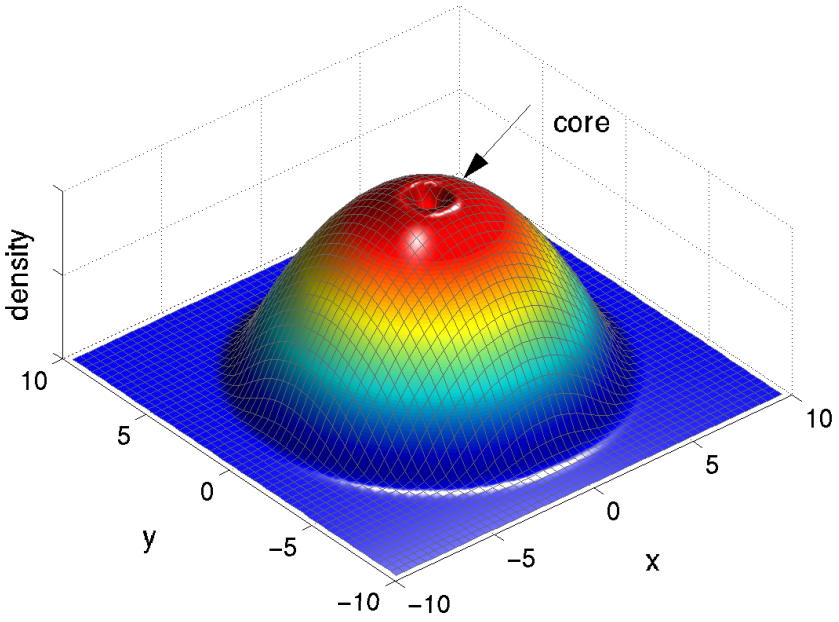

Figure 3.4: A vortex solution to the two-dimensional GP equation, for the case of unit angular momentum. The population is $N = 10^6$, and the trap frequency in the xy plane is $\nu_{xy} = 24$ Hz. Position is given in units of the harmonic oscillator length l_{xy}. The size of the core is very small, and is characterized by the healing length ξ, which is approximately $\xi = l_{xy}/8$ for the solution shown here.

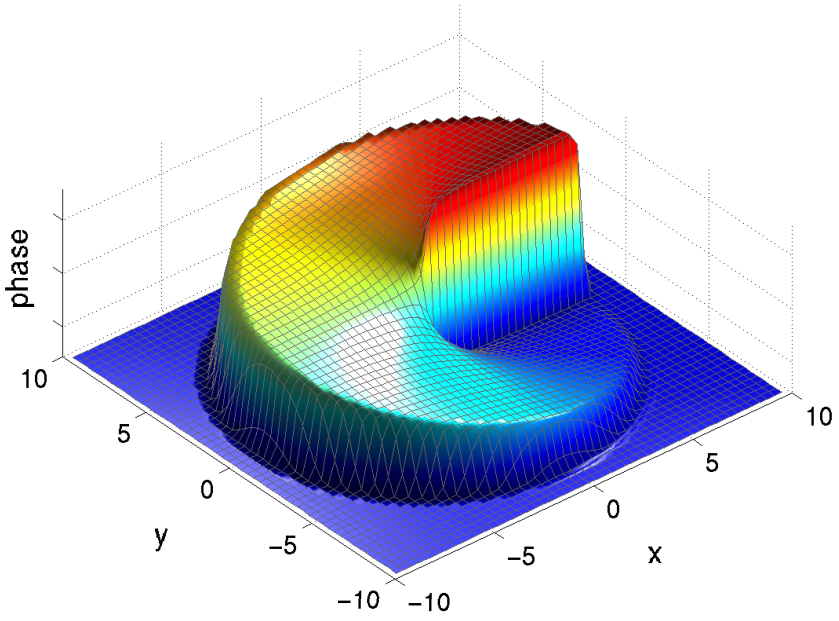

Figure 3.5: The 2π phase wrap of the vortex solution displayed in Figure 4.

Within the Thomas-Fermi limit, an approximation of the healing length is [55]

$$\frac{\xi}{r_{\rm TF}} = \left(\frac{l_{\rm sho}}{r_{\rm TF}}\right)^2, \tag{3.23}$$

where the approximate Thomas-Fermi forms for the central density $n(0)$ and radius $r_{\rm TF}$ were used for the case of a spherical trap.

If the atomic gas is being rotated during the cooling process, it is possible that the energy of the vortex state becomes lower than the ground state energy. In this case, there will be stimulated scattering into a circulating state, so that all of the atoms end up in the vortex [56]. The energy of a system rotating at the angular velocity Ω is $E_\kappa - \Omega L_z$; that is, this is the energy of the vortex mode with angular momentum $L_z = N\kappa\hbar$. When this energy becomes lower than the energy of the non-rotating ground state, condensation can occur in the vortex. This gives us the following value for the critical frequency needed to produce condensation into the vortex

$$\Omega_c = (\hbar\kappa)^{-1}\big[(E_\kappa/N) - (E_0/N)\big], \tag{3.24}$$

where E_0 is the energy of the ground state. This is just the difference in energies between the vortex and ground state. In order for the vortex to occur, the rotation frequency must satisfy $\Omega \geq \Omega_c$. An approximate expression for this quantity has been worked out in the Thomas-Fermi limit for the case of an axially symmetric trap [57]

$$\Omega_c = \frac{5\hbar}{2m\rho_{\rm TF}^2}\ln\left[\frac{0.671\rho_{\rm TF}}{\xi}\right], \tag{3.25}$$

where $\rho_{\rm TF}$ is the Thomas-Fermi radius in the xy plane. For typical values of parameters in the JILA trap, we plot this approximate form of Ω_c as a function of population N in Figure 3.6. As N increases, the splitting between the vortex and ground state decreases, so for one million atoms, the critical frequency is a few hertz.

3.4.2 Non-rotating states

An alternative class of solutions of the time-independent GP equation are those with no circulation. A dipole is one example, which in the Thomas-Fermi limit is referred to as a dark soliton. These solutions can be generated using the method described in Appendix (C) for finding excited states using imaginary time propagation. For example, the first excited state is found by subtracting out the ground state solution in each time step, starting from some appropriately chosen initial guess. Higher excited states can also be found this way. This is essentially the Graham-Schmidt orthogonalization procedure, carried out in each time step during the imaginary time propagation. In the limit of a single atom $N \to 1$, the solutions just go over to the bare Harmonic oscillator eigenstates.

We show examples of these types of solution for the one-dimensional model of Eq. (3.18) in Figure 3.7 for three different values of the principal quantum number $n = 0,\ 1,\ 2$ and for $N = 1,\ 10^4,\ 10^6$. The top row correspond to the bare harmonic oscillator eigenstates. As N increases, the mean-field interaction energy dominates the kinetic energy, so that in regions where the density goes to zero, the size of the node is determined by the healing length, just as in the case of a vortex.

In Figure 3.8 we plot the energy of each of the three states shown in Figure 3.7 as a function the population N. As $N \to 1$, the energies are spaced by $\hbar\omega_z$, corresponding to

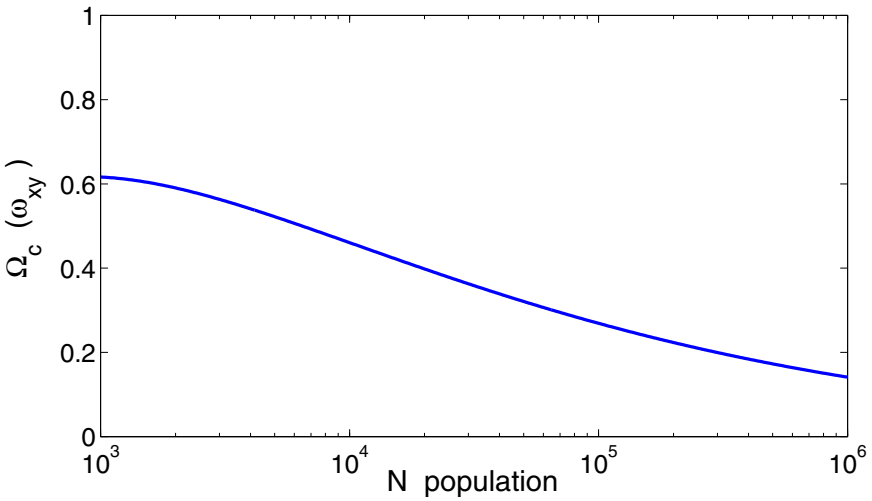

Figure 3.6: The approximate value of the critical frequency Ω_c given by Eq. (3.25), in units of the trap frequency ω_{xy}. For one million atoms in a 24 Hz trap, this frequency is approximately $\Omega_c \approx 3.5$ Hz.

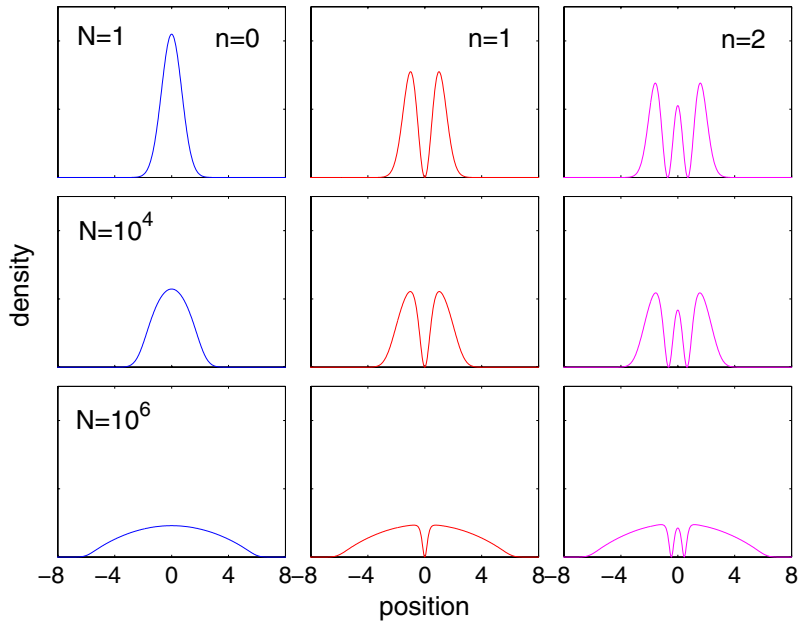

Figure 3.7: The densities of the first three excited states, for increasing population going down each column. In the Thomas-Fermi limit, dark-solitons form at the nodes of the wavefunction, with a size determined by the healing length.

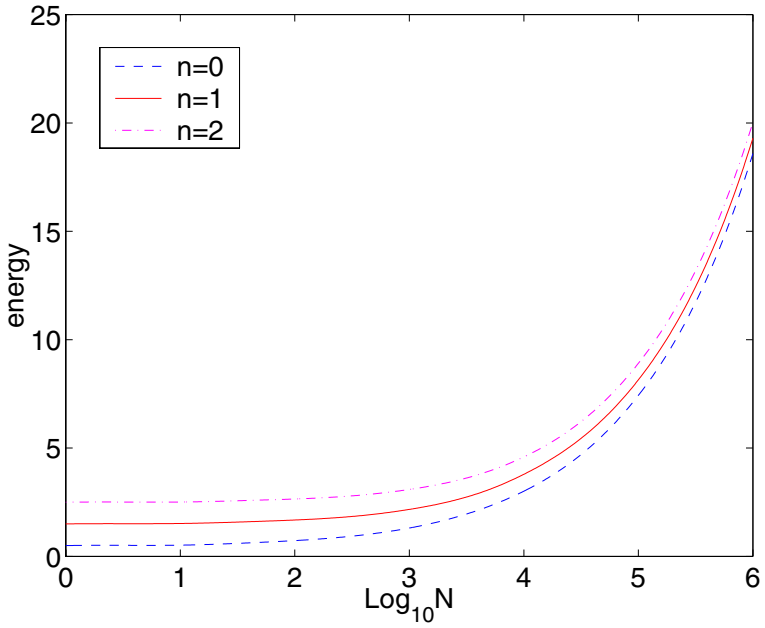

Figure 3.8: The energies of the states plotted in Figure 3.7 vs the population. As N increases, the energies grow due to the mean field interaction, while the spacing between levels decreases, similar to the vortex solution.

the solutions of the harmonic oscillator. As N increases, the energies grow according to Eq. (3.8), and the spacing between levels decreases, just as in the case of the vortex.

In the case of the vortex, it is clear how one can create a situation in which the cooled sample condenses into the rotating state. This could be done by slightly distorting the trap and rotating it at the critical frequency Ω_c during the cooling process, though so far no reports have been made of the experimental observation of a vortex generated in this fashion in a dilute Bose gas. There is no obvious analog for a similar scheme that leads to condensation into a non-rotating excited state. This leads us to the following question: If the condensate is allowed to condense into the nodeless ground state of the system, is there a way to transfer all of the atoms in the condensate from this initial state to a topological mode, such as a vortex or dark-soliton? In the next section we begin to investigate this question by considering the response of the condensate to a harmonic mechanical drive.

3.5 Condensate response to a mechanical drive

The condensate response to an external driving force can be studied in a controlled way in the present BEC experiments [58, 59, 60, 61]. Once a Bose gas has condensed into the ground state, the confining potential can be manipulated by adjusting the magnetic trapping fields, or by shining a laser on the sample to create an optical potential. We first consider the case where a weak harmonic drive is applied and show that the response of the condensate can be decomposed into a sum over the normal modes, which were introduced in Chapter 2. In this way, the elementary excitation spectrum of the condensate can be studied. We also

briefly discuss the nonlinear response of the condensate, and address the question of how to generate a topological mode from an initial ground state condensate.

3.5.1 Linear response

Let us suppose that a weak mechanical drive is applied to the condensate that varies harmonically in time. The condensate equation of motion then takes the form [62]

$$i\hbar\frac{\partial\psi(\boldsymbol{r},t)}{\partial t} = \Big[-\frac{\hbar^2}{2m}\nabla^2 + U(\boldsymbol{r}) + V_0 N\,|\psi(\boldsymbol{r},t)|^2 + f_+(\boldsymbol{r})e^{-i\omega_d t} + f_-(\boldsymbol{r})e^{i\omega_d t}\Big]\,\psi(\boldsymbol{r},t), \tag{3.26}$$

where we have included the mechanical drive described by the amplitudes $f_\pm(\boldsymbol{r})$ oscillating at the frequency ω_d. The full numerical solution of this GP equation describing the driven condensate can be calculated for arbitrary drive strengths. However, if we assume the drive is weak, we can carry out a standard linear response analysis, where we make the ansatz solution [62]

$$\psi(\boldsymbol{r},t) = e^{-i\mu t/\hbar}\big[\phi_0(\boldsymbol{r}) + u(\boldsymbol{r})e^{-i\omega_d t} + v^*(\boldsymbol{r})e^{i\omega_d t}\big]. \tag{3.27}$$

Substituting this into Eq. (3.26), keeping only linear terms in $u(\boldsymbol{r})$, $v(\boldsymbol{r})$, and $f_\pm(\boldsymbol{r})$, and equating like powers of $e^{\pm i\omega_d t}$, we obtain the following three coupled equations [62]

$$\begin{aligned}
\big[H_0 + V_0|\phi_0(\boldsymbol{r})|^2\big]\phi_0(\boldsymbol{r}) &= \mu\,\phi_0(\boldsymbol{r}) \qquad (3.28)\\
\big[H_0 - (\mu+\hbar\omega_d) + 2V_0|\phi_0(\boldsymbol{r})|^2\big]u(\boldsymbol{r}) + V_0\phi_0^2(\boldsymbol{r})v(\boldsymbol{r}) &= -f_+(\boldsymbol{r})\,\phi_0(\boldsymbol{r})\\
\big[H_0 - (\mu-\hbar\omega_d) + 2V_0|\phi_0(\boldsymbol{r})|^2\big]v(\boldsymbol{r}) + V_0\big[\phi_0^*(\boldsymbol{r})\big]^2 u(\boldsymbol{r}) &= -f_-(\boldsymbol{r})\,\phi_0(\boldsymbol{r}),
\end{aligned}$$

where $H_0 = p^2/2m + U(\boldsymbol{r})$. The first line of Eq. (3.29) is simply the time-independent GP equation for the condensate ground state. Upon setting the drive to zero $f_\pm = 0$, the other two lines in Eq. (3.29) reduce to the equations for the normal modes of the system

$$\begin{aligned}
\hat{\mathcal{H}}\,u_j(\boldsymbol{r}) - V_0\,\phi_0^2(\boldsymbol{r})v_j(\boldsymbol{r}) &= \hbar\omega_j\,u_j(\boldsymbol{r}),\\
\hat{\mathcal{H}}\,v_j(\boldsymbol{r}) - V_0\,\big[\phi_0^*(\boldsymbol{r})\big]^2 u_j(\boldsymbol{r}) &= -\hbar\omega_j\,v_j(\boldsymbol{r}),
\end{aligned} \tag{3.29}$$

where $\hat{\mathcal{H}}$ is given by

$$\hat{\mathcal{H}} = -\frac{\hbar^2}{2m}\nabla^2 + U(\boldsymbol{r}) + 2V_0|\phi_0(\boldsymbol{r})|^2 - \mu. \tag{3.30}$$

These equations are identical to the equations Eq. (2.88) and Eq. (2.89) obtained in Chapter 2 for the elementary excitations of the system in the Bogoliubov approximation, obtained by setting the fluctuations $\tilde{f}$ and $\tilde{m}$ to zero. This is not a coincidence, since the Bogoliubov spectrum was also obtained by treating the fluctuations to first order. Of course, higher order corrections, such as the collisional terms discussed in Chapter 2, can not be obtained within the present analysis, since those higher order effects are due to particle correlations unaccounted for in the $T = 0$ limit case approximated by the GP equation.

To complete the analysis, one expands the condensate wavefunction $\psi(\boldsymbol{r})$ and the drive $f(\boldsymbol{r})$ in the normal modes $u(\boldsymbol{r})$ and $v(\boldsymbol{r})$. For an arbitrary weak harmonic drive, the condensate solution in general will consist of many normal modes. However, the drive can be

chosen with a symmetry and drive frequency that preferably excite only one normal mode. This suggests an experimental procedure in which one distorts and modulates the magnetic trapping potential in such a way as to excite a normal mode. By varying the modulation frequency ω_d and measuring the amplitude of oscillation of the condensate, a response curve can be obtained that should be centered on the corresponding collective mode frequency. Several such experiments have been conducted at JILA and MIT [58, 59, 60, 61]. In experiment, damping processes not accounted for in the $T = 0$ Bogoliubov theory give rise to a width of the response curve. These experiments, in which the lowest few collective modes were studied over a range of temperatures, have generated a a large volume of work recently on the study of the elementary excitation spectrum of a trapped Bose-condensed gas (see, for example, the review by Dalfovo et al. [53] and references therein).

Conceptually, it is important to realize that the above analysis (and the related discussion in Chapter 2) can also be applied to a vortex. That is, instead of studying a situation where nearly all of the atoms are in the ground state and a small fraction are participating in a collective excitation about it, one can instead consider having nearly all of the atoms in a vortex solution and studing excitations about that. The corresponding Bogoliubov spectrum can be calculated within the same framework. A great deal of work has also been published recently on this topic and the related issue of vortex stability (see, for example, [63, 64, 65, 66, 67] and references therein).

3.5.2 Excitation of topological modes

Several recent studies have investigated the question raised earlier in section 3.4.2 on the possibility to excite a ground state condensate into a topological mode, such as a vortex, using a mechanical drive [67, 68, 69]. Unlike the case of collective excitations considered above, where effectively very few atoms are excited, in order to produce a condensate in a pure vortex *all* of the atoms must be excited into the same self-consistent mode. Based on recent theoretical studies, as well as experimental efforts, a pure vortex seems difficult to generate using a mechanical drive. In [69], for example, the authors investigated the use of a far-blue-detuned Gaussian laser beam to stir the condensate by numerically solving the GP equation. Typically, such a stirring of the condensate generates rather complex behavior. However, the authors of [69] found a regime where a single vortex core oscillated in and out of the condensate, so that at one point in the cycle, a pure vortex could be formed where the average angular momentum per particle is unity. Related schemes of distorting and rotating the magnetic trap, either with or without an optical potential acting as a pinning mechanism, have been explored experimentally with no observations of a vortex [70, 34].

In trying to understand the process of exciting the condensate from a ground state to a vortex using a mechanical drive, a natural starting point might be to consider the drive as weak and study the linear response of the condensate. As a concrete example, consider the stirring mechanism studied in [69]. The harmonic drive of the stirring beam could be expanded in normal modes, and the condensate solution could also be obtained in terms of the normal modes. Suppose the stirring drive preferentially excited a single normal mode possessing angular momentum, due to its symmetry and rotation frequency. Is it possible to transfer all of the atoms into this mode? An obvious problem is that for linear response to be valid, only a small fraction of the atoms must be excited, since the effect of excitations on the ground state is neglected. Therefore, it would seem that a full nonlinear treatment of the problem is required, which includes the nonlinear terms left out of the linear response analysis. Several research groups have investigated the nonlinear response

of the condensate [71, 62, 72, 73], though not in the context of exciting a pure vortex.

3.6 Summary

In this chapter we have touched upon some of the major themes of zero temperature mean field theory of a single-component Bose-condensate in a dilute trapped gas of atoms. The basic concepts of the condensate ground state, topological excitations, and the elementary excitations about the mean field have been studied extensively in the recent literature in this field; several recent review articles explore these concepts in more detail (see, for example, Dalfovo et al. [53] and references therein). Here we have given only a glimpse of these popular topics, in order to provide a broader context in which to place the specific original work of this thesis. Of particular relevance to this thesis is the question of how to transfer an initial ground-state condensate to a topological mode. In Chapter 6 we will return to this question and present a technique for preparing such a state in a strongly coupled, two-component condensate—a technique that has recently been implemented experimentally at JILA [70], resulting in the first observation of a vortex in a dilute gas BEC.

Chapter 4

Mean-Field Theory of a Coupled Two-Component System

4.1 Introduction

In this chapter we extend the mean-field theory discussed in Chapter 3 for a single component condensate to treat a coupled two component system. We begin by deriving the coupled, two-component GP equation for this system using the formalism developed in Chapter 2. Our main interest in this chapter are the stationary solutions to these equations. We first consider the case of no coupling and we numerically solve for the lowest energy solution of the two-component system. The basic ground-state properties studied will help prepare us for the study of two weakly coupled components presented in Chapter 5. We then present non-ground-state solutions for this system, such as a vortex, as was done in Chapter 3 for the single component system. This topic will resurface in Chapter 6 when we investigate a strongly coupled system. In the last part of this chapter we discuss the lowest energy stationary states of the coupled system, which we refer to as the dressed states.

4.2 The physical system

In the next three chapters we will focus on the basic system studied in experiments conducted at JILA [8, 9, 10, 11, 12, 13] investigating a trapped, Bose-condensed dilute gas of ^{87}Rb atoms, in which two internal hyperfine levels are populated. The atoms in the condensate are in the ground state electronic state, with the hyperfine structure shown in Figure 1. Typically, the $|F = 1, M_F = -1\rangle \equiv |1\rangle$ is trapped and cooled in the usual manner to the condensation point. Once the atoms in $|1\rangle$ have formed in the condensate ground state, a two photon drive can be applied that couples the $|1\rangle$ state to the $|F = 2, M_F = 1\rangle \equiv |2\rangle$ state. That is, microwave and radio-frequency (RF) electro-magnetic fields are applied to the sample. One can describe this two-photon process with as an effective coupling strength $\Omega = \Omega_a \Omega_b / (4\delta_{ab})$, where Ω_a and Ω_b are the Rabi frequencies for the individual transitions, and δ_{ab} is the intermediate state detuning [74, 75, 76]. The frequency of the drive ω_d is just the sum of the frequencies of the two photons. In principle both states could be cooled simultaneously, so that a condensate forms in a mixture of states, however the typical lifetime of atoms in the $|2\rangle$ state is ≈ 300 ms in a $\nu_z = 65$ Hz, $\nu_\rho = 24$ Hz trap due to inelastic

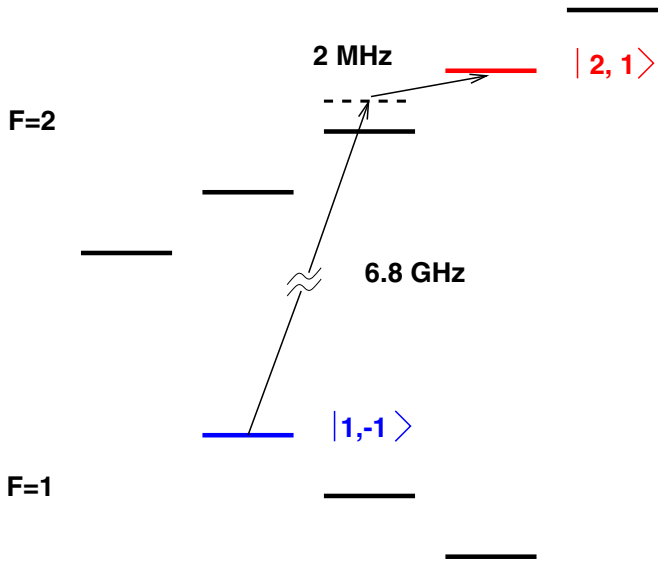

Figure 4.1: Illustration of the ground-state hyperfine levels of ^{87}Rb shown with Zeeman splitting due to the presence of a magnetic field. The two-photon transition is driven between the $|1,-1\rangle$ and $|2,1\rangle$ states.

spin-exchange collisions, which makes achieving runaway evaporation very difficult. In contrast, atoms in the $|1\rangle$ state have a much longer lifetime.

The condensate is confined in a time-averaged orbiting potential (TOP) trap, that consists of a static quadrupole magnetic field and a rotating uniform magnetic field, the combined effect of which generates an approximately harmonic axially symmetric potential with trap frequencies ω_z and ω_{xy} [9]. Due to the slightly different magnetic moments of the two states $|1\rangle$ and $|2\rangle$, as well as a state-dependent force arising from the rotating field [9], the effective potentials for the two states are offset along the vertical axis, as illustrated in 5.1. By varying the quadrupole gradient, and the intensity and frequency of the rotating field, many different trap configurations can be achieved. There are three main configurations we will consider, which consist of an axially symmetric trap with frequencies $\omega_z/2\pi = 65$ Hz, $\omega_{xy}/2\pi = 24$ Hz with the vertical separation being either $0.4\,\mu$m or zero, or a spherically symmetric trap with frequency $\omega_z/2\pi = \omega_{xy}/2\pi = 7.8$ Hz and no separation.

The scattering lengths for binary collisions depend on the internal hyperfine level of the atom. There are three different cases to consider, $|1\rangle|1\rangle \rightarrow |1\rangle|1\rangle$, $|2\rangle|2\rangle \rightarrow |2\rangle|2\rangle$, or $|1\rangle|2\rangle \rightarrow |1\rangle|2\rangle$. We designate the s-wave scattering lengths for each case as a_1, a_2, and a_{12}. For ^{87}Rb it turns out that the values of these three quantities are nearly degenerate, with the ratios $\{a_2 : a_{12} : a_1\} = \{0.97 : 1 : 1.03\}$[10]. The different scattering lengths effect the condensate through the mean-field interaction potential, as we show below.

4.3 Derivation of the coupled two-component GP equation

In Chapter 2 we derived the quantum kinetic equations for the mean field and fluctuations, Eq. (2.70) through Eq. (2.72), which are generally true for atoms possessing internal structure. We now write out explicitly the generalization of the Gross-Pitaevskii equation to treat the case of a coupled, two-component system, by setting the fluctuations to zero $\tilde{f} = \tilde{m} = 0$ in Eq. (2.70) and projecting $|\psi(t)\rangle$ onto the position vector $|\boldsymbol{r}\rangle$ and an internal state vector $|\alpha\rangle$. Upon setting the fluctuations to zero, Eq. (2.70) becomes

$$i\hbar\frac{d}{dt}\,|\psi(t)\rangle = \big(H_0 + 1\,U_{f^{(c)}}\big)\,|\psi(t)\rangle \tag{4.1}$$

We define the amplitude $\psi_\alpha(\boldsymbol{r},t) = \langle \boldsymbol{r},\alpha|\psi(t)\rangle$, with $\alpha = 1,2$. The matrix elements of H_0 can be found from Eq. (2.22) and are

$$\langle \boldsymbol{r},\alpha|H_0|\boldsymbol{r}',\beta\rangle = \Big[\Big(-\frac{\hbar^2}{2m}\nabla^2 + U_\alpha(\boldsymbol{r}) + \epsilon_\alpha\Big)\delta_{\alpha\beta} + H^{\rm d}_{\alpha\beta}(t)\Big]\,\delta^3(\boldsymbol{r}-\boldsymbol{r}'). \tag{4.2}$$

We take the driving field $H^{\rm d}(t)$ to have the specific form

$$H^{\rm d}(t) = \Omega\cos(\omega_d t)\big(\,|1\rangle\langle 2| + |2\rangle\langle 1|\,\big), \tag{4.3}$$

where we have assumed Ω to be real. The matrix elements of the mean-field interaction can be found from Eq. (2.24) and are

$$\langle \boldsymbol{r},\alpha|U_{f^{(c)}}|\boldsymbol{r}',\beta\rangle = V_{\alpha\beta}\,|\psi_\alpha(\boldsymbol{r})|^2\,\delta^3(\boldsymbol{r}-\boldsymbol{r}'), \tag{4.4}$$

with the interaction strength given as $V_{\alpha\beta} = 4\pi\hbar^2 a_{\alpha\beta}/m$.

With these matrix elements defined, we project Eq. (4.1) on to $\langle \boldsymbol{r},\alpha|$ and expand the operators in this basis to obtain the two coupled equations

$$\begin{aligned}
i\hbar\dot{\psi}_1(\boldsymbol{r},t) &= \Big[-\frac{\hbar^2}{2m}\nabla^2 + U_1(\boldsymbol{r}) + \epsilon_1 + V_1|\psi_1(\boldsymbol{r},t)|^2 + V_{12}|\psi_2(\boldsymbol{r},t)|^2\Big]\psi_1(\boldsymbol{r},t)\\
&+ \Omega\cos(\omega_d t)\psi_2(\boldsymbol{r},t)\\
i\hbar\dot{\psi}_2(\boldsymbol{r},t) &= \Big[-\frac{\hbar^2}{2m}\nabla^2 + U_2(\boldsymbol{r}) + \epsilon_2 + V_2|\psi_1(\boldsymbol{r},t)|^2 + V_{12}|\psi_1(\boldsymbol{r},t)|^2\Big]\psi_2(\boldsymbol{r},t)\\
&+ \Omega\cos(\omega_d t)\psi_1(\boldsymbol{r},t).
\end{aligned} \tag{4.5}$$

Here, $V_1 = V_{11}$ and $V_2 = V_{22}$. Since we are focussed on the experimental situation described in references [8, 9, 10, 11, 12, 13], we take the following specific form for the trapping potentials

$$\begin{aligned}
U_1(\boldsymbol{r}) &= \frac{1}{2}m\Big[\omega_{xy}^2\rho^2 + \omega_z^2\big(z-z_0\big)^2\Big],\\
U_2(\boldsymbol{r}) &= \frac{1}{2}m\Big[\omega_{xy}^2\rho^2 + \omega_z^2\big(z+z_0\big)^2\Big].
\end{aligned} \tag{4.6}$$

These describe cylindrically symmetric harmonic traps that are displaced by $2z_0$ along the vertical axis.

It is useful to write Eq. (4.5) in a more compact form as

$$\begin{aligned} i\,\dot{\psi}_1 &= [H_1^0 + H_1^{\rm MF} - \frac{\omega_{\rm hf}}{2}]\,\psi_1 + \Omega\cos(\omega_d\,t)\psi_2, \\ i\,\dot{\psi}_2 &= [H_2^0 + H_2^{\rm MF} + \frac{\omega_{\rm hf}}{2}]\,\psi_2 + \Omega\cos(\omega_d\,t)\psi_1, \end{aligned} \tag{4.7}$$

which is written in dimensionless units from setting $\hbar = m = \omega_z = 1$. We have defined the hyperfine splitting between the two levels as $\hbar\omega_{\rm hf} = \epsilon_2 - \epsilon_1$ and reset the zero-point energy between the two states. Our notation has been made more compact by defining the quantities H_i^0 and $H_i^{\rm MF}$ as

$$\begin{aligned} H_i^0 &= -\frac{1}{2}\nabla^2 + \frac{1}{2}[\alpha^2\rho^2 + (z+\gamma_i\,z_0)^2] \\ H_i^{\rm MF} &= \lambda_{ii}|\psi_i|^2 + \lambda_{ij}|\psi_j|^2\,, \end{aligned} \tag{4.8}$$

where $\gamma_1 = -1$, $\gamma_2 = 1$, and $\alpha = \omega_{xy}/\omega_z$ gives the aspect ratio of the trap. We have defined the mean-field interaction strength now as $\lambda_{ij} = 4\pi N(a_{ij}/l_z)$ (with $a_{ii} \equiv a_i$ and $\lambda_{ii} \equiv \lambda_i$). This is consistent with the following normalization

$$\int (|\psi_1|^2 + |\psi_2|^2) d^3r = 1. \tag{4.9}$$

The coupled equations in Eq. (4.7) can be simplified somewhat by making a unitary transformation given by

$$U = e^{i\frac{\omega_d}{2}t\hat{\sigma}_z}, \tag{4.10}$$

where $\hat{\sigma_z}$ is a standard Pauli matrix. We make the rotating wave approximation by neglecting counter rotating terms, which gives us the following coupled equations

$$i\begin{pmatrix}\dot{\psi}_1\\ \dot{\psi}_2\end{pmatrix} = \begin{pmatrix} H_1^0 + H_1^{\rm MF} + \delta/2 & \Omega/2 \\ \Omega/2 & H_2^0 + H_2^{\rm MF} - \delta/2\end{pmatrix}\begin{pmatrix}\psi_1\\ \psi_2\end{pmatrix}\,, \tag{4.11}$$

The detuning δ is the difference in frequencies between the driving field and the hyperfine transition $\delta = \omega_d - \omega_{\rm hf}$. This is the main result of our derivation, which will serve as the starting point as we consider the particular cases of weak and strong coupling in Chapters 5 and 6, respectively.

4.4 Uncoupled two-component system

We begin by considering the case where there is no field coupling the two states, but assume that the system has been prepared with population in both states, given by N_1 and N_2 for states $|1\rangle$ and $|2\rangle$ respectively, with $N = N_1 + N_2$. The GP equations describing this uncoupled two-component system is obtained from Eq. (4.11) by setting the driving field parameters to zero, $\Omega = \delta = 0$, to give

$$\begin{aligned} i\,\dot{\psi}_1 &= [-\frac{1}{2}\nabla^2 + \frac{1}{2}(\alpha^2\rho^2 + (z-z_0)^2) + \lambda_1|\psi_1|^2 + \lambda_{12}|\psi_2|^2]\,\psi_1, \\ i\,\dot{\psi}_2 &= [-\frac{1}{2}\nabla^2 + \frac{1}{2}(\alpha^2\rho^2 + (z+z_0)^2) + \lambda_2|\psi_2|^2 + \lambda_{12}|\psi_1|^2]\,\psi_2, \end{aligned} \tag{4.12}$$

where we have suppressed the time and position variables in the wavefunctions. The offset between the two traps along the vertical axis is given by $2z_0$. With two different states present in the condensate, an additional mean-field interaction term appears in each equation proportional to the inter-species scattering length a_{12} and the density of the other state. This term provides a motional coupling between the two states.

4.4.1 Ground state properties

The time-independent GP equations describing the stationary state of the two-component condensates are

$$\begin{aligned}
[-\frac{1}{2}\nabla^2 + \frac{1}{2}(\alpha^2\rho^2 + (z-z_0)^2) + \lambda_1|\psi_1|^2 + \lambda_{12}|\psi_2|^2]\,\psi_1 &= \mu_1\psi_1, \\
[-\frac{1}{2}\nabla^2 + \frac{1}{2}(\alpha^2\rho^2 + (z+z_0)^2) + \lambda_2|\psi_2|^2 + \lambda_{12}|\psi_1|^2]\,\psi_2 &= \mu_2\psi_2,
\end{aligned} \tag{4.13}$$

where μ_1 and μ_2 are the chemical potentials of the two components. As already mentioned, throughout this thesis we will focus on ^{87}Rb, for which the scattering lengths are nearly degenerate. In some cases, we will make the approximation $a_1 = a_2 = a_{12}$. In this case, the mean-field interaction terms become $(\lambda_i|\psi_i|^2 + \lambda_{ij}|\psi_j|^2) \rightarrow \lambda_{ij}n_{\rm tot}$, where $n_{\rm tot} = (|\psi_1|^2 + |\psi_2|^2)$ is the total density. In the case of concentric traps ($z_0 = 0$), the time-independent GP equations Eq. (4.13) become identical for both states

$$[-\frac{1}{2}\nabla^2 + \frac{1}{2}(\alpha^2\rho^2 + z^2) + \lambda_{12}n_{\rm tot}]\,\psi_i = \mu\,\psi_i, \tag{4.14}$$

so that regardless of the population difference between states, the chemical potential, and therefore the overall size, of each component is identical. In the opposite limit of traps separated by a large distance $z_0 \gg r_{\rm TF}$, the two components act independently of one another, and the two equations in Eq. (4.13) become spatially decoupled, with $n_{\rm tot} \rightarrow n_i$ for each component. In the following section, we illustrate these points by solving Eq. (4.13) directly for various cases and we will show the role played by the trap separation z_0 and the population difference $N_1 - N_2$.

In order to get a better understanding of these properties, we now show results of numerical calculations of Eq. (4.13). Here we use the one-dimensional model of the system, where we have used the interspecies scattering length a_{12} and the total population N in the scaling factors discussed in the Chapter 3. The one-dimensional model of Eq. (4.13) is

$$\begin{aligned}
[-\frac{1}{2}\frac{\partial^2}{\partial z^2} + \frac{1}{2}(z-z_0)^2 + \tilde{\lambda}_1|\psi_1|^2 + \tilde{\lambda}_{12}|\psi_2|^2]\,\psi_1 &= \mu_1\psi_1, \\
[-\frac{1}{2}\frac{\partial^2}{\partial z^2} + \frac{1}{2}(z+z_0)^2 + \tilde{\lambda}_2|\psi_2|^2 + \tilde{\lambda}_{12}|\psi_1|^2]\,\psi_2 &= \mu_2\psi_2,
\end{aligned} \tag{4.15}$$

where we have put a tilde over the scattering length factors to remind us that these have been rescaled according to $\tilde{\lambda}_{ij} = 4\pi N\tilde{\alpha}_{\rm 1d}(a_{ij}/l_z)$, as discussed in the previous chapter. In what follows, we do not vary the scattering lengths, but fix them to the appropriate values for ^{87}Rb. One could, on the other hand, take these as free parameters and investigate how the ground state properties depend on a_1, a_2, and a_{12} [30, 31, 32].

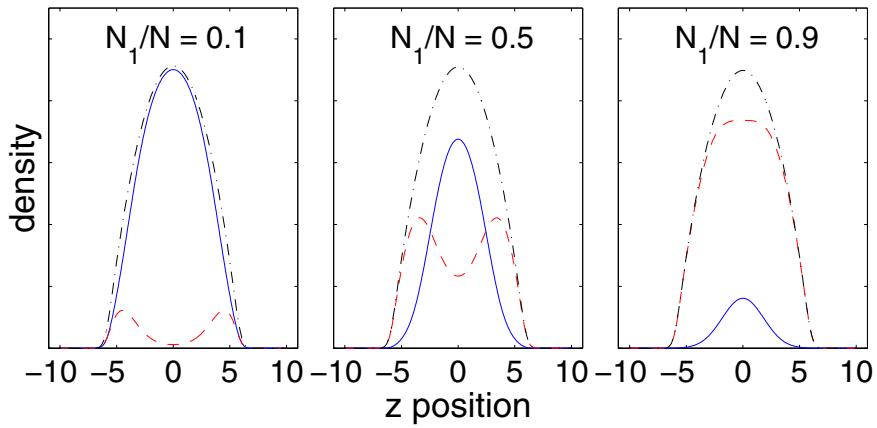

Figure 4.2: The density of the ground state solution for the two component system for zero trap displacement $z_0 = 0$. We vary the population difference while keeping the total population fixed. The blue solid line is the density of the $|2\rangle$ atoms, the red dashed line is that of the $|1\rangle$ atoms, and the black dot-dashed line is the total density. Position is in units of the oscillator length l_z. The population is $N = 10^6$ atoms and the trap frequency is $\nu_z = 65$ Hz.

Varying $\mathbf{N_1 - N_2}$ with $\mathbf{z_0 = 0}$

In Figure 4.2 we plot the ground state solution to the two-component GP equation for three different values of the population difference for the case of $z_0 = 0$. The most obvious feature of the solution is that the $|2\rangle$ atoms, which have the smaller scattering length, sit in the center while the $|1\rangle$ atoms are pushed to the outside. This feature is a consequence of the particular values of the scattering lengths for ^{87}Rb: it is energetically favorable for the $|1\rangle$ atoms to spread out due to their larger scattering length. Another feature is that the total density is very nearly preserved as the population difference is varied.

Varying $\mathbf{z_0}$ with $\mathbf{N_1 = N_2}$

In Figure 4.3 we plot the solution for four different values of the trap spacing. The key point is that only a very small trap displacement is needed to completely change the character of the solution. For the case of one million atoms considered here, the Thomas-Fermi radius is approximately $r_{\rm TF}/l_z = 6$. This means that a trap displacement less than $1/100$ the size of the condensate is enough to cause the components to separate along the z-axis. The overlap of the two components decreases as z_0 is increased, until they no longer overlap at all in the last plot where $z_0/l_z = 5$ is nearly equal to the Thomas-Fermi radius.

Varying $\mathbf{N_1 - N_2}$ with $\mathbf{z_0 = 0.15}$

Another important property of the ground state solution of the two-component system is that the overlap between the two components is nearly constant as the population difference is varied, with fixed trap separation z_0. In Figure 4.4 we demonstrate this by showing the densities of the two components for three different values of the the relative population.

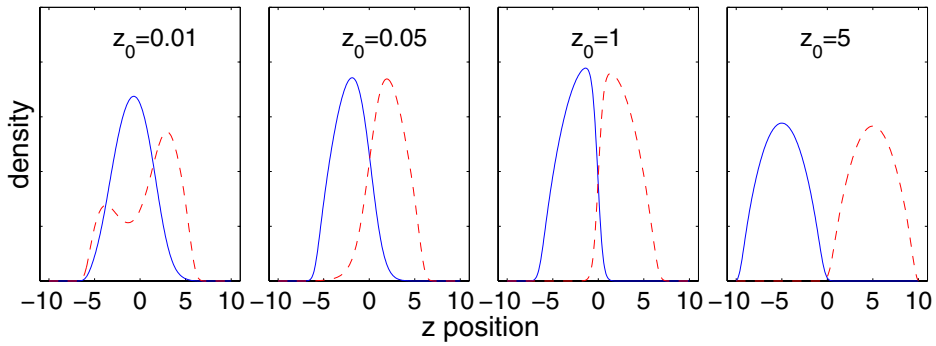

Figure 4.3: The ground state solution of the two-component system as a function of trap separation z_0, which is given in units of the oscillator length l_z. In this case the populations are equal $N_1 = N_2$. The blue solid line is the density of the $|2\rangle$ atoms and the red dashed line is that of the $|1\rangle$ atoms.

The component with the larger population (the $|1\rangle$ atoms in this case) pushes the other component away. The center of the region of overlap changes, but the overall area is nearly constant. Also note that the total density is nearly preserved as the population difference is varied.

We can demonstrate this behavior in a more quantitative manner by calculating the overlap between components as a function of the population difference. We define the overlap ζ as

$$\zeta = \int dz\, \psi_1(z)\psi_2(z). \tag{4.16}$$

In Figure 4.5 we plot the overlap ζ vs the population fraction in the $|1\rangle$ state. The overlap is nearly constant, with the largest variation occurring for larger values of the population fraction N_1/N.

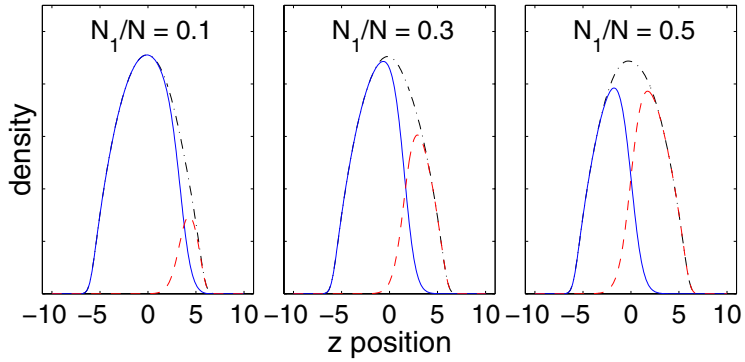

Figure 4.4: The solution with the trap separation fixed at $z_0 = 0.15$ while varying the population difference.

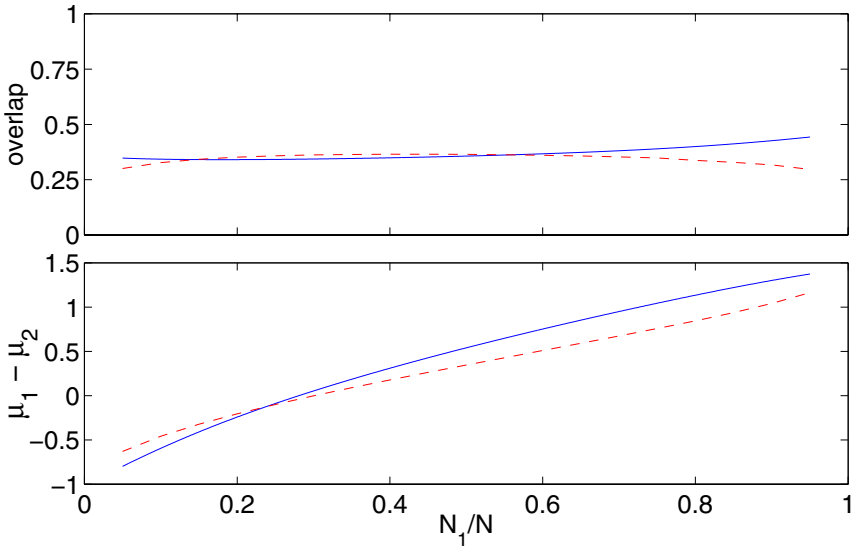

Figure 4.5: The wavefunction overlap ζ of the two components in the ground state (top graph) and the difference in chemical potentials, vs the population fraction in the $|1\rangle$ state N_1/N. The blue solid lines are obtained from the one dimensional model, and the red dashed lines are obtained from the full three dimensional solution. The trap separation is fixed at $z_0 = 0.15$.

In the bottom graph of Figure 4.5 we plot the difference in chemical potentials $\mu_1 - \mu_2$ vs N_1/N. The difference $\mu_1 - \mu_2$ is approximately a linear function of the population fraction. Also note that for equal populations, $\mu_1 - \mu_2 > 0$, which is due to the larger scattering length of $|1\rangle$. We will return to these observations in the next chapter, where we consider the case of two coherently coupled components.

It is useful to compare our one-dimensional model to the three-dimensional solution of Eq. (4.13). In Figure 4.6 we show the column-integrated density of the full three-dimensional solution for the case of equal populations and a trap separation of $z_0/l_z = 0.15$. In Figure 4.5 we plot the overlap

$$\zeta = \int d^3r\, \psi_1(\rho, z)\psi_2(\rho, z), \tag{4.17}$$

and the difference in chemical potentials $\mu_1 - \mu_2$, vs the population fraction N_1/N. The overlap ζ calculated for the one-dimensional model gives very good agreement, while the difference in chemical potentials has an overall offset compared to the three-dimensional solution. However, the slopes of the lines are nearly the same.

4.4.2 Non-ground-state two-component condensates

It is useful now to consider the situation where one of the components is not in a ground state, but possesses an alternative symmetry, like the vortex and dark-soliton solutions considered in Chapter 3 for the single component system. As one might expect, these solutions

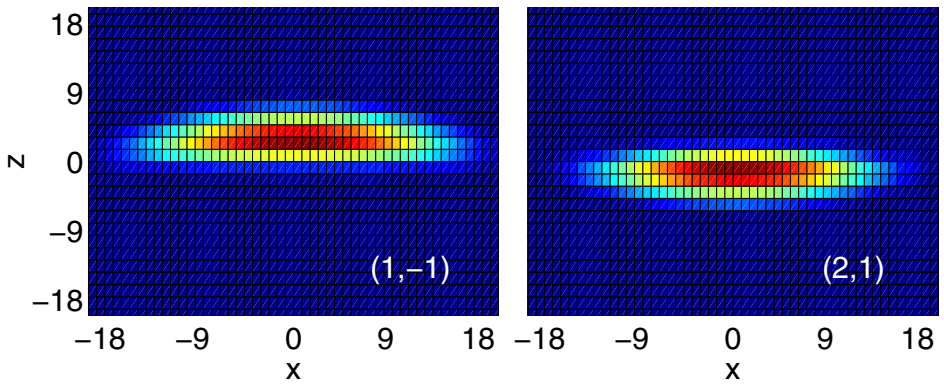

Figure 4.6: The column-integrated densities of each component for the full three-dimensional ground state solution of the two-component system, assuming axial symmetry with $\nu_z = 65$ Hz and $\nu_{xy} = 24$ Hz for one million atoms and equal populations in each component. The trap separation is $z_0/l_z = 0.15$, which corresponds to the case shown in the last graph of Figure 4.4.

have markedly different properties than their single-component counterpart related to the additional mean-field interaction term between the two components.

Vortex solution

We begin by considering the case where one component ψ_j is in a vortex while the other ψ_i remains in the nodeless ground state. We therefore make the ansatz

$$\begin{aligned} \psi_i(\boldsymbol{r}) &= \phi_0(\rho, z), \\ \psi_j(\boldsymbol{r}) &= \phi_\kappa(\rho, z) e^{i\kappa\phi}, \end{aligned} \tag{4.18}$$

where ϕ is the azimuthal coordinate around the z-axis, κ is an integer, and $\phi_\kappa(\rho, z)$ is a real-valued amplitude. This ansatz describes one component that has a phase wrap of $2\pi\kappa$ around the z-axis, and thus has angular momentum per particle of $\kappa\hbar$, while the other is a nodeless ground state. With this ansatz we find the lowest energy two-component state of the system using the imaginary-time propagation technique described in Appendix (C).

In Figure 4.7 we show the solution of this case using the two-dimensional model. We have set the scattering lengths equal in this calculation. We will consider the effect of different scattering lengths in the next section for the case of a dipole solution. The vortex shown in Figure 4.7 has a much larger core than that shown in Chapter 3 in Figure 3.4. For the case of two-components, the repulsive mean-field interaction between components has a dramatic effect on the shape of each component: the vortex core is much larger than the healing length of a single component condensate and the ground state is "pinched" by the vortex.

In Figure 4.8 we plot the chemical potentials of each component as a function of the population fraction in the ground state. Remarkably, the splitting between the vortex and ground state remains roughly constant for quite a range of N_0/N, and increases sharply as N_0/N goes to zero. The splitting is a mere fraction of $\hbar\,\omega_{xy}$ due to the large spatial scale of the excitation in terms of the size of the harmonic oscillator ground state.

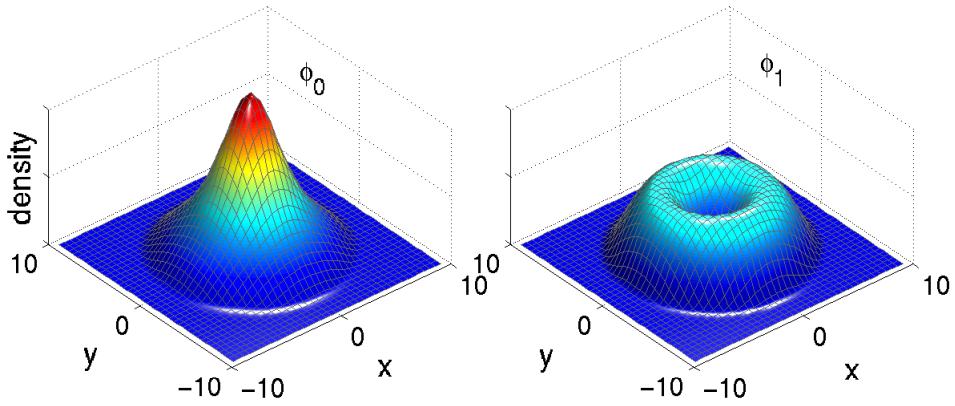

Figure 4.7: The solution to the time-independent GP equation for the case where one of the components is in a vortex with unit angular momentum per atom, while the other component is in the nodeless ground state. Here we have set the scattering lengths all equal to a_{12}, and taken concentric traps $z_0 = 0$. The components have equal population with the total population being $N = 10^6$. Position is in units of the oscillator length l_{xy} and the trap frequency was $\nu_{xy} = 8$ Hz.

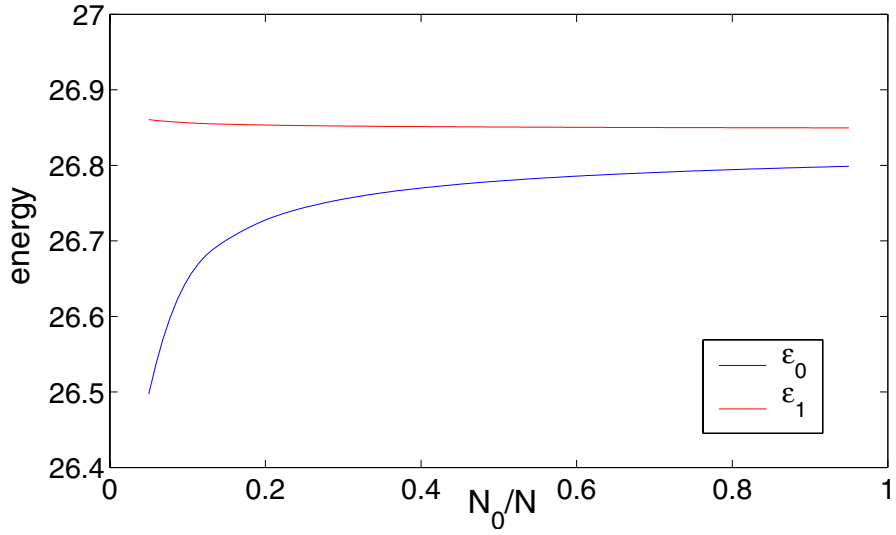

Figure 4.8: The chemical potentials of each component as a function of the population fraction in the ground state. Energy is in units of $\hbar\,\omega_{xy}$. We have set the scattering lengths all equal in this calculation.

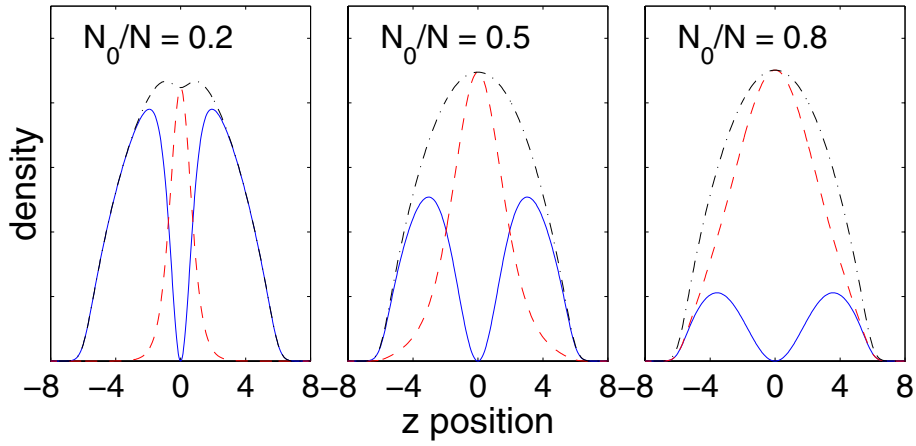

Figure 4.9: The solution of the case where one component is in the ground state, while the other has a dipole symmetry. For this calculation we took equal scattering lengths. The trap frequency was $\nu_z = 65$ Hz and the total population was $N = 10^6$.

Non-rotating states

We now consider the possibility of having one of the components ψ_j in a dipole mode, while the other ψ_i is in a ground state, which is described by the ansatz

$$\begin{aligned} \psi_i(\boldsymbol{r}) &= \phi_0(\rho, z), \\ \psi_j(\boldsymbol{r}) &= \frac{z}{|z|}\phi_1(\rho, z), \end{aligned} \tag{4.19}$$

In this ansatz we are forcing the component $\psi_j(\boldsymbol{r})$ to be an antisymmetric function along the z-axis by multiplying the solution times $z/|z|$; for $z < 0$ the wavefunction has a phase of π and for $z > 0$ the phase is 0. The other component $\psi_i(\boldsymbol{r})$ is just a nodeless ground state. With this ansatz we find the lowest energy two-component state of the system using the imaginary-time propagation technique described in Appendix (C).

In Figure 4.9 we show the solution of the one-dimensional model for three different values of the population fraction in the ground state N_0/N. Just as in the case of the vortex, the mean-field interaction between components has a large effect on the shape of the densities. This effect depends on the relative population: as N_0/N decreases, the size of the core shrinks, as it must in the limit that all of the atoms are in the dipole.

We plot the chemical potentials of each component as a function of the population fraction in the ground state N_0/N in Figure 4.10. We show three different cases of equal scattering lengths, or unequal scattering lengths with the $|1\rangle$ or $|2\rangle$ atoms in the ground state. For equal scattering lengths, the chemical potentials behave similarly as in Figure 4.8 for the vortex solution, however in this case the splitting decreases much more rapidly as N_0/N is decreased. The second plot corresponds to the case where the $|1\rangle$ atoms are in the ground state. Due the the larger scattering length of the $|1\rangle$ atoms $a_1 > a_2$, this configuration becomes unstable, as indicated by the level crossing. In the third plot, it is the $|2\rangle$ atoms that are in the ground state; this situation is energetically stable.

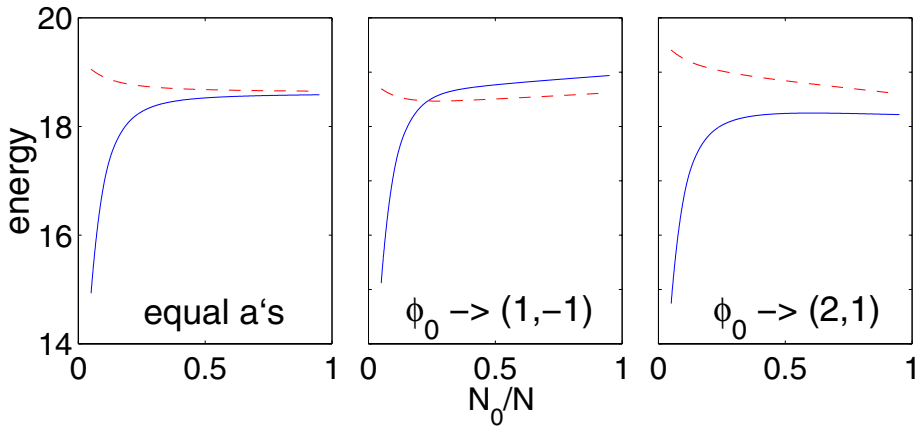

Figure 4.10: The chemical potentials of the two components vs. the population fraction N_0/N for three different cases: equal scattering lengths or unequal scattering lengths with the $|1\rangle$ atoms in the ground state or the $|2\rangle$ atoms in the ground state. Energy is given in units of $\hbar\omega_z$. The blue solid line is the ground state and the red dashed line is the dipole mode.

4.5 Coupled two-component system

We now consider the case where an external field is applied that couples the two internal states of the atoms. In this section we calculate the eigenstates of the coupled system, often referred to as the dressed states. We classify the behavior of this system into two classes, based on the strength of the coupling Ω and we will consider in detail the separate cases of weak and strong coupling in the next two chapters. We consider the coupling to be weak if the Rabi frequency is much less than the frequency of the harmonic trapping potential $\Omega << \omega_z$, so that the spatial dynamics occur on a faster time scale than the internal dynamics in this case. In other words, the densities and currents of the two components adjust instantly to the transfer of atoms on the time scale of the Rabi oscillations. In the next chapter we will consider this limit, which resembles the Josephson junction in condensed matter physics. In the opposite limit of strong coupling $\Omega >> \omega_z$, the Rabi oscillations of the internal levels occur on a much shorter time than the motional dynamics. This separation of time scales will allow us to simplify the description and consider some very novel behavior in Chapter 6.

4.5.1 External $\otimes$ internal representation

The coupled mean-field equations Eq. (4.11) can be rewritten in a more illuminating form by making a clear separation of the external and internal degrees of freedom. The system exists in a direct-product Hilbert space $\mathcal{H} = H_{\rm ex} \otimes H_{\rm in}$, where $\mathcal{H}_{\rm ex}$ is the infinite-dimensional Hilbert space describing the motional state of the system in the trap and $\mathcal{H}_{\rm in}$ is the two-dimensional Hilbert space describing the spin of the system. A general operator in $\mathcal{H}$ can be written as a sum over the direct-product of operators from $\mathcal{H}_{\rm ex}$ and $\mathcal{H}_{\rm in}$. We

rewrite Eq. (4.11) in this representation as

$$i\frac{\partial}{\partial t}|\psi(t)\rangle = [\hat{H}_0 \otimes \hat{1} + \hat{1} \otimes (\frac{\Omega}{2}\,\hat{\sigma}_x + \frac{\delta}{2}\hat{\sigma}_z) + \hat{H}_z \otimes \hat{\sigma}_z]|\psi(t)\rangle \tag{4.20}$$

where $\{\hat{\sigma}_x, \hat{\sigma}_y, \hat{\sigma}_z\}$ are the standard Pauli spin matrices and $\hat{1}$ is the identity operator. The state of the system $|\psi(t)\rangle$ in general has a nonzero projection on the internal states $|1\rangle$ and $|2\rangle$, represented by $\psi_i(\boldsymbol{r}, t) = \langle \boldsymbol{r}|\langle i|\psi(t)\rangle$, where $i = \{1, 2\}$. The position representations of $\hat{H}_0$ and $\hat{H}_z$ are local, i.e. $\langle \boldsymbol{r}|\hat{H}_0|\boldsymbol{r}'\rangle = H_0(\boldsymbol{r})\,\delta(\boldsymbol{r} - \boldsymbol{r}')$ and $\langle \boldsymbol{r}|\hat{H}_z|\boldsymbol{r}'\rangle = H_z(\boldsymbol{r})\,\delta(\boldsymbol{r} - \boldsymbol{r}')$, where $H_0(\boldsymbol{r})$ and $H_z(\boldsymbol{r})$ are given by

$$\begin{aligned} H_0(\boldsymbol{r}) &= -\frac{1}{2}\nabla^2 + \frac{1}{2}[\alpha^2\rho^2 + z^2] + \langle\psi(t)|\hat{P}_{\boldsymbol{r}} \otimes \hat{\lambda}_+|\psi(t)\rangle\ , \\ H_z(\boldsymbol{r}) &= -z_0\, z + \langle\psi(t)|\hat{P}_{\boldsymbol{r}} \otimes \hat{\lambda}_-|\psi(t)\rangle\ . \end{aligned} \tag{4.21}$$

The operator $\hat{P}_{\boldsymbol{r}}$ is the projector onto the position eigenstates $\hat{P}_{\boldsymbol{r}} = |\boldsymbol{r}\rangle\langle\boldsymbol{r}|$, and the matrix representations of $\hat{\lambda}_+$ and $\hat{\lambda}_-$ are given as

$$\begin{aligned} \hat{\lambda}_+ &= \frac{1}{2}\begin{pmatrix} \lambda_1 + \lambda_{12} & 0 \\ 0 & \lambda_2 + \lambda_{12} \end{pmatrix}\ , \\ \hat{\lambda}_- &= \frac{1}{2}\begin{pmatrix} \lambda_1 - \lambda_{12} & 0 \\ 0 & \lambda_{12} - \lambda_2 \end{pmatrix}\ . \end{aligned} \tag{4.22}$$

Note that the harmonic potential in $\hat{H}_0$ is centered at the origin. The mean-field interaction has been broken into two parts, a part that acts identically on both components $\langle\psi|\hat{P}_{\boldsymbol{r}} \otimes \hat{\lambda}_+|\psi\rangle \otimes \hat{1}$, and a part that acts with the opposite sign on each state $\langle\psi|\hat{P}_{\boldsymbol{r}} \otimes \hat{\lambda}_-|\psi\rangle \otimes \hat{\sigma}_z$.

The first two terms in Eq. (4.20) separately describe the external and internal dynamics of the system, respectively. The third term in Eq. (4.20), however, couples the internal state evolution to the condensate dynamics in the trap and can lead to interesting behavior. If the term $\hat{H}_z$ were identically zero, then the problem would be completely separable in terms of the external and internal degrees-of-freedom. The term $\hat{H}_z$ would be zero if the trap separation z_0 were zero and if the scattering lengths were all exactly equal. In fact, for ^{87}Rb the three scattering lengths are nearly degenerate, so the main effect of $\hat{H}_z$ comes from the term $-z_0 z$, which is the difference in the shifted traps. It causes there to be a spatially varying detuning across the condensate. In the strong coupling case considered in Chapter 6, we will investigate this effect in more detail.

4.5.2 Dressed states

For the driven two-level atom in quantum optics the "dressed states" are a useful way to represent the system [75]. They are simply the eigenstates of the coupled Hamiltonian. For the coupled two-component condensate described by Eq. (4.11), there exist analogous states, however, because we not only have the internal structure but also the external motion in the trap, the dressed states consist of an infinite manifold. We will only consider the lowest energy dressed states in this section. Due to the entanglement of the internal and external degrees of freedom and the nonlinear mean-field interaction term, these dressed states exhibit a much richer behavior than their counterparts in the simple two-level atom [77]. We now present results of numerical calculations of these states and investigate the weak and

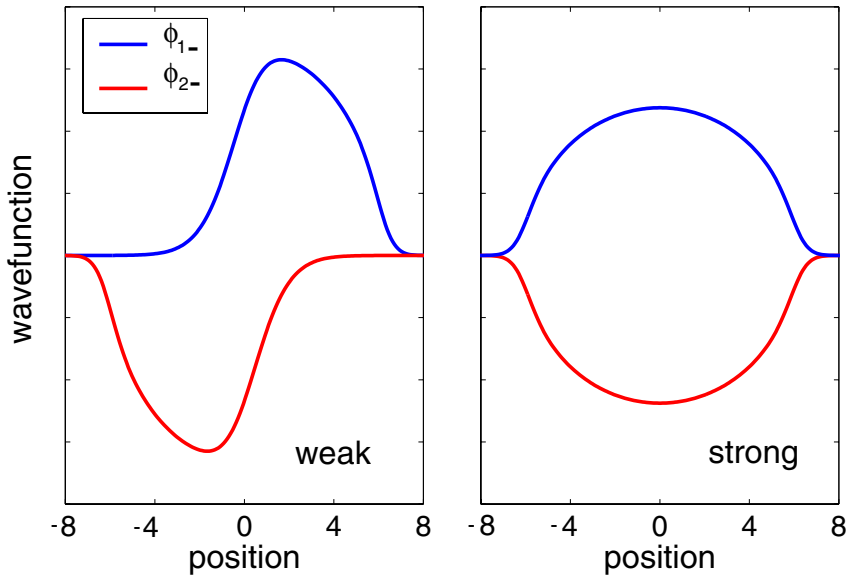

Figure 4.11: The condensate lower dressed state amplitudes in the weak and strong coupling limits. Here, $\phi_{1-}(z) = \langle z|\langle 1|\phi_-\rangle$ and $\phi_{2-}(z) = \langle z|\langle 2|\phi_-\rangle$. The trap frequency is $\nu_z = 65$ Hz, the population is $N = 10^6$ and the trap separation is $z_0/l_z = 0.15$m. The coupling strength was $\Omega = 6.5$ Hz in the weak-coupling limit and $\Omega = 650$ Hz in the strong-coupling limit. The detuning is zero and the scattering lengths were all equal.

strong coupling limits. We make use of the one dimensional model, which is sufficient to demonstrate the main features.

We are looking for stationary solutions of the coupled mean-field equations of the form

$$[\hat{H}_0 \otimes \hat{1} + \hat{1} \otimes (\frac{\Omega}{2}\,\hat{\sigma}_x + \frac{\delta}{2}\hat{\sigma}_z) + \hat{H}_z \otimes \hat{\sigma}_z]|\phi_\pm\rangle = \mu_\pm|\phi_\pm\rangle. \tag{4.23}$$

where μ_- is the energy of the ground dressed state and μ_+ is that of the excited dressed state. These states can be found numerically via the method of imaginary-time propagation described in Appendix (C). An alternative method, which is more closely tied to recent experiments at JILA, is based on the technique of adiabatic passage where the system is taken from the uncoupled ground state to the lower dressed state by ramping the detuning δ from minus infinity to zero. Ramping the detuning from plus infinity to zero takes the excited uncoupled state to the upper dressed state.

In Figure 4.11 we show the lower dressed state for both weak and strong coupling limits for zero detuning and with a trap separation of $z_0/l_z = 0.15$. The two cases yield dramatically different results. In the weak coupling limit $\Omega/\omega_z \ll 1$, the two components are pushed apart, while in the strong coupling case they overlap nearly completely. This property of the dressed states has been observed experimentally at JILA [13, 70].

This behavior can be understood by considering each case separately. In the weak coupling limit, we break up the Hamiltonian as $H = H^0 + H^1$ with

$$\begin{aligned} H^0 &= \hat{H}_0 \otimes \hat{1} + \hat{H}_z \otimes \hat{\sigma}_z \\ H^1 &= \hat{1} \otimes \frac{\Omega}{2}\,\hat{\sigma}_x. \end{aligned} \tag{4.24}$$

The Hamiltonian H^0 is diagonal in the internal-state space. The lowest energy eigenstates of H^0 then are simply $|\psi_1\rangle|1\rangle$ and $|\psi_2\rangle|2\rangle$, where the states $\psi_i = \langle z|\psi_i\rangle$ correspond to the ground state solutions of the time-independent GP equation, plotted in the last graph of Figure 4.4. The dressed states are then simply

$$|\phi_\pm\rangle = \frac{1}{\sqrt{2}}(|\psi_1\rangle|1\rangle \pm |\psi_2\rangle|2\rangle). \tag{4.25}$$

In the strong coupling limit $\Omega/\omega_z \gg 1$, we break up the Hamiltonian as $H = H^0 + H^1$ with

$$\begin{aligned} H^0 &= \hat{H}_0 \otimes \hat{1} + \hat{1} \otimes \frac{\Omega}{2}\,\hat{\sigma}_x \\ H^1 &= \hat{H}_z \otimes \hat{\sigma}_z. \end{aligned} \tag{4.26}$$

If the size of the trap separation is small $z_0/l_z \ll 1$, then H^1 can be treated as a perturbation. The zeroth order solution for the dressed states is then simply

$$|\phi_\pm\rangle = \frac{1}{\sqrt{2}}|\phi_0\rangle(|1\rangle \pm |2\rangle), \tag{4.27}$$

where $\phi_0 = \langle z|\phi_0\rangle$ is the ground-state solution to

$$[-\frac{1}{2}\frac{\partial^2}{\partial z^2} + \frac{1}{2}z^2 + \lambda_{12}\,|\phi_0(z)|^2]\,\phi_0(z) = \mu\,\phi_0(z), \tag{4.28}$$

This can be the starting point for a perturbative treatment of H^1. For the dressed state given here in the strong coupling limit, the internal and external degrees are approximately decoupled, with both components having the same spatial structure, as shown in Figure 4.11. This is in sharp contrast to the solution given in Eq. (4.25) for the weak coupling limit, where the density profiles of the two components are very distinct, being separated along the z-axis.

Here we have only given a qualitative discussion in order to gain some insight into the behavior of the dressed states shown in Figure 4.11. A more thorough investigation could be made including the effect of different scattering lengths and extending to cases with nonzero detuning [77].

4.6 Summary

In this chapter we have studied the stationary states of a two-component condensate, with the two components sitting in harmonic traps that are separated along the z-axis. After deriving the coupled, two-component GP equation, we then studied various properties of the ground state of the uncoupled system, $\Omega = 0$. An important property is that as the relative population changes between the two components, the overlap ζ is nearly constant and the difference in chemical potentials varies almost linearly with the relative population. This behavior will allow us to make a close connection to the double-well tunneling problem when we consider the case of weak coupling in Chapter 5.

We then introduced the notion of a topological excitation in the two component system, showing several examples of rotating and non-rotating solutions. Of particular interest is the case shown in Figure 4.7, where one of the components is in a vortex wrapped around the other component in the center. In Chapter 6 we will describe a method of dynamically preparing such novel solutions of the GP equation in a strongly coupled two-component condensate. An important property is that the energies of the two components change very little as population is transfered between components, as shown in Figure 4.8.

We concluded the chapter by presenting a more useful representation of the coupled GP equations, which makes a clean separation of the internal and external degrees of freedom. We will make use of this in Chapter 6 when we consider the strong coupling case. Finally, we discussed the stationary states of the coupled system—the dressed states—and saw that the behavior is drastically different in the two limiting cases of strong and weak coupling.

Chapter 5

Weak Coupling—Nonlinear Josephson-Type Oscillations

5.1 Introduction

In this chapter we consider in detail the weak coupling limit of Eq. (4.11). We begin by reviewing the standard Josephson junction from condensed matter physics and discuss the analogous situation of a double-well BEC. Based on the weak coupling assumption, we then show that Eq. (4.11) can be rewritten as two nonlinear coupled equations for the relative phase and relative population. These have nearly the same form as those describing the double-well tunneling system. Next, we show results of numerical calculations of these equations for a one-dimensional model of the system, which gives qualitative agreement to the full solution of the three dimensional problem. Finally, we use results from the previous chapter to obtain a set of equations that is identical in form to those of the double-well system, and we obtain a closed form solution.

5.2 The standard Josephson junction

A hallmark experiment contributing to the conceptual development of low temperature physics is the well known Josephson junction experiment [78, 79, 80, 81, 82], in which a thin insulator is wedged between two superconductors, as illustrated in Figure 5.1. The insulator provides a weak-link between the two superconductors, allowing electron-pairs to tunnel through the barrier to the other side. A remarkable feature of this low-temperature system is that a finite current of electron-pairs flows across the barrier in the absence of a voltage drop across the link. This interesting behavior is rooted in the presence of a macroscopic condensate wavefuction $\psi(\mathbf{r})$, which has an amplitude and a phase, describing the many-particle state of the electron pairs. As the system is brought to a temperature below T_c, a condensate forms in each superconductor, with a well defined, but random, relative phase. This phase gradient sets up a current that flows across the weak-link as electron-pairs tunnel through the barrier.

Let $\psi_i = n_i^{1/2} e^{i\phi_i}$ denote the wavefunction for each superconductor, with $n_i^{1/2}$ being the amplitude and $e^{i\phi_i}$ the phase. This system can be described by the simple coupled set

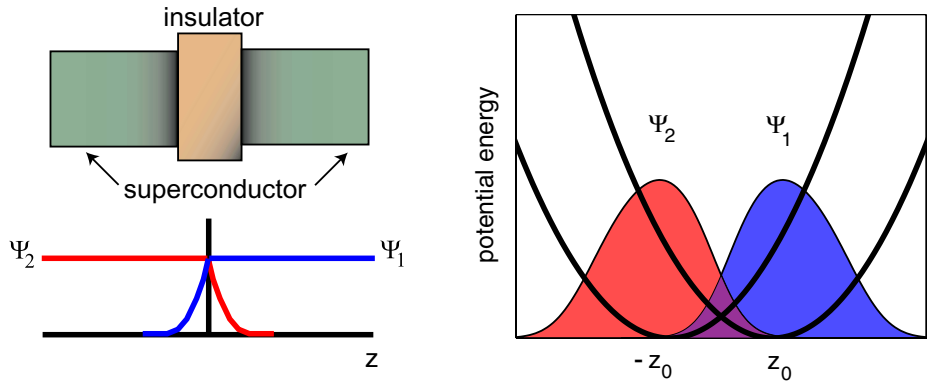

Figure 5.1: Illustration of the Josephson junction. On the left we show an illustration of the standard Josephson junction, with the top image representing the physical device, and the bottom image showing the overlap of the condensate wavefunctions due to tunneling through the barrier. On the right we show an illustration of the weakly-coupled, two-component condensate system, where the centers of the traps for each component are separated by $2z_0$.

of equations

$$\begin{aligned} i\hbar\,\dot{\psi}_1 &= E_1\psi_1 + K\psi_2 \\ i\hbar\,\dot{\psi}_2 &= E_2\psi_2 + K\psi_1, \end{aligned} \tag{5.1}$$

where E_i is the ground-state energy of the i'th superconductor and K is a coupling constant, which depends on the geometry and material of the barrier. If we substitute ψ_i given above into Eq. (5.1) and solve for the relative phase $\phi_r = \phi_1 - \phi_2$ and the current $J = n\dot{i}_1 = -n\dot{i}_2$, we get the standard Josephson junction equations

$$\begin{aligned} J &= J_0 \sin(\phi_r) \\ \dot{\phi}_r &= \frac{E_1 - E_2}{\hbar}, \end{aligned} \tag{5.2}$$

where $J_0 = 2K/\hbar n$ and $E_1 - E_2$ is proportional to the voltage drop across the barrier. These equations predict that, even in the absence of a voltage drop, the existence of an initial relative phase $\phi_r(0)$ between the superconductors results in the flow of current. This case is known as the dc Josephson effect. If a finite voltage is applied across the barrier, the current will oscillate and this is referred to as the ac Josephson effect. The linear geometry chosen here can be replaced with a circular one, which leads to a vortex solution with current flowing around a ring.

Several authors have proposed an analogous experiment for the case of a trapped atomic Bose-Einstein condensate[83, 84, 85, 86, 87, 88, 89, 90]. The basic idea is to allow the atoms to condense in a double-well potential, consisting of two regions separated by a central barrier, the height of which can be varied. This trap configuration can be achieved using the optical dipole force, for example, by shining a far-blue-detuned laser sheet of light that divides the trap into to separate wells. If the barrier height were initially infinite, the two condensates form independently in the separated wells. Once the condensates have formed, lowering the barrier height to a smaller constant value allows the atoms tunnel

through the barrier, so that the condensates become coupled. Characteristic equations similar to Eq. (5.2) have been obtained for this system [89, 90, 91]. Due to the the mean-field interaction for each condensate, the Josephson equations take on a nonlinear form, given by [89]

$$\begin{aligned} \dot{\eta} &= -(1-\eta^2)^{1/2}\sin\phi \\ \dot{\phi} &= \Delta E + \lambda\,\eta + \eta\,(1-\eta^2)^{-1/2}\cos\phi\ , \end{aligned} \tag{5.3}$$

where $\eta = (N_2 - N_1)/N$ is the relative population and $\phi = \phi_2 - \phi_1$ is the relative phase between condensates. The quantity ΔE is the difference in ground-state energies of the two wells, and λ is proportional to the mean-field interaction. In obtaining these equations, the authors have assumed the densities in the barrier region are so low the mean-field interaction *between* the condensates can be neglected.

In this chapter we investigate the case of weak coupling in the driven two-component condensate [92, 93] introduced in the previous chapter. We illustrate this system schematically in Figure 5.1. The two components sit in spatially offset traps along the vertical axis. The weak link in this system is not due to the tunneling of atoms through a barrier, but is provided by the low intensity electromagnetic field that couples the internal states of the atoms. As we will show, this system obeys nearly the same set of nonlinear Josephson equations as given in Eq. (5.3) for the double-well system.

5.3 Nonlinear Josephson-like equations

In order to make a connection to the standard Josephson effect, we must make some approximations in order to put Eq. (4.11) in a simpler form. For a very weak coupling $\Omega/\omega_z << 1$, where ω_z is the trap frequency, we can make the ansatz $\psi_i(z,\rho,t) = \sqrt{N_i(t)}\,e^{i\phi_i(t)}\,\Phi_i(z,\rho)$. Here we put the explicit time dependence into the population N_i and the phase ϕ_i of each component while putting the spatial dependence into an adiabatic solution $\Phi_i(z,\rho)$ to the time-independent uncoupled GP equations Eq (4.8)

$$(H_i^0 + H_i^{MF})\,\Phi_i(z,\rho) = \mu_i\,\Phi_i(z,\rho)\ . \tag{5.4}$$

The chemical potentials μ_i and functions $\Phi_i(z,\rho)$ vary slowly in time, being "slaved" by the populations.

If we substitute this ansatz into Eq. (4.11), we obtain the following equations of motion for the relative population $\eta = (N_2 - N_1)/N$ and the relative phase $\phi = (\phi_2 - \phi_1)$

$$\begin{aligned} \dot{\eta} &= -k\,(1-\eta^2)^{1/2}\sin\phi \\ \dot{\phi} &= -[(\mu_2-\mu_1)+\delta] + k\,\eta\,(1-\eta^2)^{-1/2}\cos\phi\ , \end{aligned} \tag{5.5}$$

where $k = \Omega\int d^3r\,\Phi_2(z,\rho)\Phi_1(z,\rho)$ is proportional to the overlap of the condensates and so also varies slowly in time. These are non-linear versions of the usual Josephson-junction equations and are nearly identical in form to those obtained in Eq. (5.3) describing the double-well tunneling problem. The major difference is that in the double-well trap, the condensates are well separated, allowing the authors in [89] to neglect the mean field in the interaction region of the barrier. In contrast, the interaction between condensates due to their significant overlap plays an important role in the evolution of the system described here, as we will show.

The coupling constant k is simply the Rabi frequency Ω times the overlap between states $\zeta = \int d^3r\, \Phi_2(z,\rho)\Phi_1(z,\rho)$, which is analogous to a Frank-Condon overlap factor. As we saw in the previous chapter, ζ is nearly a constant function of the relative population η. Furthermore, we also showed in the previous chapter that the difference in chemical potentials $\mu_2 - \mu_1$ for the two-component ground state depends linearly on the relative population η over a reasonable range of η. In the section 5.7 we will use these facts to construct a simplified, close-form solution of Eq. (5.5).

5.4 Hydrodynamic-like Bloch equations

By assuming a weak coupling, we have been able to reduce Eq. (4.11) to a form that resembles the Josephson equations describing the double-well tunneling problem. We can also write Eq. (4.11) in a form that links up with the Bloch equations describing a driven two level atom [75]. Conceptually, this is very nice, that we are able to draw analogies between two standard problems from different fields of physics. The coupled equations Eq. (4.11) can be written in an equivalent form that resembles the Bloch equations for a simple driven two-level atom. We can obtain a generalized set of Bloch equations for the densities $n_i(\mathbf{r},t) = \psi_i(\mathbf{r},t)^*\psi_i(\mathbf{r},t)$ and coherences $n_{ij}(\mathbf{r},t) = \psi_i(\mathbf{r},t)^*\psi_j(\mathbf{r},t)$ by taking the time derivatives of these quantities and substituting in Eq. (4.11) to give

$$\begin{aligned}
\dot{n}_1(\mathbf{r},t) + \nabla\cdot\mathbf{j}_1(\mathbf{r},t) &= -i\frac{\Omega}{2}[n_{12}(\mathbf{r},t) - n_{21}(\mathbf{r},t))] \\
\dot{n}_2(\mathbf{r},t) + \nabla\cdot\mathbf{j}_2(\mathbf{r},t) &= i\frac{\Omega}{2}[n_{12}(\mathbf{r},t) - n_{21}(\mathbf{r},t))] \\
\dot{n}_{12}(\mathbf{r},t) + \nabla\cdot\mathbf{j}_{12}(\mathbf{r},t) &= i\Delta(\mathbf{r})n_{12}(\mathbf{r},t) + i\frac{\Omega}{2}[n_2(\mathbf{r},t) - n_1(\mathbf{r},t)]\,. \qquad (5.6)
\end{aligned}$$

The quantities $\mathbf{j}_i(\mathbf{r},t)$ are current densities for each component given by $\mathbf{j}_i(\mathbf{r},t) = 1/2i(\psi_i^*\nabla\psi_i - \psi_i\nabla\psi_i^*)$ while the quantity $\mathbf{j}_{12}(\mathbf{r},t)$ is a coherence current density given by $\mathbf{j}_{12}(\mathbf{r},t) = 1/2i(\psi_1^*\nabla\psi_2 - \psi_2\nabla\psi_1^*)$. The quantity $\Delta(\mathbf{r}) = \delta - 2z_0 z + (H_1^{\mathrm{MF}} - H_2^{\mathrm{MF}})$ is a spatially dependent detuning. These equations are not a closed set, but rather must be augmented by the corresponding equations of motion for the current terms $\mathbf{j}_i(\mathbf{r},t)$ and $\mathbf{j}_{ij}(\mathbf{r},t)$.

In the absence of the current terms $\mathbf{j}_i(\mathbf{r},t)$ and $\mathbf{j}_{ij}(\mathbf{r},t)$ these equations would more closely resemble the usual Bloch equations. Neglecting the current terms is the same as ignoring kinetic energy, which is also equivalent to taking the infinite mass limit so as to fix the positions of the atoms. In doing this one just obtains position-dependent Bloch equations. The position-dependent detuning $\Delta(\mathbf{r})$ causes the Rabi oscillations of the population at each position to dephase across the condensate. In the weak coupling limit, this dephasing happens so slowly that the current has time to adjust, so that no damping-like behavior is observed. However, in the strong coupling limit, the dephasing happens very rapidly, so that an initial decay occurs, followed by a revival due to the fact that current will flow in response to the phase winding across the condensate. We will study this effect in more detail in Chapter 6.

This form also resembles the zero-temperature hydrodynamic-like description of the condensate found in the literature (see, for example, [24]). For a single component these equations simply reduce to the continuity equation $\dot{n}(\mathbf{r},t) + \nabla\cdot\mathbf{j}(\mathbf{r},t) = 0$. However, due to the coherent drive that couples the two states, the feeding term $-\mathrm{Im}\{\Omega\, n_{12}(\mathbf{r},t)\}$ appears, which depends on the coherence $\dot{n}_{12}(\mathbf{r},t)$ between internal states.

To make an even closer connection to the Bloch equations, we can integrate over the spatial degree of freedom in Eq. (5.6) and obtain equations for the populations N_i and the coherences $N_{ij} = \int dz\, \psi_i^*(z)\psi_j(z)$, which gives us

$$\begin{aligned} \dot{N}_1 &= -i\,\frac{\Omega}{2}\,(N_{12} - N_{21}) \\ \dot{N}_2 &= +i\,\frac{\Omega}{2}\,(N_{12} - N_{21}) \\ \dot{N}_{12} &= i\,\delta\,N_{12} + i\,\Lambda(t) + i\,\frac{\Omega}{2}\,(N_2 - N_1)\ , \end{aligned} \tag{5.7}$$

where we define the time-dependent term $\Lambda(t)$ as

$$\begin{aligned} \Lambda(t) &= -2\,z_0 \int d^3r\, z\, \psi_2^*(z,\rho)\psi_1(z,\rho) \\ &+ \int d^3r\, (H_1^{\mathrm{MF}} - H_2^{\mathrm{MF}})\, \psi_2^*(z,\rho)\psi_1(z,\rho)\ . \end{aligned} \tag{5.8}$$

The equations in Eq. (5.7) resemble the Bloch equations describing an undamped, driven two-level atom. However, because the spatial degree of freedom is correlated to the internal states of the atom, the extra term $\Lambda(t)$ appears, which includes the difference in external potentials between the two states.

The first term in Eq. (5.8) arises from the difference in the shifted harmonic traps, which is just linear in z. This term acts as a time-dependent detuning. As population is transferred from one condensate to the other, the position of the overlap region changes due to the mean-field repulsion. This will cause the system to move in and out of resonance resulting in a suppression of the transfer of atoms. The second term comes from the difference in mean-field interactions and would vanish if all three scattering lengths were exactly degenerate, which can be seen from

$$H_2^{\mathrm{MF}} - H_1^{\mathrm{MF}} = (\lambda_{22} - \lambda_{21})|\psi_2|^2 - (\lambda_{11} - \lambda_{21})|\psi_1|^2\ . \tag{5.9}$$

5.5 Preparation of the initial state

The initial state that we have assumed in writing down Eq. (5.5) is related to the dressed states we considered in the previous chapter. For the simple case of zero detuning $\delta = 0$ the dressed states correspond to equal populations $\eta(0) = 0$ and the relative phase being either $\phi(0) = 0$ or π. The case of $\phi(0) = \pi$ can be prepared by using the method of adiabatic passage; the condensate is initially in the lower internal state $|1\rangle$ and a strong drive is turned on, which is initially red detuned far off resonance. The magnitude of the detuning is then decreased slowly to zero. This prepares the system in the dressed state shown in the right plot of Figure 4.11. One can then adiabatically decrease the strength of the drive in order to satisfy the weak coupling criterion, which takes us to the dressed state shown in the left plot of Figure 4.11. This procedure prepares the condensate in a dressed state with $\eta(0) = 0$ and $\phi(0) = \pi$, which is a stationary solution to Eq. (5.5). We show an example of this in Figure 5.2, where we have solved numerically the time-dependent coupled two-component GP equation. At $t = 100$ ms we jump the phase so that the system is no longer stationary and population begins to flow back and forth between components.

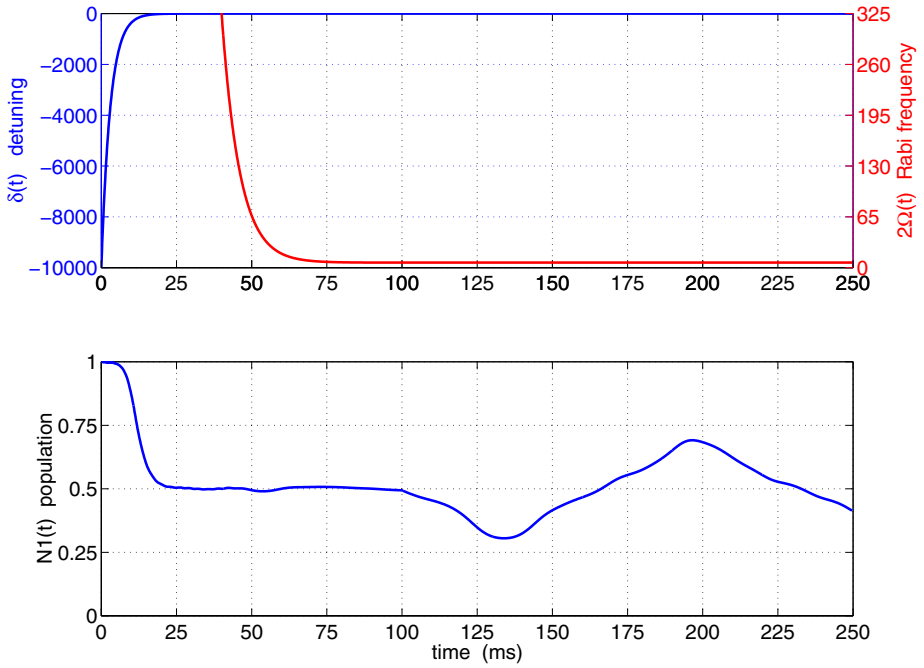

Figure 5.2: An example of using adiabatic passage to prepare the initial state for the Josephson-like equations. The top plot shows the detuning in blue and the Rabi frequency in red. The bottom plot shows the population in the $|1\rangle$ state. The phase is jumped to $3\pi/16$ at $t = 100$ ms. Therefore, $t = 100$ ms corresponds to the origin of time in Eq. (5.5).

This technique has been implemented in experiments at JILA and can, in principle, produce initial states with arbitrary relative population $\eta(0)$ and relative phase $\phi(0)$. For example, instead of ramping the detuning to zero, one could instead stop at a finite value, so as to prepare an initial state with unequal populations.

5.6 Numerical solution

We now show results of numerical calculations of both the exact solution, found by integrating the time-dependent coupled GP equation Eq. (4.11), and the approximate solution given by the Josephson-like equations Eq. (5.5). To prepare the initial state, we simply find the ground state of the two-component system for a given relative population, and then modify the relative phase. We do not generate the initial state using the more elaborate scheme shown in Figure 5.2. To integrate Eq. (5.5), the chemical potentials and the overlap factor ζ must be found self-consistently in each time step by solving the time-independent GP equation for Φ_i, given $\eta(t)$. We circumvent this elaborate procedure in the section 5.7, where we make further approximations to obtain a closed-form solution.

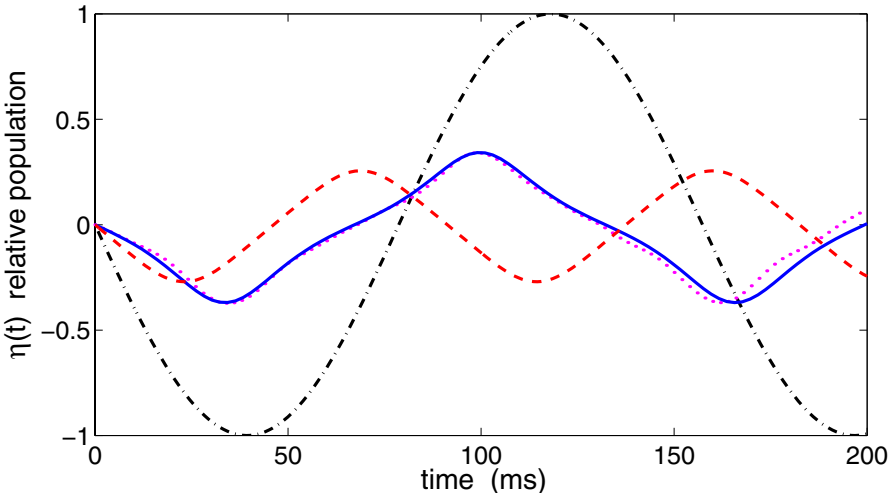

Figure 5.3: The time evolution of the relative population $\eta(t)$ for several different cases. The black dot-dashed line corresponds to the case where the mean-field interaction has been set to zero, the initial relative phase is $\phi(0) = 0$, and $\delta = 0$. The red dashed line is for the same initial relative phase of $\pi/2$, but with the mean-field interaction turned on and $\delta = 0.49$ in units of the trap frequency. The blue solid line is for $\phi(0) = 3\pi/16$ and $\delta = 0.49$. The three lines described are solutions of Eq. (5.5), whereas the purple dotted line corresponds to the exact solution of Eq. (4.11). In all cases $\nu_z = 65$ Hz, $z_0 = 0.2\,\mu$m and $N = 8 \times 10^5$.

5.6.1 One-dimensional model

We first consider the one-dimensional model first introduced in Chapter 3. In Figure 5.3 we show four curves that are described in the caption. As a point of reference, we plot the solution of Eq. (5.5) with the mean-field terms set to zero. This is the standard Rabi solution for a driven two-level atom, but here the Rabi frequency is given by $\Omega \int dz\, \Phi_2(z)\Phi_1(z)$, which includes the Frank-Condon-type overlap of the condensate wavefunctions. However, when we turn on the mean-field interaction and set $\delta = 0.49$ so that the system is initially being driven resonantly with $(\mu_2 - \mu_1 + \delta) = 0$, the amplitude is suppressed and the frequency has increased (the red dashed line). As $\phi(0)$ is decreased, the amplitude increases, as illustrated by the solid blue curve where $\phi(0) = 3\pi/16$. Also, as $\phi(0)$ is decreased, the presence of higher harmonics becomes stronger, as one can see in the shape of the solid line.

For comparison, we also plot the exact solution given by Eq. (4.11) for the case $\phi(0) = 3\pi/16$ (the purple dotted line). In this case the adiabatic solution (blue solid) agrees quite well with the exact solution given by Eq. (4.11). The validity of the adiabatic solution depends on the structure of the evolving spectrum of this nonlinear system. In particular, one must compare the time rate of change of the Hamiltonian to the spacing between the instantaneous eigenmodes of the dressed basis. These quantities will depend on the size of the mean-field interaction, the strength of the coupling, given by $\Omega \int dz\, \Phi_2(z)\Phi_1(z)$, and also on the detuning δ.

We plot a snapshot evolution of the densities of the system in Figure 5.4 in order to show that the effect of the mean field is to push the system out of resonance as population

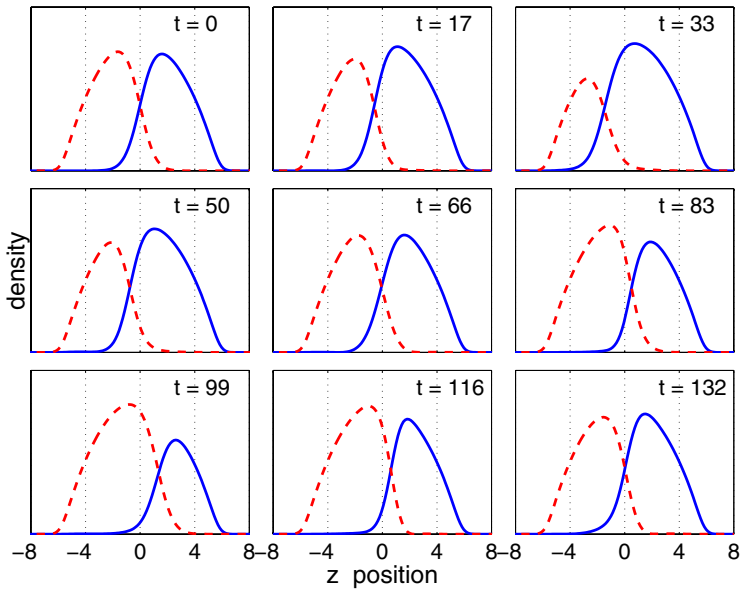

Figure 5.4: A snapshot evolution of the densities of the components. The x-axis is the position z, and the time t of each snapshot is shown in ms. This case corresponds to the purple dotted line plotted in Figure 5.3. The detuning is $\delta = 0.49$, chosen so that the system is initially being driven on resonance. As the system evolves, the $|1\rangle$ component pushes the $|2\rangle$ component out of the center of the trap so that the region of overlap becomes displaced from the origin and the system is no longer being driven on resonance.

is transferred between components. The case considered in Figure 5.4 corresponds to the purple dotted line in Figure 5.3. The detuning was chosen so as to compensate for the initial value of the term $\Lambda(0)$ in Eq. (5.7), which represents the difference in external potentials, so that initially the system is being driven on resonance. However, as the system evolves, the first term in Eq. (5.8) gets larger since the $|1\rangle$ component is pushing the $|2\rangle$ component away from the center of the trap. This causes the region of overlap to be displaced from the origin so that the system is no longer being driven on resonance. This reduces the effectiveness of the drive and accounts for the suppression of the amplitude of oscillation in the relative population plotted in Figure 5.3.

In Figure 5.5 we show some examples of different initial conditions. As a reference, we plot the solution with the mean-field interaction set to zero, with $\eta(0) = -0.5$, $\phi(0) = 0$, and $\delta = 0$ in units of the trap frequency (red dashed line). This just corresponds to the standard Rabi solution for the driven two level atom. When we turn the mean-field interaction back on and set $\delta = 0.97$, we see again that the amplitude is reduced, but also the shape of the oscillation changes dramatically. If we let the initial phase be $\phi(0) = \pi/4$ we get the black dot-dashed line, which looks more like the solutions shown in Figure 5.3.

5.6.2 Comparison to the three-dimensional case

It is instructive to double check our one dimensional model solution against the three dimensional solution. In Figure 5.6 we compare the one and three dimensional exact numer-

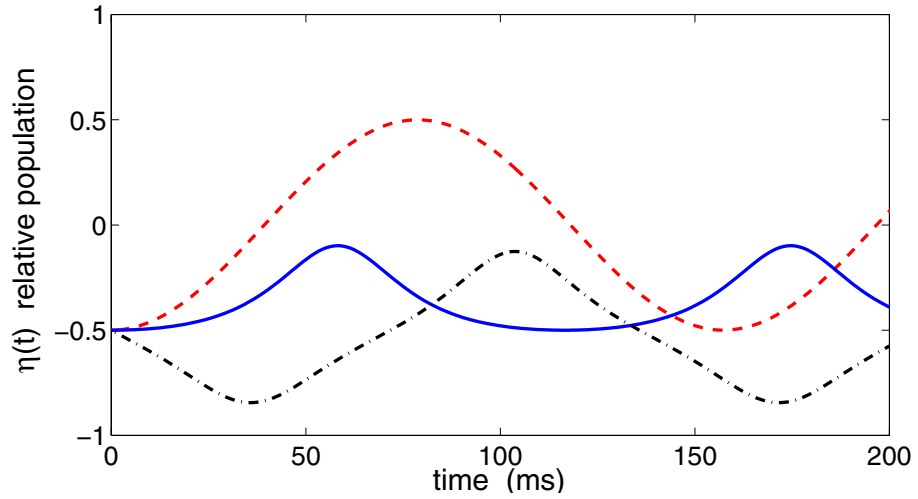

Figure 5.5: Time evolution of $\eta(t)$ for additional cases. This plot is similar to Figure 5.3, but here we have $\eta(0) = -.5$. We set the mean-field interaction term to zero for the red dashed line, with $\phi(0) = 0$ and $\delta = 0$. For the solid blue line we included the mean-field interaction, keeping $\phi(0) = 0$ and setting $\delta = .97$ so as to initially drive the system on resonance. In the black dot-dashed line we have set the initial relative phase to $\phi(0) = \pi/4$.

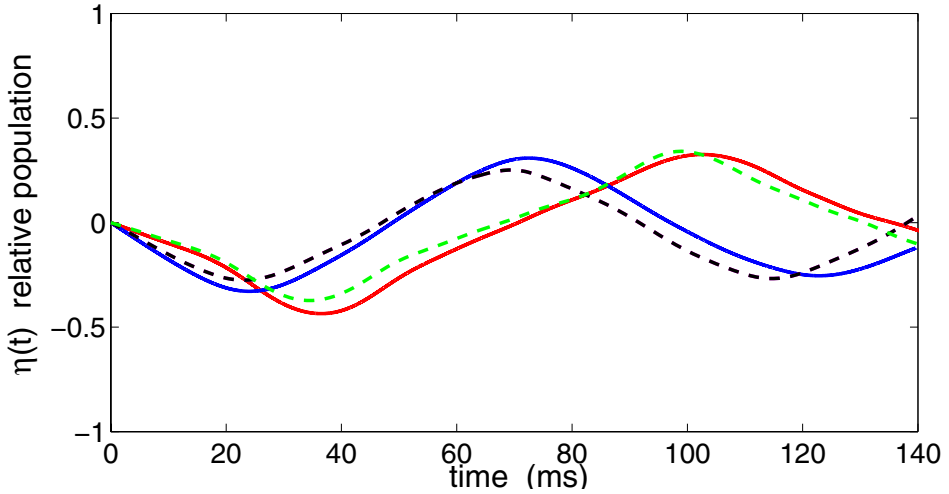

Figure 5.6: A comparison between the exact solutions of Eq. (4.11) for the one dimensional model and the full three dimensional problem. The solid lines are the three dimensional solution and the dashed correspond to the one dimensional model. The red and green lines are for an initial relative phase of $\phi(0) = 3\pi/16$, while the blue and black are for $\phi(0) = \pi/2$.

ical solutions of Eq. (4.11). The solutions agree very well, with small differences in the amplitudes and periods of oscillations. This agreement is not surprising, if we look back at Figure 4.5 in Chapter 4. There we found that the overlap ζ for both cases was nearly identical. A more significant, though small, deviation was found for the the difference in chemical potentials, where the one dimensional model has a slightly larger slope, which will give the differences shown in Figure 5.6. The one dimensional model appears to yield fairly good agreement with the three dimensional problem.

5.7 Closed-form solution

We can obtain a closed-form solution of Eq. (5.5) if we make use of the observation from Chapter 4 that the overlap ζ is approximately a constant function of η and that the difference $\mu_2 - \mu_1$ varies linearly with η, as shown in Figure 4.5. This allows us to make the approximation

$$\begin{aligned} \mu_2 - \mu_1 &= \alpha\eta + \beta, \\ k &= \gamma, \end{aligned} \tag{5.10}$$

where the parameters α, β, and γ must be determined numerically for a set of physical parameters (N, z_0, etc.). Substituting these into Eq. (5.5) we obtain

$$\begin{aligned} \dot{\eta} &= -(1-\eta^2)^{1/2}\sin\phi \\ \dot{\phi} &= \Delta + \Upsilon\,\eta + \eta\,(1-\eta^2)^{-1/2}\cos\phi\ , \end{aligned} \tag{5.11}$$

where we have made the change of variable $t \to kt$, and taken $\Upsilon = -\alpha/k$ and $\Delta = -(\delta+\beta)/k$. These equations are now identical in form to Eq. (5.3) describing the double-well tunneling problem.

It was shown by the authors of [89, 90, 91] for the double-well problem that a very nice mechanical analog of the problem can be constructed that admits a closed form solution, if we treat η and ϕ as conjugate variables, whose motion is governed by the Hamiltonian

$$H = \frac{1}{2}\Upsilon\,\eta^2 + \Delta\eta - (1-\eta^2)^{1/2}\cos(\phi), \tag{5.12}$$

This has the physical analog of describing a nonrigid pendulum of tilt angle ϕ and length proportional to $\sqrt{1-\eta^2}$ that decreases with angular momentum η [89, 90, 91]. The equations Eq. (5.11) are equivalent to

$$\begin{aligned} \dot{\eta} &= -\frac{\partial H}{\partial \phi}, \\ \dot{\phi} &= \frac{\partial H}{\partial \eta}. \end{aligned} \tag{5.13}$$

We consider the special case where $\Delta = 0$, which is achieved by setting the detuning to $\delta = -\beta$. We then rewrite the equations of motion as an integral equation

$$\frac{\Upsilon t}{2} = \int_{\eta(0)}^{\eta(t)} \frac{d\eta}{\left[(b+\eta^2)(a-\eta^2)\right]^2}, \tag{5.14}$$

where the constants a and b are

$$\begin{aligned} a &= \frac{2}{\Upsilon^2}\left[(\Upsilon^2 - 2H_0\Upsilon + 1)^{1/2} + (H_0\Upsilon - 1)\right], \\ b &= \frac{2}{\Upsilon^2}\left[(\Upsilon^2 - 2H_0\Upsilon + 1)^{1/2} - (H_0\Upsilon - 1)\right]. \end{aligned} \tag{5.15}$$

Here H_0 is the energy at $t = 0$, which is a constant of motion

$$H_0 \equiv \frac{1}{2}\Upsilon\,\eta(0)^2 + \Delta\eta(0) - (1 - \eta(0)^2)^{1/2}\cos(\phi(0)). \tag{5.16}$$

The solution to the integral equation Eq. (5.14) is found in the literature [94, 95, 96] and is written in terms of the Jacobian elliptic function $\mathrm{sn}(u \,|\, m)$, where m is the elliptic modulus (usually denoted by k)

$$\eta(t) = -a^{1/2}\mathrm{sn}(u(t) \,|\, m). \tag{5.17}$$

Here $m = -a/b$ and $u(t) = -b^{1/2}\Upsilon(t + t_0)/2$, where

$$t_0 = \frac{2}{b^{1/2}\Upsilon}F[\sin^{-1}(\eta(0)/a^{1/2}) \,|\, m]. \tag{5.18}$$

Here $F(x \,|\, m) = \int_0^x dx[1 - m^2\sin^2(x)]^{-1/2}$ is the incomplete elliptic integral of the first kind.

The elliptic functions and integrals are standard quantities that are implemented in common math packages, such as Mathematica. Given the parameters α, β, and γ in Eq. (5.10), we can easily generate plots of the amplitude, which is given by $a^{1/2}$, and the period T of oscillation, given by

$$T = \frac{-8}{b^{1/2}\Upsilon}K(m), \tag{5.19}$$

where $K(m) \equiv F(\pi/2 \,|\, m)$ is the complete elliptic integral of the first kind. We show plots of the period and amplitude as functions of the initial relative phase in Figures 5.7 and 5.8. We see that as the initial relative phase decreases from $\phi(0) = \pi$, both the period and amplitudes increase. For $\phi(0) \to 0$, we see the period increase to infinity, which signifies that this is a stationary state. Likewise, if $\phi(0) \to \pi$, the amplitude goes to zero because this is also a stationary state. These two cases just correspond to the dressed states considered in the previous chapter.

Within the nonrigid pendulum analogy, the case of $\eta(0) = 0$ and $\phi(0) = \pi$ corresponds to the pendulum hanging at rest. For values of $\phi(0)$ close to π, this corresponds to just slightly displacing the pendulum, so that it undergoes simple sinusoidal oscillations. As the tilt angle is displaced further from π, the pendulum exhibits nonlinear behavior, because the length depends on the angular momentum. The authors of [89, 90, 91] have explored the different regions of phase space of the nonrigid pendulum in detail for the case of the double-well system.

Another interesting behavior of the solution is that the presence of higher harmonics becomes more pronounced as $\phi(0)$ is decreased, as already alluded to in the previous section. In Figure 5.9 we show two cases of $\phi(0) = \pi/2$ and $\pi/16$. We plot the amplitude of the frequency component vs the frequency in units of the fundamental frequency ω_0, which is just the inverse of the period T. We see that for $\phi(0) = \pi/2$, the amplitude of the fundamental frequency is nearly unity, with the third harmonic being the next largest with an amplitude of 0.2%. Compare this to the case of $\phi(0) = \pi/16$, where the amplitude of the fundamental frequency is only 90% and the third multiple is almost 10%, with the amplitudes of the other odd multiple frequency components trailing off.

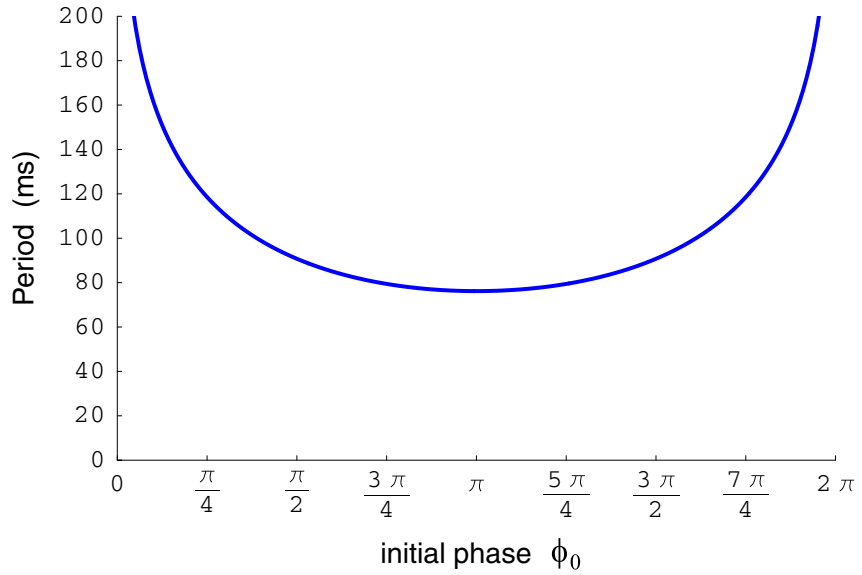

Figure 5.7: The period of oscillations as a function of the initial relative phase $\phi(0)$ using expression Eq. (5.19). The parameters $\alpha = 1.05$, $\beta = -0.482$, and $\gamma = 0.375$ were found by obtaining the solution to the time-independent GP equation as a function of the relative population. The detuning was $\delta = 0.482$, chosen to make $\Delta = 0$.

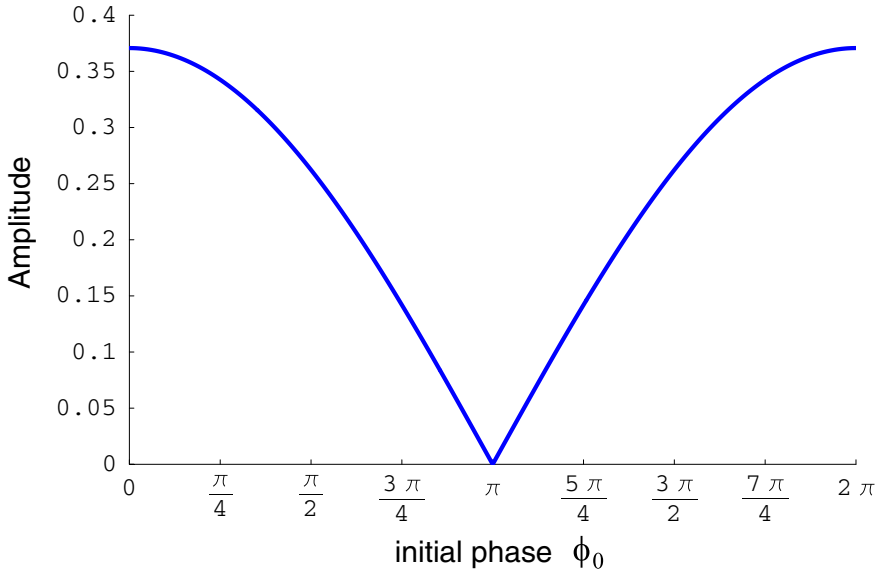

Figure 5.8: The amplitude of oscillation as a function of the initial relative phase $\phi(0)$.

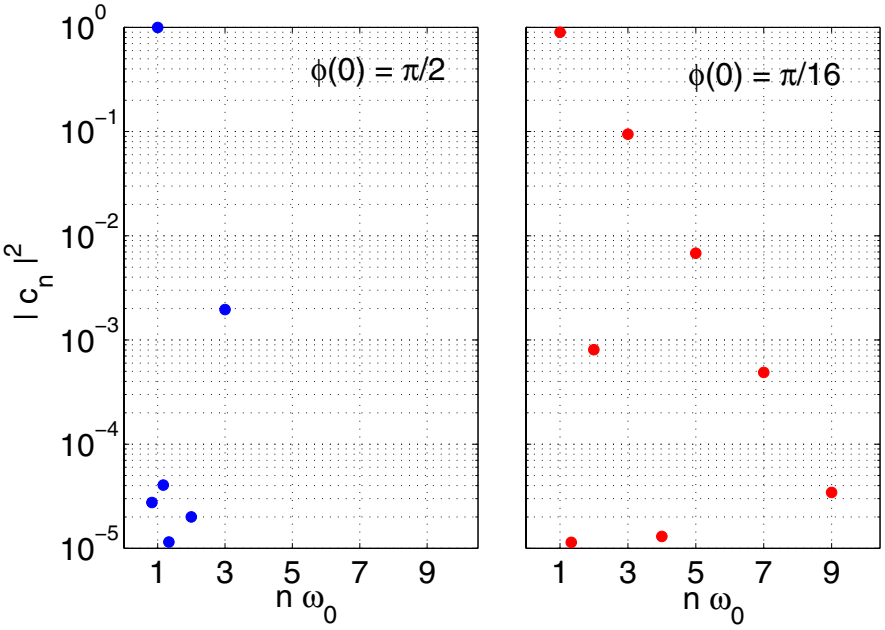

Figure 5.9: Amplitude of the frequency components obtained from a discrete FFT of $\eta(t)$ for two different cases of $\phi(0) = \pi/2$ and $\pi/16$. The frequency is plotted in units of the fundamental frequency ω_0. Note that some of the frequency components at the bottom of the graphs are not exactly multiples of the fundamental frequency—this is most likely due to numerical error.

5.8 Summary

In this chapter we have investigated the weakly coupled two-component system at zero temperature. Our main result is that this system effectively obeys the same set of nonlinear Josephson equations as the double-well tunneling system [89, 90, 91] due to the fact that the overlap between components is approximately constant, and the difference in chemical potentials is roughly a linear function of the relative population η. This gives more credence to our interpretation that the system can be thought of as a Josephson junction type of system. This also allowed us to obtain a closed form solution for the system, whose general behavior can be understood in terms of the nonrigid pendulum.

An interesting extension of this study would be to treat the system at finite temperature. In [91], the authors introduce a phenomenological damping term in Eq. (5.3), and thus model the system at finite temperatures. Starting with the quantum kinetic equations obtained in Chapter 2, we could derive an effective damping term from the collision terms in the kinetic equations, instead of postulating the term based on physical intuition.

Chapter 6

Strong Coupling—Quantum State Engineering

6.1 Introduction

The work presented in this chapter is closely tied to recent experiments at JILA lead by Eric Cornell and Carl Wieman [7, 8, 9, 10, 11, 12, 13, 14]. It is useful to give a brief history of how our present understanding of the strongly coupled two-component condensate emerged as we struggled to fully comprehend the interesting behavior observed in experiments. The most striking result of these joint experimental and theory investigations is the prediction of a vortex and the subsequent observation of it in the laboratory. It is worthwhile to describe the various stages of research leading up to this important result. This will help motivate the main results presented in this chapter.

The first work on a two component system in a dilute Bose condensed gas was done by Myatt et al. [7] at JILA, who were able to sympathetically cool atoms in two different hyperfine levels below the critical temperature and create a mixture of condensates in the $(1,-1)$ and $(2,2)$ states, which had an unexpectedly long lifetime. This was an important result, for it demonstrated that the spin-exchange scattering rate is suppressed for ^{87}Rb. This was not known at the time, and allowed theorists to place tight bounds on the singlet scattering length, assigning it a value that is nearly degenerate with the triplet scattering length [97, 98, 99]. This near coincidence of the singlet and triplet scattering lengths is very fortuitous for ^{87}Rb and is not the case in other alkali atoms, such as ^{7}Li and ^{23}Na. As a result, the spin exchange rate for ^{7}Li and ^{23}Na is much larger than that of ^{87}Rb. A spin exchange collision can flip the atoms into untrapped states, so that they are lost from the trap. This makes it very difficult to study magnetically trapped multicomponent condensates of ^{7}Li and ^{23}Na atoms. However, this problem can be overcome for these atoms by loading the condensate into a purely optical trap [28, 100].

The knowledge that magnetically trapped, multicomponent condensates could be studied in ^{87}Rb lead to the next experiment, in which a mixture of $(1,-1)$ and $(2,1)$ atoms were studied [8]. In this case, sympathetic cooling was not used, but instead, the mixture was prepared by first cooling the $(1,-1)$ atoms below the condensation point, and then transferring atoms suddenly into the $(2,1)$ by applying a two photon pulse. In the previous experiment, the mixture consisted of $(1,-1)$ and $(2,2)$ states, which experience different

trapping potentials due to their different magnetic moments. The advantage of using the $(1,-1)$ and $(2,1)$ states is that their magnetic moments are nearly the same. The trapping fields can be adjusted in such a way to cancel the effect of gravity, so that the atoms sit in concentric harmonic potentials with the same spring constants [9]. The first study of this system investigated the dynamical response of the condensate to a sudden change in the internal state by applying a very short π pulse to the $(1,-1)$ atoms that transfered them to the $(2,1)$ state. Due to the slightly different scattering lengths of the two states, the ground state of the $(2,1)$ atoms is slightly smaller in size than that of the $(1,-1)$ atoms, so that the sudden change in state resulted in a breathing of the condensate that could be characterized in terms of its collective excitations [8].

If a $\pi/2$ pulse is applied to the $(1,-1)$ atoms instead of a π pulse, a mixture can be prepared. A number of interesting properties of this system were studied at JILA [10, 11]. One interesting feature of this system that was observed is that it is energetically favorable for the atoms with the larger scattering length, $(1,-1)$ to form a lower-density shell around the $(2,1)$ atoms, which move inward [32, 101]. This behavior was studied in Chapter 4 (see Figure 4.2) for the case of concentric traps. However, if the traps are displaced only very slightly, it is energetically favorable for the two components to separate, with a finite overlap, as shown in Figure 4.3. In the experiment reported in [10], the magnetic trapping fields were adjusted so that the potentials for the two states were slightly displaced along the vertical axis. After applying a $\pi/2$ pulse to the $(1,-1)$ atoms, the system is in a highly excited state; the two components push each other apart and slosh back and forth, while undergoing breathing excitations as well. After a duration of several trap periods, the relative motion between the two components damps away with the two components separated along the vertical axis. Although some damping of the relative motion is exhibited in a numerical solution of the two-component GP equations [102], the condensates in the experiment damp more strongly. This discrepancy is most likely due to finite temperature effects not contained in the GP equation.

In an interesting extension of this experiment, the relative phase between condensates was measured using a technique based on Ramsey's method of separated oscillating fields [103]. A mixture of condensates was prepared as described in the preceding paragraph, and after waiting a time $T_{\rm R}$ long enough to allow the components to separate and settle down, a second $\pi/2$ pulse was applied to read out the phase difference accumulated between the two condensates [11, 104]. By varying the time $T_{\rm R}$ when the second pulse was applied, an interference pattern was obtained. Remarkably, even after undergoing damping processes, the visibility of the fringes was reasonably sharp, at around 50% or so.

In the experiments described so far, the coupling drive was only applied in very short pulses, much shorter than the period of the trap. However, one can imagine applying the coupling drive continuously; we showed in the previous chapter that in the limit of a very weak coupling, the system resembles a weak-link Josephson junction, which would be a feasible experiment to do. In the summer and fall of 1998, experiments at JILA were moving in this direction. A number of technical issues had to be resolved first, however, like implementing a phase-contrast imaging system, and stabilizing mechanical sloshing of the condensate. Just as the experimenters were gearing up to study the weak coupling limit, some very intriguing behavior of the condensate was observed that warranted (a great deal) of further attention. Consequently, the weak coupling case has yet to be investigated experimentally.

We now describe the intriguing data: It was found in experiments that if the strong-coupling field is applied for a long time, instead of in short pulses, the Rabi oscillations

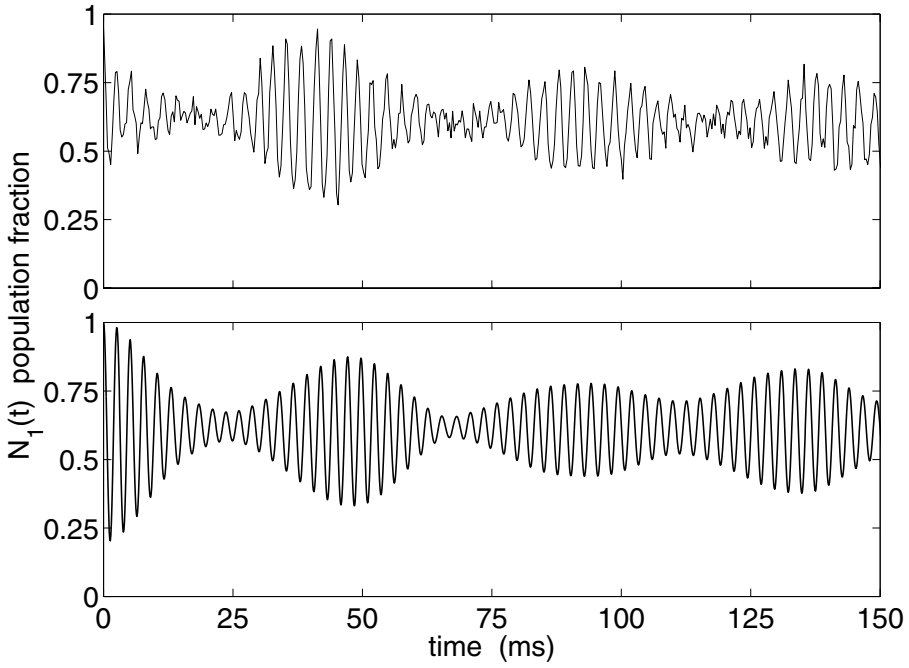

Figure 6.1: Modulation of the fractional population in the (1,-1) state. The top line is experimental data [13] while the bottom line is the result of a numerical calculation of the three-dimensional, two-component Gross-Pitaevskii equation. The coupling strength and detuning were chosen for the calculation to be $\Omega = 350\,\mathrm{Hz}$ and $\delta = -188\,\mathrm{Hz}$, respectively, while the detuning in the experiment was shifted from this.

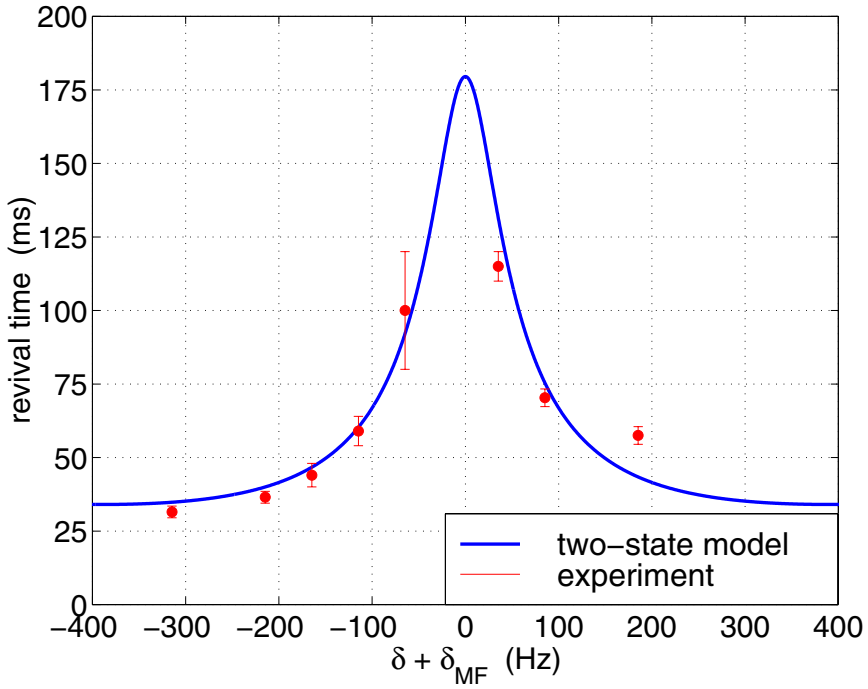

Figure 6.2: The revival time vs. the detuning. This shows the trend of the revival time to increase with decreasing detuning. The red dots are experimental data points, shown with error bars; they have been shifted along the x-axis by an overall detuning offset. The blue line corresponds to the two-mode model described in section 6.3.1. Experimental data is courtesy of M. Matthews, D. Hall, and P. Haljan.

between the two components appear to collapse and revive over a time long compared to the trap period. We show an example of this behavior in Figure 6.1. We find that the solution of the coupled GP equation also exhibits modulations of the Rabi oscillations. In both experiment and calculations of the GP equation, it is found that the revival time, or period of modulation, increases as the detuning is decreased about some central value, as shown in Figure 6.2. The most serious discrepancy between numerical solution of the GP equation and experiment was that the center of the peak in the revival time of the experimental data was not centered at the same detuning as predicted by the coupled GP equation but was shifted by about 50 Hz. We later realized this was most likely due to the spatially-dependent energy shift of the untrapped intermediate state in the two-photon transition, an effect that gives rise to a spatially dependent bare Rabi frequency[1] $\Omega(z)$. The displacement $2z_0$ between the traps also plays a crucial role in the collapse and revival behavior; when $z_0 = 0$ is set to zero, so that the two components sit in concentric traps, this effect goes away so that the Rabi oscillations are no longer modulated.

Another striking property of the system was that the densities exhibit a double-peaked

[1]This can be seen from $\Omega(z) = \Omega_a\Omega_b/4\delta'_{ab}(z)$, where the intermediate-state detuning $\delta'_{ab}(z) \approx \delta_{ab} - mgz$. Here, m is the mass of the atom and g is the gravitational acceleration. With $\delta_{ab} \gg mgz$, a Taylor expansion gives $\Omega(z) \approx \Omega + \chi z$, where $\chi = \Omega mg/\delta_{ab}$.

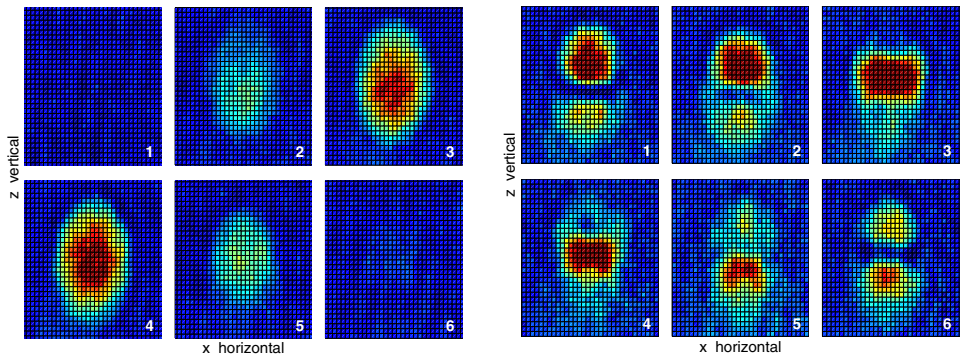

Figure 6.3: Double-peaked structures in the column-integrated density of the $(2,1)$ atoms. In each plot we show one full Rabi cycle divided into six shots. Plot (a) shows the very first Rabi cycle, where the shape of the $(2,1)$ component is the same as the ground state. In Plot (b) we show the density during a Rabi cycle taken during the collapse of the Rabi oscillations. The density cycles between the single- and double-peaked shapes. The $(1,-1)$ component exhibit the same behavior, though it is shifted by $1/2$ a Rabi cycle. Experimental data is courtesy of M. Matthews, D. Hall, and P. Haljan.

structure that appeared gradually, becoming most apparent during the collapse of the Rabi oscillations, and then gradually disappeared as the Rabi oscillations revived. An example is shown in Figure 5.4. During the first Rabi cycle after the drive is turned on, the densities of each component are identical, and have the shape of the ground state (plot (a)). However, a double peaked structure gradually forms in the densities of both components. In plot (b) we show an example of the density of the $(2,1)$ component taken from the region around 25 ms, where the collapse occurs. During one Rabi cycle, the density of the $(2,1)$ atoms goes from the double-peaked structure in frame 1 to being single-peaked in frame 4 and then back again to the double-peaked structure in frame 6. By the time the Rabi oscillations revive, the shape of the density also revives to their initial shapes shown in plot (a). This behavior was very reproducible in experiments. Also, numerical solutions of the coupled GP equations exhibit the same behavior.

Two different approaches emerged in our collaborative efforts to understand this unexpected behavior, which, at first glance, seem to have very little in common. One approach is motivated by previous work done in condensed matter physics on the A-phase of superfluid ^{3}He [105]. The other approach, which will be the focus in this chapter, is based on ideas familiar from quantum optics.

The first approach is useful in gaining an intuitive understanding of the phenomenon. We can describe the coupled two-component system in terms of the hydrodynamic-like Bloch equations Eq. (5.6) presented in section 5.4. There we saw that in the unphysical infinite-mass limit, where the atoms are "frozen" in place at each position, the current terms $\mathbf{j}_i(\mathbf{r},t)$ and $\mathbf{j}_{ij}(\mathbf{r},t)$ can be neglected, leaving us with a set of position dependent Bloch equations; atoms at each position undergo Rabi oscillations independently of their neighbors. Due to the spatially dependent detuning $\Delta(z)$ caused by the displaced traps, the Rabi oscillations at each position dephase across the condensate. If we wait long enough

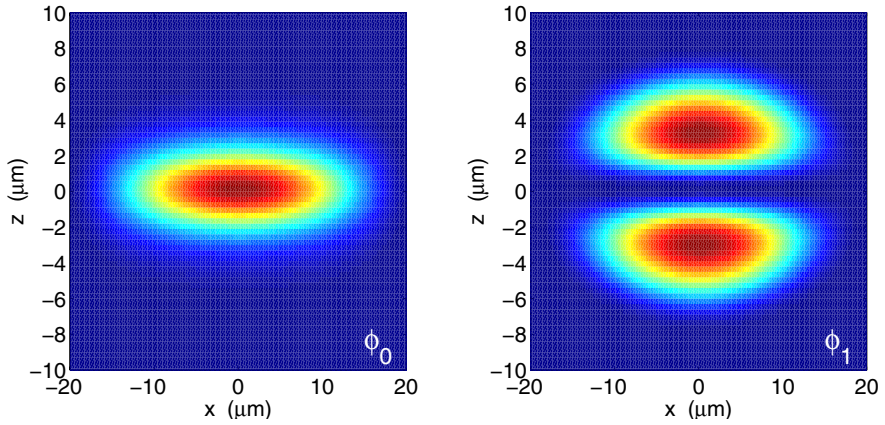

Figure 6.4: Dipole topological mode for a two-component condensate. The ground state (left) and first excited state (right) have equal macroscopic populations and must be found self-consistently (see Appendix (C)). The mean-field interaction between the states causes the ground state to be "pinched", so that it is much narrower than it would be if all of the atoms were in the ground state. The peculiar two-peaked structure in plot (b) of Figure 6.3 corresponds to the dipole topological mode plotted here.

we will see a decay in the integrated population of either state. In order to get a revival, however, we must account for the spatial coherence in the condensate described by the current terms. Due to the interplay of the spatial coherence and the coherent internal dynamics, the condensate can untwist its winding phase, so as to get back to its original state. This twisting and untwisting of the condensate phase is an example of a more general phenomenon found in any system where the $U(1)$ gauge transformation[2] is mixed up with some other continuous symmetry, in this case the $SU(2)$ symmetry of the spin [105]. We will not discuss this approach in any detail, but refer to the rigorous development presented in the work of Ho [105].

In the second approach, the system is described by the following "two-mode" model

$$\begin{aligned} |\psi(t)\rangle &= (\alpha_1(t)c_0(t)\,|\phi_0\rangle + \alpha_2(t)d_1(t)\,|\phi_1\rangle)|1\rangle \\ &+ (\alpha_2(t)c_0(t)\,|\phi_0\rangle + \alpha_1^*(t)d_1(t)\,|\phi_1\rangle)|2\rangle. \end{aligned} \tag{6.1}$$

The states $|1\rangle$ and $|2\rangle$ are the internal hyperfine states, while the states $|\phi_0\rangle$ and $|\phi_1\rangle$ are spatial states; $|\phi_0\rangle$ is the ground state, while $|\phi_1\rangle$ is a dipole topological mode, which we introduced in Chapter 4. In Figure 4.9 we considered such a topological excitation for the one-dimensional solution. In Figure 6.4, we show the corresponding states for the three dimensional problem, for the case of equal populations in each state. The coefficients α_i describe the rapid Rabi cycling, while the coefficients c_0 and d_1 describe a slow cycling between the ground state $|\phi_0\rangle$ and the dipole mode $|\phi_1\rangle$. If we project Eq. (6.1) onto an internal state $|i\rangle$, we find that each component cycles rapidly between the two modes $|\phi_0\rangle$ and $|\phi_1\rangle$. For short times, the coefficient d_1 is very small, so that its contribution to the density is negligible. However, as d_1 grows in magnitude due to an effective dipole coupling z caused by the displaced traps, the two-peaked structure of the dipole becomes

[2]The Gross-Pitaevskii equation is invarient with respect to a change in the global phase of the condensate.

prominent. The two mode model accounts for all of the major features of system observed experimentally in a very quantitative manner. We will derive this model and discuss it in detail throughout the chapter.

Once we had developed a detailed model to describe the system, it was clear that the behavior observed in the experiment was only one specific case of a more general behavior and we soon realized that other situations could be implemented. The displacement of the traps along the vertical axis acts as a kind of drive that couples the initial ground state condensate to a dipole mode. We generalized this driving mechanism in order to excite other modes with alternative symmetries. In particular, we considered the hypothetical situation of displacing the traps and then rotating them about the origin, as shown in Figure 6.12. Our two-mode model was easily extended to treat this situation, and we found that one of the components could be prepared in a vortex with one unit of angular momentum per atom if the trap rotation frequency was taken to be approximately equal to the effective Rabi frequency. We have encountered such a state in Figure 4.7 of Chapter 4. With the two-mode model providing some guidance, an experimental implementation of the idea was soon realized at JILA in the laboratory of Eric Cornell, and the first observations of a vortex in a dilute gas BEC were made.

In the following section, we present a derivation of our model for arbitrary driving symmetries. We then consider the specific case of static, offset traps in section 6.3 where a dipole mode is excited. We present results of calculations that help further clarify the behavior of the system. In section 6.4 we present a technique for preparing somewhat arbitrary topological modes and show results of calculations for various examples, including a vortex.

6.2 Derivation of the model

We now develop a simplified model based on a series of approximations that will lead us to the rather elegant two-mode description. For this problem, the external $\otimes$ internal representation presented in section 4.5 is most useful. We start with a more general GP equation than Eq. (4.20) by replacing the linear offset $z_0 z$ of the traps by a more general time-dependent term $\hat{H}_1(\boldsymbol{r},t)$ and we will include the possibility that the bare Rabi frequency varies linearly with z—as mentioned earlier, this is due to the spatially dependent detuning from the intermediate state in the two photon transition.. The most general form of the GP equation describing our system, then, is

$$i\frac{\partial}{\partial t}|\psi(t)\rangle = \left[\hat{H}_0\otimes\hat{1}+\hat{1}\otimes\left(\frac{\Omega}{2}\,\hat{\sigma}_x+\frac{\delta}{2}\hat{\sigma}_z\right)+\left(\hat{H}_1(t)+\hat{H}_2\right)\otimes\hat{\sigma}_z+\hat{H}_3\otimes\hat{\sigma}_x\right]|\psi(t)\rangle. \quad (6.2)$$

The term $\hat{H}_0\otimes\hat{1}$ acts on each internal state identically, with $H_0(\boldsymbol{r})$ given by

$$H_0(\mathbf{r}) = -\frac{1}{2}\nabla^2+\frac{1}{2}\left[\alpha^2\rho^2+z^2\right]+\langle\psi(t)|\hat{P}_{\mathbf{r}}\otimes\hat{\lambda}_+|\psi(t)\rangle\ . \quad (6.3)$$

The first term is the kinetic energy, and the second is a harmonic potential centered at the origin. The last term is a mean-field interaction term, with the matrix $\hat{\lambda}_+$ given in Eq. (4.22) in Chapter 4. The term $(\hat{H}_1(t)+\hat{H}_2)\otimes\hat{\sigma}_z$ can be thought of as a time dependent and spatially varying detuning. The term $\hat{H}_1(t)\otimes\hat{\sigma}_z$ acts with opposite sign on each state. In general, $H_1(\boldsymbol{r},t)$ is time-dependent and spatially varying with the form

$$H_1(\boldsymbol{r},t) = \kappa\big[f(\boldsymbol{r})\cos(\omega_r t)+g(\boldsymbol{r})\sin(\omega_r t)\big]. \quad (6.4)$$

We will consider specific forms for $H_1(\boldsymbol{r},t)$ throughout the chapter and specify κ, f, and g in particular cases. The term $\hat{H}_2 \otimes \hat{\sigma}_z$ also acts on each state with opposite sign and originates in the mean-field interaction with the form

$$H_2(\mathbf{r}) = \langle\psi(t)|\hat{P}_{\mathbf{r}} \otimes \hat{\lambda}_-|\psi(t)\rangle. \tag{6.5}$$

The matrix $\hat{\lambda}_-$ is given in Eq. (4.22) in Chapter 4. Finally, the term $\hat{H}_3 \otimes \hat{\sigma}_x$ couples the internal states, with $H_3(z)$ being a static term varying linearly with position along the vertical axis

$$H_3(z) = \frac{\chi}{2} z. \tag{6.6}$$

This term arises due to a subtle effect related to intermediate state in the two-photon transition not being trapped, which causes an effective linear variation in the bare Rabi frequency, where χ is the slope of this variation (see footnote 1 above).

6.2.1 Simplifying the mean-field terms

Throughout the chapter, we will present numerical calculations of Eq. (6.2). However, in order to gain an intuitive understanding of the behavior described by Eq. (6.2), we now make a series of approximations that will lead us to a rather simple model, which provides us with a great deal of predictive insight. The first simplification we make is to observe that for ^{87}Rb, the term H_2 can be rewritten as

$$H_2(\mathbf{r}) = \frac{\lambda_D}{2N}\, n(\mathbf{r},t), \tag{6.7}$$

where[3] $\lambda_D = \lambda_1 - \lambda_{12} = \lambda_{12} - \lambda_2$, and $n(\mathbf{r},t)$ is the total density. We have found in most of our calculations that the total density is very nearly invariant in time. We therefore assume here that $n(\mathbf{r})$ is static, and, in addition, we approximate it by the Thomas-Fermi limiting form. This allows us finally to write H_2 as

$$H_2(\mathbf{r}) = \frac{\delta_{\mathrm{MF}}}{2} + f_{\mathrm{MF}}(\mathbf{r}), \tag{6.8}$$

where $\delta_{\mathrm{MF}} = \lambda_D\, \mu_{\mathrm{TF}}/\lambda_{12}$ is an overall mean-field shift of the internal hyperfine levels, μ_{TF} is the chemical potential for the total population in the Thomas-Fermi limit, and $f_{\mathrm{MF}}(\mathbf{r}) = \lambda_D(\alpha^2\rho^2 + z^2)/(4\lambda_{12})$ is the Thomas-Fermi form of the density. Typically, for populations in the range $N = 8\times10^5$ to 10^6 atoms, we find this shift is $\delta_{\mathrm{MF}} = 30$ Hz to 35 Hz in a trap with $\nu_z = 65$ Hz and $\nu_{xy} = 24$ Hz.

The mean field term in Eq. (6.3) can also be simplified if we make the approximations that $(\lambda_{12}+\lambda_1)/2 \approx \lambda_{12}$ and $(\lambda_{12}+\lambda_2)/2 \approx \lambda_{12}$. Within this approximation we write $H_0 \to H_0'$ as

$$H_0'(\mathbf{r}) = -\frac{1}{2}\nabla^2 + \frac{1}{2}[\alpha^2\rho^2 + z^2] + \lambda_{12}(|\psi_1(\mathbf{r},t)|^2 + |\psi_2(\mathbf{r},t)|^2). \tag{6.9}$$

Note that for this term we do not take the total density to be static, but allow it to evolve in time.

[3] This simplification can be made for ^{87}Rb, and is only approximately true (i.e. within the error of the determination of the singlet and triplet scattering lengths).

Incorporating these two approximations into Eq. (6.2) gives us

$$i\frac{\partial}{\partial t}|\psi(t)\rangle = \left[\hat{H}_0'\otimes\hat{1}+\hat{1}\otimes\Big(\frac{\Omega}{2}\,\hat{\sigma}_x+\frac{\delta'}{2}\hat{\sigma}_z\Big)+\big(\hat{H}_1(t)+\hat{f}_{\rm MF}\big)\otimes\hat{\sigma}_z+\hat{H}_3\otimes\hat{\sigma}_x\right]|\psi(t)\rangle, \quad (6.10)$$

where we have rewritten the detuning to include the mean-field shift $\delta' = \delta + \delta_{\rm MF}$. Looking at Eq. (6.10), we can see that in the absence of the last three terms (eg. $H_1 = f_{\rm MF} = H_3 = 0$), the spatial and spin degrees of freedom are uncoupled, so that the internal states simply undergo the usual Rabi cycling independently of the motion of the condensate. It is useful to think of H_1 as a driving term that excites a topological mode in the system. We will consider specific examples in later sections. For the purposes of exciting a topological mode, the term $f_{\rm MF}$ due to the mean-field interaction acts as a contamination. We will show that the physical parameters can be chosen to suppress its effect on the system. We will show that the term H_3 helps explain an overall shift in the peak of the revival time (shown in Figure 6.2) for the case of offset traps.

6.2.2 Interaction picture representation

In this chapter we are concentrating on the situation where the coupling is strong, so that the frequency of the Rabi oscillations Ω is significantly larger than the trap frequency ν_z. In this case, the internal spin dynamics and the motion of the condensate in the trap occur on two different time scales. Therefore, it is useful to go to a rotating frame that eliminates the second term in Eq. (6.10) describing the fast Rabi oscillations between the two internal states. In the rotating frame, we will be able to understand more clearly how the terms $H_1(t)$, $f_{\rm MF}$, and H_3 in Eq. (6.10), which couple the motional and spin dynamics of the condensate, effect the system on a time scale much longer than the period of Rabi oscillation.

We go to the rotating frame, or interaction picture, by making a unitary transformation using the operator

$$U_I(t) = e^{-i\,\hat{1}\otimes(\frac{\Omega}{2}\hat{\sigma}_x+\frac{\delta'}{2}\hat{\sigma}_z)\,t}. \quad (6.11)$$

This can be rewritten in the equivalent form

$$U_I(t) = \hat{1}\otimes\Big(\cos(\Omega_{\rm eff}/2\,t)\hat{1} - \frac{i}{\Omega_{\rm eff}}\sin(\Omega_{\rm eff}/2\,t)\big[\Omega\hat{\sigma}_x+\delta'\hat{\sigma}_z\big]\Big), \quad (6.12)$$

where $\Omega_{\rm eff} = \sqrt{\Omega^2+\delta'^2}$. The state vector $|\psi^{(I)}(t)\rangle$ in the rotating frame is related to the state vector in the lab frame $|\psi(t)\rangle$ by

$$|\psi^{(I)}(t)\rangle = U_I^\dagger\,|\psi(t)\rangle\ . \quad (6.13)$$

In the rotating frame, the system evolves according to

$$i\frac{\partial}{\partial t}|\psi^{(I)}(t)\rangle = \hat{H}^{(I)}(t)|\psi^{(I)}(t)\rangle\ , \quad (6.14)$$

where $\hat{H}^{(I)}(t)$ is the interaction Hamiltonian

$$\begin{aligned}\hat{H}^{(I)}(t) &= \hat{H}_0'\otimes\hat{1}+\big(\hat{H}_1(t)+\hat{f}_{\rm MF}\big)\otimes\big(\alpha_{\rm x}(t)\hat{\sigma}_{\rm x}+\alpha_{\rm y}(t)\hat{\sigma}_{\rm y}+\alpha_{\rm z}(t)\hat{\sigma}_{\rm z}\big)\\ &+ \hat{H}_3\otimes\big(\beta_{\rm x}(t)\hat{\sigma}_{\rm x}+\beta_{\rm y}(t)\hat{\sigma}_{\rm y}+\beta_{\rm z}(t)\hat{\sigma}_{\rm z}\big). \quad (6.15)\end{aligned}$$

Note that $\hat{H}_0'$, $\hat{H}_1(t)$, $\hat{f}_{\rm MF}$, and $\hat{H}_3$ are unaffected by the unitary transformation to the rotating frame. The time-varying coefficients $\alpha_{\rm x}(t)$, $\alpha_{\rm y}(t)$, and $\alpha_{\rm z}(t)$ are

$$\begin{aligned}\alpha_{\rm x}(t) &= \frac{\Omega}{\Omega_{\rm eff}}\frac{\delta'}{\Omega_{\rm eff}}\big[1-\cos(\Omega_{\rm eff}t)\big]\\ \alpha_{\rm y}(t) &= \frac{\Omega}{\Omega_{\rm eff}}\sin(\Omega_{\rm eff}t)\\ \alpha_{\rm z}(t) &= \frac{\delta'^2}{\Omega_{\rm eff}^2}+\frac{\Omega^2}{\Omega_{\rm eff}^2}\cos(\Omega_{\rm eff}t),\end{aligned} \tag{6.16}$$

while the coefficients $\beta_{\rm x}(t)$, $\beta_{\rm y}(t)$, and $\beta_{\rm z}(t)$ are

$$\begin{aligned}\beta_{\rm x}(t) &= \frac{\Omega^2}{\Omega_{\rm eff}^2}+\frac{\delta'^2}{\Omega_{\rm eff}^2}\cos(\Omega_{\rm eff}t)\\ \beta_{\rm y}(t) &= -\frac{\delta'}{\Omega_{\rm eff}}\sin(\Omega_{\rm eff}t)\\ \beta_{\rm z}(t) &= \frac{\Omega}{\Omega_{\rm eff}}\frac{\delta'}{\Omega_{\rm eff}}\big[1-\cos(\Omega_{\rm eff}t)\big],\end{aligned} \tag{6.17}$$

6.2.3 Coarse graining approximation

At first sight it appears that we have actually made the problem more complicated by going to the interaction picture representation due to the appearance of the extra time-varying terms proportional to $\alpha_i(t)$ and $\beta_i(t)$. However, in this rotating frame, we expect the system $|\psi^{(I)}(t)\rangle$ to evolve on a much slower time scale than the period of Rabi oscillation. We therefore time average over the rapidly oscillating terms, which is equivalent to coarse-graining Eq (6.14). The time averaging depends on the frequency ω_r of $H_1(t)$, so we consider two cases separately, a slow or static drive $\omega_r \approx \omega_z$, and a fast drive $\omega_r \approx \Omega_{\rm eff}$ (remember we are considering the strong coupling limit so that $\omega_z << \Omega_{\rm eff}$).

Slow or static drive $\omega_r \approx \omega_z$ and small detuning $\delta' \ll \Omega$

If the drive varies slowly on the time scale of the period of Rabi oscillation, then we can assume $H_1(t)$ is approximately constant over one Rabi cycle. In this case, coarse graining Eq (6.14) allows us to reduce the coefficients $\alpha_i(t)$ and $\beta_i(t)$ to $\alpha_{\rm x} = \beta_z = \delta'\,\Omega/\Omega_{\rm eff}^2$, $\alpha_{\rm y} = \beta_y = 0$, $\alpha_{\rm z} = \delta'^2/\Omega_{\rm eff}^2$, and $\beta_x = \Omega^2/\Omega_{\rm eff}^2$. This leads to the simplified form of Eq (6.15)

$$\begin{aligned}\hat{H}^{(I)}(t) &= \hat{H}_0'\otimes\hat{1}+\big(\hat{H}_1(t)+\hat{f}_{\rm MF}\big)\otimes\Big(\frac{\delta'\,\Omega}{\Omega_{\rm eff}^2}\hat{\sigma}_{\rm x}+\frac{\delta'^2}{\Omega_{\rm eff}^2}\hat{\sigma}_{\rm z}\Big)\\ &+ \hat{H}_3\otimes\Big(\frac{\Omega^2}{\Omega_{\rm eff}^2}\hat{\sigma}_{\rm x}+\frac{\delta'\,\Omega}{\Omega_{\rm eff}^2}\hat{\sigma}_{\rm z}\Big)\end{aligned} \tag{6.18}$$

The interaction Hamiltonian can be brought to an even simpler form if we assume the detuning is small $\delta' \ll \Omega$. In this case, we can drop the term proportional to $\delta'^2/\Omega_{\rm eff}^2$. We also assume that H_3 is much smaller in magnitude than H_1, which allows us to also drop the term $\hat{H}_3\otimes\delta'\,\Omega/\Omega_{\rm eff}^2\hat{\sigma}_{\rm z}$. This finally leaves us with

$$\hat{H}^{(I)}(t) = \hat{H}_0'\otimes\hat{1}+\Big[\frac{\delta'\,\Omega}{\Omega_{\rm eff}^2}\big(\hat{H}_1(t)+\hat{f}_{\rm MF}\big)+\frac{\Omega^2}{\Omega_{\rm eff}^2}\hat{H}_3\Big]\otimes\hat{\sigma}_{\rm x}. \tag{6.19}$$

In the sections that follow, we will investigate this regime—of a slow or static drive and a small detuning—in detail for specific choices of $H_1(t)$.

Fast drive $\omega_r \approx \Omega_{\rm eff}$ and large detuning $\delta' \gg \Omega$

In the case of a fast drive we must time average the product of $H_1(t)$ and the coefficients $\alpha_i(t)$ and $\beta_i(t)$. These products can be written in terms of cosines and sines of the sum $(\Omega_{\rm eff} + \omega_r)$ and difference $(\Omega_{\rm eff} - \omega_r)$. If we make the assumption that $\omega_r \approx \Omega_{\rm eff}$, then we can drop all of the counter-rotating terms oscillating at the frequency $(\Omega_{\rm eff} + \omega_r)$, but keep the terms rotating at $(\Omega_{\rm eff} - \omega_r)$ when we time average. As for the static terms proportional to $f_{\rm MF}$ and H_3, the same time averaging we did in the previous subsection applies. The result is the following approximate form of the interaction Hamiltonian

$$\begin{aligned}\hat{H}^{(I)}(t) &= \hat{H}'_0 \otimes \hat{1} + \hat{f}_{\rm MF} \otimes \Big(\frac{\delta'\,\Omega}{\Omega_{\rm eff}^2}\hat{\sigma}_{\rm x} + \frac{\delta'^2}{\Omega_{\rm eff}^2}\hat{\sigma}_{\rm z}\Big) + \hat{H}_3 \otimes \Big(\frac{\Omega^2}{\Omega_{\rm eff}^2}\hat{\sigma}_{\rm x} + \frac{\delta'\,\Omega}{\Omega_{\rm eff}^2}\hat{\sigma}_{\rm z}\Big) \\ &+ \frac{\kappa}{2}\frac{\Omega}{\Omega_{\rm eff}}\Big\{\frac{\delta'}{\Omega_{\rm eff}}\big[\varrho\, g\sin(\Delta t) - f\cos(\Delta t)\big]\sigma_x + \big[\varrho\, g\cos(\Delta t) + f\sin(\Delta t)\big]\sigma_y \\ &+ \frac{\Omega}{\Omega_{\rm eff}}\big[f\cos(\Delta t) - \varrho\, g\sin(\Delta t)\big]\sigma_z\Big\}, \qquad (6.20)\end{aligned}$$

where $\Delta = \Omega_{\rm eff} - \omega_r$ and $\varrho = \omega_r/|\omega_r|$ gives the direction of rotation.

This looks like a rather complicated result, however, it can be further simplified by assuming a very large detuning $\delta' \gg \Omega$. This allows us to neglect terms of order $(\Omega/\Omega_{\rm eff})^2$. If we further take $|\delta'| \approx \Omega_{\rm eff}$ then we can write $\hat{H}^{(I)}(t)$ as

$$\begin{aligned}\hat{H}^{(I)}(t) &= \hat{H}'_0 \otimes \hat{1} + \hat{f}_{\rm MF} \otimes \Big(\hat{\sigma}_{\rm z} + \frac{\Omega}{\Omega_{\rm eff}}\hat{\sigma}_{\rm x}\Big) + \hat{H}_3 \otimes \frac{\Omega}{\Omega_{\rm eff}}\hat{\sigma}_{\rm z} \\ &- \frac{\kappa}{2}\frac{\Omega}{\Omega_{\rm eff}}\Big(\hat{a}_s^\dagger\hat{\sigma}_+ e^{i\Delta t} + \hat{a}_s\hat{\sigma}_- e^{-i\Delta t}\Big), \qquad (6.21)\end{aligned}$$

for $\delta > 0$, and

$$\begin{aligned}\hat{H}^{(I)}(t) &= \hat{H}'_0 \otimes \hat{1} + \hat{f}_{\rm MF} \otimes \Big(\hat{\sigma}_{\rm z} - \frac{\Omega}{\Omega_{\rm eff}}\hat{\sigma}_{\rm x}\Big) - \hat{H}_3 \otimes \frac{\Omega}{\Omega_{\rm eff}}\hat{\sigma}_{\rm z} \\ &+ \frac{\kappa}{2}\frac{\Omega}{\Omega_{\rm eff}}\Big(\hat{a}_s\hat{\sigma}_+ e^{-i\Delta t} + \hat{a}_s^\dagger\hat{\sigma}_- e^{i\Delta t}\Big), \qquad (6.22)\end{aligned}$$

for $\delta < 0$. Here we have defined $\hat{a}_s = \hat{f} - i\,\hat{g}$ and $\hat{a}_s^\dagger = \hat{f} + i\,\hat{g}$, and we have taken $\varrho = 1$. Also, the matrices $\hat{\sigma}_+$ and $\hat{\sigma}_-$ are defined as $\hat{\sigma}_+ = (\hat{\sigma}_x + i\hat{\sigma}_y)/2$ and $\hat{\sigma}_- = (\hat{\sigma}_x - i\hat{\sigma}_y)/2$. We will investigate these results in more detail later in this chapter when we consider this regime of a fast drive and a large detuning.

6.3 Static drive due to offset traps

As described in Chapter 4, a typical situation for a condensate of ^{87}Rb atoms in a TOP trap is for there to be a static offset between the traps for the two hyperfine states $|1\rangle$ and $|2\rangle$. This offset was a primary ingredient in drawing an analogy to the Josephson junction in the weak-coupling limit described in the previous chapter. By adjusting the quadrupole gradient and the intensity and frequency of the rotating field, various trap configurations

can be attained. In this section, we consider the case where $\nu_z = 65$, $\nu_\rho = 24$ Hz, and the traps for each state are separated by $2z_0 = 0.4\,\mu$m along the vertical axis (see Figure 5.1). This corresponds to setting the drive term to $\hat{H}_1(t) = -z_0 z$ in Eq. (6.19), so that $\hat{H}^{(I)}(t)$ can be written as

$$\hat{H}^{(I)}(t) = \hat{H}_0' \otimes \hat{1} + \big[-C_1 z + C_2(\gamma^2\rho^2 + z^2)\big] \otimes \hat{\sigma}_{\rm x}, \tag{6.23}$$

where $C_1 = (z_0\delta' - \chi\Omega/2)(\Omega/\Omega_{\rm eff}^2)$ and $C_2 = [\lambda_D/(4\lambda_{12})](\delta'\Omega/\Omega_{\rm eff}^2)$. The parameter C_1 varies linearly with detuning δ', with an overall offset given by $(\chi/2)\Omega^2/\Omega_{\rm eff}^2$. For now, we will neglect this offset in the development that follows, by taking $\chi \to 0$, so that $C_1 \to z_0\delta'\Omega/\Omega_{\rm eff}^2$. Later in this section we will return to this issue and briefly discuss how this offset modifies our results. For typical values of the physical parameters, the third term in Eq. (6.23) arising from the mean-field interaction due to the difference in scattering lengths is small, with $C_2 \approx 0.002$, compared to $C_1 \approx 0.04$. Therefore, we also neglect this term by taking $C_2 \to 0$.

With the approximations $\chi \approx 0$ and $C_2 \approx 0$, Eq. (6.23) becomes

$$\hat{H}^{(I)}(t) = \hat{H}_0' \otimes \hat{1} - C_1 z \otimes \hat{\sigma}_{\rm x}, \tag{6.24}$$

We refer to this result Eq. (6.23) as the coarse-grained, small detuning (CGSD) model to distinguish it from the two-mode model presented below, which makes further assumptions.

6.3.1 Two-mode model

It is useful to define a basis of motional states with which to describe the system in the rotating frame. A natural choice is the set of instantaneous eigenstates of $\hat{H}_0'$, which satisfy

$$\begin{aligned} \Big[-\frac{1}{2}\nabla^2 + \frac{1}{2}\big(\gamma^2\rho^2 + z^2\big) + \lambda_{12}\tilde{n}(\mathbf{r},t)\Big]\phi_i(\mathbf{r}) &= \epsilon_i\,\phi_i(\mathbf{r}) \\ \int_{-\infty}^{\infty} \phi_i(\mathbf{r})\,\phi_j(\mathbf{r})\,d^3r &= \delta_{i,j}\ , \end{aligned} \tag{6.25}$$

where the index i refers to all of the relevant quantum numbers that uniquely specify each eigenstate, $i = \{n_z, n_\rho, n_\phi\}$, given the cylindrical symmetry of the system. In general, many modes can be occupied and the state vector is written

$$|\psi^{(I)}(t)\rangle = \sum_i \Big[c_i(t)|\phi_i\rangle|1\rangle + d_i(t)|\phi_i\rangle|2\rangle\Big]\ , \tag{6.26}$$

where $\phi_i(\mathbf{r}) = \langle\mathbf{r}|\phi_i\rangle$. The density appearing in Eq. (6.25) is then

$$\tilde{n}(\mathbf{r},t) = \Big|\sum_i c_i(t)\phi_i(\mathbf{r})\Big|^2 + \Big|\sum_i d_i(t)\phi_i(\mathbf{r})\Big|^2. \tag{6.27}$$

It is clear that the set of coupled eigenvalue equations given in Eq. (6.25) is nonlinear and requires a numerical procedure that will converge upon the solution in a self-consistent manner. The eigenstates $\phi_i(\mathbf{r})$ and eigenenergies ϵ_i depend on time implicitly through the coefficients $c_i(t)$ and $d_i(t)$, however we do not show this time dependence in order to simplify the notation. We assume that the eigenbasis evolves slowly in time so that the adiabatic condition is satisfied [106]. These topological modes $\phi_i(\mathbf{r})$ are similar to the

states plotted in Figure 3.7 for the single component and in Figure 4.9 in the two-component case.

Based on the experiment reported in [13] the initial motional state of the system is $\psi_1^{(\mathrm{I})}(\mathbf{r},0) = \phi_0(\mathbf{r} - z_0\hat{z})$; the system is in the ground state of $\hat{H}_0'$, but displaced from the origin along the vertical axis by z_0. This displacement is small compared to the width w_z of the condensate $z_0/w_z \approx 0.01$. We therefore approximate the initial state of the system as $|\psi^{(I)}(t)\rangle = |\phi_0\rangle|1\rangle$.

The system in the rotating frame evolves according to the Hamiltonian described by Eq. (6.24). The term $-C_1 z \otimes \hat{\sigma}_{\mathrm{x}}$ couples the internal states $|1\rangle$ and $|2\rangle$ via $\hat{\sigma}_{\mathrm{x}}$. It also drives transitions between motional states via the dipole operator $\hat{z}$. The dipole matrix element $\langle z\rangle_{ij} = \langle\phi_i|\hat{z}|\phi_j\rangle$ is the largest between neighboring states and falls off quickly as $|i-j|$ increases. For a small coupling parameter C_1, we expect the coupling to the first excited state $|\phi_1\rangle$ to dominate the other transitions, making the evolution of the system predominantly a two state evolution. We therefore make the approximation that the system occupies only two modes

$$|\psi^{(I)}(t)\rangle = c_0(t)\,|\phi_0\rangle|1\rangle + d_1(t)\,|\phi_1\rangle|2\rangle\ , \tag{6.28}$$

where $|\phi_0\rangle$ is the ground state $i = \{0,0,0\}$ and $|\phi_1\rangle$ is the first excited state with odd parity along the z-axis $i = \{1,0,0\}$.

If we substitute this ansatz into Eq. (6.14), using the Hamiltonian described by Eq. (6.24), we get the equation of motion for the coefficients $c_0(t)$ and $d_1(t)$

$$i\begin{pmatrix}\dot{c}_0\\ \dot{d}_1\end{pmatrix} = \begin{pmatrix}\epsilon_0 & -C_1\langle z\rangle_{01}\\ -C_1\langle z\rangle_{01} & \epsilon_1\end{pmatrix}\begin{pmatrix}c_0\\ d_1\end{pmatrix}\ , \tag{6.29}$$

where we have neglected the time rate-of-change of the slowly-varying adiabatic eigenbasis. This coupled pair of equations must be solved numerically by updating the energies ϵ_i and the dipole matrix element $\langle z\rangle_{01}$ from solving Eq. (6.25) at each time step. However, in order to see how the behavior depends on the various physical parameters, one can obtain a simple estimate of the solution by fixing ϵ_i and $\langle z\rangle_{01}$ to their initial values. In this case the solution of Eq. (6.29) is trivial and is given by $c_0(t) = \cos(\Omega_{01}/2\,t) - i(\Delta\epsilon_{01}/\Omega_{01})\sin(\Omega_{01}/2\,t)$ and $d_1(t) = -i(2C_1\langle z\rangle/\Omega_{01})\sin(\Omega_{01}/2\,t)$, where $\Delta\epsilon_{01} = \epsilon_1 - \epsilon_0$ and $\Omega_{01} = \sqrt{4C_1^2\langle z\rangle^2 + \Delta\epsilon_{01}^2}$. In the rotating frame, the system oscillates between the two states at a frequency of Ω_{01}, which is much slower than the effective Rabi frequency Ω_{eff}.

The oscillation frequency Ω_{01} increases with increasing detuning δ' and increasing trap separation z_0 through the coupling parameter C_1. The amplitude of oscillation depends on the energy spacing between modes $\Delta\epsilon_{01}$. This splitting is a fraction of $\hbar\omega_z$ due to the effect of the mean-field interaction: $\Delta\epsilon_{01}$ decreases with increasing population N. In addition, the dipole matrix element $\langle z\rangle$ increases with increasing N, since the width of the condensate increases with increasing population. The effect of the mean-field, then, is to enhance the coupling between the ground and dipole modes.

The solution in the lab frame can be obtained by applying $U_{\mathrm{I}}(t)$ from Eq (6.12) to $|\psi^{(\mathrm{I})}\rangle$ in Eq. (6.28) to yield

$$\begin{aligned}|\psi(t)\rangle &= (\alpha_1(t)c_0(t)\,|\phi_0\rangle + \alpha_2(t)d_1(t)\,|\phi_1\rangle)|1\rangle\\ &+ (\alpha_2(t)c_0(t)\,|\phi_0\rangle + \alpha_1^*(t)d_1(t)\,|\phi_1\rangle)|2\rangle\ ,\end{aligned} \tag{6.30}$$

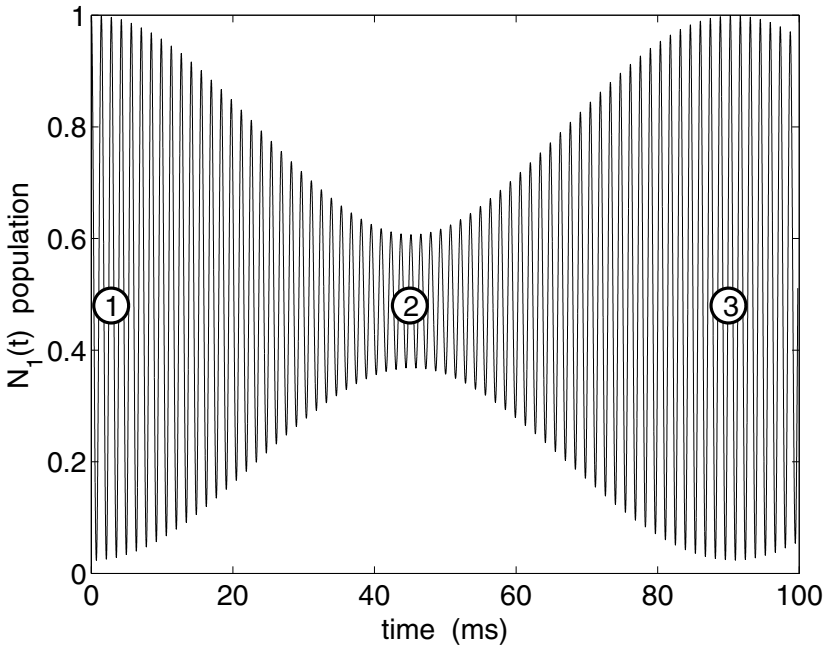

Figure 6.5: Modulation of the Rabi oscillations. The fractional population in state $|1\rangle$ is plotted as a function of time, obtained from a numerical solution of the one dimensional version of Eq. (6.10). The values of the various parameters are given in the text. In Figure 6.6, the densities for both states are shown for three different Rabi cycles designated by the circled numbers in this plot.

where the rapidly varying coefficients are $\alpha_1(t) = \cos(\Omega_{\text{eff}}/2\,t) - i(\delta'/\Omega_{\text{eff}})\sin(\Omega_{\text{eff}}/2\,t)$ and $\alpha_2(t) = -i(\Omega/\Omega_{\text{eff}})\sin(\Omega_{\text{eff}}/2\,t)$. Eq. (6.30) is the main result of this section, with which we can explain the essential properties of the system. During the first few Rabi cycles $t \approx 1/\Omega_{\text{eff}}$, the coefficient $d_1(t) \approx 0$, so that the solution for short times is $|\psi(t)\rangle = (\alpha_1(t)|1\rangle + \alpha_2(t)|2\rangle)\,|\phi_0\rangle$. That is, for short times, the internal and external degrees of freedom appear to be decoupled and the system simply oscillates rapidly between internal states. However, for longer times, the coefficient $d_1(t)$ grows in magnitude as $c_0(t)$ correspondingly decreases. This results in a modulation of the Rabi oscillations. Furthermore, a two-peaked structure in the density appears, associated with the first-excited state $|\phi_1\rangle$.

6.3.2 Results of calculations

The main goal of this section is to illustrate the behavior of the system by showing results of numerical calculations. For this purpose, it is useful to treat the system in only one dimension—along the vertical axis. Values of most of the physical parameters are given in Table 6.3.2. Values of the remaining parameters are stated for each case considered in the text.

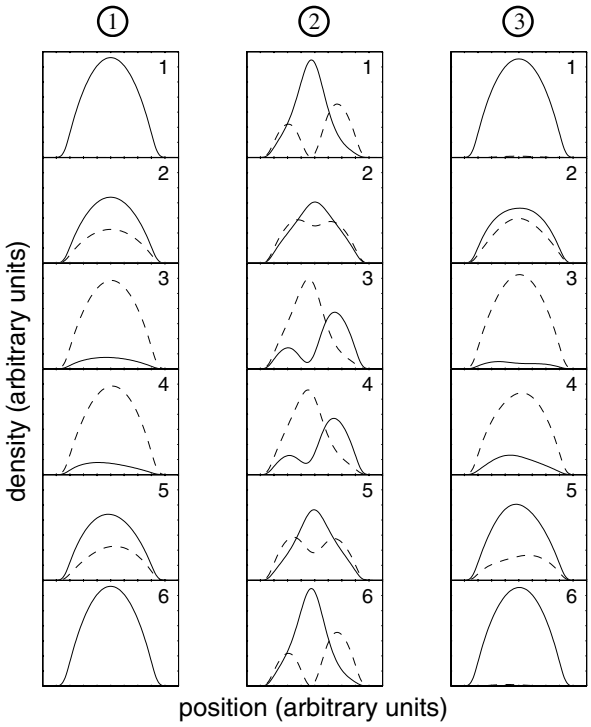

Figure 6.6: Snapshots of the density of each state for three different Rabi cycles corresponding to the three circled numbers in Figure 6.5. The first two strips resemble the two strips of snapshots taken from experimental data shown in Figure 6.3. The solid line is the density of the $|1\rangle$ state, while the dashed line is that of the $|2\rangle$ state. Each snapshot within a set is numbered in sequential order. The first set starts at $t = 0$ ms, and runs for a full Rabi cycle 1.41 ms. The second and third sets begin at $t = 45.2$ ms and $t = 90.3$ ms, respectively. The time increment between snapshots is $\Delta t = 0.28$ ms for all three sets.

Understanding the dual dynamics

In Figure 6.5 we plot the fractional population of state $|1\rangle$, given by $N_1(t) = \int |\langle z|\langle 1|\psi(t)\rangle|^2 dz$, for the case of $\Omega = 700$ Hz and $\delta' = 100$ Hz. This is a numerical solution of Eq. (6.10) with the terms $f_{\rm MF}$ and H_3 set to zero. The population is cycling rapidly at the effective Rabi frequency $\Omega_{\rm eff} = 707$ Hz, while simultaneously being modulated at a much lower frequency of about 11 Hz.

In order to visualize how the spin and motional dynamics become entangled over a time long compared to the Rabi period, we show snapshots of the density of each state in Figure 6.6. Three different sets of snapshots are shown, corresponding to the three circled numbers in Figure 6.5. A full Rabi cycle is shown for each set. The first two strips resemble the two strips of snapshots taken from experimental data shown in Figure 6.3. The first set begins at $t = 0$ with all of the atoms in the $|1\rangle$ internal state and in the mean-field ground state of the trap $|\phi_0\rangle$. During this first Rabi cycle, the shape of the density profile for each internal state does not change much—only the height changes. That is, the motional state remains the ground state while population cycles rapidly between internal states, as

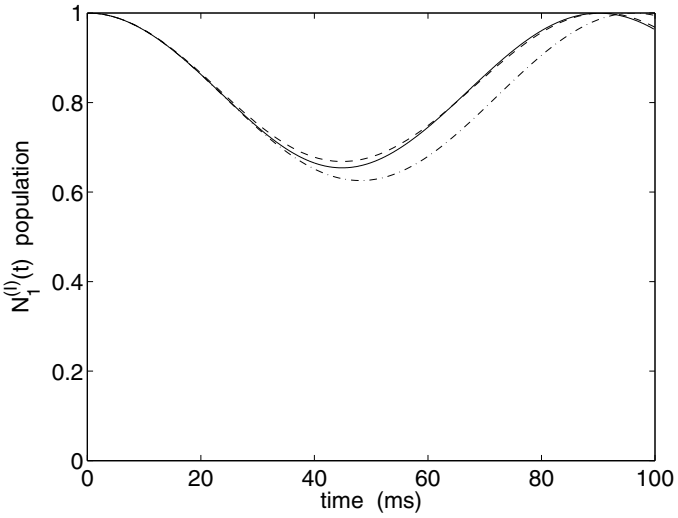

Figure 6.7: The fractional population of the $|1\rangle$ state in the rotating frame. The solid line is the solution given by the CGSD model, while the dot-dashed line corresponds to the solution of the two-mode model. If the two-mode model is extended to include coupling to the first even-parity excited mode, then we get better agreement to the CGSD model, as shown by the dashed line.

discussed below Eq. (6.30).

The second set of snapshots in Figure 6.6 is taken at around $t = 45$ ms, which is halfway through the modulation. The density profiles for each spin state cycle rapidly between a single-peaked and a double-peaked structure. For example, in the first snapshot, the $|1\rangle$ state is in the single-peaked structure, while the $|2\rangle$ state is in the double-peaked structure, but halfway through the Rabi cycle the situation is reversed, as shown in the third and fourth snapshots. Finally, at about $t = 90$ ms when the amplitude of the Rabi oscillations has revived, the third set shows that the motional and spin degrees of freedom appear to be decoupled again, with the density profile of each spin state appearing as it did during the first Rabi cycle.

This peculiar behavior is most easily understood by going to the rotating frame. In Figure 6.7, we plot the fractional population in the $|1\rangle$ state in the rotating frame $N_1^{(I)}(t) = \int |\langle z|\langle 1|\psi^{(I)}(t)\rangle|^2 dz$. The solid line corresponds to the CGSD model. In the rotating frame, population is slowly transferred out of the $|1\rangle$ state due to the coupling from $\hat{H}'_z \otimes \hat{\sigma}_x$ in Eq. (6.18).

In the rotating frame, the system is being excited out of the ground state $|\phi_0\rangle$ due to the dipole coupling H'_z. This can be seen in the top strip of snapshots in Figure 6.8, where the density of each spin state in the rotating frame is shown, corresponding to the solid line in Figure 6.7. Initially, all of the atoms are in the $|1\rangle$ internal state and the mean-field ground state of the trap $|\phi_0\rangle$. Due to the dipole coupling, population is transferred out of the ground state. The strongest coupling is between the ground $|\phi_0\rangle$ and the first excited $|\phi_1\rangle$ modes. These eigenmodes are shown in the bottom strip of Figure 6.8. They evolve slowly in time as the coefficients $c_0(t)$ and $d_1(t)$ change. For example, initially the ground state is just the Thomas-Fermi-like ground state, since all of the population is in that state. However, at

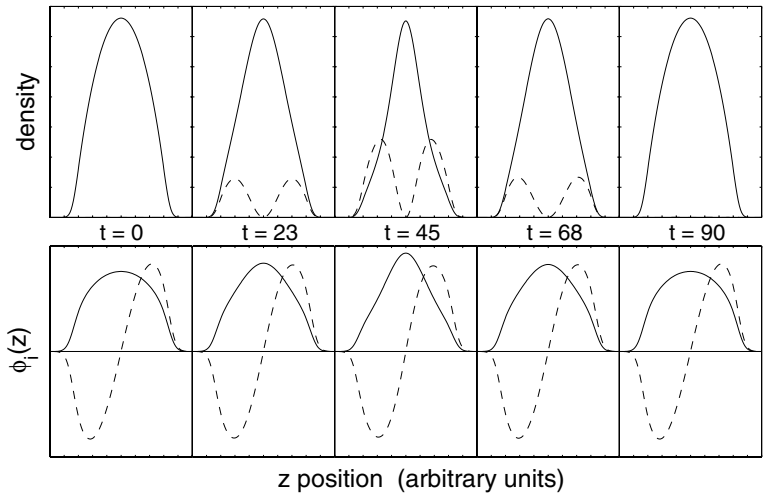

Figure 6.8: Ground and dipole states. The top strip of this plot shows snapshots of the density of each state corresponding to the solution of the CGSD model given by the solid line in Figure 6.7. The bottom strip shows the corresponding two self-consistent eigenmodes given by the solution of Eq. (6.25). The times of each snapshot are shown in the region between the two strips, in units of milliseconds. The solid line corresponds to the density of the $|1\rangle$ state, while the dashed is that of the $|2\rangle$ state.

$t = 45$ ms, about one-third of the population is in the first excited mode, which pinches the ground state due to the mean-field interaction term. That is why the self-consistent ground state at $t = 45$ ms is narrower than at $t = 0$.

It is clear from Figure 6.7 that the low-frequency modulation of the rapid Rabi oscillations in the lab frame is just the frequency of oscillation in the rotating frame between the states $|\phi_0\rangle|1\rangle$ and $|\phi_1\rangle|2\rangle$. This is reflected in the two-mode solution given by Eq. (6.30), which also helps explain the peculiar behavior of the densities shown in Figure 6.6. In the lab frame the system is cycling rapidly between the two modes shown in Figure 6.8. The initial values of the energies are $\epsilon_0 = 13.6\,\hbar\omega_z$ and $\epsilon_1 = 13.7\,\hbar\omega_z$, which makes $\Delta_{01} = 0.1\,\hbar\omega_z$. This small energy splitting is due to the effect of the mean field, since in the limit $N \to 1$ these energies move apart by a factor of ten, which greatly reduces the coupling between the modes and thus greatly reduces the modulation effect.

If we make the two-mode ansatz and solve Eq. (6.29), we get the dot-dashed line in Figure 6.7. The discrepancy from the solid line arises due to a weak coupling between the first $|\phi_1\rangle$ and second $|\phi_2\rangle$ excited modes. If we extend our two-state model to include this third mode, we get the dashed line in Figure 6.7, which nearly sits on top of the solid line. In this case, the second excited mode $|\phi_2\rangle$ gains less than 5% of the total population.

Dependence on detuning

In Figure 6.9, we show how the behavior of the system depends on the detuning δ'. The Rabi frequency $\Omega = 700$ Hz was held fixed for each plot while the detuning was varied from zero at the top $\delta' = 0$ to $\delta' = 200$ Hz in the bottom plot. As predicted by the coupling parameter $C_1 = z_0\,\delta'\,\Omega/\Omega_{\rm eff}^2$ in the CGSD model, no coupling between motional states

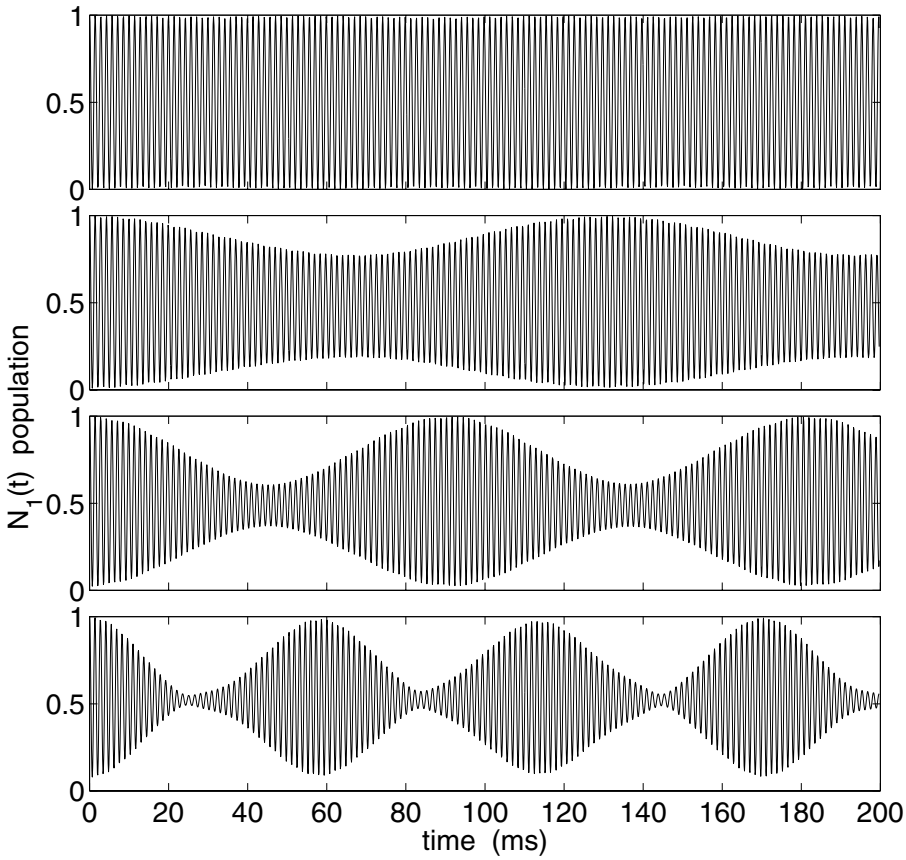

Figure 6.9: The fractional population in the $|1\rangle$ state for four different values of the detuning, obtained from a numerical solution of Eq (6.10). Starting from the top, the detuning is $\delta' = 0$, $\delta' = 50$ Hz, $\delta' = 100$ Hz, and $\delta' = 200$ Hz. The values of the other parameters are given in the text.

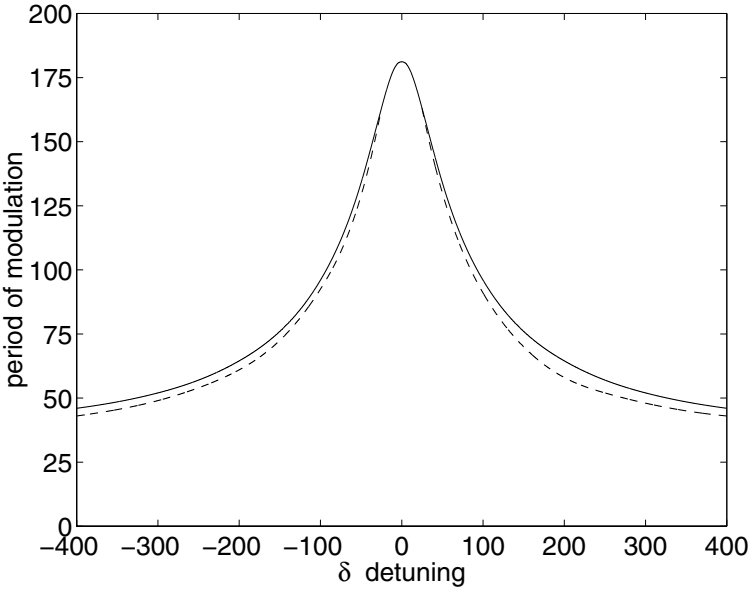

Figure 6.10: The period of modulation as a function of detuning δ'. The dashed line corresponds to the numerical solution of the one-dimensional version of Eq. (6.10), while the solid line was obtained from a numerical solution of the two-mode model Eq. (6.29). The Rabi frequency was $\Omega = 700$ Hz.

occurs if $\delta' = 0$, and thus the Rabi oscillations experience no modulation. As δ' is increased the motional-state coupling becomes stronger and we expect the modulation frequency to increase. The amplitude of modulation also increases as the detuning is increased.

We show the dependence of the period of modulation on detuning more explicitly in Figure 6.10. The dashed line is the numerical solution of the full problem given by Eq. (6.10), while the solid line is the numerical solution of the two-mode model given by Eq. (6.29). Here we would like to point out that, had we included the spatial variation of the bare Rabi frequency described by H_3, the peak of the curve in Figure 6.9 would not sit at zero detuning, but would be shifted by $(\chi/2)\Omega^2/\Omega_{\text{eff}}^2$, where χ is the slope of the spatial variation of the bare Rabi frequency. (see Eq. (6.23)). In the experiments at JILA, a shift was also seen, and we attribute it to this effect.

Dependence on trap displacement

In Figure 6.11, we show how the behavior of the system depends on the trap displacement z_0. The Rabi frequency $\Omega = 700$ Hz and the detuning $\delta' = 100$ Hz were held fixed, while the trap displacement was varied from zero $z_0 = 0$ in the top plot to $z_0 = 1\,\mu$m in the bottom plot. Again, the coupling parameter C_1 predicts no modulation if $z_0 = 0$. As z_0 is increased, the frequency of modulation increases as the system is driven harder. However, for the large separation in the bottom plot, the modulation becomes highly irregular and the two-mode model most certainly breaks down. This behavior may be chaotic and warrants further investigation.

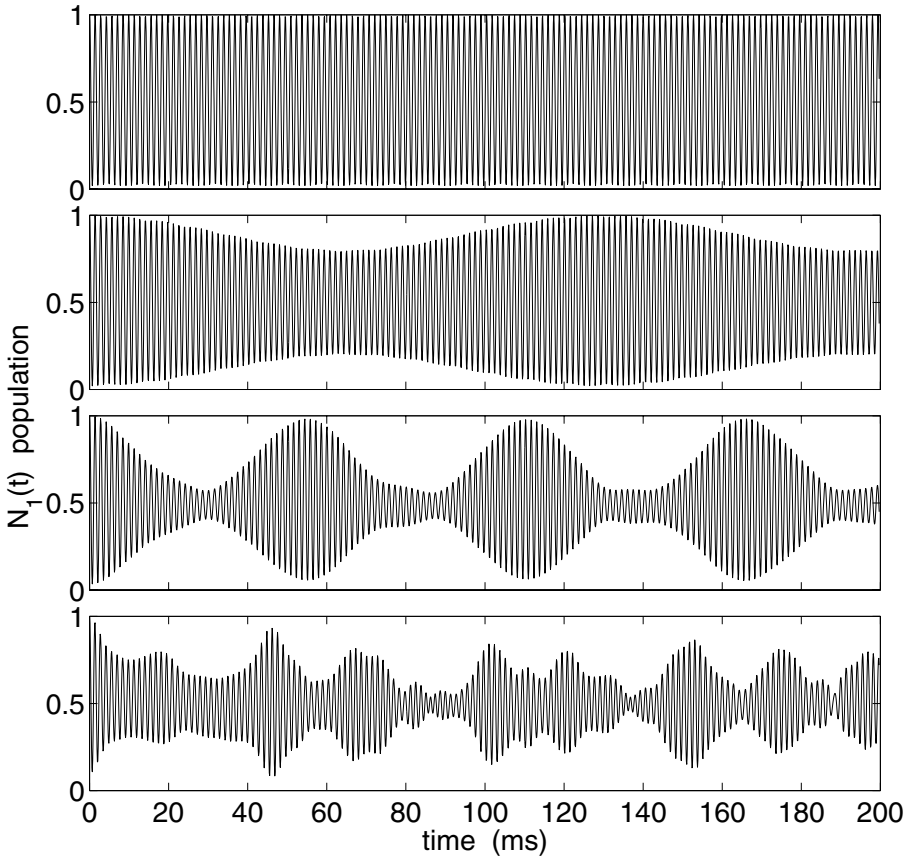

Figure 6.11: The fractional population in the $|1\rangle$ state for four different values of the trap displacement z_0, obtained from a numerical solution of Eq (6.10). Starting from the top, the displacement is $z_0 = 0$, $z_0 = 0.1\,\mu$m, $z_0 = 0.4\,\mu$m, and $z_0 = 1.0\,\mu$m. The values of the other parameters are given in the text.

Table 6.1: Values used for the various physical parameters appearing in our calculations. The scattering lengths are taken from [10].

N	8×10^5	ν_z	$65\,\mathrm{Hz}$
a_{21}	$5.5(3)\,\mathrm{nm}$	ν_ρ	$24\,\mathrm{Hz}$
a_{22}	$0.97\,a_{21}$	z_{sho}	$1.3\,\mu\mathrm{m}$
a_{11}	$1.03\,a_{21}$	z_0	$0.2\,\mu\mathrm{m}$

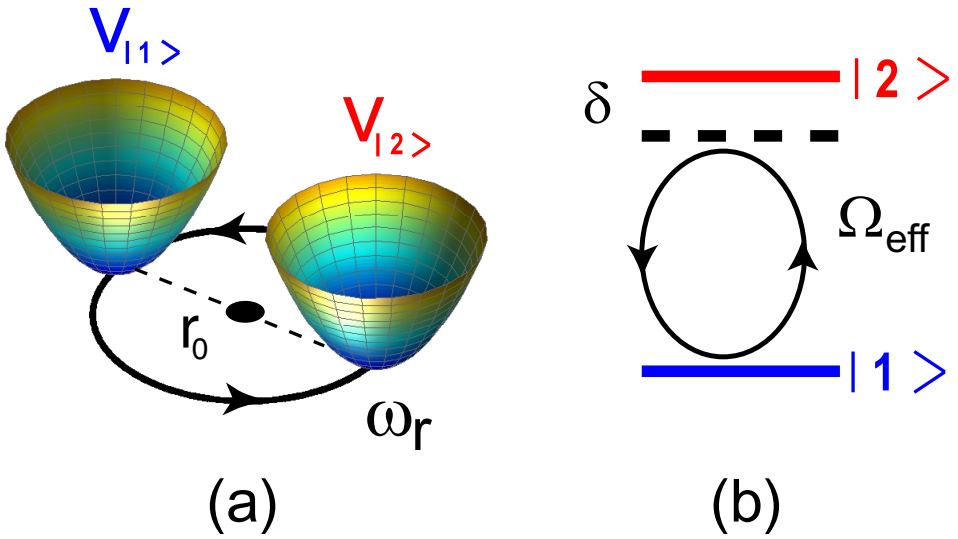

Figure 6.12: State preparation scheme. (a) If the two traps are rotated in the xy-plane about the z axis at a frequency ω_r, (b) while simultaneously driving transitions between the two internal states at the effective Rabi frequency Ω_{eff}, a vortex mode possessing one unit of angular momentum can be prepared if $\omega_r \approx \Omega_{\text{eff}}$.

6.4 Harmonic drive: A refined state preparation scheme

In the previous section we considered the case of a static drive $H_1 = -z_0 z$ that resulted in the excitation of a dipole mode due to the symmetry of the dipole operator $\hat{z}$. Suppose we want to excite a vortex mode; what particular form for $H_1(\boldsymbol{r}, t)$ should we take? A reasonable hypothesis is to displace the traps by some distance r_0 in the $x - y$ plane and then rotate the traps around the origin at some frequency ω_r, as illustrated in Figure 6.12. This corresponds to taking $f(\boldsymbol{r}) = x$, $g(\boldsymbol{r}) = y$, and $\kappa = m\omega_{xy}^2 r_0$ for the drive $H_1(\boldsymbol{r}, t)$ in Eq. (6.4). So, the centers of the two traps rotate about the origin, while at the same time the internal states of the atoms undergo Rabi oscillations. We will show that this configuration does indeed excite a unit vortex in one of the components in a very controlled way.

To achieve this experimentally , one can shine a laser beam along the z axis into the trap, so that the cloud sits in the middle of the Gaussian beam waist where the gradient of the beam intensity is approximately linear; this gives rise to a constant force on the atoms. If the frequency of the laser is tuned between the two hyperfine states, the optical dipole force acts in opposite directions for each state—this gives the form $\hat{\sigma}_z$ for the internal part, and the linear potential for the external part. If the beam is then rotated continuously, we obtain the desired result shown in Figure 6.12. There is one drawback, however: there will be heating due to spontaneous emission, which can limit the lifetime of the trap. For our system, however, this turns out not to be a limiting factor.

Now that we have the basic form of the drive H_1, we must decide on a frequency ω_r at which to rotate the traps. Looking back to section 6.2, we see there are basically two

choices, corresponding to the two main frequencies in the problem: we can either rotate the traps slowly at a frequency close to the trap frequency $\omega_r \approx \omega_{xy}$, or we can rotate them close to the effective Rabi frequency $\omega_r \approx \Omega_{\rm eff}$. We have considered both cases, and although both work, the fast drive is much more effective. The main problem with the slow drive is that the time scale for coupling to the vortex is very long, on the order of seconds in a $\nu_{xy} = 10$ Hz trap. In sharp contrast, for a fast rotation $\omega_r \approx \Omega_{\rm eff}$, a vortex can be prepared in less than 100 ms. If we wanted to show the details for the slow drive, we would start with Eq. (6.19) and derive a two-mode model, just as we did in the previous section for the static drive. Instead, we will focus on the fast drive case.

6.4.1 Two-mode model

A two-mode model can be derived, similarly to the case of static offset traps that we considered in section 6.3. We start with the coarse-grained, large detuning model derived in section 6.2.3 for the case of a fast drive

$$\hat{H}^{(I)}(t) = \hat{H}'_0 \otimes \hat{1} - \frac{\kappa}{2}\frac{\Omega}{\Omega_{\rm eff}}\Big(\hat{a}_s^\dagger \hat{\sigma}_+ e^{i\Delta t} + \hat{a}_s \hat{\sigma}_- e^{-i\Delta t}\Big), \tag{6.31}$$

where we have dropped the terms proportional to H_3 and $f_{\rm MF}$ from Eq. (6.21), assuming they are so small they can be neglected. This equation corresponds to a positive detuning $\delta' > 0$; we will later discuss the effect the sign of the detuning has on the behavior of the system. This is the Hamiltonian in the interaction picture. The term $\hat{H}'_0 \otimes \hat{1}$ acts identically on both states, with $\hat{H}'_0$ given in Eq. (6.3) describing a harmonic trap centered at the origin with a mean-field potential proportional to the total density. The operator $\hat{a}_s^\dagger \hat{\sigma}_+$ simultaneously raises the spin and creates a motional excitation according to $\hat{a}_s^\dagger = \hat{f} + i\,\hat{g}$. For the drive shown in Figure 6.12, this is $\hat{a}_s^\dagger = x + iy$. Instead of coupling to a dipole mode as in the previous section, the symmetry of the drive shown in Figure 6.12 couples to a state with one unit of angular momentum.

We therefore make the two-mode ansatz as in section 6.3.1 by assuming that the state vector in the interaction picture has the simple form

$$|\psi^{(I)}(t)\rangle = c_0(t)\,|\phi_0\rangle|1\rangle + c_n(t)\,|\phi_n\rangle|2\rangle\ , \tag{6.32}$$

where the coefficients evolve in time according to

$$i\hbar \begin{pmatrix} \dot{c}_0 \\ \dot{c}_n \end{pmatrix} = \begin{pmatrix} \epsilon_0 & \frac{1}{2}\beta\langle\phi_n|f+ig|\phi_0\rangle e^{i\Delta t} \\ \frac{1}{2}\beta\langle\phi_0|f-ig|\phi_n\rangle e^{-i\Delta t} & \epsilon_n \end{pmatrix} \begin{pmatrix} c_0 \\ c_n \end{pmatrix}. \tag{6.33}$$

Here $\beta = \kappa\Omega/|\delta'|$ is the coupling coefficient, and ϵ_0 and ϵ_n are the energy eigenvalues of $|\phi_0\rangle$ and $|\phi_n\rangle$, respectively. For the case of a unit vortex (n=1), these states $\phi_0(\boldsymbol{r})$ and $\phi_1(\boldsymbol{r})$ are plotted in Figure 4.7 of Chapter 4 and the corresponding eigenenergies ϵ_0 and ϵ_1 are plotted in Figure 4.8. As shown in Figure 4.8, the splitting between these energies is very small (a fraction of $\hbar\omega_{xy}$) and is nearly constant as a function of the relative population, except for when most of the atoms are in the vortex. If we make a unitary transformation according to

$$U = e^{it[\Delta\hat{\sigma}_z - (\epsilon_0+\epsilon_n)]/2}, \tag{6.34}$$

Eq. (6.33) can be brought to the form

$$i\hbar \begin{pmatrix} \dot{c}_0 \\ \dot{c}_n \end{pmatrix} = \frac{1}{2}\begin{pmatrix} -(\epsilon_n - \epsilon_0 - \Delta) & \beta\langle\phi_n|f+ig|\phi_0\rangle \\ \beta\langle\phi_0|f-ig|\phi_n\rangle & (\epsilon_n - \epsilon_0 - \Delta) \end{pmatrix} \begin{pmatrix} c_0 \\ c_n \end{pmatrix}. \tag{6.35}$$

This is the main result; we now summarize the crucial information contained in it:

1. In order to get this result, we had to make the following assumptions

$$\Omega_{\rm eff} \gg \omega_0, \quad \omega_r \approx \Omega_{\rm eff}, \quad \delta' \gg \Omega. \tag{6.36}$$

   We also made the further approximation $\delta' \approx \Omega_{\rm eff}$, which follows from the last inequality. The first inequality $\Omega_{\rm eff} \gg \omega_0$ allowed us to separate out the internal and external evolution by going to the interaction picture and coarse-graining over rapidly oscillating terms, which also required the second inequality $\omega_r \approx \Omega_{\rm eff}$. The third inequality allowed us to drop extra terms that would otherwise contaminate the pure coupling given by $\hat{a}_s$.

2. Eq. (6.35) tells us the timescale for coupling to the vortex, given by $\beta = \kappa\Omega/|\delta'|$. For the drive shown in Figure 6.12, $\kappa = m\omega_{xy}^2 r_0$, so that $\beta = m\omega_{xy}^2 r_0 \Omega/|\delta'|$. This tells us that we can couple more strongly to the vortex by increasing the displacement r_0, or by increasing the ratio $\Omega/|\delta'|$—which is constrained by the third inequality in Eq. (6.36).

3. We can also see from Eq. (6.35) that if Δ is chosen to be $\Delta = \epsilon_n - \epsilon_0$, we can drive the system on resonance. For a fixed $\Omega_{\rm eff}$, this means that the trap rotation frequency ω_r should be adjusted to compensate for the splitting $\epsilon_n - \epsilon_0$. However, this is almost a moot point, since the splitting $\epsilon_n - \epsilon_0$ is so small, as shown in in Figure 4.8. In other words, in practice we can take $\omega_r \sim \Omega$ as the resonance.

4. In obtaining Eq. (6.35), we have neglected the mean-field term $f_{\rm MF}$ arising from the scattering lengths a_1, a_2, a_{12} being different. We are very fortunate that for ^{87}Rb these scattering lengths are nearly degenerate, so that the size of the terms in Eq. (6.21) proportional to $f_{\rm MF}$ are small. By making κ large, the relative importance of the $f_{\rm MF}$ terms diminish. If the scattering lengths were drastically different, then the mean-field terms would dominate and generating a pure vortex would be very difficult.

Equation 6.35 is valid only for positive detuning, for we based our two-mode model on Eq. (6.21); for negative detuning, we should use Eq. (6.22). It is straightforward to show that in the case of negative detuning $\delta' < 0$, we get essentially the same results, but $\hat{a}_s^\dagger = f - ig$, instead of $f + ig$. In other words, changing the sign of the detuning, with the direction of rotation of the trap centers fixed, causes the vortex to rotate in the opposite direction. This is a very intriguing property of our state preparation scheme because the direction of circulation of the vortex can be opposite to that of the rotating trap centers. This emphasizes the fact that we are not simply stirring angular momentum into the condensate, as was considered by the authors of [69] for the case of a stirring beam in a single component, for example. A further remarkable feature is that a vortex containing a large fraction of the atoms can be generated when ω_r is much larger than the trap oscillation frequency ω_0, so that in our scheme only a fraction of a trap period is required to generate a macroscopic population of the vortex state.

The solution in the lab frame can be obtained by applying $U_{\rm I}(t)$ from Eq (6.12) to $|\psi^{(\rm I)}\rangle$ in Eq. (6.32) to yield

$$\begin{aligned} |\psi(t)\rangle &= (\alpha_1(t)c_0(t)\,|\phi_0\rangle + \alpha_2(t)c_n(t)\,|\phi_n\rangle)|1\rangle \\ &+ (\alpha_2(t)c_0(t)\,|\phi_0\rangle + \alpha_1^*(t)c_n(t)\,|\phi_n\rangle)|2\rangle\ , \end{aligned} \tag{6.37}$$

where the rapidly varying coefficients are $\alpha_1(t) = \cos(\Omega_{\rm eff}/2\,t) - i(\delta'/\Omega_{\rm eff})\sin(\Omega_{\rm eff}/2\,t)$ and $\alpha_2(t) = -i(\Omega/\Omega_{\rm eff})\sin(\Omega_{\rm eff}/2\,t)$. This resembles the analogous equation Eq. (6.30) in section 6.3.1. However, in the present situation, we have the limit of a large detuning $\delta' \gg \Omega$, so that the Rabi oscillations will look quite distinct from the case of the static drive, where a small detuning was assumed. In the large detuning limit, the coefficients α_i become

$$\begin{aligned} \alpha_1(t) &\approx \cos(\Omega_{\rm eff}/2\,t) - i\sin(\Omega_{\rm eff}/2\,t) \\ \alpha_2(t) &\approx 0, \end{aligned} \tag{6.38}$$

so that Eq. (6.37) can be written

$$|\psi(t)\rangle \approx e^{-i\Omega_{\rm eff}\,t/2}\Big(c_0(t)\,|\phi_o\rangle\,|1\rangle + c_n(t)\,|\phi_n\rangle\,|2\rangle\Big). \tag{6.39}$$

This is rather spectacular: even though we are driving the system off resonance $\delta' \gg \Omega$, it is possible to transfer a significant fraction of the population from the $|1\rangle$ state to the $|2\rangle$ state due to the subtle interplay between the external drive $H_1(\boldsymbol{r}, t)$ and the internal Rabi coupling. We also see that the cycling between spatial modes for each internal state is minimal, so that there is little contamination from the other mode during the evolution; that is, on average the $|1\rangle$ state is almost purely in the ground state $|\phi_0\rangle$ and the $|2\rangle$ state is almost purely in the excited mode $|\phi_n\rangle$.

Intuitively, we can see why our scheme couples a non-rotating condensate to a vortex state if we consider the frame co-rotating with the trap centers at angular frequency ω_r so that $\hat{H}_1$ becomes time-independent. The free Hamiltonian in the co-rotating frame is given by $\hat{H}_0 - \omega_r \hat{L}_z$. The energy of the vortex with one unit of angular momentum is therefore shifted by $\hbar\omega_r$ in the rotating frame relative to its value in the lab frame. When this energy shift compensates for both the energy mismatch $\hbar\delta$ of the internal coupling field and the small chemical potential difference between the vortex and non-rotating condensate, resonant transfer of population may take place. Within this picture, we can also understand intuitively how changing the sign of the detuning while keeping the trap rotation direction fixed couples to a vortex with opposite circulation. Vortices with opposite circulations experience opposite energy shifts in transforming to the rotating frame and therefore require opposite signs of detuning in order to achieve resonant coupling.

6.4.2 Results of calculations

We now show results of numerical calculations of the coupled GP equation. In our calculations, we are solving a two-dimensional version of Eq. (6.10), with $f_{\rm MF}$ and H_3 set to zero; we are not solving the two-mode model Eq. (6.35). We found in section 6.3 that the two-mode model for that system gave good agreement to the full solution. Here, we also find that all of the predictions embedded in the two-mode model are exhibited in the full solution of Eq. (6.10). The two-mode model was indispensable in pinpointing the specific region in parameter space where a pure vortex could be generated.

In Figures 6.13 and 6.14 we show an example of the dynamical state preparation of a unit vortex. Initially all of the atoms are in the $|1\rangle$ internal level and the mean-field ground state $|\phi_0\rangle$. The two traps are displaced by $r_0 = 1.7\mu$m and rotated around at $\omega_r = 205.4$ Hz, so that we have taken $f = x$ and $g = y$. The two internal levels are being driven, with the bare Rabi frequency $\Omega = 50$ Hz, and the detuning is $\delta' = 200$ Hz. The trap frequency

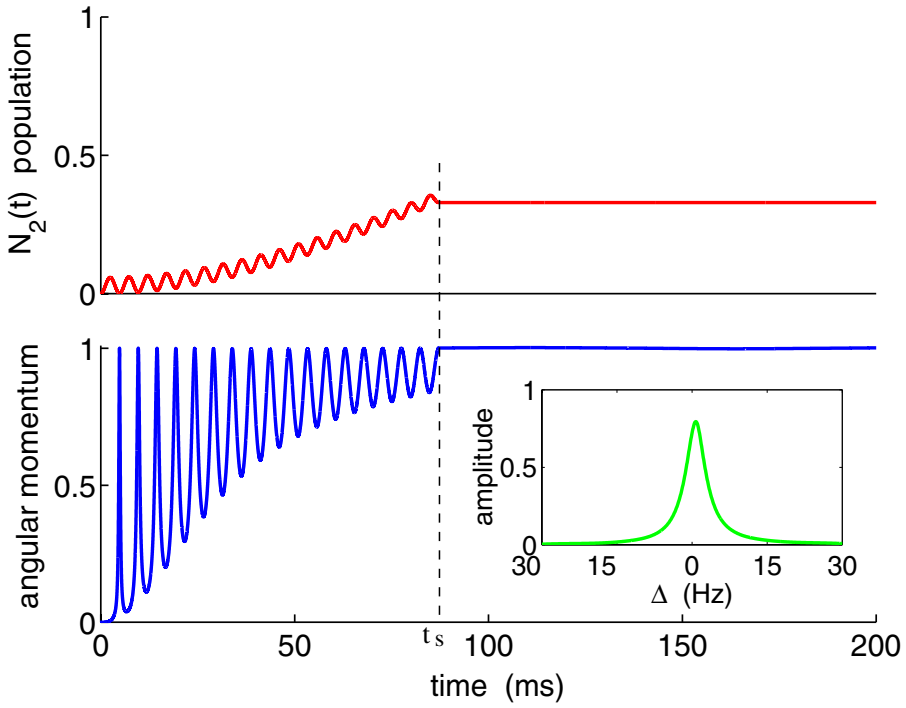

Figure 6.13: Dynamical evolution to a vortex. The top graph shows the fractional population of atoms in the $|2\rangle$ internal state. The bottom graph shows the angular momentum of the $|2\rangle$ state, in units of Planck's constant $\hbar$. The inset shows the maximum amplitude of population transfer to the $|2\rangle$ state as a function of the trap rotation frequency ω_r, with $\Delta = \Omega_{\text{eff}} - \omega_r$.

is $\omega_{xy} = 10$ Hz and the number of atoms is $N = 8 \times 10^5$ atoms. Both internal and external drives are turned off at $t = t_s$, i.e. $\Omega = 0$ and r_0=0, after which the system evolves freely.

In Figure 6.13 we plot the fractional population (top) and the angular momentum per atom (bottom) of the $|2\rangle$ state as a function of time. The small-amplitude rapid oscillations of the top line correspond to the cycling between internal levels due to the off-resonant coupling. The gradual rise of this line is due to coupling from the ground state to the vortex mode caused by the drive H_1 in Eq. (6.4). This is just what we expect from the two-mode model. The rise and fall of the angular momentum in the bottom curve corresponds to a rapid cycling of the $|2\rangle$ atoms between the non-rotating condensate and the vortex. Once during each Rabi cycle, the angular momentum approaches unity and at that time the $|2\rangle$ state wave function approaches a pure vortex mode.

The maximum population transfer between the two states obeys a Lorentzian response curve as ω_r is varied near Ω_{eff} exhibiting a narrow resonance. This is shown in the inset of Figure 6.13, where $\Delta = \Omega_{\text{eff}} - \omega_r$. The peak of this curve sits at $\Delta = \epsilon_1 - \epsilon_0$, which is around $0.05\hbar\omega_{xy}$, which corresponds to the splitting shown in Figure 4.8. We find that the maximum population that can be transferred to the vortex is around 80%. This makes sense from looking at Figure 4.7, since the energy splitting $\epsilon_1 - \epsilon_0$ is roughly constant until most of the atoms are in the vortex, when the energy splitting starts to increase rapidly. With

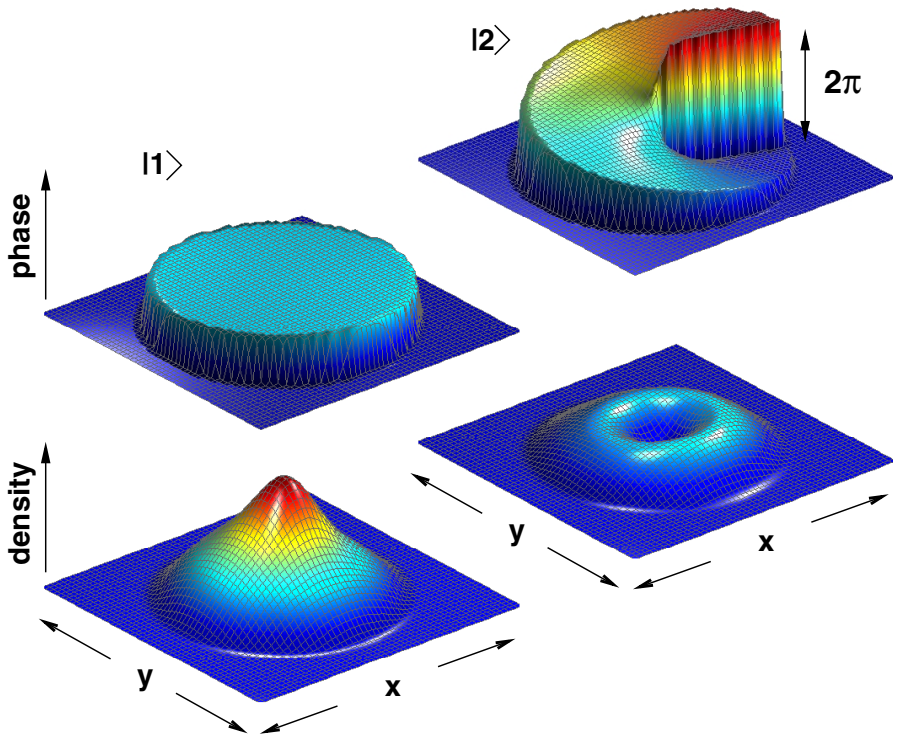

Figure 6.14: Densities and phases of the two states $|1\rangle$ and $|2\rangle$, at time $t = 200$ms. At this time, one third of the atoms are in the $|2\rangle$ state, which is in a pure vortex mode with unit angular momentum. A characteristic feature of a vortex mode is the $2n\pi$ phase wrap about the core, where n is an integer that is equal to unity in this case.

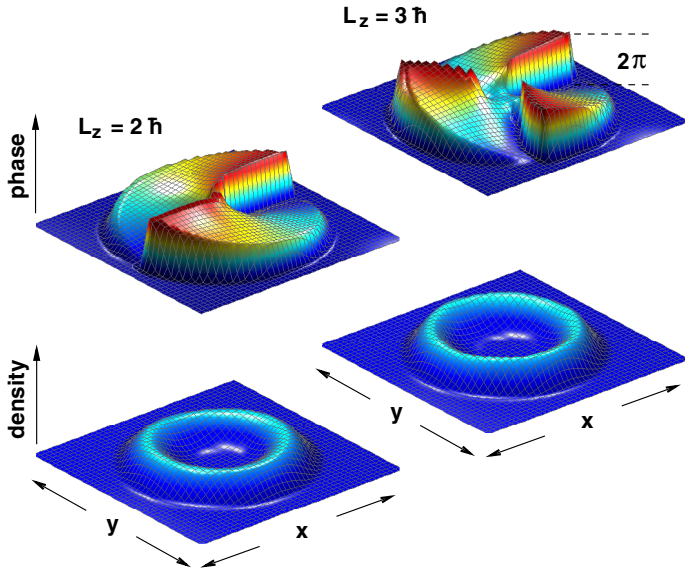

Figure 6.15: Double and triple vortex preparation. Shown are the densities and phases modulo 2π of the $|2\rangle$ state after a dynamical evolution similar to that shown in Figure 6.13, but with different symmetries of the drive H_1. In the case of $L_z = 2\hbar$, $f = x^2 - y^2$ and $g = 2xy$, while for $L_z = 3\hbar$, $f = x^3 - 3xy^2$ and $g = 3x^2y - y^3$. In both cases, the system was evolved from the same initial condition as that for the calculation described in Figure 6.13, with one third of the atoms in the $|2\rangle$ state at the time t_s. The values taken for the various parameters were the same, except for the trap rotation frequency, which was $\omega_r = 204.3$ Hz for the $L_z = 2\hbar$ case, and $\omega_r = 200.2$ Hz for the $L_z = 3\hbar$ case.

ω_r fixed, this means that the system pushes itself out of resonance, a behavior also seen in Chapter 5 in the weak-coupling case.

Our key idea is that by turning off the coupling at a precise time, t_s, on a given Rabi cycle, the $|2\rangle$ state can be prepared to have unit angular momentum. In Figure 6.14 we show a snapshot of the numerically calculated densities and phases of the two components at time 200 ms. The snapshot illustrates the preparation of a high-quality vortex in state $|2\rangle$ state, with the $|1\rangle$ state providing a natural "pinning" mechanism that stabilizes the vortex core due to a repulsive mean-field barrier along the symmetry axis.

The symmetry of the coupling is determined by $f + ig$, which has the form $x + iy$ as previously stated for the case of the unit vortex. In order to produce a vortex with n units of angular momentum (i.e. $\langle \hat{L}_z \rangle = n\hbar$), $f + ig$ should take on the form $(x + iy)^n$. So for $n = 2$, we must construct a $\hat{H}_1$ in which $f = x^2 - y^2$ and $g = 2xy$, corresponding to a rotating saddle potential. In Figure 6.15, we illustrate vortex generation with two and three units of angular momentum.

The generalization of our scheme for the preparation of new states in a trapped Bose condensed gas with arbitrary symmetry is straightforward. For example, to generate a mode with a dipole symmetry one superimposes a left and right circulating vortex so that $f = \mathrm{Re}\{x + iy\}$ and $g = 0$. A quadrapole symmetry would be generated by $f = \mathrm{Im}\{(x + iy)^2\}$ and $g = 0$. The dynamical state preparation of these two examples is illustrated in

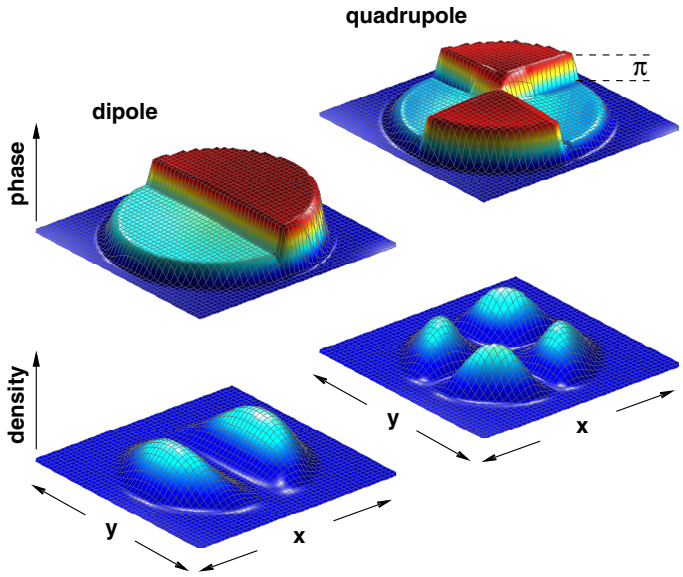

Figure 6.16: Dipole and quadrupole preparation. Different symmetries were constructed using specific forms for the drive H_1 in order to prepare the $|2\rangle$ state in non-circulating modes. Instead of having a $2n\pi$ phase wrap corresponding to a current flowing around a central core, these modes have regions of constant phase separated by a discontinuous jump of π where the wave function changes sign. To generate the dipole mode, we used $f = x$ and $g = 0$ with $\omega_r = 205.4$ Hz; while for the quadrupole, we used $f = xy$ and $g = 0$ with $\omega_r = 204.3$ Hz.

Figure 6.16.

6.5 Experimental observation of a vortex

The proposed scheme for generating a vortex presented in section 6.4 has been implemented in the laboratory of Eric Cornell and Carl Wieman here at JILA, resulting in the first experimental report of a vortex in a dilute Bose-condensed gas [14]. The experimental data is remarkably clean with excellent shot-to-shot reproducibility, showing clearly that the prepared state has the required vortex topology. The basic experimental scheme described earlier on page 101 was implemented; the details of the experimental apparatus are given in [14].

In Figure 6.17 we show the dynamical evolution of a vortex over a 80 ms time period. Shown are phase contrast images for the $|2\rangle$ atoms, with each frame corresponding to a time-averaging of the signal for 9 ms. The evolution shown in Figure 6.17 corresponds to the first 80 ms of the evolution of the similar case considered in Figure 6.13. The time averaging washes out the spatial structure from the interference between the ground $|\phi_0\rangle$ and vortex $|\phi_1\rangle$ states that occurs during the rapid Rabi cycling. In Figure 6.18 we show a single snapshot of the $|2\rangle$ atoms, taken approximately when $\alpha_2(t) = 0$ in Eq. (6.37) during a Rabi cycle, so that the $|2\rangle$ atoms are nearly in a pure vortex mode.

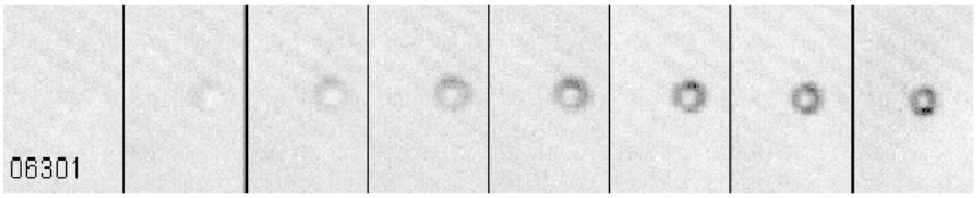

Figure 6.17: Experimental production of a vortex. Shown are phase contrast images of the $|2\rangle$ atoms, with dark regions corresponding to higher density in the cloud. Each frame corresponds to a 9 ms signal integration and 10 ms between frames, so that by the end of the sequence 80 ms have elapsed. Initially, all of the atoms are in the $|1\rangle$ state and gradually population is built up into the $|2\rangle$ state into a vortex, similar to the case shown in Figure 6.13. Experimental data is courtesy of M. Matthews, B. Anderson, and P. Haljan.

In order to show that the prepared state is a vortex that has a 2π phase wrap, and is not simply a uniform-phase ring, an interference of the two states $|1\rangle$ and $|2\rangle$ can be measured and the sine of the phase of the vortex can be calculated. In Figure 6.19 we show experimental data taken for this case. A vortex is prepared in the $|2\rangle$ atoms, shown in the first frame. A π pulse is applied (the two-photon drive is applied for half of a Rabi cycle), which transfers the atoms to the $|1\rangle$ state, which is in the ground state $|\phi_0\rangle$. Halfway through the pulse, the two states interfere, with the distinctive density pattern shown that indicates a spatially-nonuniform relative phase. The data from the three plots was used to calculate the cosine of the phase, which matched the expectations for a vortex solution [14].

6.6 Summary

In this chapter we have studied a strongly-coupled two-component condensate and have found that topological modes can be excited if the traps of the two states are spatially offset. We have presented a novel state-preparation scheme based on this mechanism that allows for the generation of pure vortices in this two-component system, as well as other types of non-ground-state modes, such as dipole and quadrupole modes. Our approach grew out of a collaborative effort at JILA, between our group and the laboratory of Eric Cornell and Carl Wieman, to understand the initially unexplained data (examples shown in Figures 6.1 through 6.3.) of the first observations of this system. The culmination of these efforts is the first observation of a vortex in a dilute Bose-condensed gas [14].

It should be mentioned that prior to our work, there had been several similar proposals for the dynamical production of a vortex through the use of the internal structure of the atoms [107, 108, 74]. For example, Dum et al. [74] discuss the preparation of dark solitons and vortices using a Raman coupling scheme in which the light beams have a particular spatial intensity pattern chosen with the right symmetry for coupling to the desired mode. As discussed in [107] and [108], such an intensity pattern could be attained through the use of a laser beam with a higher-order Laguerre-Gaussian mode profile. The spirit of the basic approach described in [74], for example, is much the same as in our work, however, the specific underlying mechanism for coupling to a vortex that we consider is quite distinct

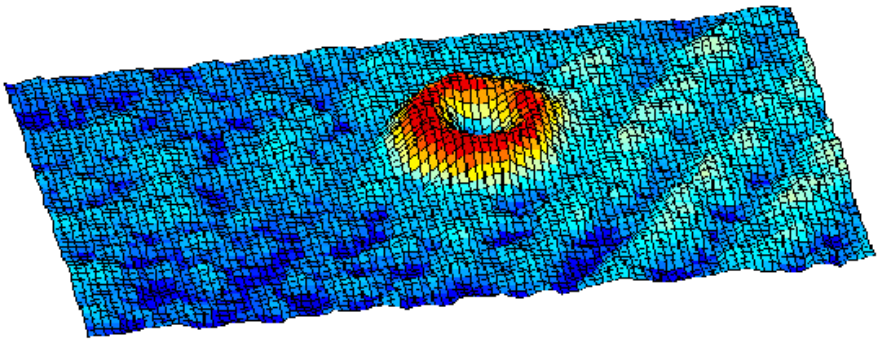

Figure 6.18: Snapshot of a vortex. Shown is the density profile of atoms in the $|2\rangle$ state for a single snapshot taken during the dynamical evolution shown in Figure 6.17. The snapshot was taken approximately when the $|2\rangle$ atoms were in a pure vortex. Experimental data is courtesy of M. Matthews, B. Anderson, and P. Haljan.

from these earlier works. In our system it is the combined effect of spatially homogeneous coupling fields and time-varying spatially offset traps that gives rise to the required symmetry for coupling to a topological mode. This effect is rather nonintuitive and only occurred to us while trying to interpret the experimental data described in section 6.1.

The experimental realization of the state-preparation scheme presented in this thesis has opened the door to a whole new class of problems related to topological modes in a two-component system. This is an extremely rich system that has been almost untapped in the the literature, since most of the recent efforts have been on the study of vortices in single component systems. Issues like vortex stability, the role of different scattering lengths, collective modes of the system, and the relation to the phenomenon of superfluidity are essentially open problems waiting to be investigated, both theoretically and experimentally. Similar properties can be investigated for the dipole and quadrupole modes as well. One could also study the preparation scheme in more detail to find the optimal path for generating a pure vortex with no remaining $|1\rangle$ atoms. This might entail chirping the trap rotation frequency ω_r in a specified time-dependent way so as to adiabatically follow the mean-field shifted energies between the two modes [74]. A further extension would be to treat finite temperature effects by including the collision terms in the kinetic equation for the mean field and fluctuations, given in Chapter 2.

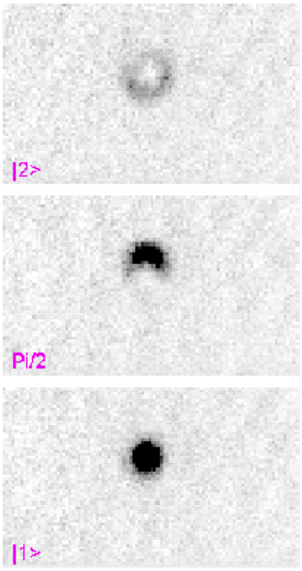

Figure 6.19: Interference between the ground state and vortex. Shown are phase contrast images with darker regions corresponding to higher density. Initially all of the vortex atoms are in the $|2\rangle$ internal state. A π pulse is applied that transfers the atoms into the $|1\rangle$ state. The middle frame is taken halfway through the pulse, and shows the interference between the vortex and ground states. The third frame shows the atoms at the end of the π pulse, when they are in the ground state. The top frame and bottom frame correspond to the two states shown in Figure 6.14. Experimental data is courtesy of M. Matthews, B. Anderson, and P. Haljan.

Chapter 7

Trajectory Simulation of the Quantum Boltzmann Equation

7.1 Introduction

In experiments producing Bose-Einstein condensation of a dilute alkali vapor, the temperature of a gas is reduced by several orders of magnitude using the crucial technique of evaporative cooling [33, 34]. The theoretical study of this important technique and the description of condensate formation requires a kinetic theory that treats non-equilibrium, open systems in both the classical and quantum degenerate regimes. It is also necessary to consider a system of finite size as determined by the form of the confining potential [109, 110].

We present a novel approach to describing quantum kinetics which is motivated by the quantum trajectory methods developed in quantum optics to describe the dissipative evolution of open systems [111, 112, 113, 114, 115, 116, 117]. The basic principle on which these models are built is that the evolution of the open system, described by a density operator master equation, can be obtained by accumulating an infinite number of stochastic realizations of a wave-function trajectory. A simple example of an open system is an excited atom coupled to the radiation vacuum reservoir. A trajectory in this case consists of the interruption of the continuous evolution of the atomic wave function by a quantum jump to the ground state when a spontaneous photon is emitted.

We have applied this trajectory method to a fundamentally different problem. In our case, we wish to describe the evolution of a gas of atoms which are not coupled to a reservoir at all. The jumps which occur in the single-atom trajectory that lead to the irreversible evolution of the system are caused by atomic collisions with other atoms in the gas. Thus, the role of the reservoir in our problem is played by the system itself. This inherent nonlinearity is illustrated by the kinetic equation we are trying to simulate. We have previously applied this approach to treat the classical Boltzmann equation in order to describe the evaporative cooling process [118]. In this chapter, we extend the theory to treat Bose-Einstein condensation.

This chapter is divided into three parts. We first present the theory for kinetic evolution in section7.2. In section7.3, we describe our trajectory approach and outline in detail the corresponding simulation procedure. Finally, in section7.4, we present applications of the method for thermodynamics, condensate growth, and evaporative cooling.

7.2 Ergodic quantum Boltzmann equation

In this section, we outline our mathematical description of kinetic theory and highlight the physical assumptions made in its derivation. We present the quantum Boltzmann equation (QBE), which is the starting point for our treatment. An ergodic assumption is made, which simplifies the problem by assuming that the population of a state only depends on its energy. We show how the ergodic QBE goes to the ergodic classical Boltzmann equation in the appropriate limit, a result which greatly simplifies the trajectory simulation presented in section 7.3.

7.2.1 Quantum Boltzmann equation

We consider a dilute system of atoms confined in an isotropic harmonic oscillator of frequency ω. The Hamiltonian $H = H_0 + H_I$ consists of a free part H_0, and an interaction term H_I due to binary collisions

$$\begin{aligned} H_0 &= \sum_{\vec{n}} E_{\vec{n}}\, a^\dagger_{\vec{n}} a_{\vec{n}} \ , \\ H_I &= \frac{1}{2} \sum_{\vec{n}\vec{m}\vec{q}\vec{p}} C(\vec{n},\vec{m};\vec{q},\vec{p})\, a^\dagger_{\vec{n}} a^\dagger_{\vec{m}} a_{\vec{q}} a_{\vec{p}} \ , \end{aligned} \tag{7.1}$$

where $E_{\vec{n}} = (n_x + n_y + n_z + \frac{3}{2})\hbar\omega$ is the energy eigenvalue of H_0 with quantum number $\vec{n} = (n_x, n_y, n_z)$. Here $a_{\vec{n}}$ is the annihilation operator which removes an atom from the single-particle eigenstate $\phi_{\vec{n}}$. The transition amplitude is

$$C(\vec{n},\vec{m};\vec{q},\vec{p}) = \int d^3x d^3x' \phi^*_{\vec{n}}(\vec{x}) \phi^*_{\vec{m}}(\vec{x}') V(\vec{x},\vec{x}') \phi_{\vec{q}}(\vec{x}) \phi_{\vec{p}}(\vec{x}'), \tag{7.2}$$

where $V(\vec{x},\vec{x}')$ is a two-particle potential. In the temperature range of interest, s-wave scattering predominates and collisions are characterized by a contact potential

$$V(\vec{x},\vec{x}') = \frac{4\pi\hbar^2 a}{m} \delta^3(\vec{x} - \vec{x}') \ , \tag{7.3}$$

where a is the scattering length. This gives the quantum mechanical cross section for the collision $\sigma = 8\pi a^2$.

The correlation time arising from the duration of a collision in Bose-Einstein condensation experiments is typically much shorter than the time scale on which the system relaxes to equilibrium. The time scale for pair correlations is given by $\tau_{\rm cor} = a/\bar{v}$, where $\bar{v}$ is the mean velocity . The relaxation time is determined by the time between elastic collisions $\tau_{\rm col}$ in the gas . For example, in the experiments described in Ref. [1], at the critical temperature $\tau_{\rm cor} \approx 1\ \mu$s, compared to $\tau_{\rm col} \approx 0.1$ s. In this regime, Wick's theorem [119, 120, 38] may be applied to give the evolution under the Born and Markov approximations of the atomic population

$$f_{\vec{n}} = {\rm Tr}\{\rho a^\dagger_{\vec{n}} a_{\vec{n}}\} \ , \tag{7.4}$$

where ρ is the N-particle density matrix for the system. In the representation of the bare harmonic oscillator states, off-diagonal elements $f_{\vec{n}\vec{n}'} = {\rm Tr}\{\rho a^\dagger_{\vec{n}} a_{\vec{n}'}\}$, $\vec{n} \neq \vec{n}'$, [38] are

negligible when $\omega\tau_{col} \gg 1$. This gives the QBE [38, 39], derived in Chapter 2 in section 2.4.2

$$\frac{\partial f_{\vec{n}}}{\partial t} = \sum_{\vec{m}\vec{q}\vec{p}} W(\vec{n},\vec{m};\vec{q},\vec{p})\left[f_{\vec{q}} f_{\vec{p}}(1+f_{\vec{n}})(1+f_{\vec{m}}) - f_{\vec{n}} f_{\vec{m}}(1+f_{\vec{q}})(1+f_{\vec{p}})\right], \quad (7.5)$$

where the transition rate $W(\vec{n},\vec{m};\vec{q},\vec{p})$ appearing in Eq. (7.5) is obtained from Fermi's Golden Rule

$$W(\vec{n},\vec{m};\vec{q},\vec{p}) = \frac{2\pi}{\hbar}|C(\vec{n},\vec{m};\vec{q},\vec{p})|^2 \frac{\delta_{E_{\vec{n}}+E_{\vec{m}},E_{\vec{q}}+E_{\vec{p}}}}{\hbar\omega}, \quad (7.6)$$

and δ is the Kronecker delta function giving energy conservation. The total number of particles in the system N determines the normalization of $f_{\vec{n}}$ by $\sum_{\vec{n}} f_{\vec{n}} = N$.

7.2.2 Ergodic assumption

A practical problem for simulating the QBE is that the degeneracy of states increases rapidly with increasing energy. The degeneracy of a level for the isotropic harmonic oscillator is proportional to the square of the energy so that even for very low temperatures, the number of states whose populations must be calculated may be very large. For example, if $k_B T = 10\hbar\omega$, we would have to consider approximately 10^5 states. This is a severe limitation on the computation speed.

We resolve this difficulty by assuming that the population within a degenerate subspace is uniformly distributed among the degenerate states. In other words, in the spherical basis we assume that the population $f_{\vec{n}}$ depends only on the principle quantum number n and not on the angular momentum quantum numbers l and m. This assumption is true at equilibrium since then the distribution function is purely a function of the Hamiltonian. In many cases of interest, the system remains close to equilibrium and we expect the approximation to be valid. In Ref. [121], it was shown that, for a homogeneous system originally in equilibrium, if one of the three degenerate states in the first excited level is depleted, and the system is allowed to evolve back to equilibrium, the population gets redistributed equally among the three degenerate states in a time on the order of the mean collision time in the gas. Essentially, the ergodic approximation corresponds to detailed balance amongst the angular momentum levels, i.e. l-changing collisions are rapid compared to rates in and out of n.

This ergodic assumption is defined as

$$f_{\vec{n}} = \sum_{\epsilon_n} \delta_{\epsilon_n, E_{\vec{n}}} f_{\epsilon_n} \ . \quad (7.7)$$

Each state $\phi_{\vec{n}}$ in the degenerate subspace has the same population f_{ϵ_n}. Therefore, a sum over all of the degenerate states is just

$$g_{\epsilon_n} f_{\epsilon_n} = \sum_{\vec{n}} \delta_{\epsilon_n, E_{\vec{n}}} f_{\vec{n}} \ , \quad (7.8)$$

where g_{ϵ_n} is the degeneracy of energy level ϵ_n, which is given by

$$g_{\epsilon_n} = \frac{1}{2}(n+1)(n+2). \quad (7.9)$$

With the ergodic assumption, Eq. (7.5) can be reduced to

$$g_{\epsilon_n}\frac{\partial f_{\epsilon_n}}{\partial t} = \sum_{\epsilon_m\epsilon_q\epsilon_p} W(\epsilon_n,\epsilon_m;\epsilon_q,\epsilon_p)\left[f_{\epsilon_q}f_{\epsilon_p}(1+f_{\epsilon_n})(1+f_{\epsilon_m}) - f_{\epsilon_n}f_{\epsilon_m}(1+f_{\epsilon_q})(1+f_{\epsilon_p})\right] . \tag{7.10}$$

The collision kernel $W(\epsilon_n,\epsilon_m;\epsilon_q,\epsilon_p)$ is now a sum over all of the rates corresponding to the possible degenerate states which could participate in the collision

$$W(\epsilon_n,\epsilon_m;\epsilon_q,\epsilon_p) = \frac{2\pi}{\hbar}\frac{\delta_{\epsilon_n+\epsilon_m,\epsilon_q+\epsilon_p}}{\hbar\omega}\sum_{\vec{n}\vec{m}\vec{q}\vec{p}}\Big(|C(\vec{n},\vec{m};\vec{q},\vec{p})|^2\prod_j \delta_{\epsilon_j,E_{\vec{j}}}\Big), \tag{7.11}$$

where $j \in \{n,m,q,p\}$ in the product. The normalization of the distribution becomes $\sum_{\epsilon_n} g_{\epsilon_n} f_{\epsilon_n} = N$.

We have made a great simplification by reducing the QBE to Eq. (7.10). Considering our previous example of $k_BT = 10\hbar\omega$, the number of levels occupied is approximately 100, which is much less than the corresponding number of states 10^5.

7.2.3 Classical limit

Although the ergodic assumption presented in section 7.2.2 greatly simplifies the problem of simulating the QBE, it is desirable to reduce the problem further in order to describe the evaporative cooling technique used to reach the critical density for Bose-Einstein condensation. During the evaporation process, the temperature of the gas is reduced by several orders of magnitude. Even with the ergodic assumption, a very large number of energy levels must be considered to describe the system in this entire range. The process can be described by the classical Boltzmann equation for most of this range, down to some point close to the critical temperature when quantum statistics becomes important. In this critical region, the QBE must be used.

The problem may be simplified if a smooth transition connecting these two regions can be found, which would allow energy levels above some cutoff to be treated classically. Taking the classical limit of Eq. (7.10) corresponds to taking $\epsilon_n \to \infty$, and assuming that $T > T_c$ so that the $(1 + f_{\epsilon_n})$ Bose-enhancement factors go to unity.

Eq. (7.10) can be written in dimensionless form

$$\begin{aligned} g_{e_n}\frac{\partial f_{e_n}}{\partial \tau} &= \sum_{e_m e_q e_p} \delta_{e_n+e_m,e_q+e_p}\, g(e_n,e_m;e_q,e_p) \\ &\times \left[f_{e_q}f_{e_p}(1+f_{e_n})(1+f_{e_m}) - f_{e_n}f_{e_m}(1+f_{e_q})(1+f_{e_p})\right] , \end{aligned} \tag{7.12}$$

where time and energy are in the natural units of the problem, $\tau = \frac{m\sigma\omega^2}{\pi^2\hbar}t$ and $e_n = \epsilon_n/\hbar\omega$. The collision kernel given in Eq. (7.11) is now dimensionless and given by

$$g(e_n,e_m;e_q,e_p) = \frac{4}{\pi^2}\sum_{\vec{n}\vec{m}\vec{q}\vec{p}}\Big(|\prod_i N_{n_i}N_{m_i}N_{q_i}N_{p_i}I_{n_im_iq_ip_i}|^2\prod_j \delta_{e_j,E_{\vec{j}}}\Big) , \tag{7.13}$$

where $i \in \{x,y,z\}$ in the first product and $N_{n_i} = (2^{n_i}n_i!)^{-1/2}$ is the normalization factor for component i of the state $\phi_{\vec{n}}$. The overlap integral of the four Hermite polynomials $H_{n_i}(u_i)$ is

$$I_{n_im_iq_ip_i} = \int du_i H_{n_i}H_{m_i}H_{q_i}H_{p_i}e^{-2u_i^2}. \tag{7.14}$$

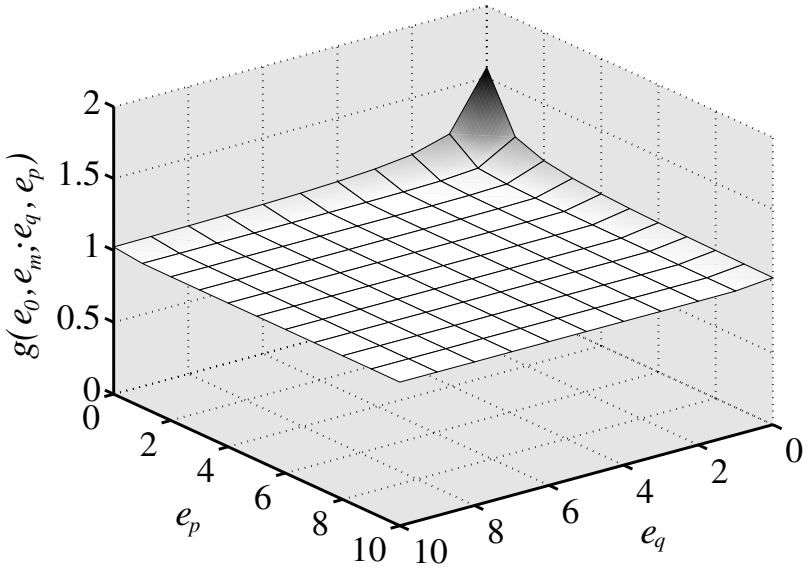

Figure 7.1: Plot of $g(e_{\min}, e_m; e_q, e_p)$ vs. (e_q, e_p) for the minimum energy being in the ground state $e_{\min} = e_0$, where e_m is determined by energy conservation. It is a very flat function, differing from its asymptotic form, $g_{e_0} = 1$, only when Δ_e is very small.

In taking the limit $e_n \to \infty$, f_{e_n} is replaced by a continuous function of energy $f(e_n)$, each sum over e_n is replaced by an integral, and the Kronecker delta $\delta_{\epsilon_n+\epsilon_m,\epsilon_q+\epsilon_p}/\hbar\omega$ is replaced by a Dirac delta function $\delta(\epsilon_n + \epsilon_m - \epsilon_q - \epsilon_p)$. For temperatures well above T_c, the Bose-enhancement factors $(1 + f_{e_n})$ can be put to unity. The collision kernel $g(e_n, e_m; e_q, e_p)$ has a rather simple limiting form which may be found by computing numerically the quantity on the RHS of Eq. (7.13). We use the following expression for the overlap integral [122]

$$I_{nmqp} = \frac{m!n!}{\pi} \sum_{t=0}^{\min(m,n)} \frac{2^t}{t!(m-t)!(n-t)!} 2^{k-\frac{1}{2}} \Gamma(k-p+\frac{1}{2}) \Gamma(k-m-n+2t+\frac{1}{2}) \Gamma(k-q+\frac{1}{2}) \ , \tag{7.15}$$

where $2k = \sigma_n - 2t$ and $\sigma_n = n + m + p + q$ must be even. The integral is zero if σ_n is odd.

We calculated the kernel $g(e_n, e_m; e_q, e_p)$ numerically for $e_0 \le e_j \le e_{20}$, where $e_j \in \{e_n, e_m, e_q, e_p\}$, and obtained a remarkable result. This collision kernel converges very quickly to the degeneracy g_{e_n}, given by Eq. (7.9), as the differences $\Delta_e \equiv e_j - e_{\min}$ between the minimum energy and the other three energies increase

$$g(e_{\min}, e_m; e_q, e_p) \overset{\Delta_e \to \infty}{\to} g_{e_{\min}} \ , \tag{7.16}$$

where $e_{\min} = \min\{e_n, e_m, e_q, e_p\}$ is the minimum energy. Figure 7.1 shows a plot of $g(e_{\min}, e_m; e_q, e_p)$ vs. (e_p, e_q) for $e_{\min} = e_0$, with e_m determined by energy conservation. It is a very flat function differing from its asymptotic form only when Δ_e is very small. From our calculations, we found that the convergence in Eq. (7.16) becomes faster as $e_{\min}$

increases. Furthermore, as e_j increases, the degeneracy factor g_{e_j} converges to the density of states $\rho(e_j) \equiv \frac{1}{2}e_j^2$

$$g_{e_j} \overset{e_j \to \infty}{\to} \rho(e_j) \ . \tag{7.17}$$

In our simulation procedure described below, we use the limiting form Eq. (7.16) for $g(e_n, e_m; e_q, e_p)$ when any one of the energies is greater than the tenth level e_{10}, and use the limiting form Eq. (7.17) when all of the energies are greater than a cutoff energy e_c chosen such that $(1 + f_{e_c}) \approx 1$.

The comparison with the ergodic classical Boltzmann equation can now be made. The classical limit of Eq. (7.12) is

$$\rho(e_n)\frac{\partial f(e_n)}{\partial \tau} = \int de_m de_q de_p \delta(e_n + e_m - e_q - e_p)\rho(e_{min})(f(e_q)f(e_p) - f(e_n)f(e_m)) \ , \tag{7.18}$$

where the same natural units given below Eq. (7.12) are used here. This agrees with the classical Boltzmann equation given by Eq. (14) in Ref. [109].

7.3 Trajectory simulation

In this section, we explain our novel approach to simulating the QBE using simulated single-particle trajectories. We first show that the time evolution of f_{e_n} given by Eq. (7.12) can be described by a sum over all possible single-particle trajectories. We then outline the specific simulation procedure.

7.3.1 Trajectory decomposition of the QBE

We can now incorporate quantum statistics into the trajectory method using the results of section 7.2. We can not expect the simulation to be valid far below the critical temperature when a large proportion of atoms are in the ground state since we neglect the effect of the mean field on the system and work in the representation of the bare harmonic oscillator basis. However, in the regime where $\omega\tau_{col} \gg 1$ holds, the buildup of the condensate can still be investigated. This simulation method is now ideal for describing the evaporative cooling of atoms all the way down to temperatures below T_c.

The trajectory decomposition of the ergodic QBE closely resembles that given in Ref. [118] for the classical case. Still working in the natural units of time and energy given below Eq. (7.12), we begin by defining a trajectory function $f(e_n, t \,|\, t_\eta, e_\eta, \ldots, t_1, e_1)$, which describes a specific collision history with energy e_n at time t: The trajectory is labeled by its history of η collisions occurring at times $t_1, \ldots, t_\eta$, with $t > t_\eta > \ldots > t_1$, and with the energy before each collision given by $e_1, \ldots, e_\eta$.

Our task is to correctly describe the time evolution of this trajectory function so that upon accumulating all possible realizations of trajectories, $f_{e_n}(t)$ is attained with the correct time evolution governed by Eq. (7.12). To obtain $f_{e_n}(t)$ from the accumulated trajectories, we form a distribution of the energies collected from M trajectories at the particular time t. Then in the limit $M \to \infty$, the distribution should converge upon $f_{e_n}(t)$. Realistically, the number of trajectories we accumulate is in the range $10^4 - 10^5$. Of course, the trajectories must be weighted so that the final distribution obtained from the accumulated trajectories is normalized to N.

This sum over trajectories can be written explicitly as

$$g_{e_n} f_{e_n}(t) = \sum_{\eta=0}^{\infty} \sum_{e_\eta \ldots e_1} \int_{t_0}^{t} dt_\eta \int_{t_0}^{t_\eta} dt_{\eta-1} \cdots \int_{t_0}^{t_2} dt_1 f(e_n, t \,|\, t_\eta, e_\eta, \ldots, t_1, e_1) \ , \quad (7.19)$$

where we sum over the number η of possible collisions, sum over all possible energies occurring before each collision, and integrate over the possible times at which each collision can occur. Each trajectory has a weight given by N/M, where M goes to infinity in Eq. (7.19).

The time evolution of $f_{e_n}(t)$ in terms of the trajectory decomposition is found by differentiating Eq. (7.19)

$$\begin{aligned} g_{e_n} \frac{\partial f_{e_n}(t)}{\partial t} \ &= \ \sum_{\eta=0}^{\infty} \sum_{e_\eta \ldots e_1} \Big\{ \int_{t_0}^{t} dt_\eta \cdots \int_{t_0}^{t_2} dt_1 \frac{\partial f(e_n, t \,|\, t_\eta, e_\eta, \ldots)}{\partial t} \\ &\qquad + \int_{t_0}^{t} dt_{\eta-1} \cdots \int_{t_0}^{t_2} dt_1 f(e_n, t \,|\, t, e_\eta, \ldots) \Big\} \ . \end{aligned} \quad (7.20)$$

We must find the correct time evolution of the trajectory function $f(e_n, t \,|\, t_\eta, e_\eta, \ldots, t_1, e_1)$ so that the time evolution given by this decomposition is equivalent to the QBE. The first term on the RHS of Eq. (7.20) gives the time evolution of the trajectory between collisions, while the second term is related to the instantaneous change in the trajectory's energy when a collision occurs.

Between collisions, the trajectory's norm will decay due to the probability for a collision to occur with an atom from the rest of the gas

$$\frac{\partial f(e_n, t \,|\, t_\eta, e_\eta, \ldots)}{\partial t} = -\gamma(e_n, t) f(e_n, t \,|\, t_\eta, e_\eta, \ldots) \ . \quad (7.21)$$

The rate of decay $\gamma(e_n, t)$ is equal to the collision rate. A particle in the system with energy e_n has a rate of colliding with any other particle in the system given by

$$\gamma(e_n, t) = \sum_{e_m e_q e_p} \delta_{e_n + e_p, e_q + e_p} \frac{g(e_n, e_m; e_p, e_q)}{g_{e_n}} f_{e_m}(t)(1 + f_{e_q}(t))(1 + f_{e_p}(t)) \ . \quad (7.22)$$

Because of Bose statistics, some of the collisions will be enhanced by the factors $(1 + f_{e_q}(t))$ if the populations in those output channels are large. This dependence on the population in summing over the output channels is absent in the trajectory method presented for the classical Boltzmann equation in Ref. [118]. In that case, the integrals over the output channels can be done analytically, which makes the problem scale linearly with the number of energy bins used to store $f(e)$. We can not make that simplification here.

The function $f(e_n, t \,|\, t, e_\eta, \ldots)$ indicates that a collision has occurred at time t, changing the energy from e_η to e_n. We interpret the function $f(e_n, t \,|\, t, e_\eta, \ldots)$ as the rate that a particle with energy e_η will collide with any atom in the system and attain the energy e_n afterwards. Thus, $f(e_n, t \,|\, t, e_\eta, \ldots)$ can be obtained by omitting the sum over the output channel e_n in Eq. (7.22) and weighting the rate by the norm of the trajectory before the collision

$$\begin{aligned} f(e_n, t \,|\, t, e_\eta, \ldots) \ &= \ \sum_{e_m e_p} \delta_{e_\eta + e_p, e_n + e_m} \frac{g(e_\eta, e_p; e_n, e_m)}{g_{e_\eta}} \\ &\qquad \times f_{e_p}(t)(1 + f_{e_n}(t))(1 + f_{e_m}(t)) f(e_\eta, t \,|\, t_{\eta-1}, e_{\eta-1} \ldots) \ . \end{aligned} \quad (7.23)$$

With the above description of the time evolution of a trajectory, one can easily verify that the decomposition in Eq. (7.20) is equivalent to Eq. (7.12) by substituting Eq. (7.21), Eq. (7.22), and Eq. (7.24) into Eq. (7.20) and using Eq. (7.19) to reduce the expression.

One crucial point, however, has not been addressed in our proof. Because the rates given in Eq. (7.22) and Eq. (7.24) depend on $f_{e_n}(t)$, which is the quantity being calculated, the problem is nonlinear and must be solved self-consistently. A self-consistent solution can be found if we make the incremental time of evolution dt much smaller than the mean collision time τ_{col}, so that $f_{e_n}(t)$ does not change appreciably during the coarse-grained time steps.

7.3.2 Simulation procedure

We now describe the procedure for simulating the QBE using the trajectory method. One begins by creating the initial distribution $f_{e_n}(t_0)$, the time evolution of which is desired over a chosen time interval. This distribution is evolved incrementally, by adding up M trajectories over a time interval dt that must be chosen smaller than the average single-particle collision time τ_{col}. Then, the simulated distribution at the end of the time $t_0 + dt$ is used as the starting distribution for the next time step, and so on, until the desired time is reached. In more detail, this procedure is as follows:

1. Create an empty distribution function $f_{e_n}(t_0 + dt)$ with zero population throughout the levels.

2. Choose an initial energy e_1 for the trajectory from the initial distribution $g_{e_n} f_{e_n}(t_0)$.

3. Calculate the initial collision rate $\gamma(e_1, t_0)$ using $f_{e_n}(t_0)$ for the distribution

$$\gamma(e_1, t_0) = \sum_{e_m e_q e_p} \delta_{e_1+e_m, e_q+e_p} \frac{g(e_1, e_m; e_p, e_q)}{g_{e_1}} f_{e_m}(t_0)(1+f_{e_q}(t_0))(1+f_{e_p}(t_0)) \ . \tag{7.24}$$

4. Simulate a realization of a uniform random variable $R_1 \in [0, 1]$ and find the time the particle will next collide given by $t_c = t_0 - \ln(R_1)/\gamma(e_1, t_0)$.

5. If $t_c > t_0 + dt$, record the atom in $f_{e_n}(t_0 + dt)$ by incrementing the level corresponding to its energy by the amount N/M.

6. If $t < t_0 + dt$, a collision occurs. Simulate a second random variable $R_2 \in [0, 1]$. The energy after the collision is found from the solution of $e_{\rm sim}$ in

$$\sum_{e_n}^{e_{\rm sim}} \sum_{e_m e_p} \delta_{e_1+e_p, e_n+e_m} \frac{g(e_1, e_p; e_n, e_m)}{g_{e_1}} f_{e_p}(t_0)(1+f_{e_n}(t_0))(1+f_{e_m}(t_0)) = R_2 \gamma(e_1, t_0) \tag{7.25}$$

7. Continue steps 3 - 6 until the end of the interval $t_0 + dt$ is reached. Because dt must be much smaller than τ_{col}, multiple collisions should be rare.

8. Calculate the next trajectory by choosing another initial energy in step 2 and carrying out steps 3 - 7. Continue the process for M trajectories.

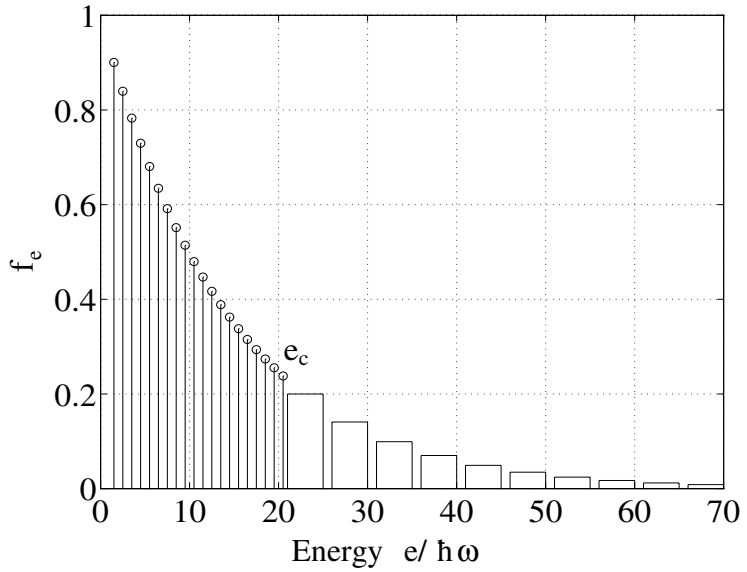

Figure 7.2: An illustration of the distribution of populations f_e over the discrete and continuous regions. Above the cutoff e_c, we drop the $(1 + f_{e_n})$ factors and the levels are put in bins as though they formed a continuous spectrum.

9. When all of the trajectories have been accumulated, a good approximation to $f_{e_n}(t_0 + dt)$ has been determined. One can then move on to the next time step, and repeat steps 1 - 8 by using $f_{e_n}(t_0 + dt)$ as the initial distribution. This coarse-grained time evolution can be continued until $f_{e_n}(t)$ has been obtained for the desired time duration.

This trajectory simulation scales quadratically with the number of levels whose populations must be stored, which is an improvement over the cubic scaling of a direct numerical integration of Eq. (7.12). However, as already pointed out, the trajectory simulation of the classical Boltzmann equation scales linearly with the number of bins used to store $f(e)$. It is now very clear that making the ergodic assumption and using the classical, limiting form of the ergodic, QBE will increase the speed of the simulation enormously by decreasing the number of discrete energy levels whose populations must be simulated. By treating most of the levels above some cutoff e_c classically according to Eq. (7.18), the linear scaling of the method described in Ref. [118] can almost be restored.

In order to speed up the simulation by using the smooth transition to the ergodic, classical Boltzmann equation described in section 7.2.3, we use a distribution that has discrete levels below a cutoff energy e_c and a continuous spectrum of energies above this point, as shown in Figure 7.2. Below e_c, we retain the $(1+f_{e_n})$ factors. We also use $g(e_n, e_m; e_q, e_p)$ if all four energies are less than or equal to e_{10}, and use its limiting form $g_{e_{\min}}$ if any of the four energies is greater than e_{10}. Above e_c, we drop the $(1 + f_{e_n})$ factors, and use the density of states $\rho(e)$ as the limiting form of the degeneracy factor. When all four energies are above e_c, the simplifications made on the integrals in the collision rate, shown in Ref. [118], can be used.

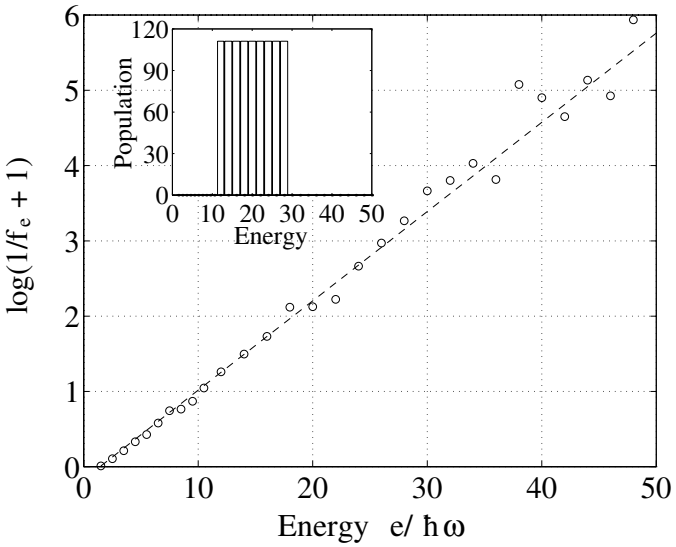

Figure 7.3: The system evolves to equilibrium from the distribution shown in the sub-plot, where a single trajectory has on average 100 collisions. The final, stationary distribution (circles) agrees with the Bose-Einstein equilibrium distribution (dashes).

7.4 Simulation results

In this section, we carry out the simulation procedure described in section 7.3 to investigate physical properties of a condensing gas of atoms trapped in an isotropic, harmonic potential. We show results demonstrating the equilibrium properties of a finite system, the build-up of the ground state population starting from zero, and evaporative cooling of atoms in the trap.

A simple test of the trajectory simulation is to start the distribution $f_{e_n}(t_0)$ in a non-equilibrium state and allow it to evolve to equilibrium. In the sub-plot of Figure 7.3, the initial non-equilibrium distribution is shown for $N = 10^3$, and a mean energy of $20.5\,\hbar\omega$. It is allowed to evolve to the stationary state shown in Figure 7.3, where each trajectory had, on average, 100 collisions. The simulation data is compared with the Bose-Einstein equilibrium distribution

$$f_{e_n} = \frac{1}{e^{\beta(e_n-\mu)} - 1} \,, \tag{7.26}$$

where $\beta = 1/k_B T$ and μ is the chemical potential. Both β and μ are chosen in the plot so that $g_{e_n} f_{e_n}$ is normalized to N and the mean energy matches that of the simulated distribution. As Figure 7.3 shows, the trajectory simulation evolves $f_{e_n}(t_0)$ to the correct equilibrium distribution for a finite number of atoms without a mean field interaction.

7.4.1 Finite number effects on equilibrium

Finite number effects can be studied by allowing the distribution $f_{e_n}(t)$ to evolve to equilibrium. In Figure 7.4, the ground state fraction is plotted vs. the temperature for the case

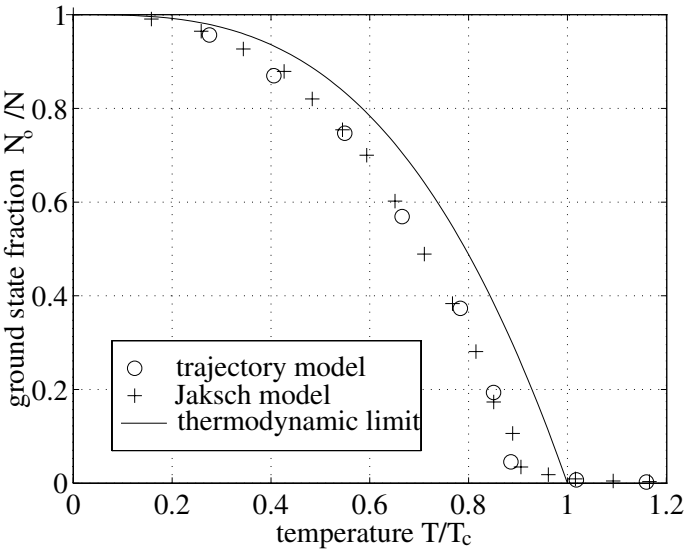

Figure 7.4: Ground state fraction versus temperature for 500 atoms. Each point is obtained by allowing a system of 500 atoms with a known mean energy to evolve to equilibrium. Once equilibrium is obtained, the fraction in the ground state is recorded. The plot shows our data, data from Ref. [121], and the thermodynamic limit.

of $N = 500$. The graph shows three different sets of data: the trajectory simulation, results from Ref. [121], and the thermodynamic limit. The trajectory data agrees with the results of Ref. [121], where a different approach to simulating the QBE is used. The line for a finite number of atoms has the same qualitative shape as in the thermodynamic limit, but it is shifted toward lower temperatures [121, 123, 124]. In Figure 7.5, the same plot is shown for the case of 2×10^4 atoms. As expected, the line is shifted less from the thermodynamic limit. The effect of finite size on the mean energy of the system can also be studied. In Figure 7.6, the mean energy is plotted vs. temperature for the case of $N = 500$. Again, the trajectory simulation agrees with the results of Ref. [121]. The same plot is shown in Figure 7.7 for the case of 2×10^4 atoms. The mean energy for a finite number of atoms is larger than that in the thermodynamic limit below T_c. In the thermodynamic limit, the number and volume are taken to infinity, with the local density held fixed. For the case of atoms in a trap, taking the volume to infinity is achieved by allowing ω to go to zero. For a finite system, the effect of the potential remains, thus giving the system a higher mean energy than it would in the limit of $\omega \to 0$.

7.4.2 Dynamic buildup of the condensate

The buildup of the condensate can be investigated by starting in a non-equilibrium distribution f_{e_n} with no atoms in the ground state initially, and allowing the distribution to evolve to equilibrium. One can monitor the occupation of the ground state over time. As Figure 7.8 shows, the time dependence of the population in the ground state is given by $N_0(t) = N_0(\infty)(1 - e^{-t/\tau_0})$, where the time constant τ_0 is determined by fitting the data.

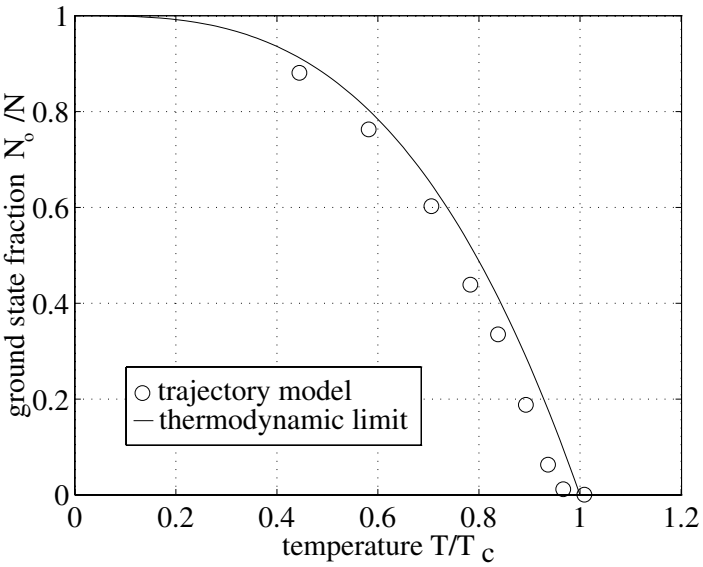

Figure 7.5: Same procedure as in Figure 7.4, but with 2×10^4 atoms.

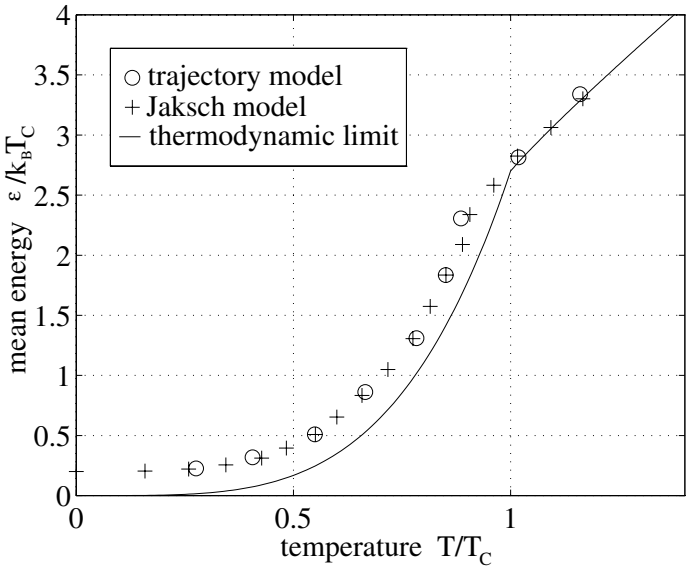

Figure 7.6: Mean energy versus temperature for 500 atoms. Each point is obtained by allowing a system of 500 atoms with a known mean energy to evolve to equilibrium. The plot shows our data, data from Ref. [121], and the thermodynamic limit.

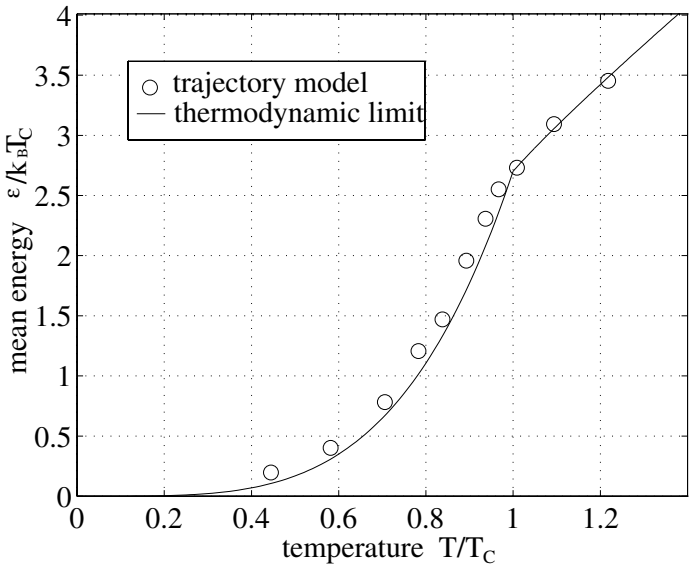

Figure 7.7: Same procedure as in Figure 7.6, but with 2×10^4 atoms.

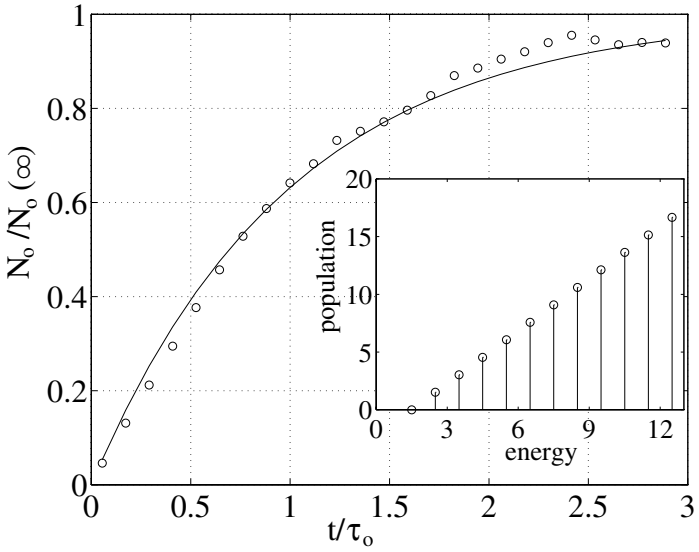

Figure 7.8: The population in the ground state increases as the system of 100 atoms evolves to equilibrium, starting in the initial distribution shown in the sub-plot (where energy is given in units of $\hbar\omega$). The ground state fraction increases according to $N_0(t) = N_0(\infty)(1 - e^{-t/\tau_0})$.

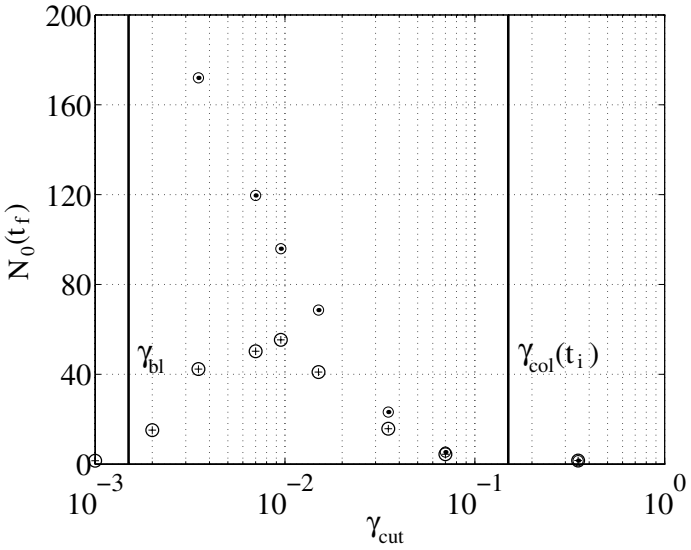

Figure 7.9: The final number in the ground state $N_0(t_f)$ as a function of the cut rate $\gamma_{\rm cut}$, with (circled-cross) and without (circled-dot) background loss. The cut rate must be slower than the initial single particle collision rate $\gamma_{\rm col}(t_i)$ and faster than the background loss rate $\gamma_{\rm bl}$ for the evaporation to be successful.

This result also agrees with that given in Ref. [121]. The initial distribution, shown in the sub-plot in Figure 7.8, had 100 atoms with 10% in the ground state after it had reached equilibrium.

It was found that τ_0 depends slightly on the initial distribution: With the mean energy and total number fixed, the further the atoms are from e_0, the longer it will take to reach the ground state. This is also why the time constant τ_0 decreases as $N_0(\infty)$ increases while keeping N fixed, since the mean energy decreases, requiring atoms to reside in levels closer to e_0. As N gets large, more energy levels will be occupied and one might expect there to be a delay time for the atoms to begin filling the ground state [121]. Finally, it was found that τ_0/τ_{col} increases with increasing N, while keeping $N_0(\infty)/N$ fixed [125]. For the case of 100 atoms shown in Figure 7.8, $\tau_0/\tau_{col} \approx 25$, compared to a separate case for 50 atoms, where $\tau_0/\tau_{col} \approx 10$.

7.4.3 Evaporative cooling simulation

A practical use of our simulation method is to study the evaporative cooling of a gas of atoms in an isotropic harmonic trap. Evaporative cooling may be described by allowing trajectories with an energy above a time-dependent energy threshold $e_{\rm cut}(t)$ to be lost from the trap. We can also allow there to be a finite probability for trajectories to be lost due to collisions with background atoms, which occur at a rate $\gamma_{\rm bl}$.

In Figure 7.9, we show data points collected from simulations of a particular evaporative cooling scenario. We began with $N = 10^4$ atoms in thermal equilibrium at a temperature $T = 15\,T_c$. We then allowed the system to evolve while lowering the energy threshold

$e_{\rm cut}(t)$ exponentially in time at a rate $\gamma_{\rm cut}$, with no background losses. As the temperature approached T_c, when there was one atom in the ground state with 500 atoms left in the trap, we stopped the simulation. We then proceeded cutting exponentially to $e_{\rm cut}(t_f) = e_2$, the second energy level, at varying rates $\gamma_{\rm cut}$, as well as with and without background loss. Figure 7.9 shows a semi-log plot of the final number in the ground state $N_0(t_f)$ vs. $\gamma_{\rm cut}$.

The result is intuitive: With no background loss, $N_0(t_f)$ decreases as the cut rate increases. If we cut faster than the collision rate $\gamma_{\rm col}$, then the evaporation completely fails because the gas does not have time to equilibrate as the threshold is lowered. When background loss is included, one can see that the lower limit on $\gamma_{\rm cut}$ is determined by the background loss rate $\gamma_{\rm bl}$. If we cut slower than the background loss rate, all of the atoms are lost from the trap before the evaporation process is finished. Thus, there is an optimum cut rate $\gamma_{\rm cut}$ bracketed by these two physical properties.

7.5 Summary

We have presented a novel approach to treating quantum kinetics which is based on a decomposition of the ergodic QBE into single-particle trajectories. We presented the underlying physical theory, explained our trajectory approach to simulating quantum kinetics, and displayed results of our method applied to some contemporary problems concerning Bose-Einstein condensation. As a test of the validity of our method, it agrees well with independent studies on the processes studied in section 7.4 [121]. Our approach gives an efficient simulation of quantum kinetics and is valid for the entire range of phase-space densities, excluding at this stage the region close to $T = 0$ when the mean field effect on the system must be considered.

The trajectory approach of quantum kinetics described in this chapter is applicable to many problems of interest. One such problem is that of finding the optimum way to lower $e_{\rm cut}(t)$ during the evaporative cooling process, while taking into account all of the various loss mechanisms, such as loss due to collisions with background atoms and heating due to two-body and three-body inelastic collisions. Another interesting problem is that of including the mean field effect on the system during the kinetic evolution close to $T = 0$. To address this problem using the QBE, we will have to work in the representation of the mean-field states, which requires finding the mean field eigenstates self-consistently after each time-step in the simulation. Finally, it may also be interesting to use the trajectory approach to treat Fermi-Dirac statistics and describe the time-evolution of a gas of fermions.

Chapter 8

Achieving Steady-State Bose-Einstein Condensation

8.1 Introduction

In the usual method of evaporative cooling used so far in BEC experiments [109, 110, 118, 126, 127, 128], a finite number of atoms are collected in a magnetic trap after being laser cooled to a phase space density at least five orders of magnitude below the critical density needed for BEC. The frequency of an external RF radiation field, which spin-flips the atoms to an un-trapped state, is then lowered continuously. This further cools the gas by removing high energy atoms from the tail of the distribution. This evaporative cooling procedure increases the phase space density above the critical point needed to reach BEC. The success of this method is well established experimentally, allowing many fundamental properties of Bose-Einstein condensation to be investigated [33, 34].

This standard method of achieving BEC has one critical drawback: once a condensate has been obtained, it has a finite lifetime in the trap determined by various loss mechanisms, such as collisions with hot atoms from the background gas, and inelastic collisions between the trapped atoms. Although the finite lifetime of the condensate does not prevent many crucial properties of the system to be studied, it is still very desirable to achieve a steady state situation so that a condensate can be sustained for an indefinite period of time. Such a situation is essential for the continuous output of a coherent beam of atoms in an atom laser [17, 129, 130, 131, 132, 133]. To date, no experiment has demonstrated a steady state condensation.

We address this problem by constructing an intuitive model describing the two aspects to such an experiment: The continuous loading of atoms into the magnetic trap and the classical kinetic evolution of the trapped atoms toward a steady state during the evaporation. Our description of the loading procedure is based on the experimental setup described in [134], where the authors loaded a magnetic trap with atoms which had been cooled in a separate MOT. This allows us to estimate the rate $\gamma_{\rm f}$ that atoms enter the trap below the RF cut, as well as the mean energy $e_{\rm f}$ of the injected atoms.

To model the classical kinetic evolution, we assume a truncated Boltzmann distribution for the trapped atoms and obtain rate equations for the total number $N(t)$ and energy $E(t)$ of the system [109, 118, 126, 127, 128]. These rate equations include the loss of atoms

due to elastic collisions with the background-gas atoms, inelastic 3-body collisions, and evaporation, as well as the gain of atoms due to loading. We then numerically calculate the steady state solution of these equations and show plots of the peak phase space density ρ_0 as a function of the various physical parameters of the system. We show that the critical regime $\rho_0 \geq 2.612$ may be reached in order to obtain BEC in steady state.

8.2 Description of the model

In constructing a model of steady state evaporative cooling, there are several experimental schemes one could consider for describing the loading of atoms into the magnetic trap, as well as several layers of approximation in describing the kinetic evolution of the trapped gas toward steady state. However, we consider only one realization of the loading procedure, assuming the atoms are first trapped and cooled in a MOT and then transferred to a separate magnetic trap [134, 135, 7]. Furthermore, we consider a simplified model of evaporative cooling that assumes classical statistics, and is therefore valid only for phase space densities below the critical point $\rho_0 = 2.612$; one would have to include quantum statistics in order to properly model the system above this point. These two parts to our model are described in the following subsections.

8.2.1 Description of the loading procedure

In a real experiment, irreversibility is introduced at each step of the transfer of the atoms from the MOT to the magnetic trap; the atoms are first pushed out of the MOT, they then travel through a magnetically-confining tube, and finally must be caught in the magnetic trap and optically pumped into a trapped hyperfine state. In order not to get lost in the details of modeling all of these heating and loss mechanisms, we consider two extreme idealizations of the transfer: an adiabatic transfer which preserves the phase space density ρ_0 and a sudden, irreversible transfer which decreases ρ_0.

We assume the atoms feel an isotropic, linear restoring force in both the MOT and the magnetic trap, neglecting the possibility of a radiation pressure in the MOT, which would distort the effective harmonic trapping potential [136]. Then the free Hamiltonian of an atom in either trap can be written

$$H_i(r,p) = \frac{p^2}{2m} + \frac{1}{2}m\omega_i^2 r^2 \ , \tag{8.1}$$

where m is the mass of the atom, and ω_i is the effective radial frequency of the trapping potential. The index $i = 1$ indicates the MOT, while $i = 2$ indicates the magnetic trap.

We model the transfer of atoms in order to obtain a reasonable estimate of the feed rate $\gamma_{\rm f}$ and the mean energy $e_{\rm f}$ of atoms injected into the trap below the RF cut. We treat this transfer process as a succession of discrete transfers each consisting of a finite number of atoms. We only need to consider a snapshot of this transfer process: a finite number of atoms N_1 are collected in the MOT at a temperature T_1 in equilibrium, they are then either adiabatically or suddenly transfered to the magnetic trap. In our model, we allow these N_1 atoms to come to an equilibrium in the magnetic trap, characterized by a new temperature T_2. We then place the RF cut $e_{\rm cut}$ and calculate the fraction of atoms $\alpha_{\rm f}$ which remain in the magnetic trap below $e_{\rm cut}$, as well as the mean energy per atom $e_{\rm f}$ of these atoms

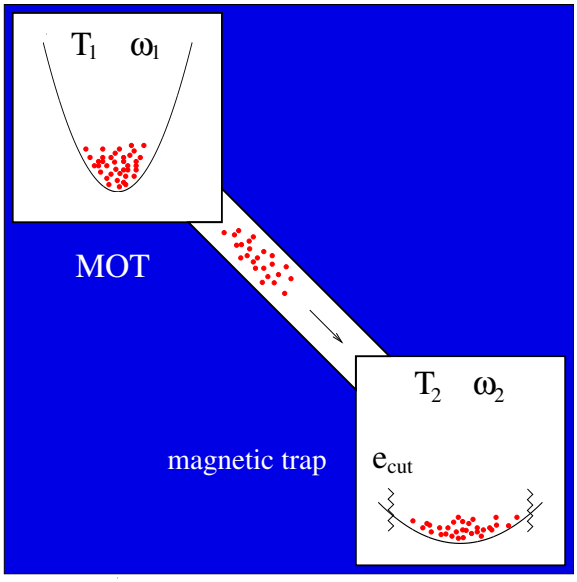

Figure 8.1: Illustration of the transfer process described in section 8.2.1. A finite number of atoms are cooled in the MOT to a temperature T_1 in equilibrium. We approximate the potential in the MOT as an isotropic harmonic oscillator at frequency ω_1. They are then transferred to the magnetic trap, either suddenly, or adiabatically. We also approximate the magnetic trap as forming an isotropic harmonic oscillator potential, with a different frequency ω_2. In equilibrium, the atoms have a temperature T_2 in the magnetic trap. Then, the RF energy threshold $e_{\rm cut}$ is applied and only a portion of the original atoms from the MOT remain. This transfer can be repeated many times in order to obtain a piecewise continuous transfer of atoms.

$$\alpha_{\rm f} = \frac{\int_0^{e_{\rm cut}} e^2 e^{-e/k_{\rm B}T_2} de}{\int_0^{\infty} e^2 e^{-e/k_{\rm B}T_2} de} \ , \tag{8.2}$$

$$e_{\rm f} = \frac{\int_0^{e_{\rm cut}} e^3 e^{-e/k_{\rm B}T_2} de}{\int_0^{e_{\rm cut}} e^2 e^{-e/k_{\rm B}T_2} de} \ . \tag{8.3}$$

The e^2 factor appears due to the density of states for an isotropic harmonic oscillator potential. A schematic diagram in Figure 8.1 illustrates the transfer process.

This process can be repeated many times each second so that atoms are transfered to the magnetic trap at a rate $\gamma_{\rm t}$. The rate that atoms enter below the RF threshold $e_{\rm cut}$ is then given by $\gamma_{\rm f} = \alpha_{\rm f}\,\gamma_{\rm t}$. We estimate an upper limit on the number of these transfers each second to be on the order of 100.

The equilibrium temperature T_2 which the atoms attain after a sudden transfer can be obtained by considering the sudden change in the energy of the atoms after the instantaneous change in trapping frequencies $\omega_1 \rightarrow \omega_2$. Then for a sudden transfer, the temperature T_2 is related to the temperature T_1 in the MOT according to

$$T_2 = \frac{T_1}{2}(1 + \frac{\omega_2^2}{\omega_1^2}) \quad \text{(sudden)} \ . \tag{8.4}$$

The adiabatic case can be treated as a succession of infinitesimal steps $\omega_1 \rightarrow \omega_1 + \delta\omega$, each treated as a sudden transfer. This yields the relationship

$$T_2 = T_1 \frac{\omega_2}{\omega_1} \quad (\text{adiabatic}) \ . \tag{8.5}$$

Note that both cases give $T_2 = T_1$ when $\omega_2 = \omega_1$ as they must. With the peak phase space density $\rho_0 = n_0 \Lambda^3$ of the trapped atoms given by

$$\rho_0 = N_1 (\frac{\hbar \omega_i}{k_{\rm B} T_i})^3 \ , \tag{8.6}$$

it is clear that ρ_0 is invariant through an adiabatic transfer, while it decreases after a sudden transfer. Here, Λ is the deBroigle wavelength and n_0 is the peak spatial density.

The two quantities $\gamma_{\rm f}$ and $e_{\rm f}$ depend on the frequency in the lower trap ω_2, as well as the RF field threshold $e_{\rm cut}$; as the trap is made looser, more atoms will make it into the trap below the cut so that $\gamma_{\rm f}$ increases. The feed rate is also increased as $e_{\rm cut}$ is raised, however the mean energy $e_{\rm f}$ of those atoms increases as well.

8.2.2 Description of evaporative cooling

With the feeding rate $\gamma_{\rm f}$ and mean energy per atom $e_{\rm f}$ of the injected atoms given by the above model of the loading procedure, it remains to describe the kinetic evolution of the atoms in the magnetic trap during evaporation. Our model can be constructed on phenomenological considerations, with the goal of characterizing the steady state of the system.

We characterize the trapped atoms by a single-particle distribution over energy $\rho(e)\, f(e,t)$ instead of retaining the more detailed description in phase space using $f(\vec{x}, \vec{p}, t)$ [109]. Here $\rho(e)$ is the density of states for an isotropic harmonic potential. We also make an assumption that the non-equilibrium distribution $f(e,t)$ of the system can be well approximated by a truncated Boltzmann distribution [109, 118, 126, 127, 128]

$$f(e,t) = \begin{cases} \eta(t) e^{-\beta(t) e} & e < e_{\rm cut} \\ 0 & e \geq e_{\rm cut} \ , \end{cases} \tag{8.7}$$

where $\eta(t)$ and $\beta(t) = 1/k_{\rm b} T(t)$ are functions of time. They are related to the total number $N(t)$ and total energy $E(t)$ of the atoms according to

$$N(t) = \int_0^{e_{\rm cut}} de\, \rho(e)\, f(e,t) \ , \tag{8.8}$$

$$E(t) = \int_0^{e_{\rm cut}} de\, \rho(e)\, e\, f(e,t) \ . \tag{8.9}$$

With the assumption of the truncated Boltzmann form for $f(e,t)$, the description of the system can be reduced to finding the equations of motion for the total number and energy.

The equations of motion for $N(t)$ and $E(t)$ will be written in terms of the various gain and loss processes which occur. There are four competing processes which take place during the evaporation: the constant feeding of atoms into the trap at a rate $\gamma_{\rm f}$ with a mean energy per atom $e_{\rm f}$, the loss of atoms from the trap due to collisions with the atoms from the hot background gas, characterized by a constant rate $\gamma_{\rm bl}$, the loss of atoms and heating due

to 3-body inelastic collisions, given by the rate γ_3', and the rethermalization due to elastic collisions which will eject atoms from the trap which obtain an energy above $e_{\rm cut}$ after a collision. We can include all of these effects in the kinetic equation for $f(e,t)$

$$\rho(e)\frac{\partial f(e,t)}{\partial \tau} = \gamma_{\rm f}\, g_{\rm f}(e) - \gamma_{\rm bl}\,\rho(e) f(e,t) - \gamma_3'\,(\rho(e) f(e,t))^3 + \Gamma_{\rm col}(t)\ , \qquad (8.10)$$

where the distribution of atoms injected into the trap is $g_{\rm f}(e)$ and the density of states is $\rho(e) = \frac{1}{2}e^2/(\hbar\omega_2)^3$. $\Gamma_{\rm col}(t)$ is the collision integral given by [109]

$$\Gamma_{\rm col}(t) = \gamma_0 \int de_{\rm r} de' de_{\rm r}' \delta(e + e_{\rm r} - e' - e_{\rm r}')\rho(e_{\rm min})[f(e')f(e_{\rm r}') - f(e)f(e_{\rm r})]\ , \quad (8.11)$$

where $\gamma_0 = m\sigma/(\pi^2\hbar^3)$ and $e_{\rm min} = \min\{e, e_{\rm r}, e', e_{\rm r}'\}$ is the minimum energy.

By substituting Eq. (8.7) into Eq. (8.10), and using Eq. (8.8) and Eq. (8.9), we obtain the following equations of motion for the total number and total energy

$$\dot{N} = \gamma_{\rm f} - \gamma_{\rm bl}\, N - \gamma_3\, N^3 - \Gamma_{\rm N}\ , \qquad (8.12)$$

$$\dot{E} = \gamma_{\rm f}\, e_{\rm f} - \gamma_{\rm bl}\, E(t) - \frac{2}{3}\gamma_3\, N^2\, E - \Gamma_{\rm E}\ , \qquad (8.13)$$

where the 3-body loss rate for the total number is $\gamma_3 = 3^{1.5} K_3 (m\omega_2^2/2\pi k_{\rm B}T)^3$. K_3 is an experimentally determined constant to be specified [137]. In obtaining the 3-body loss terms, an approximation has been made that $e_{\rm cut} \gg k_{\rm B}T(t)$ in order to simplify the terms. Initially during the evolution, this assumption may not hold, but the density is low enough initially that the 3-body loss terms are negligible in any case. By the time the density has increased enough so that 3-body losses are significant, the assumption does hold. The factor of $2/3$ in Eq. (8.13) signifies that the energy will decrease at a slower rate than the number due to 3-body losses, which gives rise to an effective heating.

The two terms $\Gamma_{\rm N}$ and $\Gamma_{\rm E}$ represent the loss of number and energy due to evaporation and are given by

$$\Gamma_{\rm N} = \gamma_0 \int_0^{e_{\rm cut}} de \int_{e_{\rm cut}-e}^{e_{\rm cut}} de_{\rm r} \int_0^{e+e_{\rm r}-e_{\rm cut}} de_{\rm r}'\ \rho(e_{\rm r}') f(e,t) f(e_{\rm r},t)\ , \qquad (8.14)$$

$$\Gamma_{\rm E} = \gamma_0 \int_0^{e_{\rm cut}} de \int_{e_{\rm cut}-e}^{e_{\rm cut}} de_{\rm r} \int_0^{e+e_{\rm r}-e_{\rm cut}} de_{\rm r}'\ e'\rho(e_{\rm r}') f(e,t) f(e_{\rm r},t)\ . \qquad (8.15)$$

The fourth atom in these equations is lost from the trap since its energy is always greater than the RF cut $e' > e_{\rm cut}$. Due to energy conservation and the truncated form of $f(e)$, this means that $e_{\rm min} = e_{\rm r}'$, as indicated in Eq. (8.14) and Eq. (8.15). Also, the energy which appears in the term $\Gamma_{\rm E}(t)$ is that of the escaping atom $e' = e + e_{\rm r} - e_{\rm r}'$.

8.3 Results

In order to carry out explicit calculations, we choose realistic values of the various physical parameters needed in our model. These are listed in Table 8.1 for a gas of ^{87}Rb atoms. The parameters ω_2 and $e_{\rm cut}$ are not listed in the table but are variables to be specified in the following calculations. We have specified a reference point for the MOT parameters which yields a phase space density in the MOT of $\rho_0 = 6.9 \times 10^{-6}$, if one assumes that $N_1 = 5 \times 10^5$ at 20 transfers per second [136].

$\sigma_{\rm Rb}$	$7.5 \times 10^{-16}{\rm m}^2$
$\tau_{\rm bl} \equiv 1/\gamma_{\rm bl}$	200 s
K_3	$4.9 \times 10^{-29}{\rm cm}^6/{\rm s}$
$T_1^{(\rm ref)}$	$20\,\mu$K
$\omega_1^{(\rm ref)}/2\pi$	100 Hz
$\gamma_{\rm t}^{(\rm ref)}$	10^7 atoms/s

Table 8.1: Values used for the various physical parameters needed in the model. $\sigma_{\rm Rb}$ is the s-wave scattering cross section for ^{87}Rb. The explanations for the other parameters are given in the text.

8.3.1 Time evolution

We first consider the dynamical evolution of the system toward steady state. In Figure 8.2 we show results of a numerical integration of the rate equations in Eq. (8.12) and Eq. (8.13) for the total number $N(t)$ and energy $E(t)$. Since the magnetic trap frequency ω_2 is matched to the MOT frequency ω_1 in this calculation, the adiabatic and sudden transfers are equivalent. For case 1 in the figure, we chose the optimum value of $e_{\rm cut}$ to yield the highest phase space density ρ_0, while in case 2 the value chosen for $e_{\rm cut}$ is ten times higher than that in case 1. There are some interesting features to consider from this plot.

It is instructive to take a simple limiting case of Eq. (8.12) and Eq. (8.13) in order to learn something about the build-up time for steady state to occur. If we let $e_{\rm cut} \to \infty$ and $\gamma_3 = 0$, then the solution to the rate equations for $N(t)$ and $E(t)$ is given by

$$\begin{aligned} N(t) &= \frac{\gamma_{\rm t}}{\gamma_{\rm bl}}\left(1 - e^{-\gamma_{\rm bl}\,t}\right) , \\ E(t) &= \frac{\gamma_{\rm t}}{\gamma_{\rm bl}}\,e_{\rm f}\left(1 - e^{-\gamma_{\rm bl}\,t}\right) . \end{aligned} \tag{8.16}$$

The time-scale for steady state to occur in this simple case is just the lifetime of the trap as determined by background losses, $\tau_{\rm bl}$. In the case where the RF cut is present and evaporation is occurring, while still neglecting 3-body losses, the build-up time for steady state will be on the order of magnitude of $\tau_{\rm bl}$, although it will be shorter, based on results of numerical calculations. We define this build-up time to be the time at which $N(t) = (1 - e^{-1})N_{\rm ss}$. When 3-body losses are included, the build up time can be very short compared to $\tau_{\rm bl}$ if the density is high enough for 3-body losses to dominate. So this gives us an upper limit of the build-up time to be $\tau_{\rm bl}$, and if steady state occurs on a much shorter time scale than this, it indicates that 3-body losses are dominating the other loss mechanisms.

In Figure 8.2, the build-up time in case 1 is slightly less than $\tau_{\rm bl}$, which is 200 seconds. This indicates that the choice of $e_{\rm cut}$ in case 1 minimizes 3-body losses. In case 2, on the other hand, where $e_{\rm cut}$ is ten times larger than that in case 1, the build-up time is much shorter at roughly 25 seconds. This is because in case 2, $\gamma_{\rm f}$ is larger, causing the density to build-up more quickly which allows 3-body losses to dominate. This also stops the evaporative cooling quickly and so one does not obtain as high of a phase space density ρ_0 as in case 1. It should be noted that when we calculated case 2 with $\gamma_3 = 0$, the build-up time was approximately equal to $\tau_{\rm bl}$, and the steady state value of the phase space density was close to being optimized at that value of $e_{\rm cut}$, with $\rho_0 = 3.9$ in steady state.

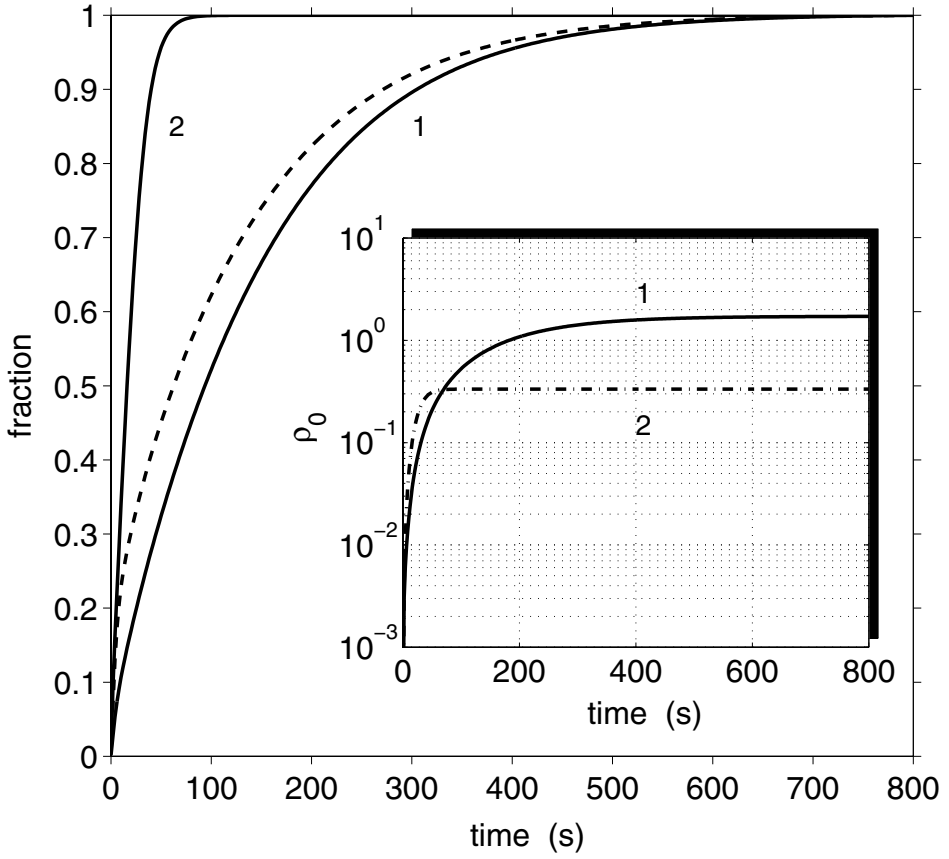

Figure 8.2: Time evolution of the total number $N(t)$ and total energy $E(t)$ for the values of the parameters listed in Table 8.1. The magnetic trap frequency is equal to the MOT frequency $\omega_2 = \omega_1$ in this calculation. Two values of $e_{\rm cut}$ were chosen: 1.1 μK, labeled by 1, and 11 μK, labeled by 2. Each of the curves is normalized by its final steady state value. The solid curve is the total number and reaches a steady state value of $N_{\rm ss} = 2.0 \times 10^4$ for case 1, and $N_{\rm ss} = 2.8 \times 10^6$ for case 2. The dashed curve is the total energy and reaches a steady state value of $E_{\rm ss} = 0.33\,\mu{\rm K} \times N_{\rm ss}$ for case 1 (case 2 is not shown). The evolution of the peak phase space density ρ_0 is shown in the inset for the two cases.

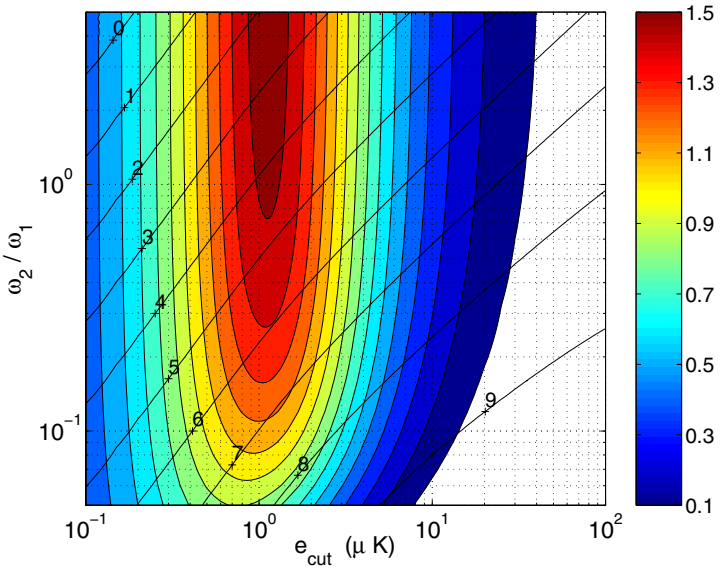

Figure 8.3: Two overlaying contours of the steady state value of the phase space density and the total number vs. the ratio of trap frequencies and RF cut threshold for an adiabatic transfer. The shaded contours represent the steady state value of ρ_0, with the gray-scale bar shown to the right. The numbered lines represent $\log_{10} N_{\rm ss}$ (i.e. a value of 6 for the line in the center corresponds to $N_{\rm ss} = 10^6$). It is ω_2 which is varied in the ratio, while ω_1 is fixed at 2π 100 Hz. The values used for the other parameters are displayed in Table 8.1.

8.3.2 Steady state solution

Now that we have characterized the time scale for steady state to occur, it is useful to solve Eq. (8.12) and Eq. (8.13) directly for the steady state values of $N_{\rm ss}$ and $E_{\rm ss}$ by setting the left-hand sides equal to zero. We were not able to solve the resulting coupled algebraic equations analytically, since they are transcendental in form. However, they are straightforward to solve numerically. In the following sections, we present calculations of the steady state value of ρ_0 while varying some of the physical parameters in order to discern what values of the parameters yield $\rho_0 = 2.612$ so that BEC can be achieved in steady state.

Varying $e_{\rm cut}$ and ω_2

In trying to understand what it takes to reach a steady state BEC, it is useful to look at how ρ_0 varies with ω_2 and $e_{\rm cut}$. In Figure 8.3 and Figure 8.4, we show shaded contour plots of the steady state value of ρ_0, for both an adiabatic and a sudden transfer. Also shown are contours of the total number $N_{\rm ss}$ overlaying the shaded contours. Again, we use the reference point of parameters displayed in Table 8.1. The two different idealizations of the transfer process yield quite distinct shapes for the surfaces of ρ_0 and $N_{\rm ss}$.

For the adiabatic case shown in Figure 8.3, ρ_0 increases with increasing ω_2, keeping $e_{\rm cut}$ fixed. However, it levels off quite quickly, varying from 1.1 to 1.5 with an order of magnitude increase in ω_2/ω_1 from 0.1 to 1.0 at $e_{\rm cut} = 1\,\mu$K. Also, with ω_2 fixed, the

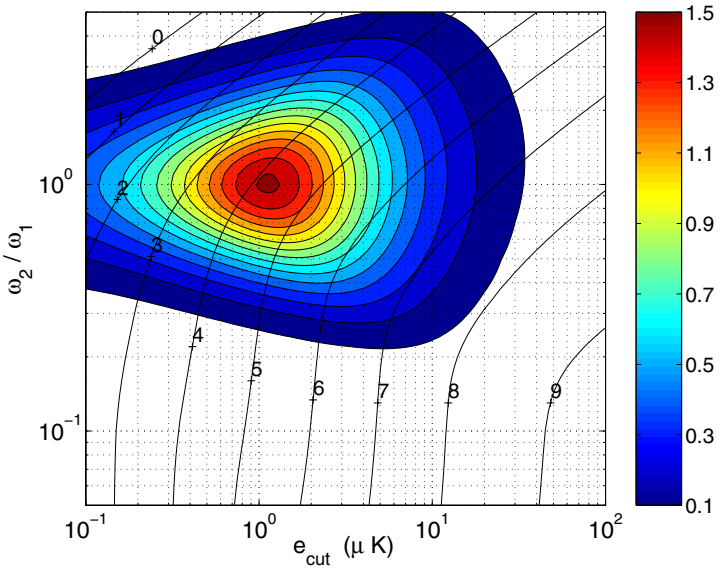

Figure 8.4: Same as described in the caption of Figure 8.3 except for a sudden transfer of atoms from the MOT to the magnetic trap, instead of an adiabatic one.

optimum value of $e_{\rm cut}$ which yields the highest ρ_0 does not depend much on ω_2, but is roughly a straight line at $e_{\rm cut} = 1\,\mu$K. Perhaps the most interesting and crucial feature exhibited in the plot is that $N_{\rm ss}$ decreases very rapidly as ω_2 is increased, going from 10^7 down to 10^4 as ω_2/ω_1 goes from 0.1 to 1.0. This is because 3-body losses increase as the trap is tightened, since the density increases. Therefore, one will gain a lot in number by keeping the magnetic trap shallow, while losing only a small amount in phase space density.

The results of a sudden transfer are shown in Figure 8.4. The most striking difference between this and the plot shown in Figure 8.3 for an adiabatic transfer is a strong peak which occurs at $\omega_2/\omega_1 = 1$. This can be attributed to the fact that the phase space density always decreases in a sudden transfer, with a peak occurring at $\omega_2 = \omega_1$ where the sudden and adiabatic transfers are equivalent. Notice also that ρ_0 drops off much more rapidly as ω_2/ω_1 is varied from unity, compared to the adiabatic case. Another difference between the two cases is that the optimum value for $e_{\rm cut}$ increases as ω_2/ω_1 is varied from unity. Finally, it can be seen also that one does not gain that much in number as ω_2 is decreased, in sharp contrast to the adiabatic case.

Varying T_1 and $\gamma_{\rm t}$

We now have an understanding of how the steady state values of ρ_0 and $N_{\rm ss}$ vary with $e_{\rm cut}$ and ω_2. Another useful calculation is to see how ρ_0 depends on the MOT temperature T_1 and the transfer rate $\gamma_{\rm t}$. In the plots below, $e_{\rm cut}$ is chosen so as to maximize ρ_0, for a given T_1, $\gamma_{\rm t}$, and ω_2. Then, given $\gamma_{\rm t}$ and ω_2, T_1 is chosen so as to reach $\rho_0 = 2.612$. This is done for $10^6 \leq \gamma_{\rm t} \leq 10^8$, as well as three values of the trap frequency ratio $\omega_2/\omega_1 \in \{0.1,\, 0.5,\, 1\}$, with $\omega_1 = 2\pi\,100$ Hz.

The results of an adiabatic transfer are shown in Figure 8.5. Along each of the three

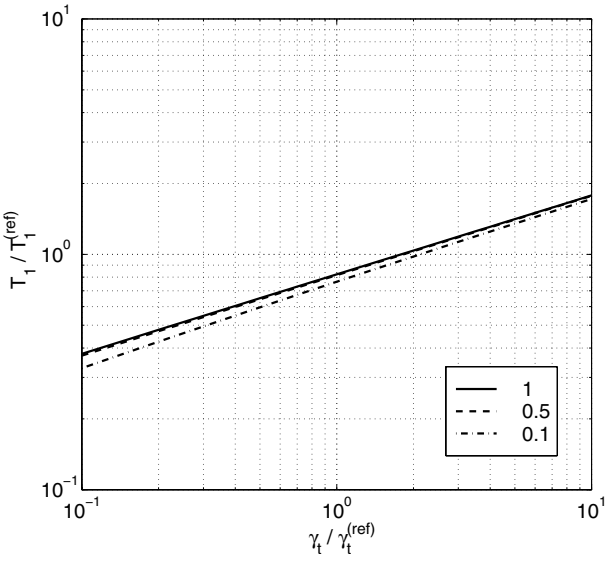

Figure 8.5: Values of T_1 and ω_2 one must achieve in order to reach $\rho_0 = 2.612$ in the case of an adiabatic transfer. Three different values of ω_2/ω_1 are shown: $\omega_2/\omega_1 \in \{0.1,\, 0.5,\, 1\}$, with $\omega_1 = 2\pi\, 100$ Hz. For each line, $e_{\rm cut}$ was chosen so as to maximize ρ_0. The reference values are $T_1^{(\rm ref)} = 20\,\mu$K and $\gamma_{\rm t}^{(\rm ref)} = 10^7$ atoms/s.

lines $\rho_0 = 2.612$. The most important feature of this plot is that the three lines lie nearly on top of each other. This agrees with Figure 8.3 in that ρ_0 decreases vary little as ω_2 is lowered. The plot also shows that ρ_0 depends more critically on T_1 than on $\gamma_{\rm t}$. Starting from the reference point in the center, one has to either decrease T_1 by 20%, or increase $\gamma_{\rm t}$ by 100% in order to get to the $\rho_0 = 2.612$ line.

The sudden transfer is shown in Figure 8.6. In contrast to the adiabatic case, the three lines are separated, so that as ω_2 is decreased, one has to try much harder to reach $\rho_0 = 2.612$, which is also consistent with Figure 8.4.

The total number $N_{\rm ss}$ curves corresponding to the $\rho_0 = 2.612$ lines in Figure 8.5 and Figure 8.6 are shown in Figure 8.7. The results are the same in both the sudden and adiabatic cases (thus there are only three lines instead of six). For the adiabatic case, by loosening the magnetic trap, one does not have to vary T_1 and $\gamma_{\rm t}$ much at all in order to stay at $\rho_0 = 2.612$ while increasing the number $N_{\rm ss}$ by orders of magnitude. On the other hand, for the sudden transfer, one has to decrease T_1 and increase $\gamma_{\rm t}$ a lot in order to stay at $\rho_0 = 2.612$ as ω_2 is decreased. However, one will achieve the same increase in number as in the adiabatic case.

Finally, in Figure 8.8 we show a plot of the ratio $e_{\rm cut}/T_2$ corresponding to the $\rho_0 = 2.612$ lines shown in Figures 8.5-8.7. This ratio of the optimum cut to the temperature T_2 of atoms being injected into the trap is the same in both the adiabatic and sudden transfers. As ω_2 is decreased, one does not have to exclude as much of the distribution from the trap. Also, as $\gamma_{\rm t}$ is increased, one has to cut further into the injected distribution in order to prevent 3-body losses from dominating.

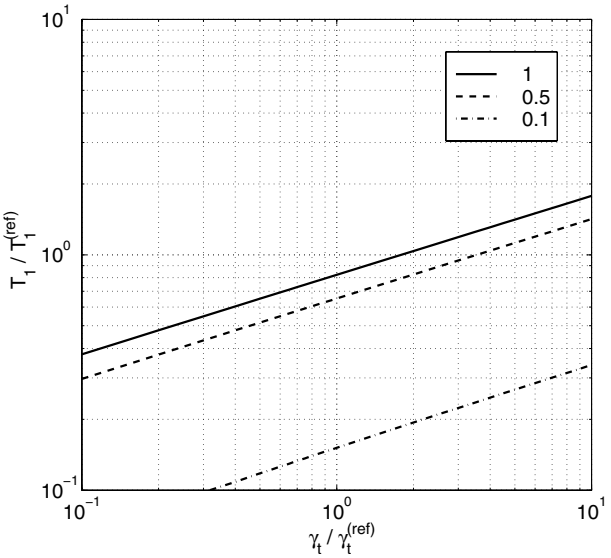

Figure 8.6: Same as described in the caption of Figure 8.5 but for the case of a sudden transfer.

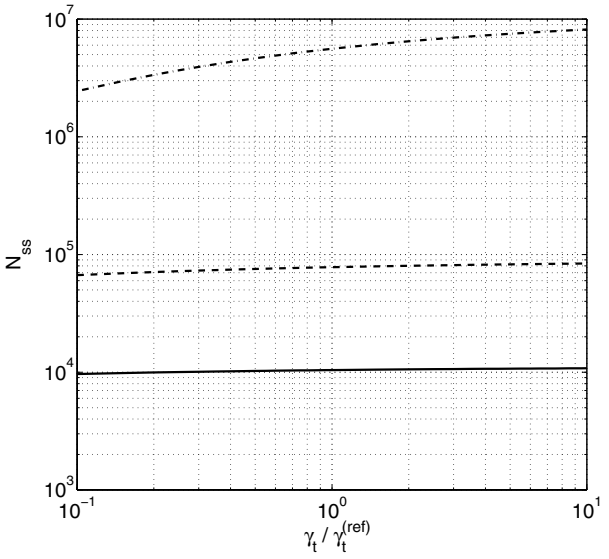

Figure 8.7: Corresponds to the three lines in both Figure 8.5 and Figure 8.6, showing the total number of atoms in steady state $N_{\rm ss}$ as a function of the transfer rate $\gamma_{\rm t}$. Along each of these curves, $\rho_0 = 2.612$. The legend in Figure 8.5 and Figure 8.6 applies to this plot also.

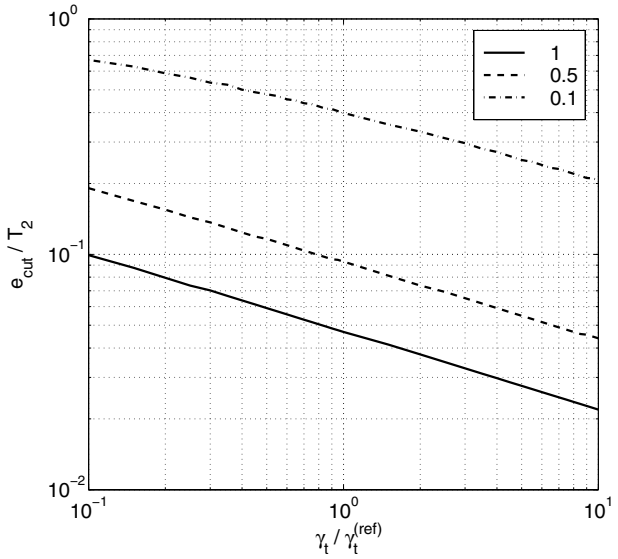

Figure 8.8: Curves correspond to those in Figures 8.5-8.7, showing the ratio of the RF cut to the temperature of atoms injected into the trap, $e_{\rm cut}/T_2$ as a function of the transfer rate $\gamma_{\rm t}$. Along each of these curves, $\rho_0 = 2.612$.

8.4 Summary

In this chapter we have addressed the problem of achieving a steady state condensation by continuously feeding atoms into the magnetic trap below a fixed RF threshold. We have included losses due to elastic collisions with atoms from the background gas, as well as inelastic 3-body collisions. Our model of the loading of atoms into the magnetic trap treats two idealizations of transferring atoms from a separate MOT; either an adiabatic or a sudden transfer. The description of the kinetic evolution to steady state assumes a truncated Boltzmann form for the non-equilibrium distribution $f(e,t)$, reducing the problem to that of solving coupled rate equations for the total number $N(t)$ and total energy $E(t)$ of the gas. Our calculations show that it is possible to achieve a steady state condensation using optimistic values of the relevant physical parameters.

We have shown several results of numerical solutions of the rate equations in Eq. (8.12) and Eq. (8.13). First, we addressed the build-up time for steady state to occur and determined that an upper limit on the build-up time is given by the background loss lifetime $\tau_{\rm bl}$. If 3-body losses are dominating due to a high density, then the build-up time will be much shorter than this. We next looked at how the steady state value of the peak phase space density ρ_0 depends on the magnetic trap frequency ω_2 and the RF cut $e_{\rm cut}$. We found that in the adiabatic case, one can gain a large increase in the total number in steady state $N_{\rm ss}$ by loosening the magnetic trap, while only losing a small amount in ρ_0. This is not true for a sudden transfer. Finally, we looked at how one must vary the transfer rate $\gamma_{\rm t}$ and the MOT temperature T_1 in order to reach $\rho_0 = 2.612$. We found that ρ_0 depends more critically on T_1 than $\gamma_{\rm t}$. Also, it was shown that one must try much harder to reach the critical point while achieving a large $N_{\rm ss}$ in the sudden case compared to the adiabatic case.

There are several shortcomings of our model which might be improved, however, we

believe that the present calculations are qualitatively correct and are sufficient for experimental guidance. An obvious extension to our model would be to include the effect of the growth of the condensate which will make the evaporation more efficient but at the same time increasing 3-body losses due to the increase in density in the center of the trap. [126, 121, 138, 21] Another improvement would be to construct a more accurate model of the transfer process by understanding the relationship between T_1, ω_1 and γ_t, since these can not be varied independently in an experiment. Alternatively, one could construct a model of the loading procedure based on an entirely different experimental method than that described in [134, 135, 7].

Appendix A

Wick's Theorem

The quantum kinetic equations in Chapter 2 for the mean field Eq. (2.70) and fluctuations Eq. (2.71) and Eq. (2.72) were derived from the Born-Markov form of the generalized kinetic equation Eq. (2.60) for a general relevant observable γ_q. We do not provide the details in getting from Eq. (2.60) to Eq. (2.70) through Eq. (2.72), however it is important to understand the main steps, which involve evaluating the averages of multiple operator products. Due to the Gaussian structure of our reference distribution $\sigma^{(0)}(t)$ in Eq. (2.9), we can utilize Wick's theorem to simplify the calculation [42].

We are interested in calculating the average of a product of s operators

$$\langle \hat{A}_1 \hat{A}_2 \cdots \hat{A}_s \rangle^t_{(0)} = \mathrm{Tr}\{\sigma^{(0)}(t)\, \hat{A}_1 \hat{A}_2 \cdots \hat{A}_s\}, \tag{A.1}$$

where we are denoting $\hat{A}_i$ to represent either a raising $\hat{a}^\dagger_i$ or a lowering operator $\hat{a}_i$. These averages arise in the kinetic equations. For example, in the kinetic equation for the normal fluctuations, the second order collisional terms involve a product of ten operators due to terms of the form $\sim \langle V^2 \tilde{f} \rangle^\dagger_{(0)}$, since the interaction V contains a product of four operators $V \sim \hat{a}^\dagger_i \hat{a}^\dagger_j \hat{a}_k \hat{a}_l$ and the normal fluctuations have the form $\tilde{f} \sim \hat{a}^\dagger_j \hat{a}_i$.

Wick's theorem is valid for averages taken over a Gaussian distribution that can involve both normal $\hat{a}^\dagger_j \hat{a}_i$ and anomalous pairs $\hat{a}_i \hat{a}_j$ in the exponent, as our reference distribution does in Eq. (2.9). We do not derive Wick's theorem here, but simply state the results. The interested reader can find derivations of Wick's theorem in Louisell [119] (p. 182) for the case of bosons, and in Zubarev [39] (p. 172) for fermions. Both of these derivations assume a Gaussian form with only normal pairs $\hat{a}^\dagger_j \hat{a}_i$ in the exponent; one can find a more general derivation including anomalous pairs (for a squeezed vacuum) in Vaglica [43]. To include the anomalous pairs in the proof, one can simply make a canonical transformation of the operators $\hat{a}_i$ and $\hat{a}^\dagger_i$ so that only normal pairs appear in the exponent for the new set of operators; doing this allows one to use the standard proof, which treats only normal pairs.

Wick's theorem states that the average value of a product of creation and annihilation operators is equal to the sum of all complete systems of pairings, which can be stated more formally as

$$\langle \hat{A}_1 \hat{A}_2 \cdots \hat{A}_s \rangle^t_{(0)} = \sum_{P_d} \langle \hat{A}_1 \hat{A}_2 \rangle^t_{(0)} \langle \hat{A}_3 \hat{A}_4 \rangle^t_{(0)} \cdots \langle \hat{A}_{s-1} \hat{A}_s \rangle^t_{(0)}, \tag{A.2}$$

where the sum runs over all P_d distinct permutations of the s indices. An alternative way

to write Eq. (A.2) is

$$\begin{aligned}\langle \hat{A}_1 \hat{A}_2 \cdots \hat{A}_s \rangle^t_{(0)} &= \langle \hat{A}_1 \hat{A}_2 \rangle^t_{(0)} \langle \hat{A}_3 \hat{A}_4 \cdots \hat{A}_s \rangle^t_{(0)} + \langle \hat{A}_1 \hat{A}_3 \rangle^t_{(0)} \langle \hat{A}_2 \hat{A}_4 \cdots \hat{A}_s \rangle^t_{(0)} \\ &+ \langle \hat{A}_1 \hat{A}_s \rangle^t_{(0)} \langle \hat{A}_2 \hat{A}_3 \cdots \hat{A}_{s-1} \rangle^t_{(0)}, \end{aligned} \tag{A.3}$$

and then applying this relation recursively to all of the multiple operator averages until only pairs of operators remain. If the number of operators s is odd, Wick's theorem reduces to the simple result

$$\langle \hat{A}_1 \hat{A}_2 \cdots \hat{A}_s \rangle^t_{(0)} = 0 \qquad \text{if } s \text{ is odd}. \tag{A.4}$$

Wick's theorem is augmented by the further rules for averages of pairs of operators, which hold for bosons

$$\begin{aligned}\langle \hat{a}_1 \hat{a}_2^\dagger \rangle^t_{(0)} &= \delta_{12} + \langle \hat{a}_1^\dagger \hat{a}_2 \rangle^t_{(0)}, \\ \langle \hat{a}_1 \hat{a}_2 \rangle^t_{(0)} &= \langle \hat{a}_2 \hat{a}_1 \rangle^t_{(0)}, \\ \langle \hat{a}_1^\dagger \hat{a}_2^\dagger \rangle^t_{(0)} &= \langle \hat{a}_2^\dagger \hat{a}_1^\dagger \rangle^t_{(0)}. \end{aligned} \tag{A.5}$$

As an example, we consider the product of four operators $\langle \hat{A}_1 \hat{A}_2 \hat{A}_3 \hat{A}_4 \rangle^t_{(0)}$, which can be reduced according to Wick's theorem to

$$\langle \hat{A}_1 \hat{A}_2 \hat{A}_3 \hat{A}_4 \rangle^t_{(0)} = \langle \hat{A}_1 \hat{A}_2 \rangle^t_{(0)} \langle \hat{A}_3 \hat{A}_4 \rangle^t_{(0)} + \langle \hat{A}_1 \hat{A}_3 \rangle^t_{(0)} \langle \hat{A}_2 \hat{A}_4 \rangle^t_{(0)} + \langle \hat{A}_1 \hat{A}_4 \rangle^t_{(0)} \langle \hat{A}_2 \hat{A}_3 \rangle^t_{(0)} \tag{A.6}$$

The application of Wick's theorem to the kinetic equation Eq. (2.60) for our set of relevant operators is complicated by the fact that the operators $\hat{a}_i$ are shifted by the c-number mean-field ψ_i. The evaluation of the average of a product of ten shifted operators involves 2^{10} terms, each of which must be reduced according to Wick's theorem. Even a demonstration on the example in Eq. (A.6) for the case four operators would involve on the order of $\sim 3 \cdot 2^4 = 48$ terms. A symbolic algebra package using Mathematica was developed by Reinhold Walser in our group to carry out all of these steps.

Appendix B

Collisional Terms

In Chapter 2 we derived the quantum kinetic equations for the mean field and fluctuations, which lead to Eq. (2.70) through Eq. (2.72), however we did not display the explicit forms of the second order collisional terms since they are rather involved, and furthermore are never used in the calculations of this thesis. However, it is the full inclusion of collisional effects embodied in these terms that gives our theory its real power. Future studies of the coupled, two-component system, which we treated at zero temperature in this thesis, will involve extending the calculations to finite temperature, an endeavor that will benefit greatly from having derived the full quantum kinetic equations.

On page 146 we write the second-order collision terms: $L_{\psi}^{(2)}[\psi, \tilde{f}, \widetilde{m}]$ for the mean field, $L_{\tilde{f}}^{(2)}[\psi, \tilde{f}, \widetilde{m}]$ for the normal fluctuations, and $L_{\widetilde{m}}^{(2)}[\psi, \tilde{f}, \widetilde{m}]$ for the anomalous fluctuations.

$$
\begin{aligned}
L^{(2)}_{\psi}[\psi,\tilde{f},\widetilde{m}] &= \left(\Gamma_{\tilde{f}\tilde{f}(1+\tilde{f})} - \Gamma_{(1+\tilde{f})(1+\tilde{f})\tilde{f}} + 2\,\Gamma_{\widetilde{f}\widetilde{m}n} - 2\,\Gamma_{(1+\tilde{f})\widetilde{m}\widetilde{n}}\right)|\psi\rangle + \\
&+ 2\left(\Gamma_{\widetilde{f}\widetilde{m}(1+\tilde{f})} - \Gamma_{(1+\tilde{f})\widetilde{m}\tilde{f}}\right)\angle\langle\psi| \qquad \text{(B.1)}
\end{aligned}
$$

$$
\begin{aligned}
L^{(2)}_{\tilde{f}}[\psi,\tilde{f},\widetilde{m}] &= \left(\Gamma_{\tilde{f}\tilde{f}(1+\tilde{f})} + 2\,\Gamma_{f^{(c)}\tilde{f}(1+\tilde{f})} + \Gamma_{\tilde{f}\tilde{f}f^{(c)}} + 2\,\Gamma_{\tilde{f}(m^{(c)}+\widetilde{m})n}\widetilde{\sim} + 2\,\Gamma_{\widetilde{f}\widetilde{m}n^{(c)}} + 2\,\Gamma_{f^{(c)}\widetilde{m}n}\widetilde{\sim}\right)(1+\tilde{f}) \qquad \text{(B.2)} \\
&- \left(\Gamma_{(1+\tilde{f})(1+\tilde{f})\tilde{f}} + 2\,\Gamma_{f^{(c)}(1+\tilde{f})\tilde{f}} + \Gamma_{(1+\tilde{f})(1+\tilde{f})f^{(c)}} + 2\,\Gamma_{(1+\tilde{f})(m^{(c)}+\widetilde{m})n}\widetilde{\sim} + 2\,\Gamma_{(1+\tilde{f})\widetilde{m}n^{(c)}} + 2\,\Gamma_{f^{(c)}\widetilde{m}n}\widetilde{\sim}\right)\tilde{f} \\
&+ 2\Big(\Gamma_{\tilde{f}(m^{(c)}+\widetilde{m})(1+\tilde{f})} + \Gamma_{f^{(c)}\widetilde{m}(1+\tilde{f})} + \Gamma_{\tilde{f}\widetilde{m}f^{(c)}} - \Gamma_{(1+\tilde{f})(m^{(c)}+\widetilde{m})\tilde{f}} - \Gamma_{f^{(c)}\widetilde{m}\tilde{f}} - \Gamma_{(1+\tilde{f})\widetilde{m}f^{(c)}}\Big)\angle\widetilde{n} + \text{h.c.}
\end{aligned}
$$

$$
\begin{aligned}
L^{(2)}_{\widetilde{m}}[\psi,\tilde{f},\widetilde{m}] &= \left(\Gamma_{\tilde{f}\tilde{f}(1+\tilde{f})} + \Gamma_{\tilde{f}\tilde{f}f^{(c)}} + 2\,\Gamma_{\tilde{f}f^{(c)}(1+\tilde{f})} + 2\,\Gamma_{\tilde{f}\widetilde{m}(n^{(c)}+\widetilde{n})} + 2\,\Gamma_{\tilde{f}\widetilde{m}n^{(c)}}\widetilde{\sim}\right)\angle\widetilde{m} \qquad \text{(B.3)} \\
&- \left(\Gamma_{(1+\tilde{f})(1+\tilde{f})\tilde{f}} + \Gamma_{(1+\tilde{f})(1+\tilde{f})f^{(c)}} + 2\,\Gamma_{(1+\tilde{f})f^{(c)}\tilde{f}} + 2\,\Gamma_{(1+\tilde{f})\widetilde{m}(n^{(c)}+\widetilde{n})} + 2\,\Gamma_{(1+\tilde{f})\widetilde{m}n^{(c)}}\widetilde{\sim}\right)\angle\widetilde{m} + \\
&+ \left(2\,\Gamma_{\tilde{f}(m^{(c)}+\widetilde{m})(1+\tilde{f})} + 2\,\Gamma_{\tilde{f}\widetilde{m}f^{(c)}} + 2\,\Gamma_{f^{(c)}\widetilde{m}(1+\tilde{f})} + \Gamma_{\widetilde{m}\widetilde{m}(n^{(c)}+\widetilde{n})}\widetilde{\sim} + 2\,\Gamma_{\widetilde{m}\widetilde{m}n^{(c)}}\widetilde{\sim}\right)\angle\tilde{f} + \\
&- \left(2\,\Gamma_{(1+\tilde{f})(m^{(c)}+\widetilde{m})\tilde{f}} + 2\,\Gamma_{(1+\tilde{f})\widetilde{m}f^{(c)}} + 2\,\Gamma_{f^{(c)}\widetilde{m}\tilde{f}} + \Gamma_{\widetilde{m}\widetilde{m}(n^{(c)}+\widetilde{n})}\widetilde{\sim} + 2\,\Gamma_{\widetilde{m}\widetilde{m}n^{(c)}}\widetilde{\sim}\right)\angle(1+\tilde{f}) + \text{transp.}
\end{aligned}
$$

In these expressions we have defined the following collision operators and pseudo operators

$$\begin{aligned}
\Gamma_{fff} &= 2\,C(1,2';3',4')\,C_\varepsilon(1'',2'';3'',4'')\,f_{3'1''}f_{4'2''}f_{4''2'}\;|1\rangle\langle 3''|\,, && \text{(B.4)}\\
\Gamma_{fmf} &= 2\,C(1,2';3',4')\,C_\varepsilon(1'',2'';3'',4'')\,f_{3'1''}m_{4'3''}f_{4''2'}\;|1\rangle|2''\rangle\,, && \text{(B.5)}\\
\Gamma_{fmn} &= 2\,C(1,2';3',4')\,C_\varepsilon(1'',2'';3'',4'')\,f_{3'1''}m_{4'3''}n_{2''2'}\;|1\rangle\langle 4''|\,, && \text{(B.6)}\\
\Gamma_{mmn} &= 2\,C(1,2';3',4')C_\varepsilon(1'',2'';3'',4'')\,m_{3'4''}m_{4'3''}n_{2''2'}\;|1\rangle|1''\rangle\,. && \text{(B.7)}
\end{aligned}$$

The transition amplitudes $C(1,2;3,4)$ are given by

$$C(1,2;3,4) = V_0\int d^3r\phi_1^*(\boldsymbol{r})\phi_2^*(\boldsymbol{r})\phi_3(\boldsymbol{r})\phi_4(\boldsymbol{r}). \tag{B.8}$$

The amplitude $C_\varepsilon(1,2;3,4)$ arose from evaluating the time-integral over the free propagator. The details of obtaining this term can be found in [27]; here we give the result

$$C_\varepsilon(1,2;3,4) = C(1,2;3,4)\left(\pi\delta_\varepsilon(\Delta_{1234}) + i\mathcal{P}_\varepsilon\frac{1}{\Delta_{1234}}\right). \tag{B.9}$$

This is non-zero only if the energy difference $\Delta_{1234} = \epsilon_1(t) + \epsilon_2(t) - \epsilon_3(t) - \epsilon_4(t)$ is smaller than ε, where we define

$$\frac{1}{\varepsilon - i\Delta} \quad = \quad \pi\,\delta_\varepsilon(\Delta) + i\,\mathcal{P}_\varepsilon\frac{1}{\Delta}. \tag{B.10}$$

Here we have expanded in terms of the mean-field states $|1\rangle$ and their energies, defined by

$$\left(H_0 + Q_\gamma\right)|1\rangle = \epsilon_1(t)\,|1\rangle\,. \tag{B.11}$$

Appendix C

Numerical solution of the GP equation

In this appendix we give the details of the numerical procedure used to solve the Gross-Pitaevskii equation. In the first part, we consider evolving the wavefunction in time, starting with some initial condition $\psi(0)$, which we do by using the Crank-Nicholson procedure. We describe this procedure for the case of one spatial dimension, $\psi(z,t)$, and then briefly discuss the extension of the Crank-Nicholson method to two spatial dimensions, $\psi(x,y,t)$ or $\psi(\rho,z,t)$, which is called the alternating-direction implicit (ADI) method. We also describe the numerical procedure for treating the coupled, two-component system using the split-operator approximation.

In the second part, we describe the technique of propagating the wavefunciton in imaginary time in order to find the ground state of the system, and we discuss the extension of this to also obtain excited eigenstates. One can also use imaginary-time propagation (ITP) to obtain topological solutions of the GP equation, which we discuss. Finally, we briefly describe the application of this method to find the dressed states for a coupled, two-component system.

C.1 Time evolution using the Crank-Nicholson method

C.1.1 One spatial dimension

We are interested in propagating the wavefunction $\psi(z,t)$ forward in time, starting with some initial state $\psi(z,0)$. The GP equation in dimensionless units (i.e. taking $\hbar = \omega_z = m = 1$) is written

$$i\frac{\partial\psi(z,t)}{\partial t} = [-\frac{1}{2}\frac{\partial^2}{\partial z^2} + \frac{1}{2}z^2 + \lambda_{1\mathrm{d}}\left|\psi(z,t)\right|^2]\,\psi(z,t), \tag{C.1}$$

where $\lambda_{1\mathrm{d}}$ is proportional to the s-wave scattering length and is given explicitly below Eq. (3.15) in Chapter 3. We represent this equation numerically as a difference equation, with position z broken up into a grid of points z_j space by a distance h, and time t as discrete steps of length τ. The wavefunction is defined on this grid as as vector of length

M

$$\begin{aligned} \psi_j^n &\equiv \psi(z_j, t_n), \\ z_j &= (j-1)h, \\ t_n &= (n-1)\tau, \end{aligned} \tag{C.2}$$

where $j = 1, 2, \cdots, M$ is an integer, and n is an integer. The GP equation can be written in this discrete representation as

$$i\frac{\psi_j^{n+1} - \psi_j^n}{\tau} = -\frac{1}{2}\frac{\psi_{j+1}^n - 2\psi_j^n + \psi_{j-1}^n}{h^2} + \Big[\frac{1}{2}(j-1)^2h^2 + \lambda_{1\mathrm{d}}|\psi_j^n|^2\Big]\psi_j^n, \tag{C.3}$$

where we have represented the time derivative as a forward difference, and the Laplacian as a central difference [139]. It is convenient to write this as the matrix equation

$$\boldsymbol{\psi}^{n+1} = \Big(\boldsymbol{I} - i\tau\boldsymbol{H}^n\Big)\boldsymbol{\psi}^n, \tag{C.4}$$

where $\boldsymbol{I}$ is the identity matrix and the matrix elements of $\boldsymbol{H}^n$ are

$$H_{ij}^n = -\frac{1}{2h^2}\big(\delta_{i,j+1} - 2\delta_{i,j} + \delta_{i,j-1}\big) + \Big[\frac{1}{2}(i-1)^2h^2 + \lambda_{1\mathrm{d}}|\psi_i^n|^2\Big]\delta_{ij}. \tag{C.5}$$

The result Eq. (C.4) is called the *explicit* form of the discrete representation of Eq. (C.1). It is numerically unstable if the time step τ is too large [139, 140]. We can obtain an alternative form if we notice that Eq. (C.4) is the expansion of the unitary matrix $\boldsymbol{U} = \exp[-i\tau\boldsymbol{H}^n]$, keeping only the first two terms. That is, the exact solution $\boldsymbol{\psi}^{n+1}$ is given by

$$\boldsymbol{\psi}^{n+1} = e^{-i\tau H^n}\boldsymbol{\psi}^n. \tag{C.6}$$

If τ is small enough, then Eq. (C.4) is a reasonably good approximation to Eq. (C.6). However, a better solution can be obtained by writing Eq. (C.6) as

$$e^{+i\tau H^n}\boldsymbol{\psi}^{n+1} = \boldsymbol{\psi}^n. \tag{C.7}$$

Here, we are propagating the, as yet unknown, solution $\boldsymbol{\psi}^{n+1}$ backward in time to $\boldsymbol{\psi}^n$. Expanding $\boldsymbol{U}^\dagger$ to first order in τ, this can be rewritten as [139, 140]

$$\boldsymbol{\psi}^{n+1} = \Big(\boldsymbol{I} + i\tau\boldsymbol{H}^n\Big)^{-1}\boldsymbol{\psi}^n. \tag{C.8}$$

This is known as the *implicit* discrete representation of Eq. (C.1). Although it seems like a subtle change from Eq. (C.4), it is actually unconditionally stable, whereas Eq. (C.4) is unstable.

There is a problem with both the explicit and implicit methods, in that they do not preserve the norm of ψ. That is, the approximate forms of the unitary operator used in Eq. (C.4) and Eq. (C.8) are not unitary. This can be remedied if we use the Cayley form of $\boldsymbol{U}$, which is essentially an average between the explicit and implicit forms, so as to construct an approximation that is unitary [140, 141, 139]

$$\boldsymbol{\psi}^{n+1} = \Big(\boldsymbol{I} + i\frac{\tau}{2}\boldsymbol{H}^n\Big)^{-1}\Big(\boldsymbol{I} - i\frac{\tau}{2}\boldsymbol{H}^n\Big)\boldsymbol{\psi}^n. \tag{C.9}$$

This result is known as the Crank-Nicholson form of the discrete representation of Eq. (C.1). It is stable, unitary, and accurate to second order in space and time [141].

We have not discussed the fact that $\boldsymbol{H}^n$ is a nonlinear Hamiltonian that depends on the state ψ through the mean-field interaction (this is the source of the superscript n, which indicates that $\boldsymbol{H}^n$ depends on time). Strictly speaking, one would have to use the generalization of $U = T\exp[-i\int_0^\tau H(t)dt]$ to account for the time dependence in $\boldsymbol{H}^n$, which involves a time-ordered integration from $t = 0$ to $t = \tau$. However, if ψ is slowly varying, then we can take it as constant over the short time interval τ and approximate $\boldsymbol{U}$ as given inEq. (C.9).

In order to implement the Crank-Nicholson scheme, it is useful to rewrite Eq. (C.9) as

$$\boldsymbol{\psi}^{n+1} = \chi - \boldsymbol{\psi}^n. \tag{C.10}$$

The vector χ is found by solving the matrix equation

$$\boldsymbol{Q}\chi = \boldsymbol{\psi}^n, \tag{C.11}$$

with $\boldsymbol{Q} = [\boldsymbol{I} + (i\tau\boldsymbol{H}^n/2)]/2$. Writing Eq. (C.9) in this way let us avoid taking the matrix inverse. The matrix $\boldsymbol{Q}$ is a tridiagonal matrix, so that equation Eq. (C.11) can be solved using a simple Gaussian elimination algorithm tailored for a tridiagonal system [139].

C.1.2 Two spatial dimensions—the ADI method

We now consider the case of having two spatial dimensions in Cartesian coordinates, with the GP equation given by

$$i\frac{\partial\psi(x,y,t)}{\partial t} = [-\frac{1}{2}(\frac{\partial^2}{\partial x^2} + \frac{\partial^2}{\partial y^2}) + \frac{1}{2}(x^2+y^2) + \lambda_{2\mathrm{d}}|\psi(x,y,t)|^2]\,\psi(x,y,t), \tag{C.12}$$

where $\lambda_{2\mathrm{d}}$ is given below Eq. (3.17) in Chapter 3. The discrete form of $\psi(x,y,t)$ is now an M_x by M_y matrix instead of a vector, given as

$$\begin{aligned} \psi^n_{i,j} &\equiv \psi(x_i, y_j, t_n), \\ x_i &= (i-1)h, \\ y_j &= (j-1)h, \\ t_n &= (n-1)\tau, \end{aligned} \tag{C.13}$$

where $i = 1, 2, \cdots, M_x$, $j = 1, 2, \cdots, M_y$, and n are integers. We have taken the grid spacing h to be the same along each axis. The discrete form of the GP equation now takes the form

$$\begin{aligned} i\frac{\psi^{n+1}_{i,j} - \psi^n_{i,j}}{\tau} &= -\frac{1}{2}\frac{\psi^n_{(i+1),j} - 2\psi^n_{i,j} + \psi^n_{(i-1),j}}{h^2} - \frac{1}{2}\frac{\psi^n_{i,(j+1)} - 2\psi^n_{i,j} + \psi^n_{i,(j-1)}}{h^2} \\ &+ \left(\frac{1}{2}\Big[(i-1)^2h^2 + (j-1)^2h^2\Big] + \lambda_{2\mathrm{d}}|\psi^n_{i,j}|^2\right)\psi^n_{i,j}. \end{aligned} \tag{C.14}$$

As written, the Laplacian is a fourth rank tensor operating on the second rank tensor representation of ψ. This is difficult to represent numerically, so we instead introduce a vector representation of $\psi^n_{i,j}$ as [142]

$$v^n_r = \psi^n_{i,j}, \qquad \text{with } r = (i-1)M_y + j. \tag{C.15}$$

Conversely, $i = \mathrm{int}[(r-1)/M_y] + 1$ and $j = [(r-1)\mathrm{mod}(M_y)] + 1$. We have simply linked together the rows of $\psi^n_{i,j}$ to form a vector of length $M_x \times M_y$. In this representation, the GP equation takes the form [142]

$$i\frac{v_r^{n+1} - v_r^n}{\tau} = -\frac{1}{2}\frac{v^n_{r-M_y} + v^n_{r-1} - 4v^n_r + v^n_{r+1} + v^n_{r+M_y}}{h^2} + V_r{}^n v^n_r, \tag{C.16}$$

where V_r^n corresponds to the harmonic and mean-field potentials. The Laplacian in this representation is a pentadiagonal $M_x \times M_y$ by $M_x \times M_y$ matrix.

At this stage we could simply carry out the Crank-Nicholson procedure to propagate the vector v from our initial condition. However, we would have to solve a pentadiagonal matrix equation instead of a tridiagonal one. There is a more efficient method that breaks the Laplacian up into two tridiagonal matrices, and then makes use of the split operator approximation. To do this, we first define an alternative vector representation of the matrix $\psi^n_{i,j}$ by stacking the columns up, instead of linking the rows, to obtain w^n_r defined as [142]

$$w^n_r = \psi^n_{i,j}, \qquad \text{with } r = (j-1)M_x + i. \tag{C.17}$$

Conversely, $i = \mathrm{int}[(r-1)/M_x] + 1$ and $j = [(r-1)\mathrm{mod}(M_x)] + 1$. The vector w^n_r contains the same information as v^n_r, both of which contain the same information as $\psi^n_{i,j}$. With this definition of w^n_r, Eq. (C.16) can be written in the simpler form [142]

$$i\frac{v_r^{n+1} - v_r^n}{\tau} = -\frac{1}{2}\frac{v^n_{r+1} - 2v^n_r + v^n_{r-1}}{h^2} - \frac{1}{2}\frac{w^n_{r+1} - 2w^n_r + w^n_{r-1}}{h^2} + V_r{}^n v^n_r. \tag{C.18}$$

It is convenient to write this in the matrix form

$$\boldsymbol{v}^{n+1} = \Big[\boldsymbol{I} - i\tau\big(\boldsymbol{D}^{(2)} + \boldsymbol{D}^{(2)}\boldsymbol{M}_{\mathrm{re}} + \boldsymbol{V}\big)\Big]\boldsymbol{v}^n, \tag{C.19}$$

where $\boldsymbol{V}$ corresponds to the harmonic and mean-field potentials and we have defined the matrix $\boldsymbol{D}^{(2)}$ as

$$D^{(2)}_{rs} = -\frac{1}{2h^2}\big(\delta_{r,s+1} - 2\delta_{r,s} + \delta_{r,s-1}\big). \tag{C.20}$$

The matrix $\boldsymbol{M}_{\mathrm{re}}$ defines the reordering transformation that takes us from the vector $\boldsymbol{v}$ to the vector $\boldsymbol{w}$, $\boldsymbol{w} = \boldsymbol{M}\cdot\boldsymbol{v}$.

In order to make use of the split operator approximation, we rewrite Eq. (C.19) as

$$\boldsymbol{v}^{n+1} = e^{-i\tau\left(\mathbf{D_x}^{(2)} + \mathbf{D_y}^{(2)} + \mathbf{V}\right)}\boldsymbol{v}^n, \tag{C.21}$$

where we have made the simple definitions $\boldsymbol{D}^{(2)}_{\mathbf{x}} = \boldsymbol{D}^{(2)}$ and $\boldsymbol{D}^{(2)}_{\mathbf{y}} = \boldsymbol{D}^{(2)}\boldsymbol{M}_{\mathrm{re}}$. For a given pair of operators F_1 and F_2, the exponential can be written as [143]

$$e^{\tau(F_1+F_2)} = e^{\tau F_1/2}e^{\tau F_2}e^{\tau F_1/2} + \mathcal{O}(\tau^3). \tag{C.22}$$

This is known as the split-operator approximation and is accurate to second order in τ, which is consistent with the Crank-Nicholson procedure. This can be extended to the case of three or more operators in the sum [144], so that applied to Eq. (C.21) we obtain

$$\boldsymbol{v}^{n+1} = e^{-i\tau\mathbf{D_x}^{(2)}/2}e^{-i\tau\mathbf{D_y}^{(2)}/2}e^{-i\tau\mathbf{V}}e^{-i\tau\mathbf{D_y}^{(2)}/2}e^{-i\tau\mathbf{D_x}^{(2)}/2}\boldsymbol{v}^n. \tag{C.23}$$

This amounts to propagating the solution in increments of $\tau/2$, alternating between the x and y axes. Each segment can be propagated according to the Crank-Nicholson procedure

by using the Cayley approximation for the exponential operator, allowing us to simply carry over the results of the previous section, where we discussed the one-dimensional case.

In the case of a cylindrical geometry, $\psi(\rho, z, t)$, we must be careful with the singularity at the origin, where the radial terms in the kinetic energy diverge. In Ref. [145], Holland et al. describe a discrete representation of the radial part of the Laplacian that carefully avoids these difficulties through an adaptive differencing scheme: at $\rho = 0$, forward differencing is used, and as ρ is increased, a combination of forward and central differencing is used such that for large ρ a pure central difference is used. This does not change the ADI procedure described above, for we are simply redefining the discrete representation of the Laplacian to avoid numerical instability near the origin $\rho = 0$.

C.1.3 Treating the internal-state dynamics

In Chapters 4 to 6 we treat a two-component condensate. The basic Crank-Nicholson and ADI procedures described above can easily be extended to treat the case of having two internal states. For concreteness, let us consider the system defined in one spatial dimension z. We define a vector representation of the wavefunction as $\psi^n_{j,\alpha}$, where, as before, n denotes the time index and j denotes the spatial index. The index $\alpha = 1, 2$ denotes the internal state. The explicit vector form $\vec{\boldsymbol{\psi}}^n$ is written

$$\vec{\boldsymbol{\psi}}^n = \begin{pmatrix} \psi^n_{1,1} \\ \psi^n_{2,1} \\ \cdot \\ \cdot \\ \cdot \\ \psi^n_{M,1} \\ \psi^n_{1,2} \\ \psi^n_{2,2} \\ \cdot \\ \cdot \\ \cdot \\ \psi^n_{M,2} \end{pmatrix}, \tag{C.24}$$

which can be written in the more compact form

$$\vec{\boldsymbol{\psi}}^n = \begin{pmatrix} \boldsymbol{\psi}^n_1 \\ \boldsymbol{\psi}^n_2 \end{pmatrix}. \tag{C.25}$$

The explicit discrete representation of the two-component GP equation Eq. (4.11) from Chapter 4 is

$$\begin{pmatrix} \boldsymbol{\psi}^{n+1}_1 \\ \boldsymbol{\psi}^{n+1}_2 \end{pmatrix} = \left[\begin{pmatrix} \boldsymbol{I} & \boldsymbol{0} \\ \boldsymbol{0} & \boldsymbol{I} \end{pmatrix} - i\tau \begin{pmatrix} \boldsymbol{H}^n_1 & \boldsymbol{\Omega}/2 \\ \boldsymbol{\Omega}/2 & \boldsymbol{H}^n_2 \end{pmatrix} \right] \begin{pmatrix} \boldsymbol{\psi}^n_1 \\ \boldsymbol{\psi}^n_2 \end{pmatrix}. \tag{C.26}$$

The quantities $\boldsymbol{I}$, $\boldsymbol{H}^n_\alpha$, and $\boldsymbol{\Omega}$ are M by M matrices. Here, $\boldsymbol{H}^n_\alpha$ is the discrete representation of the spatial part of the Hamiltonian for state i

$$H_\alpha = -\frac{1}{2}\frac{\partial^2}{\partial z^2} + \frac{1}{2}(z + \gamma_\alpha)^2 + \left[\lambda_\alpha |\psi_\alpha(z,t)|^2 + \lambda_{\alpha\beta} |\psi_\beta(z,t)|^2\right] - \gamma_\alpha \frac{\delta}{2}, \tag{C.27}$$

where $\gamma_1 = -1$ and $\gamma_2 = 1$. The matrix $\mathbf{\Omega}$ is diagonal, given by $\mathbf{\Omega} = \Omega\, \boldsymbol{I}$.

If we define the $2M$ by $2M$ matrices $\boldsymbol{\sigma_1}$, $\boldsymbol{\sigma_2}$, and $\boldsymbol{\sigma_x}$ as

$$\boldsymbol{\sigma_1} = \begin{pmatrix} \boldsymbol{I} & \mathbf{0} \\ \mathbf{0} & \mathbf{0} \end{pmatrix}, \tag{C.28}$$

$$\boldsymbol{\sigma_2} = \begin{pmatrix} \mathbf{0} & \mathbf{0} \\ \mathbf{0} & \boldsymbol{I} \end{pmatrix}, \tag{C.29}$$

$$\boldsymbol{\sigma_x} = \begin{pmatrix} \mathbf{0} & \boldsymbol{I} \\ \boldsymbol{I} & \mathbf{0} \end{pmatrix}, \tag{C.30}$$

we can write Eq. (C.26) in the more compact form

$$\vec{\boldsymbol{\psi}}^{n+1} = e^{-i\tau\left(\boldsymbol{H}_1\boldsymbol{\sigma_1} + \boldsymbol{H}_2\boldsymbol{\sigma_2} + \mathbf{\Omega}\,\boldsymbol{\sigma_x}/2\right)}\vec{\boldsymbol{\psi}}^{n}. \tag{C.31}$$

We now invoke the split operator approximate form of Eq. (C.31) using Eq. (C.22), so that we can write

$$\vec{\boldsymbol{\psi}}^{n+1} = e^{-i\tau\mathbf{\Omega}\,\boldsymbol{\sigma_x}/4} e^{-i\tau\left(\boldsymbol{H}_1\boldsymbol{\sigma_1} + \boldsymbol{H}_2\boldsymbol{\sigma_2}\right)} e^{-i\tau\mathbf{\Omega}\,\boldsymbol{\sigma_x}/4}\vec{\boldsymbol{\psi}}^{n}. \tag{C.32}$$

This allows us to solve the internal and spatial parts of the evolution separately. The spatial part of the evolution can be solved for each component in separate sequential steps using the Crank-Nicholson or ADI method described above. The internal evolution can be solved exactly, since the unitary operator can be written explicitly

$$e^{-i\tau\mathbf{\Omega}\,\boldsymbol{\sigma_x}/4} = \begin{pmatrix} \cos(\Omega\tau/4)\,\boldsymbol{I} & -i\sin(\Omega\tau/4)\,\boldsymbol{I} \\ -i\sin(\Omega\tau/4)\,\boldsymbol{I} & \cos(\Omega\tau/4)\,\boldsymbol{I} \end{pmatrix}. \tag{C.33}$$

C.1.4 Diagnostics of numerical stability

In order to check for numerical stability, there are a few diagnostic tools at our disposal. The norm of the wavefunction should always be preserved, so that $N = (\psi, \psi)$ is a constant in time. In the case of a single component in one dimension, for example, the discretized form of the inner product is just

$$N = (\boldsymbol{\psi}^n, \boldsymbol{\psi}^n) = h\sum_j \psi_j^{n\,*}\psi_j^n, \tag{C.34}$$

which should be constant as the time step n increases. For a two component system this is

$$N = (\vec{\boldsymbol{\psi}}^n, \vec{\boldsymbol{\psi}}^n) = h\sum_j \left[\psi_{j,1}^{n\,*}\psi_{j,1}^n + \psi_{j,2}^{n\,*}\psi_{j,2}^n\right]. \tag{C.35}$$

If the two components are coupled, population can cycle between the two states, but the total N is a constant in time. We monitor N in our calculations.

If the Hamiltonian does not have any explicit time dependence, then we can check the total energy of the system, which should be a constant in time. In the case of a single component in one dimension, for example, the matrix elements of the energy operator $\boldsymbol{E}$ are given as

$$E_{ij} = -\frac{1}{2h^2}\left(\delta_{i,j+1} - 2\delta_{i,j} + \delta_{i,j-1}\right) + \left[\frac{1}{2}(i-1)^2h^2 + \frac{\lambda_{1\mathrm{d}}}{2}|\psi_i^n|^2\right]\delta_{ij}. \tag{C.36}$$

The total energy is then given by $E = (\boldsymbol{\psi}^n, \boldsymbol{E}\,\boldsymbol{\psi}^n)$. Note that the energy differs from the Hamiltonian by the factor of $1/2$ in the mean-field potential energy term [53]. The total energy E is a constant in time and serves as a very useful diagnostic for testing for numerical instability. This can be extended also to the two-component system.

One final technique for testing for instability is to simply halve the time step τ and/or the spatial grid size h to see if the solution changes. The criterion $\tau < 2h^2$ should always be met [141], so that as the spatial grid resolution increases, the time resolution must also increase. We find the Crank-Nicholson and ADI methods to be stable, so long as this criterion is met. However, in some cases, when very fine spatial structure begins to develop, the Crank-Nicholson method becomes very ineffective, for in order to resolve such fine-scale features, one must crank up the number of grid points and the number of time steps, making the algorithm very slow in these extreme cases.

C.2 Stationary state solutions using the ITP method

C.2.1 Ground state solution

In order to find the self-consistent ground state solution of the GP equation, we propagate the wavefunction in imaginary time, starting from some initial state that is a first guess of the solution. To see how this works, we set $\tilde{\tau} = -i\tau$ in the unitary evolution operator so that the solution in imaginary time is given by

$$\psi(\boldsymbol{r}, \tilde{\tau}) = e^{-\tilde{\tau}H}\psi(\boldsymbol{r}, 0). \tag{C.37}$$

If we expand $\psi(\boldsymbol{r}, 0)$ in the eigenbasis of H as

$$\psi(\boldsymbol{r}, 0) = \sum_{i=0}^{\infty} c_i \phi_i(\boldsymbol{r}), \tag{C.38}$$

then the solution in Eq. (C.37) becomes [146]

$$\psi(\boldsymbol{r}, \tilde{\tau}) = \sum_{i=0}^{\infty} c_i e^{-\tilde{\tau}\epsilon_i}\phi_i(\boldsymbol{r}). \tag{C.39}$$

The coefficients $c_i = \big(\phi_i, \psi(0)\big)$ and ϵ_i are the eigenenergies of H, i.e. $H\phi_i = \epsilon_i\phi_i$. In imaginary time, the norm of the solution decays away exponentially. The crucial point, however, is that the lowest energy state of the decomposition Eq. (C.39) has the smallest decay constant, so that it decays away the slowest. Our initial guess $\psi(\boldsymbol{r}, 0)$ for the ground state $\phi_0(\boldsymbol{r})$ will contain some finite contribution from excited states in the decomposition. This "contamination" in our initial guess will decay away faster than the ground state part of the decomposition. After a sufficiently long time interval T_0, the solution is then

$$\psi(\boldsymbol{r}, T_0) \approx c_0 e^{-T_0\epsilon_0}\phi_0(\boldsymbol{r}). \tag{C.40}$$

The ITP method is also referred to as the method of steepest descents.

In general, when one carries out this procedure, it is a good idea to re-normalize the wavefunction $\psi(\boldsymbol{r}, \tilde{\tau})$ periodically in time to avoid trouble with round-off errors due to the decaying norm of the solution. In the case of solving the nonlinear GP equation, one *must* re-normalize the solution incrementally, since the Hamiltonian depends on the density $|\psi(\boldsymbol{r}, t)|^2$ of the solution. The basic steps for carrying out the ITP procedure are as follows

1. Choose an initial guess $\psi(\boldsymbol{r}, 0)$. If the system is in the Thomas-Fermi regime, an effective guess is to take the Thomas-Fermi approximate solution, given by Eq. (3.5) in Chapter 3.

2. Propagate the solution for a short time interval $\tilde{\tau}$ in imaginary time. The Crank-Nicholson or ADI method described above can be used.

3. Re-normalize the solution to the value of the norm it had before the time evolution

$$\psi'(\boldsymbol{r}, \tilde{\tau}) = \sqrt{\frac{\big(\psi(\boldsymbol{r}, 0), \psi(\boldsymbol{r}, 0)\big)}{\big(\psi(\boldsymbol{r}, \tilde{\tau}), \psi(\boldsymbol{r}, \tilde{\tau})\big)}}\psi(\boldsymbol{r}, \tilde{\tau}). \tag{C.41}$$

4. Calculate the chemical potential as

$$\mu(\tilde{\tau}) = \big(\psi'(\boldsymbol{r}, \tilde{\tau}), H\,\psi'(\boldsymbol{r}, \tilde{\tau})\big). \tag{C.42}$$

   As the solution converges onto the proper ground state, the chemical potential should converge to a constant value—it serves as a useful quantitative measure of convergence.

5. Repeat steps 2 through 4, using ψ' as the initial state.

6. When the chemical potential converges to a constant value within the desired accuracy, the procedure can be stopped.

As a double check on the final solution, one can perform an additional integration by propagating the solution in real time to make sure that it is a stationary solution of H. That is, if allowed to propagate in real time, the density should be constant in time, while the phase should vary as $\exp(-i\mu t)$. We find the ITP method to be robust and to work remarkably well in solving for the condensate ground state $\phi_0(\boldsymbol{r})$. The procedure described here for a single-component system can easily be extended to treat an uncoupled, two-component system, as well as a coupled system to find the dressed states.

C.2.2 Solution of topological modes

Throughout Chapters 3 through 6 we discussed what we called "topological" solutions to the Gross-Pitaevskii equation, for both single and double component condensates. This is somewhat of a misnomer, for we apply it not only to vortex solutions, but also to noncirculating modes, such as a dipole or quadrupole. We use the term "topological" in this general way in order to distinguish between macroscopically occupied excited modes (what we are calling topological modes) and the elementary excitations (or equivalently collective modes for a Bose-consensed system), which only involve a small fraction of atoms being excited.

Symmetry ansatz

In the text, we have defined the topological modes in two distinct ways. In the first approach, we force the solution to have the desired symmetry through an appropriate ansatz solution, as was done in Chapter 3 for a single component where we made the ansatz $\psi(\boldsymbol{r}) = \phi_\kappa(\rho, z)e^{i\kappa\phi}$ for the vortex in section 3.4.1. This method was also used in Chapter 4 for the two-component system in both cases of a vortex and a dipole mode in section 4.4.2. For the case of the dipole, we forced the solution of one of the components to have a phase of π for $z < 0$ and a phase of 0 for $z > 0$.

The numerical implementation of this approach can be carried out using the ITP method, discussed in section C.2.1 for the solution of the ground state; one need only modify steps (1) and (3) in the procedure above. In step (1), obviously a different choice of initial guess is required. For example, in the case of the unit vortex, an appropriate guess is $\psi(\boldsymbol{r}, 0) = \phi_{\rm TF}(\rho, z)e^{i\phi}$, where $\phi_{\rm TF}(\rho, z)$ is the Thomas-Fermi ground state solution. Secondly, in addition to renormalizing the solution in step (3), one must also "imprint" the desired symmetry onto the solution. In the case of the vortex, this extra step simply involves multiplying the solution by $e^{i\kappa\phi}$. This was the method used to solve for the vortex shown in Figure 3.4 on page 43.

Eigenbasis solution

In the second approach, one solves for the eigenbasis of the Hamiltonian of the GP equation. In the limit of a single atom $N \to 1$, this is a well defined and trivial problem: one is simply finding the eigenbasis of the simple harmonic oscillator. However, in general, the problem of solving for the eigenbasis of the GP Hamiltonian is ill-defined due to the nonlinear term $|\psi|^2$. One can overcome this difficulty by specifying the decomposition of ψ in the, as yet undetermined, eigenbasis

$$|\psi\rangle = \sum_i c_i |\phi_i\rangle. \tag{C.43}$$

In section 3.4.2, we calculated the eigenstates and energies of the ground and first two excited eigenmodes, shown in Figure 3.7, for the one-dimensional version of the GP equation. In each case, we assumed all of the atoms in the system occupied the state shown. So, for example, in the case of the dipole mode, we took $c_1 = 1$ and $c_i = 0$, for $i \neq 1$ in Eq. (C.43). To clarify, the modes shown in Figure 3.7 are not considered to be part of the same eigenbasis; there are three different eigenbases, one for each choice of the decomposition Eq. (C.43).

In general, a macroscopic number of atoms in the condensate can occupy multiple modes, rather than simply one. In section 6.3.1, we discussed a two-mode model, in which there is a macroscopic population in two modes. Of course, for a two-component system, the decomposition Eq. (C.43) was generalized to

$$|\psi\rangle = \sum_i \Big[c_i |\phi_i\rangle|1\rangle + d_i |\phi_i\rangle|2\rangle \Big] . \tag{C.44}$$

In the two-mode problem presented in section 6.3.1, we assumed that c_0 and d_1 were the only nonzero coefficients in the expansion, so that both the ground state $|\phi_0\rangle$ and the dipole $|\phi_1\rangle$ states were macroscopically occupied.

The numerical implementation of this method can also be carried out using the ITP method. The basic idea is to supplement the ITP method with a Gram-Schmidt orthogonalization of eigenstates [147] in each time increment; one must do an imaginary-time propagation for all of the eigenstates being considered. The modifications to the ITP procedure (steps (1) through (6) above) are most easily understood by considering a specific example. Consider the case of a single component in the one dimensional model of the GP equation. Suppose we want to calculate the first excited, or dipole mode shown in Figure 3.7. In this case, we set $\psi = \psi_1$ in the nonlinear Hamiltonian and add the following steps to the ITP procedure

- Since we are interested in the first excited state, we must solve for both the ground ψ_0 and dipole ψ_1 states simultaneously, by propagating both solutions in imaginary time. In general, if we were looking for the nth excited mode, we would have to do an ITP on the first n states. In the simple limiting case of $N \to 1$, for which the nonlinear term in the Hamiltonian drops out, one would not have to solve for all of the states self-consistently, but could apply the ITP in sequence, starting with the ground state and progressing up to higher states after having found the solutions to all of the lower states.

- In step (1), we must now specify an initial guess for the ground state $\psi_0(\boldsymbol{r})$ and an initial guess for the first excited mode $\psi_1(\boldsymbol{r})$.

- In addition to renormalizing the solutions in step (3), we must now also orthogonalize the two states ψ_0 and ψ_1, using the Gram-Schmidt procedure (see, for example, section 9.3 of Arfken [147]).

This generalization of the ITP procedure to the solution of excited states can be understood by expanding each each function $\psi_0(\boldsymbol{r}, 0)$ and $\psi_1(\boldsymbol{r}, 0)$ in the eigenstates $\phi_i(\boldsymbol{r})$ of the Hamiltonian

$$\begin{aligned} \psi_0(\boldsymbol{r}, 0) &= \sum_i c_i \phi_i(\boldsymbol{r}), \\ \psi_1(\boldsymbol{r}, 0) &= \sum_i d_i \phi_i(\boldsymbol{r}). \end{aligned} \tag{C.45}$$

A "good" initial guess means that hopefully the coefficients in the expansions are such that $|c_0|^2 \approx 1$ and $|d_1|^2 \approx 1$, with the contribution from the other modes being minimal. Propagating these states in imaginary time by some small increment $\tilde{\tau}$ gives us

$$\begin{aligned} \psi_0(\boldsymbol{r}, \tilde{\tau}) &= \sum_i c_i e^{-\epsilon_i \tilde{\tau}} \phi_i(\boldsymbol{r}), \\ \psi_1(\boldsymbol{r}, \tilde{\tau}) &= \sum_i d_i e^{-\epsilon_i \tilde{\tau}} \phi_i(\boldsymbol{r}). \end{aligned} \tag{C.46}$$

We then perform the Gram-Schmidt orthogonalization, which amounts to subtracting out the ground-state contribution to the expansion of $\psi_1(\boldsymbol{r}, \tilde{\tau})$, so that the lowest energy state in the expansion of $\psi_1(\boldsymbol{r}, \tilde{\tau})$ becomes $\phi_1(\boldsymbol{r})$. As a result of this, $\phi_1(\boldsymbol{r})$ becomes the lowest energy state in the expansion and will have the slowest decay constant. For long times, it will be the only remaining term.

Bibliography

[1] M. H. ANDERSON, J. R. ENSHER, M. R. MATTHEWS, C. E. WEIMAN, AND E. A. CORNELL. Observation of Bose-Einstein condensation in a dilute atomic vapor. *Science*, 269:198, 1995.

[2] K. B. DAVIS, M.-O. MEWES, M. R. ANDREWS, N. J. VAN DRUTEN, D. S. DURFEE, D. M. KURN, AND W. KETTERLE. Bose-Einstein condensation in a gas of sodium atoms. *Phys. Rev. Lett.*, 75:3969, 1995.

[3] See the WWW page http://amo.phy.gasou.edu/bec.html/.

[4] STEVEN CHU. The manipulation of neutral particles. *Rev. Mod. Phys.*, 70(3):685, July 1998.

[5] CLAUDE N. COHEN-TANNOUDJI. Manipulating atoms with photons. *Rev. Mod. Phys.*, 70(3):707, July 1998.

[6] WILLIAM D. PHILLIPS. Laser cooling and trapping of neutral atoms. *Rev. Mod. Phys.*, 70(3):721, July 1998.

[7] C. J. MYATT, E. A. BURT, R. W. GHRIST, E. A. CORNELL, AND C. E. WIEMAN. Production of two overlapping Bose-Einstein condensates by sympathetic cooling. *Phys. Rev. Lett.*, 78(4):586, January 1997.

[8] M. R. MATTHEWS, D. S. HALL, D. S. JIN, J. R. ENSHER, C. E. WIEMAN, E. A. CORNELL, F. DALFOVO, C. MINNITI, AND S. STRINGARI. Dynamical response of a Bose-Einstein condensate to a discontinuous change in internal state. *Phys. Rev. Lett.*, 81(2):243, July 1998.

[9] D. S. HALL, J. R. ENSHER, D. S. JIN, M. R. MATTHEWS, C. E. WIEMAN, AND E. A. CORNELL. Recent experiments with Bose-condensed gases at JILA. *Proc. SPIE*, 3270:98, April 1998.

[10] D. S. HALL, M. R. MATTHEWS, J. R. ENSHER, C. E. WIEMAN, AND E. A. CORNELL. The dynamics of component separation in a binary mixture of Bose-Einstein condensates. *Phys. Rev. Lett.*, 81(8):1539, August 1998.

[11] D. S. HALL, M. R. MATTHEWS, C. E. WIEMAN, AND E. A. CORNELL. Measurements of relative phase in two-component Bose-Einstein condensates. *Phys. Rev. Lett.*, 81(8):1543, August 1998.

[12] E. A. CORNELL, D. S. HALL, M. R. MATTHEWS, AND C. E. WIEMAN. Having it both ways: Distinguishable yet phase-coherent mixtures of Bose-Einstein condensates. *J. Low Temp. Phys.*, 113:151, 1998.

[13] M. R. MATTHEWS, B. P. ANDERSON, P. C. HALJAN, D. S. HALL, J. E. WILLIAMS, M. J. HOLLAND, C. E. WIEMAN, AND E. A. CORNELL. Watching a superfluid untwist itself: Recurrence of Rabi oscillations in a Bose-Einstein condensate. *cond-mat/9906288*.

[14] M. R. MATTHEWS, B. P. ANDERSON, P. C. HALJAN, D. S. HALL, C. E. WIEMAN, AND E. A. CORNELL. *unpublished*.

[15] M. R. ANDREWS, C. G. TOWNSEND, H.-J. MIESNER, D. S. DURFEE, D. M. KURN, AND W. KETTERLE. Observation of interference between two Bose-Einstein condensates. *Science*, 275(0):637, January 1997.

[16] A. LEGGET. Low temperature physics, superconductivity and superfluidity. In P. Davies, editor, *The New Physics*. Cambridge University Press, Cambridge, 1989.

[17] M. O. MEWES, M. R. ANDREWS, D. M. KURN, D. S. DURFEE, C. G. TOWNSEND, AND W. KETTERLE. Output coupler for Bose-Einstein condensed atoms. *Phys. Rev. Lett.*, 78(4):582, 1997.

[18] E. W. HAGLEY, L. DENG, M. KOZUMA, J. WEN, K. HELMERSON, S. L. ROLSTON, AND W. D. PHILLIPS. A well-collimated quasi-continuous atom laser. *Science*, 283:1706, March 1999.

[19] I. BLOCH, T. W. HANSCH, AND T. ESSLINGER. Atom laser with a cw output coupler. *Phys. Rev. Lett.*, 82:3008, 1999.

[20] C. W. GARDINER AND P. ZOLLER. Quantum kinetic theory: A quantum kinetic master equation for condensation of a weakly interacting Bose gas without a trapping potential. *Phys. Rev. A*, 55:2902, 1997.

[21] C. W. GARDINER AND P. ZOLLER. Quantum kinetic theory III. Quantum kinetic master equation for strongly condensed trapped systems. *Phys. Rev. A*, 58:536, 1998.

[22] S. GIORGINI. Damping in dilute Bose gases: A mean-field approach. *Phys. Rev. A*, 57(4):2949, April 1998.

[23] A. MINGUZZI, M. L. CHIOFALO, AND M. P. TOSI. Generalized quantum hydrodynamics of a trapped dilute Bose gas. *Phys. Lett. A*, 236:237, 1997.

[24] E. ZAREMBA, T. NIKUNI, AND A. GRIFFIN. Dynamics of trapped Bose gases at finite temperature. *cond-mat/9903029*.

[25] M. RUSCH AND K. BURNETT. Mean-field theory for excitations of trapped Bose condensates at finite temperatures. *Phys. Rev. A*, 59:3851, 1999.

[26] H. T. C. STOOF. Coherent versus incoherent dynamics during Bose-Einstein condensation in atomic gases. *J. of Low Temp. Phys.*, 114:11, 1999.

[27] R. WALSER, J. WILLIAMS, J. COOPER, AND M. HOLLAND. Quantum kinetic theroy for a condensed bosonic gas. *Phys. Rev. A*, 59:3878, 1999.

[28] D. M. STAMPER-KURN, M. R. ANDREWS, A. P. CHIKKATUR, S. INOUYE, H.-J. MIESNER, J. STENGER, AND W. KETTERLE. Optical confinement of a Bose-Einstein condensate. *Phys. Rev. Lett.*, 80(10):2027, March 1998.

[29] T.-L. HO AND V.B. SHENOY. Binary mixtures of Bose condensates of alkali atoms. *Phys. Rev. Lett.*, 77:3276, 1996.

[30] C.K. LAW, H. PU, N.P. BIGELOW, AND J.H. EBERLY. Stability signature in two-species dilute Bose-Einstein condensates. *Phys. Rev. Lett.*, 79:3105, 1997.

[31] B.D. ESRY, C.H. GREENE, J.P. BURKE, AND J.L. BOHN. Hartree-Fock theory for double condensates. *Phys. Rev. Lett.*, 78:3594, 1997.

[32] H. PU AND N.P. BIGELOW. Properties of two-species Bose-condensates. *Phys. Rev. Lett.*, 80:1130, 1998.

[33] E. A. CORNELL, J. R. ENSHER, AND C. E. WIEMAN. Experiments in dilute atomic Bose-Einstein condensation. *Enrico Fermi summer school lectures, 1998*.

[34] W. KETTERLE, D.S. DURFEE, AND D.M. STAMPER-KURN. Making, probing and understanding Bose-Einstein condensates. *Enrico Fermi summer school lectures, 1998*.

[35] A. GRIFFIN. Conserving and gapless approximations for an inhomogeneous Bose gas at finite temperatures. *Phys. Rev. A*, 53:9341, 1996.

[36] N. P. PROUKAKIS, S. A. MORGAN, S. CHOI, AND K. BURNETT. Comparison of gapless mean-field theories for trapped Bose-Einstein condensates. *Phys. Rev. A*, 58:2435, 1998.

[37] S. CHAPMAN AND T. G. COWLING. *The Mathematical Theory of Non-Uniform Gases*. Cambridge University Press, London, 1960.

[38] A.I. AKHIEZER AND S.V. PELETMINSKII. *Statistical Methods of Statistical Physics*. Pergamon Press, Oxford, 1996.

[39] D. ZUBAREV, V. MOROZOV, AND G. ROPKE. *Statistical Mechanics of Nonequilibrium Processes*, volume 1. Akademie Verlag, Berlin, 1996.

[40] J. W. KANE AND L. P. KADANOFF. Green's functions and superfluid hydrodynamics. *Journal of Mathematical Physics*, 6, 1965.

[41] L. P. KADANOFF AND G. BAYM. *Quantum statistical mechanics: Green's function methods in equilibrium and nonequilibrium problems*. W.A. Benjamin, New York, 1962.

[42] G.C. WICK. The evaluation of the collision matrix. *Phys. Rev.*, 80:268, 1950.

[43] A. VAGLICA, C. LEONARDI, AND G. VETRI. Generalized Wick's theorem for a bosonic field in the squeezed vacuum. *J. of Mod. Opt.*, 37:1487, 1990.

[44] A.K. RAJAGOPAL AND E.C.G. SUDARSHAN. Some generalizations of the Marcinkiewicz theorem and its implications to certain approximation schemes in many-particle physics. *Phys. Rev. A*, 10:1852, 1974.

[45] D. ZUBAREV, V. MOROZOV, AND G. ROPKE. *Statistical Mechanics of Nonequilibrium Processes*, volume 2. Akademie Verlag, Berlin, 1996.

[46] K. HUANG AND C. N. YANG. Quantum-mechanical many-body problem with hard-sphere interaction. *Phys. Rev.*, 105:767, 1957.

[47] E. W. SMITH, J. COOPER, AND C. R. VIDAL. Unified Classical Path treatment of Stark broadening in plasmas. *Phys. Rev.*, 185:140, 1969.

[48] N. P. PROUKAKIS AND K. BURNETT. Generalized mean fields for trapped atomic Bose-Einstein condensates. *J. of Res. Natl. Inst. Stand. Technol.*, 101:457, 1996.

[49] M.J. BIJLSMA AND H. T. C. STOOF. Collisionless modes of a trapped Bose gas. *cond-mat/9902065*.

[50] E. P. GROSS. Structure of a quantized vortex in boson systems. *Nuovo Cimento*, 20:454, 1961.

[51] L. P. PITAEVSKII. Vortex lines in an imperfect Bose gas. *Sov. Phys. JETP*, 13:451, 1961.

[52] B.D. ESRY. Hartree-Fock theory for Bose-Einstein condensates and the inclusion of correlation effects. *Phys. Rev. A*, 55:1147, 1997.

[53] F. DALFOVO, S. GIORGINI, L. P. PITAEVSKII, AND S. STRINGARI. Theory of Bose-Einstein condensation in trapped gases. *Rev. of Mod. Phys.*, 71:463, 1999.

[54] F. DALFOVO, L. PITAEVSKII, AND S. STRINGARI. Order parameter at the boundary of a trapped Bose gas. *Phys. Rev. A*, 54:4213, 1996.

[55] G. BAYM AND C.J. PETHICK. Ground-state properties of magnetically trapped Bose-condensed rubidium gas. *Phys. Rev. Lett.*, 76:6, 1996.

[56] A. FETTER. Theory of a dilute low-temperature trapped Bose condensate. *Enrico Fermi summer school lectures, 1998*.

[57] E. LUNDH, C.J. PETHICK, AND H. SMITH. Vortices in Bose-Einstein-condensed atomic clouds. *Phys. Rev. A*, 58:4816, 1998.

[58] D. S. JIN, J. R. ENSHER, M. R. MATTHEWS, C. E. WIEMAN, AND E. A. CORNELL. Collective excitations of a Bose-Einstein condensate in a dilute gas. *Phys. Rev. Lett.*, 77(3):420, July 1996.

[59] M.-O. MEWES, M. R. ANDREWS, N. J. VAN DRUTEN, D. S. DURFEE, C. G. TOWNSEND, AND W. KETTERLE. Collective excitations of a Bose-Einstein condensate in a magnetic trap. *Phys. Rev. Lett.*, 77(6):988, August 1996.

[60] D. S. JIN, M. R. MATTHEWS, J. R. ENSHER, C. E. WIEMAN, AND E. A. CORNELL. Temperature-dependent damping and frequency shifts in collective excitations of a dilute Bose-Einstein condensate. *Phys. Rev. Lett.*, 78(5):764, February 1997.

[61] D. M. STAMPER-KURN, H.-J. MIESNER, S. INOUYE, M. R. ANDREWS, AND W. KETTERLE. Colisionless and hydrodynamic excitations of a Bose-Einstein condensate. *Phys. Rev. Lett.*, 81(3):500, July 1998.

[62] P.A. RUPRECHT, M. EDWARDS, K. BURNETT, AND C.W. CLARK. Probing the linear and nonlinear excitations of Bose-condensed neutral atoms in a trap. *Phys. Rev. A*, 54:4178, 1996.

[63] A.L. FETTER. Nonuniform states of an imperfect Bose gas. *Annals of Physics*, 70:67, 1972.

[64] R.J. DODD, K. BURNETT, M. EDWARDS, AND C.W. CLARK. Excitation spectroscopy of vortex states in dilute Bose-Einstein condensed gases. *Phys. Rev. A*, 56:587, 1997.

[65] A.A. SVIDZINSKY AND A.L. FETTER. Normal modes of a vortex in a trapped Bose-Einstein condensate. *Phys. Rev. A*, 58:3168, 1998.

[66] D. A. BUTTS AND D. S. ROKHSAR. Predicting signatures of rotating Bose-Einstein condensates. *Nature*, 397:327, 1999.

[67] D.L. FEDER, C.W. CLARK, AND B.I. SCHNEIDER. Vortex stability of interacting Bose-Einstein condensates confined in anisotropic harmonic traps. *cond-mat/9904269*.

[68] A.A. SVIDZINSKY AND A.L. FETTER. Stability of a vortex in a trapped Bose-Einstein condensate. *cond-mat/9811348*.

[69] B.M. CARADOC-DAVIES, R.J. BALLAGH, AND K. BURNETT. Coherent dynamics of vortex formation in trapped Bose-Einstein condensates. *cond-mat/9902092*.

[70] E. CORNELL. private communication.

[71] S.C. BENJAMIN, L. QUIROGA, AND N.F. JOHNSON. Analytic results for the linear and nonlinear reponse of atoms in a trap with a model interaction. *Phys. Rev. A*, 54:4309, 1996.

[72] M. BREWCZYK, K. RZAZEWSKI, AND C.W. CLARK. Strong-field driving of a dilute atomic Bose-Einstein condensate. *Phys. Rev. A*, 57:488, 1998.

[73] S.A. MORGAN, S. CHOI, K. BURNETT, AND M. EDWARDS. Nonlinear mixing of quasiparticles in an inhomogeneous Bose condensate. *Phys. Rev. A*, 57:3818, 1998.

[74] R. DUM, J.I. CIRAC, M. LEWENSTEIN, AND P. ZOLLER. Creation of dark solitons and vortices in Bose-Einstein condensates. *Phys. Rev. Lett.*, 80:2972, 1998.

[75] C. COHEN-TANNOUDJI, J. DUPONT-ROC, AND G. GRYNBERG. *Atom-photon interactions*. John Wiley & Sons, Inc., New York, 1992.

[76] T. R. GENTILE, B. J. HUGHEY, D. KLEPPNER, AND T. W. DUCAS. Experimental study of one- and two-photon Rabi oscillations. *Phys. Rev. A*, 40:5103, 1989.

[77] P.B. BLAKIE, R.J. BALLAGH, AND C.W. GARDINER. Dressed states of a two component Bose-Einstein condensate. *cond-mat/9902110*.

[78] A. BARONE AND G. PATERNO. *Physics and Applications of the Josephson Effect*. Wiley, New York, 1982.

[79] S. FUJITA AND S. GODOY. *Quantum Statistical Theory of Superconductivity*. Plenum Press, New York, 1996.

[80] P. L. TAYLOR. *A Quantum Approach to the Solid State*. Prentice Hall, New Jersey, 1970.

[81] V.V. SCHMIDT. *The Physics of Superconductors*. Springer, Berlin, 1997.

[82] M. TINKHAM. *Introduction to Superconductivity*. McGraw-Hill, Inc., New York, 1996.

[83] J. JAVANAINEN. Oscillatory exchange of atoms between traps containing Bose condensates. *Phys. Rev. Lett.*, 57:3164, 1986.

[84] M. JACK, M. COLLETT, AND D. WALLS. Coherent quantum tunneling between two Bose-Einstein condensates. *Phys. Rev. A*, 54:R4625, 1996.

[85] G. MILBURN, J. CORNEY, E. WRIGHT, AND D. WALLS. Quantum dynamics of an atomic Bose-Einstein condensate in a double-well potential. *Phys. Rev. A*, 55:4318, 1997.

[86] J. RUOSTEKOSKI AND D. WALLS. Nondestructive optical measurement of relative phase between two Bose-Einstein condensates. *Phys. Rev. A*, 56:2996, 1997.

[87] I. ZAPATA, F. SOLS, AND A. LEGGETT. Josephson effect between trapped Bose-Einstein condensates. *Phys. Rev. A*, 57:R28, 1998.

[88] A. J. LEGGETT. How can we use low-temperature systems to shed light on questions of more general interest. *J. Low Temp. Phys.*, 110:719, 1998.

[89] A. SMERZI, S. FANTONI, S. GIOVANAZZI, AND S. SHENOY. Quantum coherent atomic tunneling between two trapped Bose-Einstein condensates. *Phys. Rev. Lett.*, 79(25):4950, 1997.

[90] S. RAGHAVAN, A. SMERZI, S. FANTONI, AND S.R. SHENOY. Coherent oscillations between two weakly coupled Bose-Einstein condensates: Josephson effects, pi oscillations, and macroscopic quantum self-trapping. *Phys. Rev. A*, 59:620, 1999.

[91] I. MARINO, S. RAGHAVAN, S. FANTONI, S. R. SHENOY, AND A. SMERZI. Bose-condensate tunneling dynamics: Momentum-shortened pendulum with damping. *Phys. Rev. A*, 60(1):487, July 1999.

[92] P. VILLAIN AND M. LEWENSTEIN. Dephasing of Josephson oscillations between two coupled Bose-Einstein condensates. *Phys. Rev. A*, 59:2250, 1999.

[93] P. OHBERG AND S. STENHOLM. Internal Josephson effect in trapped double condensates. *Phys. Rev. A*, 59:3890, 1999.

[94] N.I. AKHIEZER. *Elements of the Theory of Elliptic Functions*. American Mathematical Society, Providence, 1990.

[95] P. L. WALKER. *Elliptic Functions: A Constructive Approach*. Wiley and Sons, England, 1996.

[96] A. G. GREENHILL. *The Applications of Elliptic Functions*. Dover, New York, 1959.

[97] P. S. JULIENNE, F. H. MIES, E. TIESINGA, AND C. J. WILLIAMS. Collisional stability of double Bose condensates. *Phys. Rev. Lett.*, 78(10):1880, March 1997.

[98] S. J. J. M. F. KOKKELMANS, H. M. J. M BOESTEN, AND B. J. VERHAAR. Role of collisions in creation of overlapping Bose condensates. *Phys. Rev. A*, 55(3):R1589, March 1997.

[99] JAMES P. BURKE, JR., JOHN L. BOHN, B. D. ESRY, AND CHRIS H. GREENE. Impact of the ^{87}Rb singlet scattering length on suppressing inelastic collisions. *Phys. Rev. A*, 55(4):R2511, April 1997.

[100] J. STENGER, S. INOUYE, D. M. STAMPER-KURN, H.-J. MIESNER, A. P. CHIKKATUR, AND W. KETTERLE. Spin domains in ground-state Bose-Einstein condensates. *Nature*, 396:345, November 1999.

[101] B.D. ESRY AND C. H. GREENE. Low-lying excitations of double Bose-Einstein condensates. *Phys. Rev. A*, 57:1265, 1998.

[102] A. SINATRA, P.O. FEDICHEV, Y. CASTIN, J. DALIBARD, AND G.V. SHLYAPNIKOV. Dynamics of two interacting Bose-Einstein condensates. *Phys. Rev. Lett.*, 82:251, 1999.

[103] N. RAMSEY. *Molecular Beams*. Clarendon Press, Oxford, 1956.

[104] A. ESCHMANN, R.J. BALLAGH, AND B.M. CARADOC-DAVIES. Formation of Ramsey fringes in double Bose-Einstein condensates. *cond-mat/9903013*.

[105] T.-L. HO. Vortices and instatons in ferromagnetic Bose gas and spin-1/2 Bose gas. *unpublished*.

[106] A. MESSIAH. *Quantum Mechanics*, volume 2. John Wiley and Sons, New York, 1966.

[107] K.-P. MARZLIN AND W. ZHANG. Vortex coupler for atomic Bose-Einstein condensates. *Phys. Rev. Lett.*, 79:4728, 1997.

[108] E.L. BOLDA AND D.F. WALLS. Creation of vortices in a Bose-Einstein condensate by a raman technique. *Phys. Lett. A*, 246:32, 1998.

[109] O. LUITEN, M. REYNOLDS, AND J. WALRAVEN. Kinetic theory of the evaporative cooling of a trapped gas. *Phys. Rev. A*, 53(1):382, 1996.

[110] W. KETTERLE AND N. J. VAN DRUTEN. Evaporative cooling of trapped atoms. In *Advances in Atomic, Molecular, and Optical Physics, vol. 37*, page 181, New York, 1996. Acedemic Press.

[111] R. DUM, P. ZOLLER, AND H. RITSCH. Monte-Carlo simulation of the atomic master eqaution for spontaneous emission. *Phys. Rev. A*, 45:4879, 1992.

[112] C. W. GARDINER, A. S. PARKINS, AND P. ZOLLER. Wave-function quantum stochastic differential-equations and quantum-jump simulation methods. *Phys. Rev. A*, 46:4363, 1992.

[113] R. DUM, A. S. PARKINS, P. ZOLLER, AND C. W. GARDINER. Monte-Carlo simulations of master-equations in quantum optics for vacuum. *Phys. Rev. A*, 46:4382, 1992.

[114] J. DALIBARD, Y. CASTIN, AND K. MØLMER. Wave-function approach to dissipative processes in quantum optics. *Phys. Rev. Lett.*, 68:580, 1992.

[115] K. MOLMBER, Y. CASTIN, AND J. DALIBARD. Monte-Carlo wave-function method in quantum optics. *J. Opt. Soc. Am. B*, 3:524, 1993.

[116] H. J. CARMICHAEL. *An Open Systems Approach to Quantum Optics*. Springer-Verlag, Berlin, 1993.

[117] N. GISIN AND I. C. PERCIVAL. Wave-function approach to dissipative processes–Are there quantum jumps? *Phys. Lett. A*, 167:315, 1992.

[118] M. HOLLAND, J. WILLIAMS, K. COAKLEY, AND J. COOPER. Trajectory simulation of kinetic equations for classical systems. *Quantum Semiclass. Opt.*, 8(3):571, 1996.

[119] W. H. LOUISELL. *Quantum Statistical Properties of Radiation*. Wiley, New York, 1973.

[120] J. P. BLAIZOT AND G. RIPKA. *Quantum Theory of Finite Systems*. MIT Press, Cambridge, USA, 1986.

[121] D. JAKSCH, C. W. GARDINER, AND P. ZOLLER. Quantum kinetic theory 2. Simulation of the quantum boltzmann master equation. *Phys. Rev. A*, 56:575, 1997.

[122] I. W. BUSBRIDGE. Some integrals involving Hermite polynomials. *London Mathematical Society Journal*, 23:135, 1948.

[123] S. GIORGINI, L. P. PITAEVSKII, AND S. STRINGARI. Condensate fraction and critical temperature of a trapped interacting Bose gas. *Phys. Rev. A*, 54(6):R4633, December 1996.

[124] W. KETTERLE AND N. J. VAN DRUTEN. Bose-Einstein condensation of a finite number of particles trapped in one or three dimensions. *Phys. Rev. A*, 54:656, 1996.

[125] D.W. SNOKE AND J.P. WOLFE. Population-dynamics of a Bose-gas near saturation. *Phys. Rev. B*, 39:4030, 1989.

[126] M. HOLLAND, J. WILLIAMS, AND J. COOPER. Bose-Einstein condensation: Kinetic evolution obtained from simulated trajectories. *Phys. Rev. A*, 55(5):3670, 1997.

[127] C. A. SACKETT, C. C. BRADLEY, AND R. G. HULET. Optimization of evaporative cooling. *Phys. Rev. A*, 55(5):3797, 1997.

[128] KIRSTINE BERG-SØRENSEN. Kinetics for evaporative cooling of a trapped gas. *Phys. Rev. A*, 55(2):1281, 1997.

[129] M. HOLLAND, K. BURNETT, C. GARDINER, J. I. CIRAC, AND P. ZOLLER. Theory of an atom laser. *Phys. Rev. A*, 54:R1757, 1996.

[130] H. WISEMAN, A. MARTINS, AND D. WALLS. An atom laser based on evaporative cooling. *Quantum Semiclass. Opt.*, 8:737, 1996.

[131] R. J. BALLAGH, K. BURNETT, AND T. F. SCOTT. Theory of an output coupler for Bose-Einstein condensed atoms. *Phys. Rev. Lett.*, 78(9):1607, 1997.

[132] J. J. HOPE. Theory of input and output of atoms from an atomic trap. *Phys. Rev. A*, 55(4):R2531, 1997.

[133] W. KETTERLE AND HANS-JOACHIM MIESNER. Coherence properties of Bose condensates and atom lasers.

[134] E. CORNELL, C. MONROE, AND C. WIEMAN. Multiply loaded, ac magnetic trap for neutral atoms. *Phys. Rev. Lett.*, 67(18):2439, 1991.

[135] C. J. MYATT, N. R. NEWBURY, R. W. GHRIST, S. LOUTZENHISER, AND C. E. WIEMAN. Multiply loaded magneto-optical trap. *Opt. Lett.*, 21:290, 1996.

[136] C. G. TOWNSEND, N. H. EDWARDS, C. J. COOPER, K. P. ZETIE, C. J. FOOT, A. M. STEANE, P. SZRIFTGISER, H. PERRIN, AND J. DALIBARD. Phase-space density in the magneto-optical trap. *Phys. Rev. A*, 52(2):1423, 1995.

[137] E. A. BURT, R. W. GHRIST, C. J. MYATT, M. J. HOLLAND, E. A. CORNELL, AND C. E. WIEMAN. Coherence, correlations, and collisions: What one learns about Bose-Einstein condensates from their decay. *Phys. Rev. Lett.*, 79(3):337, 1997.

[138] C. W. GARDINER, P. ZOLLER, R. J. BALLAGH, AND M. J. DAVIS. Kinetics of Bose-Einstein condensation in a trap. *Phys. Rev. Lett.*, 79(10):1793, September 1997.

[139] A. L. GARCIA. *Numerical Methods for Physics*. Prentice Hall, New Jersey, 1994.

[140] N. J. GIORDANO. *Computational Physics*. Prentice Hall, New Jersey, 1997.

[141] W. H. PRESS, S. A. TEUKOLSKY, W. T. VETTERLING, AND B. P. FLANNERY. *Numerical Recipes in C*. Cambridge University Press, Cambridge, 1992.

[142] F. J. VESELY. *Computational Physics: An Introduction*. Plenum Press, New York, 1994.

[143] A. ROUHI AND J. WRIGHT. Spectral implementation of a new operator splitting method for solving partial differential equations. *Computers in Physics*, 9:554, 1995.

[144] M. R. HERMANN AND J. A. FLECK. Split-operator spectral method for solving the time-dependent schrodinger equation in spherical coordinates. *Phys. Rev. A*, 38:6000, 1988.

[145] M.J. HOLLAND, D.S. JIN, M.L. CHIOFALO, AND J. COOPER. Emergence of interaction effects in Bose-Einstein condensation. *Phys. Rev. Lett.*, 78:3801, 1997.

[146] B. D. ESRY. *Many-Body Effects in Bose-Einstein Condensates of Dilute Atomic Gases*. PhD thesis, Univerity of Colorado, 1997.

[147] G. ARFKEN. *Mathematical Methods for Physicists, 3rd ed.* Academic Press, San Diego, 1985.